UNIVERSITY OF CALIFORNIA
RIVERSIDE

Well-Defined Heterogeneous Catalytically Active Ion Pairs on the Surface of Oxides

A Dissertation submitted in partial satisfaction
of the requirements for the degree of

Doctor of Philosophy

in

Chemistry

by

Damien Culver

September 2020

Dissertation Committee:
Dr. Matthew Conley, Chairperson
Dr. William Harman
Dr. Vincent Lavallo

The Dissertation of Damien Culver is approved:

Committee Chairperson

University of California, Riverside

Acknowledgements

Foremost, I would like to acknowledge the opportunity and mentorship that Dr. Matthew P. Conley has provided to me the past 5 years. Matt has been the best graduate mentor that I could have asked for. Dr. Hosein Tafazolian helped my hone my chemistry skills and provided excellent insight into chemistry research as well as many other topics. I would like to thank Jessica, Winn, Kavya, and Jiaxin for being a big part of my development and a great help over the years. I learned a lot about basic organometallic reactions and mechanisms from Professor Vincent Lavallo through his class and I thank him for being a part of my defense committee. I also thank Professor Hill Harman for being on my defense committee and for research advice during joint group meetings. The NMR facility managers Dan Borchardt and Lingchao Zhu taught me a great deal about NMR spectroscopy. The other chemistry department staff at the University of California, Riverside have been helpful in navigating the storm that is graduate school. I thank the University of California, Riverside for the opportunity to learn and develop my understanding of chemistry these past five years. Dr. Graham Lief and the Chevron-Phillips Co. were instrumental in the work completed in chapter 5 of this dissertation. The chemistry faculty at Adams state university where I completed my B.S. in chemistry inspired me to pursue inorganic chemistry at the graduate level. Finally, thank you reader for taking a look at this dissertation and I hope you enjoy and learn something new.

The text, figures, and schemes for the following chapters have been reproduced, in part, from the following published manuscripts.

Chapter 2:
Culver, D. B., Tafazolian, H. & Conley, M. P. A Bulky Pd(II) α-Diimine Catalyst Supported on Sulfated Zirconia for the Polymerization of Ethylene and Copolymerization of Ethylene and Methyl Acrylate. *Organometallics* **2018**, 37, 1001-1006.

Chapter 3:
Culver, D. B. & Conley, M. P. Activation of C-F Bonds by Electrophilic Organosilicon Sites Supported on Sulfated Zirconia. *Angew. Chem. Int. Ed.* **2018**, 57, 14902-14905.

Chapter 4:
Culver, D. B.; Venkatesh, A.; Huynh, W.; Rossini, A. J. & Conley, M. P. $Al(OR^F)_3$ (R^F = $C(CF_3)_3$) Activated Silica: A Well-Defined Weakly Coordinating Surface Anion. *Chem. Sci*. **2020,** 11, 1510-1517.

The co-author (Matthew P. Conley) listed in the above publications directed and supervised the research which forms the basis for this dissertation.

ABSTRACT OF THE DISSERATION

Well-Defined Heterogeneous Catalytically Active Ion Pairs on the Surface of Oxides

by

Damien Culver

Doctor of Philosophy, Graduate Program in Chemistry
University of California, Riverside, September 2020
Dr. Matthew P. Conley, Chairperson

Industry often prefers heterogeneous catalysts because solids are easier to remove from the reaction mixture, less likely to foul the reactor, easier to recycle, and produce unique products. However, establishing structure-activity relationships for heterogeneous catalysts is often challenging. Surface organometallic chemistry utilizes techniques similar to homogeneous chemistry to synthesize and characterize heterogeneous catalysts. Ion pairs are common catalysts for chemical transformations and in solution there is a vast library to choose from. Heterogeneous ion pairs are equally important but have been examined in far less detail. The copolymerization of ethylene and polar monomers to yield copolymers with high molecular weights and narrow polydispersities is a challenge that has not been approached by heterogeneous catalysts. Part of this work presents the synthesis of a single-site (α-diimine)$PdMe^+$ catalyst on the surface of sulfated zirconium oxide (SZO) for the copolymerization of methyl acrylate and ethylene.

Heterogeneous Lewis acids are commonly used in catalytic transformations; however, the concentration of active sites is usually very low, and the structure is ambiguous. This work approaches this challenge by synthesizing a well-defined silylium-like ion on the surface of SZO ([^{i}Pr$_3$Si][SZO]), the first example on an oxide. [^{i}Pr$_3$Si][SZO] hydrodefluorinates several inert sp^3 C-F bonds in the presence of excess triethylsilane. This study showed that SZO is not as weakly coordinating as common homogeneous weakly coordinating anions, such as carborane and $BAr^{F}_{4}^{-}$ anions. Therefore, we wanted to design a weaker coordinating heterogeneous anion on the surface of an oxide. The strong Lewis acid PhF-Al(OC(CF$_3$)$_3$)$_3$ coordinates to -OH sites on the surface of partially dehydroxylated silica forming -O(H)-Al(OC(CF$_3$)$_3$)$_3$ which upon deprotonation forms weakly coordinating ion pairs. One of the ion pairs [^{i}Pr$_3$Si][-OAl(OC(CF$_3$)$_3$)$_3$] has a ^{29}Si NMR chemical shift 17 ppm downfield of [^{i}Pr$_3$Si][SZO], supporting that the -OAl(OC(CF$_3$)$_3$)$_3^{-}$ anion is weaker coordinating than the sulfate anions on SZO. The last part of this work examines the structure of the active site in the ternary catalyst: Cp^{b}2ZrCl$_2$ + ^{i}Bu$_3$Al + Al$_2$O$_3$, a Ziegler-Natta type ethylene polymerization catalyst. Model catalysts, activity studies, and solid-state ^{2}H NMR studies show that the active catalyst structure is a Cp^{b}2Zr-H^{+} cation on the surface of Al$_2$O$_3$.

Table of Contents

List of Figures

List of schemes

List of tables

Chapter 1 Introduction to the Dissertation

Heterogeneous (solid) catalysts are preferred by industry because they are easier to separate from a reaction mixture, less likely to foul a reactor, and can often be regenerated by heat treatment.[1] Industrial heterogeneous catalysts are commonly synthesized by adsorption of a metal precursor onto the surface of an oxide and activation using a heat treatment in the presence of a substrate, air, or H_2. Catalysts synthesized by this method typically contain a distribution of metal sites, and only a small percentage of these sites are catalytically active. Therefore, characterization of the structure of the active site is challenging, which ultimately limits the application of structure-activity relationships in heterogeneous catalyst development. Organometallic complexes supported onto the surface of oxides serve as models for active sites in heterogeneous catalysts because they are usually well-defined, amenable to characterization, allow for more control of the catalyst active site structure, and are active in catalytic reactions.

The primary goal of surface organometallic chemistry is to design and characterize organometallic sites bound to oxide surfaces in an effort to understand and improve classic heterogeneous catalysts, or to discover new heterogeneous catalysts.[1–6] A variety of high surface area oxides are readily available, though most studies focus on reactions of organometallics with partially dehydroxylated silica.[1–3] The surface of silica contains hydroxyls (Si-OH), physisorbed water, and Si-O-Si bridges. Heating silica to ~140 °C removes physisorbed water, resulting in a silica surface containing isolated, vicinal, and geminal silanols (Scheme 1.1.1).[7] Higher temperature treatments under vacuum result in

dehydroxylation of vicinal silanols, which forms water and Si-O-Si bridges. For example, Aerosil-200 (200 $m^2\ g^{-1}$) heated to 700 °C under vacuum contains ~1 SiOH nm^{-2}, from the reaction of the dehydroxylated silica with a metal alkyl (e.g. RLi or RMgX) and quantification of the alkane products generated in this reaction, with minimal loss of surface area. Other oxides have more complicated surface chemistry, but the dehydroxylation step is important to remove physisorbed water and to give some degree of site-isolation.

Scheme 1.1.1. Partial dehydroxylation of silica

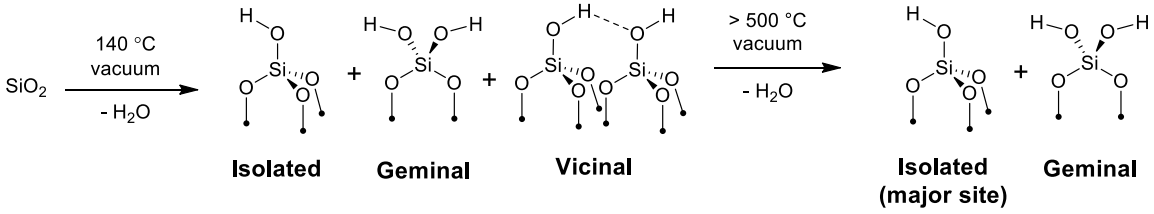

A classic example of organometallics reacting with silica is the reaction of $Zr(CH_2{}^tBu)_4$ with silica partially dehydroxylated at 500 °C ($SiO_{2\text{-}500}$) to form neopentane, and ≡SiO-$Zr(CH_2{}^tBu)_3$ (Scheme 1.1.2).[8,9] One equivalent of neopentane is released per Zr in this reaction. FT-IR spectroscopy shows that the $\nu_{O\text{-}H}$ is no longer present in $Zr(CH_2{}^tBu)_4$ contacted silica and contains the $\nu_{C\text{-}H}$ stretches for the -$CH_2{}^tBu$ groups. Solid-state ^{13}C magic angle spinning (MAS) NMR and X-ray adsorption spectroscopy are also consistent with the formation of ≡SiO-$Zr(CH_2{}^tBu)_3$.[10,11] The organozirconium sites react with H_2 at 150 °C to form methane, $(\equiv SiO)_3ZrH$ (major), and $(\equiv SiO)_2ZrH_2$ (minor),[12] showing that organometallics supported on oxides are reactive. This reaction to form these products is

complex, but involves hydrogenolysis of C-C bonds,[11] and rearrangements of Zr-H and nearby siloxane (Si-O-Si) bridges to form Zr-O and Si-H bonds.[12]

Scheme 1.1.2. Reaction of $SiO_{2\text{-}500}$ with $Zr(CH_2{}^tBu)_4$ and example surface reactions.

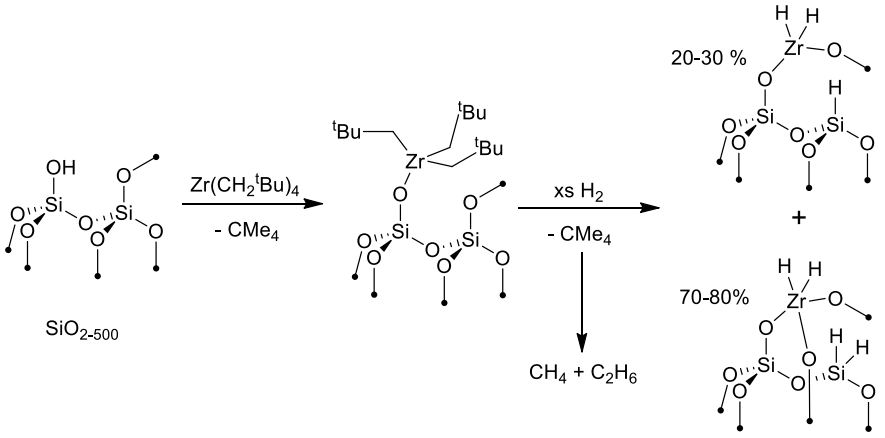

Silica is an amorphous surface. Though most organometallics react with ≡SiOH to form ≡SiO-M type surface species, not all organometallics supported on silica are in identical environments.[13] The reaction of $Ta(CH^tBu)(CH_2{}^tBu)_3$ with $SiO_{2\text{-}700}$ releases one equivalent of neopentane and the expected ≡SiO-$Ta(CH^tBu)(CH_2{}^tBu)_2$ is observed by solid-state NMR. However, Extended X-ray Absorption Fine Structure (EXAFS) data showed that the Ta center interacts with two surface oxygens. The covalent average SiO-Ta bond length is 1.898 Å and a second longer interaction with a nearby siloxane bridge ($Ta\text{-}O(SiO_x)_2$ = 2.64 Å, Figure 1.1.1A).[14] This is a common feature on silica surfaces, and several studies showed this in ≡SiO-$Re(\equiv C^tBu)(=CH^tBu)(CH_2{}^tBu)$,[15] ≡SiO-$W(=NAr)(=CH^tBu)(CH_2{}^tBu)$,[16] ≡SiO-$Lu(CHTMS_2)_2$,[17] ≡SiO-$TaCl_2Me_2$,[18] and ≡SiO-$ScCp^*{}_2$[19] surface species (Figure 1.1.1).

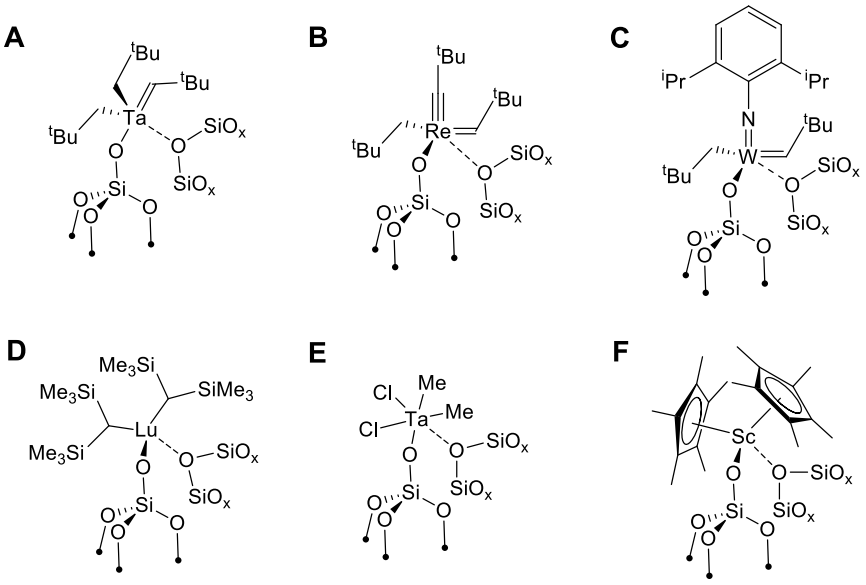

Figure 1.1.1. Representative examples of characterized κ^2 organometallic structures on $SiO_{2\text{-}700}$.

Partially dehydroxylated silica is the most common oxide used in organometallic grafting reactions. The limitation of this support is the formation of ≡SiO-ML_n species, which is undesirable if surface ion pairs [L_nM][oxide] are needed for a catalytic reaction (Scheme 1.1.3). This necessity is most obvious in olefin polymerization catalysts, a very important class of heterogeneous catalyst used in industry to produce most polyolefins. Extensive solution studies showed that organometallic M-R^+ are very active catalyst for this reaction,[20–26] which has obvious implications in the design of well-defined heterogeneous catalysts for olefin polymerization.

Scheme 1.1.3. Formation of covalent or ion paired surface species (* = Lewis acid site)

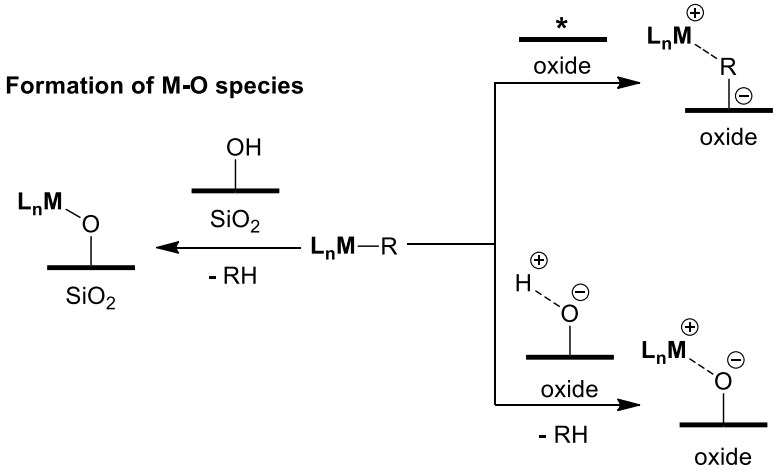

The reaction of $Cp^*_2ThMe_2$ with aluminum oxide dehydroxylated at 1000 °C, a material that lacks -OH groups, forms $[Cp^*_2ThMe][Me\text{-}Al\equiv]$ sites (Scheme 1.1.4).[27–29] This reaction probably occurs by methide abstraction by low coordinate Al sites that are strong Lewis acids.[30–34] The solution analogy to this remarkable reaction is Cp_2ZrMe_2 with $B(C_6F_5)_3$ to form $[Cp_2ZrMe][MeB(C_6F_5)_3]$,[20] but the surface reaction predates the solution chemistry by six years. Indeed, $[Cp^*_2ThMe][Me\text{-}Al\equiv]$ were discovered the same year as Jordan's $[Cp_2ZrMe(THF)][BPh_4]$,[35] and is one of the earliest examples of a characterized intermediate that relates to the proposed active site in the Ziegler Natta olefin polymerization catalyst.

Scheme 1.1.4. Reaction of $Cp^*_2ThMe_2$ with surface Lewis acid sites (* = Lewis acid site) on the surface of alumina

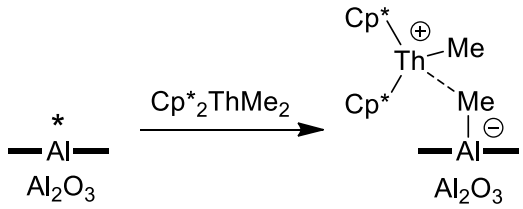

Alumina dehydroxylated at 500 °C, a lower temperature than the organothorium example mentioned above, reacts with Cp^*ZrMe_3 to form $Cp^*Zr(Me)_2$-OAl≡ and small amounts of $[Cp^*ZrMe_2][Me\text{-}Al\equiv]$ (Figure 1.1.2A).[36] Similar products were formed in reactions of Cp^*ZrMe_3 with SiO_2/Al_2O_3 (Figure 1.1.2B).[36] The cationic species are active in the polymerization of ethylene. Cp^*ZrMe_3 grafted on the surface of partially dehydroxylated silica forms $Cp^*Zr(Me)_2$-OSi≡ sites that are inactive in polymerization reactions (Figure 1.1.2C).[37] Similar to solution catalysts, $Cp^*Zr(Me)_2$-OSi≡ reacts with $B(C_6F_5)_3$ to form $[Cp^*Zr(Me)\text{-}OSi\equiv][MeB(C_6F_5)_3]$ ion pairs that are active in ethylene polymerization, but decompose under polymerization conditions (Figure 1.1.2C).[37,38] A related strategy to generate cationic organozirconium species on silica is the reaction of partially dehydroxylated silica with with $B(C_6F_5)_3$/aniline mixtures to form $[Et_2PhNH][\equiv SiOB(C_6F_5)_3]$, which react with Cp^*ZrMe_3 to form $Cp^*ZrMe_2NPhEt_2^+$ cations (Figure 1.1.2D).[36,39–41] More recently, the activator $[Et_2PhNH][(\equiv SiO)_2Al(C_6F_5)_2]$ was developed for the activation of zirconocene dichlorides in the presence of excess triisobutylaluminum in-situ to generate active polymerization catalysts.[42]

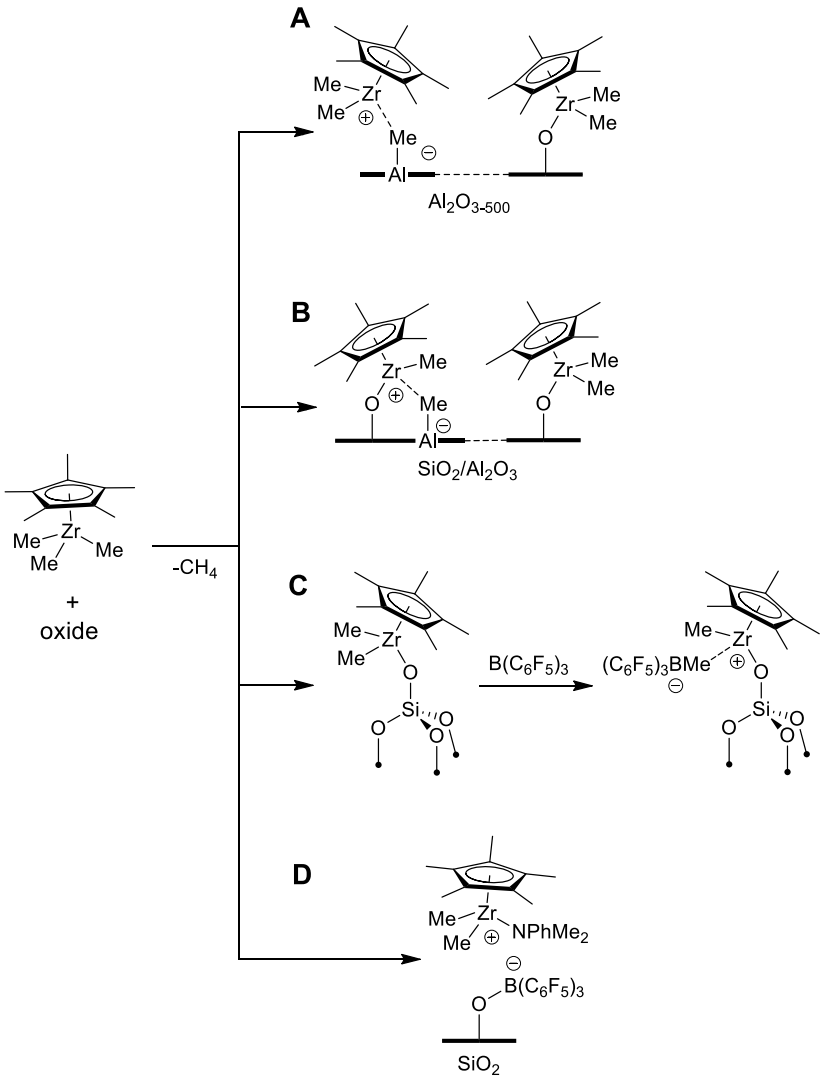

Figure 1.1.2. Representative examples of Cp^*ZrMe_2-oxide complexes.

Sulfated metal oxides (SMOs) contain surface sulfate anions.[43] Sulfated zirconium oxide (SZO) isomerizes butane at a lower temperature than 100% H_2SO_4, suggesting that these materials contain Bronsted superacid -OH sites.[44,45] Determination of acid strength on oxides is challenging,[46] but adsorption of probes to relate acid strength to molecular behavior is fairly common.[47] Colorimetric studies with 1,3,5-trinitrobenzene, a Hammet

indicator that is not protonated by neat H_2SO_4, suggested that sulfated zirconium oxide is 4 orders of magnitude stronger than 100 % H_2SO_4.[45] However, this result is inconsistent with solid-state NMR measurements of SZO contacted with pyridine-N15 and Me_3PO.[48] Recent studies showed that $tBu_2P(Ar)$ bind weakly to the SZO surface in MeCN slurries, and confirm that the -OH sites on SZO are not superacids.[49]

Periodic DFT calculations of ZrO_2 slabs show that H_2SO_4 absorbs to the surface to form tripodal sulfates in SZO (Figure 1.1.3A).[50] The tripodal sulfate is ~20 kcal mol^{-1} more stable than the bipodal sulfate.[50] This suggests that the tripodal sulfate is the major surface site in SZO, and agrees with the experimental and predicted $\nu_{S=O}$ and ν_{S-O} IR stretches.[50] The optimized SZO slabs do not contain protons interacting with the sulfate anions, but rather nearby Zr-O-Zr bridges. This is intuitive because H_2SO_4 is a strong acid and ZrO_2 is a weak base. The gas phase acidity of these sites, defined by the reaction in Figure 1.1.3B, is 280 kcal mol^{-1}.[50] This value is lower than the gas phase acidity of isolated silanol models (Figure 1.1.3C, 335 kcal mol-1).[51] This result indicates that SZO contains more acidic -OH sites than silica.

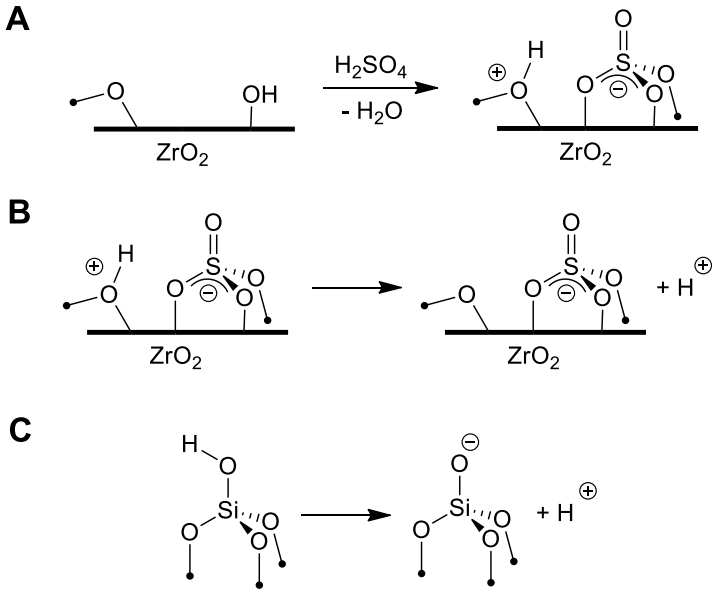

Figure 1.1.3. A) formation of sulfate anions on the surface of ZrO_2; B) equation for the deprotonation of SZO for GPA calculations; and C) equation for the deprotonation of isolated silanols for GPA calculations

The acidic -OH sites on SMOs promote the formation of [M][O] ion pairs. Cp^*ZrMe_3 reacts with sulfated metal oxides (oxide = Al_2O_3, ZrO_2, or SnO_2) forming methane and $[Cp^*ZrMe_2][SMO]$, Figure 1.1.4A.[4,52–58] The ^{13}C NMR chemical shifts of these complexes are similar to analogous homogeneous $[Cp^*ZrMe_2][WCA]$ ion pairs supporting that the SMOs are weakly coordinating. $[Cp^*ZrMe_2][SMO]$ and similar complexes have been thoroughly studied for the polymerization of ethylene, and the hydrogenation of arenes.[4,52–58] This methodology extends to organoiridium complexes for C-H activation and propene hydrogenation, showing the generality of this approach (Figure 1.1.4B).[59,60]

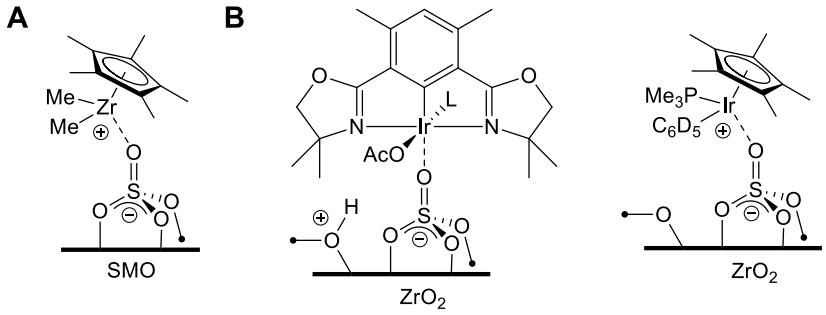

Figure 1.1.4. Representative example of an organozirconium cation on the surface of sulfated metal oxides; and B) examples of organoiridium complexes on the surface of SZO.

SMOs form weakly coordinating ion pairs with organometallic complexes [M][O], however these surface species are sometimes complicated by surface sites other than the sulfate ions that form undesirable or inactive side products. SMOs also contain pyrosulfate groups that are strong oxidants and are implicated in alkane isomerization,[61,62] interactions of SMOs with benzene,[62,63] and grafting reactions with organometallics.[64] $Cp^*Ir(PMe_3)PhMe$ reacts with surface pyrosulfates on SAO by single electron transfer and C-H activation of the Cp* ligand (Scheme 1.1.5).[64] SMOs also contain physisorbed water that interfere with formation of pyrosulfates, and result in the more typical protonolysis pathways described above. The excess water can be removed at higher dehydroxylation temperatures, but this increases the percentage of reactive pyrosulfates that also cause undesirable side reactions.[64]

Scheme 1.1.5. Pyrosulfates probed on SAO with an organoiridium complex.

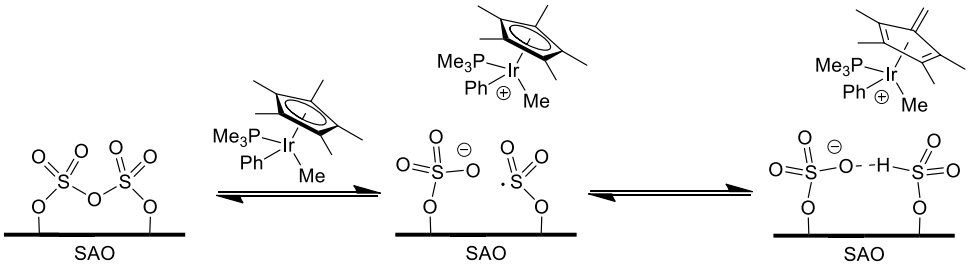

Conceptually, the ability of an anion to form a strong or a weak ion pair is related to the strength of the conjugate Brønsted acidity, which matches the behavior described above. Partially dehydroxylated silica contains -OH sites that are weak acids and react with organometallics to form SiO-M. SMOs contain acidic -OH sites that react with organometallics to form [M][O]. This behavior parallels reactivity trends in solution. Many of the 1st generation weakly coordinating anions (WCAs) shown in Figure 1.1.5 originated from studies of Brønsted superacids, defined as acids stronger than 100% H_2SO_4.[65] These anions continue to find applications in synthetic chemistry, as counter-anions for electrolytes, and counter-anions for some organometallic catalysts. More modern WCAs are the electron deficient polyhalogenated species shown in Figure 1.1.5. When the conjugate acid of these anions are isolable, they are the strongest known Bronsted acids.[66–69]

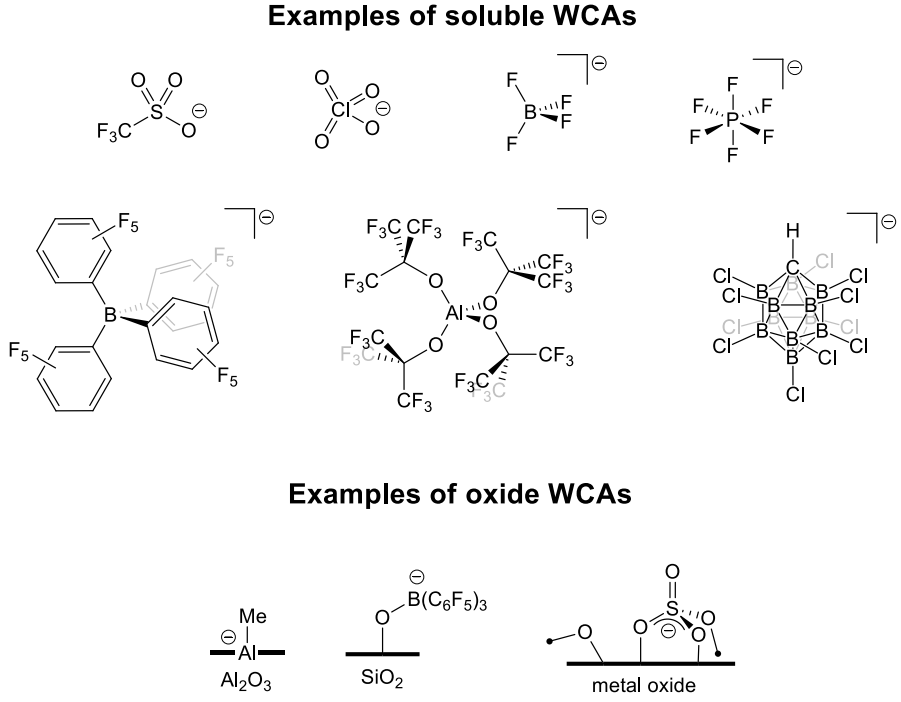

Figure 1.1.5. Examples of soluble and oxide weakly coordinating anions.

This discussion shows that the development of weakly coordinating oxide surfaces is more limited. The parallels between the behavior of solid and solution WCAs are also not clear in all cases. SMOs are obviously weakly coordinating based on the ability to support organometallic cations for olefin polymerization, but these would not be predicted to be as weakly coordinating as the perfluorinated borate anions that are more common for these catalysts in solution. The formation of surface ion pairs, and understanding how they relate to solution WCAs, is a central theme in this thesis.

Chapter 2 describes the reaction of an (α-diimine) palladium complex with sulfated zirconium oxide to form electrophilic Pd-sites. Adsorption of CO forms (α-diimine)Pd(CO)Me^+ sites that have a $\nu_{C=O}$ stretch similar to solution analogues, confirming

the electrophilic character of the Pd site. These surface species are active catalyst for the synthesis of high molecular weight polyethylene and the copolymerization of methyl acrylate and ethylene (Figure 1.1.6).[70] The incorporation of polar monomers into a growing polyethylene chain can significantly change the surface properties of the polymer,[71] and heterogeneous Pd-catalysts that form these products were not reported prior to this study.

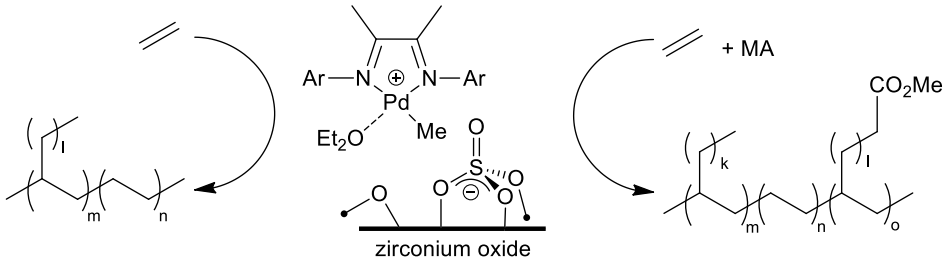

Figure 1.1.6. Heterogeneous Pd catalyst for the synthesis of polyethylene and methyl acrylate (MA) functionalized polyethylene.

Chapter 3 discusses the synthesis of [$^{i}Pr_3Si$][SZO], a well-defined silylium-like ion on the surface sulfated zirconium oxide (SZO) that initiates the hydrodefluorination of several sp^3 C-F bonds (Figure 1.1.7).[72] Strong Lewis acid sites on solid oxides are important industrial catalysts.[73,74] However, examples of well-defined silylium Lewis acids on the surface of oxides were not reported. The silylium-like surface species activate C-F bonds, and are far more active than previous heterogeneous catalysts for this reaction,[75] though are less reactive than state-of-the-art homogeneous silylium-like ions for this reaction.[76–78] Based on these studies the sulfate anions on SZO coordinate more weakly to the R_3Si^+ cation than triflate, but stronger than carborane anions.

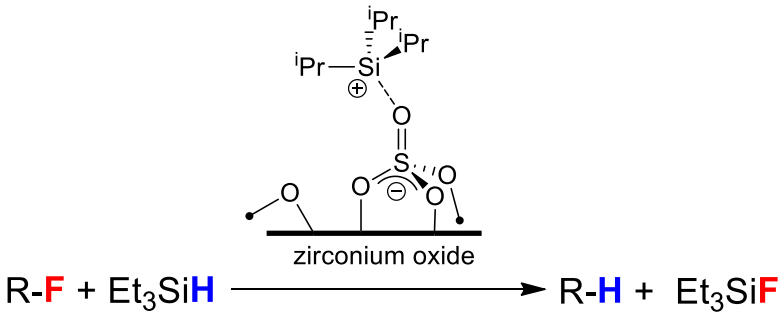

Figure 1.1.7. Hydrodefluorination of C-F bonds with [^{i}Pr$_3$Si][SZO].

Chapter 4 discusses the reaction of PhF-Al(OC(CF$_3$)$_3$)$_3$ to the surface of partially dehydroxylated silica to form ≡SiO(H)-Al(OC(CF$_3$)$_3$)$_3$, which are very strong Brønsted acids.[79] As discussed above, acidity and ion-pairing are intimately related. Reactions with trioctylamine forms [Octyl$_3$NH][≡SiOAl(OC(CF$_3$)$_3$)$_3$], and reactions with allyltriisopropylsilane forms [^{i}Pr$_3$Si][≡SiOAl(OC(CF$_3$)$_3$)$_3$]. Spectroscopic studies of these products confirm that anion is weakly coordinating and suggest that the anion is weaker coordinating than SZO surface anions, but more coordinating that common electron deficient anions (Figure 1.1.8).

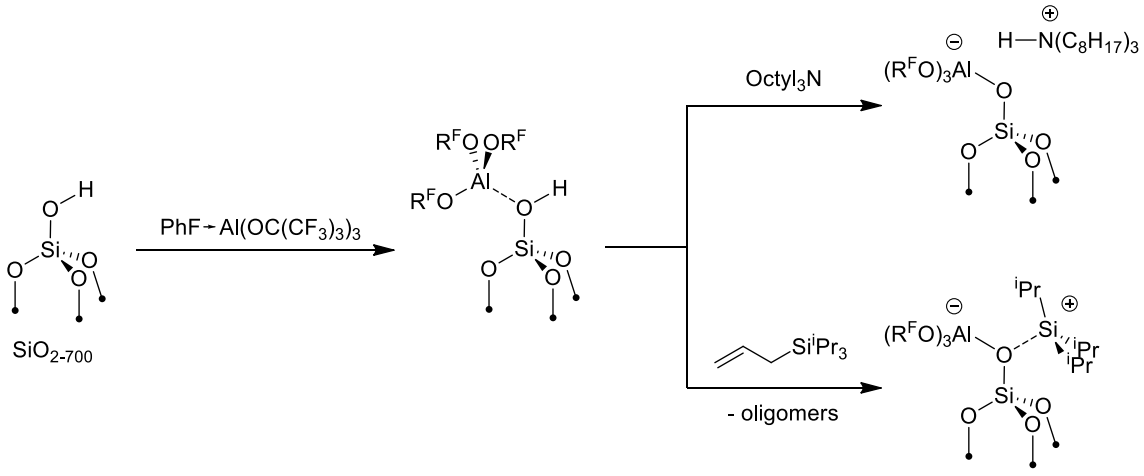

Figure 1.1.8. Synthesis of a new heterogeneous weakly coordinating anion.

Chapter 5 describes studies of mixtures of $Cp^b_2ZrCl_2$, $^iBu_3Al$, and Al_2O_3; a Ziegler-Natta type catalyst. Ziegler-Natta catalysts and their derivatives produce roughly half of all polyethylene, yet the structure of the active species is unknown. Solution NMR studies show that $^iBu_3Al$ reacts with the metallocene to form $Cp^b_2ZrH_2(HAl^iBu_2)(Al^iBu_3)$ and $Cp^b_2ZrH_2(HAl^iBu_2)(ClAl^iBu_2)$, and also reacts with alumina to form $\equiv AlO\text{-}Al(^iBu_2)\text{-}O(Al\equiv)_2$ (**TA**). The interaction of $Cp^b_2ZrH_2(HAl^iBu_2)(Al^iBu_3)$ and **TA** forms small quantities of $Zr\text{-}H^+$ species that are very active in polymerization reactions (Figure 1.1.9). The active site concentration was determined using vinyl halide probes, and these sites were characterized using solid-state NMR methods. The $Zr\text{-}H^+$ site characterized in these studies is the first example of active site determination in a "real" industrial catalyst for olefin polymerization.

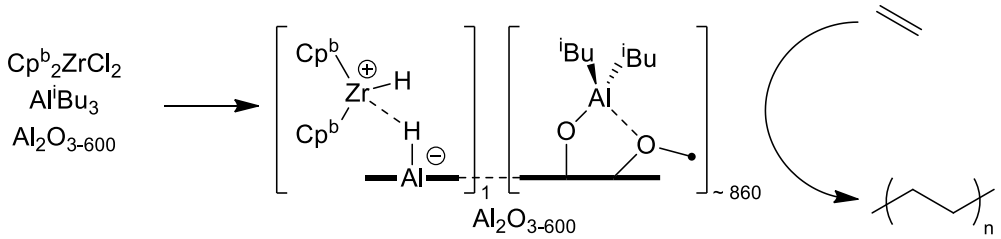

Figure 1.1.9. Proposed active site structure for the ternary catalyst mixture: $Cp^b{}_2ZrCl_2$, $^iBu_3Al$, and $Al_2O_{3\text{-}600}$ for the polymerization of ethylene.

1.1 References

(1) Copéret, C.; Comas-Vives, A.; Conley, M. P.; Estes, D. P.; Fedorov, A.; Mougel, V.; Nagae, H.; Núnez-Zarur, F.; Zhizhko, P. A. Surface Organometallic and Coordination Chemistry toward Single-Site Heterogeneous Catalysts: Strategies, Methods, Structures, and Activities. *Chem. Rev.* **2016**, *116* (2), 323–421. https://doi.org/10.1021/acs.chemrev.5b00373.

(2) Copéret, C.; Chabanas, M.; Petroff Saint-Arroman, R.; Basset, J.-M. Homogeneous and Heterogeneous Catalysis: Bridging the Gap through Surface Organometallic Chemistry. *Angew. Chemie Int. Ed.* **2003**, *42* (2), 156–181. https://doi.org/10.1002/anie.200390072.

(3) Pelletier, J. D. A.; Basset, J. M. Catalysis by Design: Well-Defined Single-Site Heterogeneous Catalysts. *Acc. Chem. Res.* **2016**, *49* (4), 664–677. https://doi.org/10.1021/acs.accounts.5b00518.

(4) Stalzer, M. M.; Delferro, M.; Marks, T. J. Supported Single-Site Organometallic Catalysts for the Synthesis of High-Performance Polyolefins. *Catal. Letters* **2015**, *145* (1), 3–14. https://doi.org/10.1007/s10562-014-1427-x.

(5) Wegener, S. L.; Marks, T. J.; Stair, P. C. Design Strategies for the Molecular Level Synthesis of Supported Catalysts. *Acc. Chem. Res.* **2012**, *45* (2), 206–214. https://doi.org/10.1021/ar2001342.

(6) Copéret, C.; Allouche, F.; Chan, K. W.; Conley, M. P.; Delley, M. F.; Fedorov, A.; Moroz, I. B.; Mougel, V.; Pucino, M.; Searles, K.; Yamamoto, K.; Zhizhko, P. A. Bridging the Gap between Industrial and Well-Defined Supported Catalysts. *Angew. Chemie Int. Ed.* **2018**, *57* (22), 6398–6440. https://doi.org/10.1002/anie.201702387.

(7) Zhuravlev, L. T. The Surface Chemistry of Amorphous Silica. Zhuravlev Model. *Colloids Surfaces A Physicochem. Eng. Asp.* **2000**, *173* (1–3), 1–38. https://doi.org/10.1016/S0927-7757(00)00556-2.

(8) Quignard, F.; Choplin, A.; Basset, J. M. Alkane Activation by a Highly Electrophilic Zirconium Hydride Complex Supported on Silica. *J. Chem. Soc. Chem. Commun.* **1991**, No. 22, 1589–1590. https://doi.org/10.1039/C39910001589.

(9) Quignard, F.; Lecuyer, C.; Bougault, C.; Lefebvre, F.; Choplin, A.; Olivier, D.; Basset, J. M. Surface Organometallic Chemistry: Synthesis And Characterization Of A Tris(Neopentyl)Zirconium(IV) Complex Grafted To The Surface Of A Partially Dehydroxylated Silica. *Inorg. Chem.* **1992**, *31* (5), 928–930. https://doi.org/10.1021/ic00031a042.

(10) Adachi, M.; Nédez, C.; Wang, X. X.; Bayard, F.; Dufaud, V.; Lefebvre, F.; Basset, J. M. Surface Organometallic Chemistry of Zirconium: Chemical Reactivity of the ≡Si-O-ZrNp3 Surface Complex Synthesized on Dehydroxylated Silica and Application to the Modification of Mordenite. *J. Mol. Catal. A Chem.* **2003**, *204–205*, 443–455. https://doi.org/10.1016/S1381-1169(03)00326-1.

(11) Corker, J.; Lefebvre, F.; Lécuyer, C.; Dufaud, V.; Quignard, F.; Choplin, A.; Evans, J.; Basset, J. M. Catalytic Cleavage of the C-H and C-C Bonds of Alkanes by Surface Organometallic Chemistry: An EXAFS and IR Characterization of a Zr-H Catalyst. *Science* **1996**, *271* (5251), 966–969. https://doi.org/10.1126/science.271.5251.966.

(12) Rataboul, F.; Baudouin, A.; Thieuleux, C.; Veyre, L.; Copéret, C.; Thivolle-Cazat, J.; Basset, J. M.; Lesage, A.; Emsley, L. Molecular Understanding of the Formation of Surface Zirconium Hydrides upon Thermal Treatment under Hydrogen of [(≡SiO)Zr(CH2tBu)3] by Using Advanced Solid-State NMR Techniques. *J. Am. Chem. Soc.* **2004**, *126* (39), 12541–12550. https://doi.org/10.1021/ja038486h.

(13) Gajan, D.; Copéret, C. Silica-Supported Single-Site Catalysts: To Be or Not to Be? A Conjecture on Silica Surfaces. *New J. Chem.* **2011**, *35* (11), 2403–2408. https://doi.org/10.1039/c1nj20506d.

(14) Le Roux, E.; Chabanas, M.; Baudouin, A.; de Mallmann, A.; Copéret, C.; Quadrelli, E. A.; Thivolle-Cazat, J.; Basset, J.-M.; Lukens, W.; Lesage, A.; Emsley, L.; Sunley, G. J. Detailed Structural Investigation of the Grafting of [Ta(CH*t*Bu)(CH_2*t*Bu)$_3$] and [Cp*TaMe_4] on Silica Partially Dehydroxylated at 700 °C and the Activity of the Grafted Complexes toward Alkane Metathesis. *J. Am. Chem. Soc.* **2004**, *126* (41), 13391–13399. https://doi.org/10.1021/ja046486r.

(15) Chabanas, M.; Baudouin, A.; Copéret, C.; Basset, J. M.; Lukens, W.; Lesage, A.; Hediger, S.; Emsley, L. Perhydrocarbyl ReVII Complexes: Comparison of Molecular and Surface Complexes. *J. Am. Chem. Soc.* **2003**, *125* (2), 492–504. https://doi.org/10.1021/ja020136s.

(16) Rhers, B.; Salameh, A.; Baudouin, A.; Quadrelli, E. A.; Taoufik, M.; Copéret, C.; Lefebvre, F.; Basset, J. M.; Solans-Monfort, X.; Eisenstein, O.; Lukens, W. W.; Lopez, L. P. H.; Sinha, A.; Schrock, R. R. A Well-Defined, Silica-Supported Tungsten Imido Alkylidene Olefin Metathesis Catalyst. *Organometallics* **2006**, *25* (15), 3554–3557. https://doi.org/10.1021/om060279d.

(17) Conley, M. P.; Lapadula, G.; Sanders, K.; Gajan, D.; Lesage, A.; Del Rosal, I.; Maron, L.; Lukens, W. W.; Copéret, C.; Andersen, R. A. The Nature of Secondary Interactions at Electrophilic Metal Sites of Molecular and Silica-Supported Organolutetium Complexes from Solid-State NMR Spectroscopy. *J. Am. Chem. Soc.* **2016**, *138* (11), 3831–3843. https://doi.org/10.1021/jacs.6b00071.

(18) Chen, Y.; Callens, E.; Abou-Hamad, E.; Merle, N.; White, A. J. P.; Taoufik, M.; Copéret, C.; Le Roux, E.; Basset, J.-M. [(≡SiO)$Ta^{V}Cl_2Me_2$]: A Well-Defined Silica-Supported Tantalum(V) Surface Complex as Catalyst Precursor for the Selective Cocatalyst-Free Trimerization of Ethylene. *Angew. Chemie Int. Ed.* **2012**, *51* (47), 11886–11889. https://doi.org/10.1002/anie.201206272.

(19) Culver, D. B.; Huynh, W.; Tafazolian, H.; Conley, M. P. Solid-State 45Sc NMR Studies of Cp*2Sc–OR (R = CMe2CF3, CMe(CF3)2, C(CF3)3, SiPh3) and Relationship to the Structure of Cp*2Sc-Sites Supported on Partially Dehydroxylated Silica. *Organometallics* **2020**, *39* (7), 1112–1122. https://doi.org/10.1021/acs.organomet.9b00840.

(20) Chen, E. Y. X.; Marks, T. J. Cocatalysts for Metal-Catalyzed Olefin Polymerization: Activators, Activation Processes, and Structure−Activity Relationships. *Chem. Rev.* **2000**, *100* (4), 1391–1434. https://doi.org/10.1021/cr980462j.

(21) Ittel, S. D.; Johnson, L. K.; Brookhart, M. Late-Metal Catalysts for Ethylene Homo- and Copolymerization. *Chem. Rev.* **2000**, *100*, 1169–1203. https://doi.org/10.1021/cr9804644.

(22) Yang, X.; Stern, C. L.; Marks, T. J. Cationic Zirconocene Olefin Polymerization Catalysts Based on the Organo-Lewis Acid Tris(Pentafluorophenyl)Borane. A Synthetic, Structural, Solution Dynamic, and Polymerization Catalytic Study. *J. Am. Chem. Soc.* **1994**, *116* (22), 10015–10031. https://doi.org/10.1021/ja00101a022.

(23) Jia, L.; Yang, X.; Stern, C. L.; Marks, T. J. Cationic Metallocene Polymerization Catalysts Based on Tetrakis(Pentafluorophenyl)Borate and Its Derivatives. Probing the Limits of Anion "Noncoordination" via a Synthetic, Solution Dynamic, Structural, and Catalytic Olefin Polymerization Study. *Organometallics* **1997**, *16* (5), 842–857. https://doi.org/10.1021/om960880j.

(24) Bochmann, M. The Chemistry of Catalyst Activation: The Case of Group 4 Polymerization Catalysts. *Organometallics* **2010**, *29* (21), 4711–4740. https://doi.org/10.1021/om1004447.

(25) Britovsek, G. J. P.; Gibson, V. C.; Wass, D. F. The Search for New-Generation Olefin Polymerization Catalysts: Life beyond Metallocenes. *Angew. Chemie Int. Ed.* **1999**, *38* (4), 428–447. https://doi.org/10.1002/(SICI)1521-3773(19990215)38:4<428::AID-ANIE428>3.0.CO;2-3.

(26) Chen, C. Designing Catalysts for Olefin Polymerization and Copolymerization: Beyond Electronic and Steric Tuning. *Nature Reviews Chemistry*. Nature Publishing Group May 1, 2018, pp 6–14. https://doi.org/10.1038/s41570-018-0003-0.

(27) He, M. Y.; Marks, T. J.; Xiong, G.; Toscano, P. J.; Burwell, R. L. Supported Organoactinides. Surface Chemistry and Catalytic Properties of Alumina-Bound (Cyclopentadienyl)-and (Pentamethylcyclopentadienyl)Thorium and -Uranium Hydrocarbyls and Hydrides. *J. Am. Chem. Soc.* **1985**, *107* (3), 641–652. https://doi.org/10.1021/ja00289a016.

(28) Toscano, P. J.; Marks, T. J. Supported Organoactinides. High-Resolution Solid-State 13C NMR Studies of Catalytically Active, Alumina-Bound (Pentamethylcyclopentadienyl)Thorium Methyl and Hydride Complexes. *J. Am. Chem. Soc.* **1985**, *107* (3), 653–659. https://doi.org/10.1021/ja00289a017.

(29) Marks, T. J. Surface-Bound Metal Hydrocarbyls. Organometallic Connections Between Heterogeneous and Homogeneous Catalysis. *Acc. Chem. Res.* **1992**, *25* (2), 57–65. https://doi.org/10.1021/ar00014a001.

(30) Wischert, R.; Copéret, C.; Delbecq, F.; Sautet, P. Dinitrogen: A Selective Probe for Tri-Coordinate Al "Defect" Sites on Alumina. *Chem. Commun.* **2011**, *47* (17), 4890–4892. https://doi.org/10.1039/c1cc10623f.

(31) Wischert, R.; Copéret, C.; Delbecq, F.; Sautet, P. Optimal Water Coverage on Alumina: A Key to Generate Lewis Acid-Base Pairs That Are Reactive Towards the C-H Bond Activation of Methane. *Angew. Chemie Int. Ed.* **2011**, *50* (14), 3202–3205. https://doi.org/10.1002/anie.201006794.

(32) Wischert, R.; Laurent, P.; Copéret, C.; Delbecq, F.; Sautet, P. Γ-Alumina: The Essential and Unexpected Role of Water for the Structure, Stability, and Reactivity of "Defect" Sites. *J. Am. Chem. Soc.* **2012**, *134* (35), 14430–14449. https://doi.org/10.1021/ja3042383.

(33) Comas Vives, A.; Schwarzwälder, M.; Copéret, C.; Sautet, P. Carbon−Carbon Bond Formation by Activation of CH3F on Alumina. *J. Phys. Chem. C* **2015**, *119* (13), 7156–7163. https://doi.org/10.1021/jp512598p.

(34) Comas-Vives, A.; Valla, M.; Copéret, C.; Sautet, P. Cooperativity between Al Sites Promotes Hydrogen Transfer and Carbon−Carbon Bond Formation upon Dimethyl Ether Activation on Alumina. *ACS Cent. Sci.* **2015**, *1* (6), 313–319. https://doi.org/10.1021/acscentsci.5b00226.

(35) Jordan, R. F.; Dasher, W. E.; Echols, S. F. Reactive Cationical Dicyclopentadienylzirconium(IV) Complexes. *J. Am. Chem. Soc.* **1986**, *108* (7), 1718–1719. https://doi.org/10.1021/ja00267a068.

(36) Jezequel, M.; Dufaud, V.; Ruiz-Garcia, M. J.; Carrillo-Hermosilla, F.; Neugebauer, U.; Niccolai, G. P.; Lefebvre, F.; Bayard, F.; Corker, J.; Fiddy, S.; Evans, J.; Broyer, J. P.; Malinge, J.; Basset, J. M. Supported Metallocene Catalysts by Surface Organometallic Chemistry. Synthesis, Characterization, and Reactivity in Ethylene Polymerization of Oxide-Supported Mono- and Biscyclopentadienyl Zirconium Alkyl Complexes: Establishment of Structure/Reactivity R. *J. Am. Chem. Soc.* **2001**, *123* (15), 3520–3540. https://doi.org/10.1021/ja000682q.

(37) Millot, N.; Soignier, S.; Santini, C. C.; Baudouin, A.; Basset, J. M. Synthesis, Characterization, and Activity in Ethylene Polymerization of Silica Supported Cationic Cyclopentadienyl Zirconium Complexes. *J. Am. Chem. Soc.* **2006**, *128* (29), 9361–9370. https://doi.org/10.1021/ja060420+.

(38) Popoff, N.; Gauvin, R. M.; De Mallmann, A.; Taoufik, M. On the Fate of Silica-Supported Half-Metallocene Cations: Elucidating a Catalyst's Deactivation Pathways. *Organometallics* **2012**, *31* (13), 4763–4768. https://doi.org/10.1021/om3003224.

(39) Walzer, J. F. Supported Ionic Catalyst Composition. US5643847A, June 7, 1995.

(40) Millot, N.; Santini, C. C.; Lefebvre, F.; Basset, J. M. Surface Organometallic Chemistry: A Route to Well-Defined Boron Heterogeneous Co-Catalyst for Olefin Polymerisation. *Comptes Rendus Chim.* **2004**, *7* (8–9), 725–736. https://doi.org/10.1016/j.crci.2004.03.011.

(41) Millot, N.; Santini, C. C.; Baudouin, A.; Basset, J. M. Supported Cationic Complexes: Selective Preparation and Characterization of the Well-Defined Electrophilic Metallocenium Cation [≡SiO-B(C6F5)3]-[Cp*ZrMe2(Et2NPh)]+ Supported on Silica. *Chem. Commun.* **2003**, *3* (16), 2034–2035. https://doi.org/10.1039/b304047j.

(42) Sauter, D. W.; Popoff, N.; Bashir, M. A.; Szeto, K. C.; Gauvin, R. M.; Delevoye, L.; Taoufik, M.; Boisson, C. The Design of a Bipodal Bis(Pentafluorophenoxy)Aluminate Supported on Silica as an Activator for Ethylene Polymerization Using Surface Organometallic Chemistry. *Chem. Commun.* **2016**, *52* (26), 4776–4779. https://doi.org/10.1039/c6cc00060f.

(43) Arata, K. Preparation of Superacidic Metal Oxides and Their Catalytic Action. In *Metal Oxide Catalysis*; John Wiley and Sons, 2009; Vol. 2, pp 665–704. https://doi.org/10.1002/9783527626113.ch17.

(44) Makoto, H.; Sakari, K.; Kazushi, A. Reactions of Butane and Isobutane Catalyzed by Zirconium Oxide Treated with Sulfate Ion. Solid Superacid Catalyst1. *J. Am. Chem. Soc.* **1979**, *101* (21), 6439–6441. https://doi.org/10.1021/ja00515a051.

(45) Hino, M.; Arata, K. Synthesis of Solid Superacid Catalyst with Acid Strength of H0 ≤ -16.04. *J. Chem. Soc. Chem. Commun.* **1980**, No. 18, 851–852. https://doi.org/10.1039/C39800000851.

(46) Farneth, W. E.; Gorte, R. J. Methods for Characterizing Zeolite Acidity. *Chem. Rev.* **1995**, *95* (3), 615–635. https://doi.org/10.1021/cr00035a007.

(47) Boronat, M.; Corma, A. Factors Controlling the Acidity of Zeolites. *Catal. Letters* **2015**, *145* (1), 162–172. https://doi.org/10.1007/s10562-014-1438-7.

(48) Haw, J. F.; Zhang, J.; Shimizu, K.; Venkatraman, T. N.; Luigi, D. P.; Song, W.; Barich, D. H.; Nicholas, J. B. NMR and Theoretical Study of Acidity Probes on Sulfated Zirconia Catalysts. *J. Am. Chem. Soc.* **2000**, *122* (50), 12561–12570. https://doi.org/10.1021/ja0027721.

(49) Rodriguez, J.; Culver, D. B.; Conley, M. P. Generation of Phosphonium Sites on Sulfated Zirconium Oxide: Relationship to Brønsted Acid Strength of Surface -OH Sites. *J. Am. Chem. Soc.* **2019**, *141* (4), 1484–1488. https://doi.org/10.1021/jacs.8b13204.

(50) Haase, F.; Sauer, J. The Surface Structure of Sulfated Zirconia: Periodic Ab Initio Study of Sulfuric Acid Adsorbed on ZrO2(101) and ZrO2(001). *J. Am. Chem. Soc.* **1998**, *120* (51), 13503–13512. https://doi.org/10.1021/ja9825534.

(51) Sauer, J.; Hill, J. R. The Acidity of Surface Silanol Groups. A Theoretical Estimate Based on Ab Initio Calculations on a Model Surface. *Chem. Phys. Lett.* **1994**, *218* (4), 333–337. https://doi.org/10.1016/0009-2614(94)00002-6.

(52) Williams, L. A.; Marks, T. J. Chemisorption Pathways and Catalytic Olefin Polymerization Properties of Group 4 Mono- and Binuclear Constrained Geometry Complexes on Highly Acidic Sulfated Alumina. *Organometallics* **2009**, *28* (7), 2053–2061. https://doi.org/10.1021/om801106c.

(53) Williams, L. A.; Marks, T. J. Synthesis, Characterization, and Heterogeneous Catalytic Implementation of Sulfated Alumina Nanoparticles. Arene Hydrogenation and Olefin Polymerization Properties of Supported Organozirconium Complexes. *ACS Catal.* **2011**, *1* (4), 238–245. https://doi.org/10.1021/cs100119w.

(54) Nicholas, C. P.; Marks, T. J. Zirconium Hydrocarbyl Chemisorption on Sulfated Metal Oxides: New Supports, Chemisorption Pathways, and Implications for Catalysis. *Langmuir* **2004**, *20* (22), 9456–9462. https://doi.org/10.1021/la0492106.

(55) Ahn, H.; Nicholas, C. P.; Marks, T. J. Surface Organozirconium Electrophiles Activated by Chemisorption on "Super Acidic" Sulfated Zirconia as Hydrogenation and Polymerization Catalysts. A Synthetic, Structural, and Mechanistic Catalytic Study. *Organometallics* **2002**, *21* (9), 1788–1806. https://doi.org/10.1021/om020056x.

(56) Stalzer, M. M.; Nicholas, C. P.; Bhattacharyya, A.; Motta, A.; Delferro, M.; Marks, T. J. Single-Face/All- Cis Arene Hydrogenation by a Supported Single-Site D0 Organozirconium Catalyst. *Angew. Chemie Int. Ed.* **2016**, *55* (17), 5263–5267. https://doi.org/10.1002/anie.201600345.

(57) Gu, W.; Stalzer, M. M.; Nicholas, C. P.; Bhattacharyya, A.; Motta, A.; Gallagher, J. R.; Zhang, G.; Miller, J. T.; Kobayashi, T.; Pruski, M.; Delferro, M.; Marks, T. J. Benzene Selectivity in Competitive Arene Hydrogenation: Effects of Single-Site Catalyst···Acidic Oxide Surface Binding Geometry. *J. Am. Chem. Soc.* **2015**, *137* (21), 6770–6780. https://doi.org/10.1021/jacs.5b03254.

(58) Williams, L. A.; Guo, N.; Motta, A.; Delferro, M.; Fragalà, I. L.; Miller, J. T.; Marks, T. J. Surface Structural-Chemical Characterization of a Single-Site D0 Heterogeneous Arene Hydrogenation Catalyst Having 100% Active Sites. *Proc. Natl. Acad. Sci. U. S. A.* **2013**, *110* (2), 413–418. https://doi.org/10.1073/pnas.1220240110.

(59) Kaphan, D. M.; Klet, R. C.; Perras, F. A.; Pruski, M.; Yang, C.; Kropf, A. J.; Delferro, M. Surface Organometallic Chemistry of Supported Iridium(III) as a Probe for Organotransition Metal-Support Interactions in C-H Activation. *ACS Catal.* **2018**, *8* (6), 5363–5373. https://doi.org/10.1021/acscatal.8b00855.

(60) Syed, Z. H.; Kaphan, D. M.; Perras, F. A.; Pruski, M.; Ferrandon, M. S.; Wegener, E. C.; Celik, G.; Wen, J.; Liu, C.; Dogan, F.; Goldberg, K. I.; Delferro, M. Electrophilic Organoiridium(III) Pincer Complexes on Sulfated Zirconia for Hydrocarbon Activation and Functionalization. *J. Am. Chem. Soc.* **2019**, *141* (15), 6325–6337. https://doi.org/10.1021/jacs.9b00896.

(61) Fărcaşiu, D.; Ghenciu, A.; Li, J. Q. The Mechanism of Conversion of Saturated Hydrocarbons Catalyzed by Sulfated Metal Oxides: Reaction of Adamantane on Sulfated Zirconia. *J. Catal.* **1996**, *158* (1), 116–127. https://doi.org/10.1006/jcat.1996.0013.

(62) Ghenciu, A.; Fărcaşiu, D. The Mechanism of Conversion of Hydrocarbons on Sulfated Metal Oxides. Part II. Reaction of Benzene on Sulfated Zirconia. *J. Mol. Catal. A Chem.* **1996**, *109* (3), 273–283. https://doi.org/10.1016/1381-1169(96)00015-5.

(63) Jatia, A.; Chang, C.; MacLeod, J. D.; Okubo, T.; Davis, M. E. ZrO2 Promoted with Sulfate, Iron and Manganese: A Solid Superacid Catalyst Capable of Low Temperature n-Butane Isomerization. *Catal. Letters* **1994**, *25* (1–2), 21–28. https://doi.org/10.1007/BF00815411.

(64) Klet, R. C.; Kaphan, D. M.; Liu, C.; Yang, C.; Kropf, A. J.; Perras, F. A.; Pruski, M.; Hock, A. S.; Delferro, M. Evidence for Redox Mechanisms in Organometallic Chemisorption and Reactivity on Sulfated Metal Oxides. *J. Am. Chem. Soc.* **2018**, *140* (20), 6308–6316. https://doi.org/10.1021/jacs.8b00995.

(65) Olah, G. A.; Surya Prakash, G. K.; Molnr, R.; Sommer, J. Superacid Chemistry. In *Superacid Chemistry*; Wiley, 2008; pp 1–34. https://doi.org/10.1002/9780470421604.

(66) Stoyanov, E. S.; Kim, K. C.; Reed, C. A. An Infrared VNH Scale for Weakly Basic Anions. Implications for Single-Molecule Acidity and Superacidity. *J. Am. Chem. Soc.* **2006**, *128* (26), 8500–8508. https://doi.org/10.1021/ja060714v.

(67) Reed, C. A. H+,CH3+, and R3Si+ Carborane Reagents: When Triflates Fail. *Acc. Chem. Res.* **2010**, *43* (1), 121–128. https://doi.org/10.1021/ar900159e.

(68) Nava, M.; Stoyanova, I. V; Cummings, S.; Stoyanov, E. S.; Reed, C. A. The Strongest Brønsted Acid: Protonation of Alkanes by H(CHB11F11) at Room Temperature. *Angew. Chemie Int. Ed.* **2014**, *53* (4), 1131–1134. https://doi.org/10.1002/anie.201308586.

(69) Reed, C. A. Myths about the Proton. The Nature of H+in Condensed Media. *Acc. Chem. Res.* **2013**, *46* (11), 2567–2575. https://doi.org/10.1021/ar400064q.

(70) Culver, D. B.; Tafazolian, H.; Conley, M. P. A Bulky Pd(II) α-Diimine Catalyst Supported on Sulfated Zirconia for the Polymerization of Ethylene and Copolymerization of Ethylene and Methyl Acrylate. *Organometallics* **2018**, *37* (6), 1001–1006. https://doi.org/10.1021/acs.organomet.8b00016.

(71) Nakamura, A.; Ito, S.; Nozaki, K. Coordination-Insertion Copolymerization of Fundamental Polar Monomers. *Chem. Rev.* **2009**, *109*, 5215–5244. https://doi.org/10.1021/cr900079r.

(72) Culver, D. B.; Conley, M. P. Activation of C−F Bonds by Electrophilic Organosilicon Sites Supported on Sulfated Zirconia. *Angew. Chemie Int. Ed.* **2018**, *57* (45), 14902–14905. https://doi.org/10.1002/anie.201809199.

(73) Corma, A.; García, H. Lewis Acids: From Conventional Homogeneous to Green Homogeneous and Heterogeneous Catalysis. *Chem. Rev.* **2003**, *103* (11), 4307–4365. https://doi.org/10.1021/cr030680z.

(74) Román-Leshkov, Y.; Davis, M. E. Activation of Carbonyl-Containing Molecules with Solid Lewis Acids in Aqueous Media. *ACS Catal.* **2011**, *1* (11), 1566–1580. https://doi.org/10.1021/cs200411d.

(75) Ahrens, M.; Scholz, G.; Braun, T.; Kemnitz, E. Catalytic Hydrodefluorination of Fluoromethanes at Room Temperature by Silylium-Ion-like Surface Species. *Angew. Chemie Int. Ed.* **2013**, *52* (20), 5328–5332. https://doi.org/10.1002/anie.201300608.

(76) Douvris, C.; Nagaraja, C. M.; Chen, C. H.; Foxman, B. M.; Ozerov, O. V. Hydrodefluorination and Other Hydrodehalogenation of Aliphatic Carbon-Halogen Bonds Using Silylium Catalysis. *J. Am. Chem. Soc.* **2010**, *132* (13), 4946–4953. https://doi.org/10.1021/ja100605m.

(77) Scott, V. J.; Çelenligil-Çetin, R.; Ozerov, O. V. Room-Temperature Catalytic Hydrodefluorination of C(Sp3)-F Bonds. *J. Am. Chem. Soc.* **2005**, *127* (9), 2852–2853. https://doi.org/10.1021/ja0426138.

(78) Douvris, C.; Ozerov, O. V. Hydrodefluorination of Perfluoroalkyl Groups Using Silylium-Carborane Catalysts. *Science* **2008**, *321* (5893), 1188–1190. https://doi.org/10.1126/science.1158088.

(79) Culver, D. B.; Venkatesh, A.; Huynh, W.; Rossini, A. J.; Conley, M. P. Al(ORF)3 (RF = C(CF3)3) Activated Silica: A Well-Defined Weakly Coordinating Surface Anion. *Chem. Sci.* **2020**, *11* (6), 1510–1517. https://doi.org/10.1039/c9sc05904k.

Chapter 2 A Bulky (α-diimine) Palladium Catalyst Supported on the Surface of Sulfated Zirconium Oxide for the Polymerization of Ethylene and copolymerization of ethylene and Methyl Acrylate[1]

2.1 Abstract

This chapter discusses the synthesis and characterization of [LPdMe(OEt_2)][SZO] (L = (2,6-(Ph_2CH)-4-MeC_6H_2)N=CMeMeC=N(2,6-(Ph_2CH)-4-MeC_6H_2)); a heterogeneous catalyst for the polymerization of ethylene and copolymerization of ethylene and methyl acrylate. [LPdMe(OEt_2)][SZO] produces high molecular weight polyethylene with an activity of 1342 kg_{PE} mol_{cat}^{-1} hr^{-1} with narrow polymer polydispersities, indicating that the catalytically active palladium is single-site. [LPdMe(OEt_2)][SZO] incorporates methyl acrylate (0.46 mol %) into polyethylene while maintaining narrow polymer polydispersities between 1.9-2.3. Mechanistic studies show that ~ 9.4 % of the Pd in [LPdMe(OEt_2)][SZO] is active in polymerization reactions.

2.2 Introduction

Over 100 million tons of polyethylene are produced annually.[2] Nearly all of these polymers are synthesized in the presence of a heterogeneous catalyst. Roughly half of the polyethylene is produced with the Phillips CrO_x/SiO_2 catalyst,[3] and the other half is produced with Ziegler-Natta type catalysts.[4] These catalysts produce polymers with broad molecular weight distributions, indicative of multi-site behavior. More recent developments in early transition metal Ziegler-Natta catalysts on the surface of weakly coordinating oxides has improved the polydispersities of the produced polymers. The oxide

materials used for well-defined early transition metal Ziegler-Natta type catalysts are summarized in chapter 1. Early transition metal Ziegler-Natta type catalysts typically used to produce high molecular weight linear polyethylene are poisoned by polar functional groups.[5]

The incorporation of low loadings of a vinyl polar monomer (~1 %) into a polyethylene chain modifies the functionality of the polymer.[6] A list of representative vinyl polar monomers are shown in Figure 2.2.1. Late transition metals are less oxophilic than early transition metals, and are compatible with some of the polar monomers shown in Figure 2.2.1.[5] The two catalysts studied in detail for copolymerization reactions are the cationic [(α-diimine)MMeL][BAr^F_4] catalysts developed by Brookhart,[5–9] and neutral phosphinosulfonate palladium [(P,O)PdXL] complexes.[6,10]

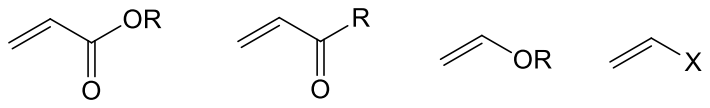

Figure 2.2.1. Representative vinyl polar monomers (R = H or alkyl, X = halide).

[(α-diimine)PdMeL][BAr^F_4] catalysts react with ethylene to produce hyperbranched polyethylene (Figure 2.2.2A).[11] [(α-diimine)PdMeL][BAr^F_4] polymerizes ethylene by a coordination-insertion mechanism (Figure 2.2.2B).[6,12] Branches form by a "chain-walking" mechanism that involves successive β-hydride elimination reinsertion steps, shown in Figure 2.2.2B. Palladium catalysts typically form ~100 branches/1000C,

and the formation of the branches are not affected by ethylene pressure. Though branching can be reduced by the incorporation of bulkier groups into the α-diimine ligand.[8]

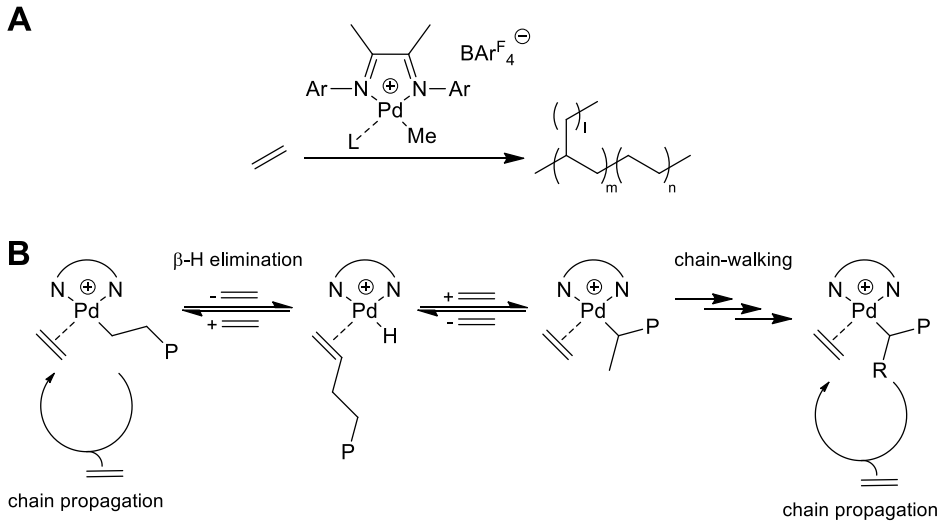

Figure 2.2.2. A) [(α-diimine)PdMeL][BAr$^F_4$] catalyst for the synthesis of hyperbranched polyethylene; and B) mechanism for the formation of branched polyethylene (P = polymer and R = branch, anion omitted for clarity).

[(α-diimine)PdMeL][BAr$^F_4$] catalysts incorporate methyl acrylate (MA) at the ends of branches (Figure 2.2.3A).[7,13] This behavior is rationalized by the key steps shown in Figure 2.2.3B. The Pd-polymeryl$^+$ intermediate insert MA into the polymer chain via a 2,1 insertion and form a four-membered chelate intermediate. Rearrangement through key chain-walking steps results in the stable 6-membered chelate that is a resting state in Pd-catalyzed copolymerizations of ethylene and MA. Opening the 6-membered chelate in the presence of ethylene forms a Pd(poylmeryl)(ethylene)$^+$ intermediate that propagates polymer growth. In general, copolymerizations of ethylene and MA show lower catalyst productivity than ethylene homopolymerizations.

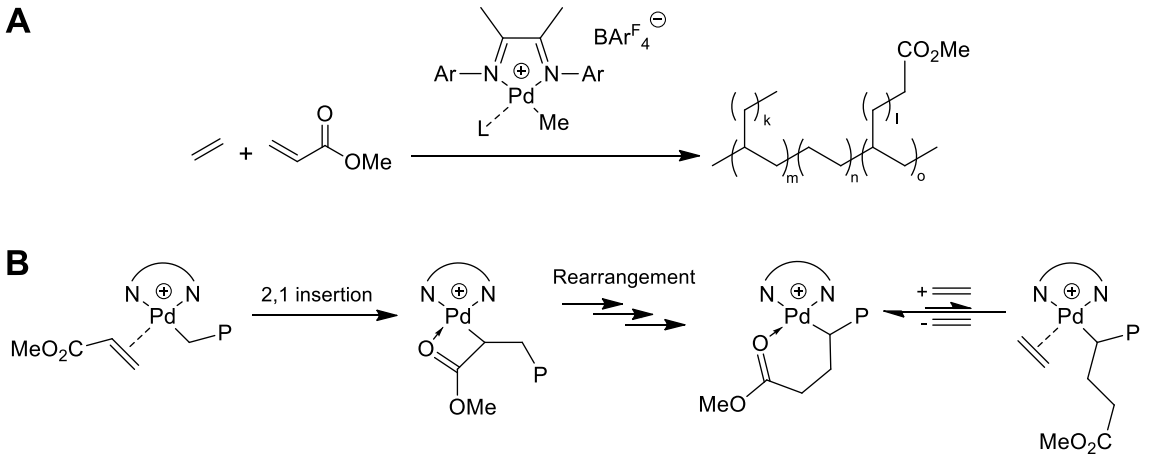

Figure 2.2.3. A) [(α-diimine)PdMeL][BAr$^F_4$] catalyst for the synthesis of polyethylene with MA incorporated into the ends of branches; and B) mechanism for the reaction of MA with (α-diimine)Pd-P$^+$ (P = polymer, anion omitted for clarity).

As mentioned above, heterogeneous catalysts are typical for polymerization processes in industry because solid catalysts do not foul the reactors and provide controllable polymer morphology.[14] In the context of late metal containing heterogeneous polymerization catalysts, α-diimine nickel catalysts supported on silica are summarized in Figure 2.2.4.[15–17] Early attempts involved the activation of (α-diimine)NiBr$_2$ complexes with MAO functionalized silica (Figure 2.2.4A).[18] Brookhart and coworkers tethered (α-diimine)NiBr$_2$ complexes through the ligand to trimethylaluminum functionalized silica with a linker forming ≡SiO-Linker-(α-diimine)NiBr$_2$, which are activated by exogenous alkyl aluminum chlorides (Figure 2.2.4B).[19,20] Basset and coworkers supported (α-diimine)Ni(CH$_2$SiMe$_3$)$_2$ onto silica forming (α-diimine)Ni(CH$_2$SiMe$_3$)-OSi≡, which is active in ethylene polymerization in the presence of gaseous BF$_3$ (Figure 2.2.4C).[21]

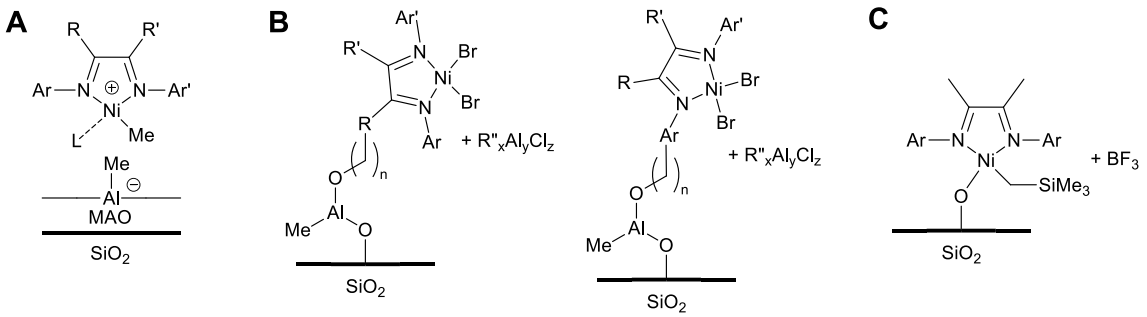

Figure 2.2.4. Examples of α-diimine nickel complexes supported on partially dehydroxylated silica. A) (α-diimine)NiMeL supported on MAO functionalized silica; B) (α-diimine)$NiBr_2$ bound to silica via the ligand through a linker, and activated by alkyl aluminum chlorides; and C) (α-diimine)$NiCH_2SiMe_3$-OSi≡ activated by BF_3.

Sulfated zirconium oxide (SZO) contains acidic -OH sites near sulfate ions that react with organometallic complexes to form weakly coordinated ion pairs.[22,23] Most of this work has been done with organozirconium and a limited number of organoiridium complexes, these studies are summarized in chapter1. Our group showed that SZO reacts with (α-diimine)$NiMe_2$ to form [(α-diimine)NiMeL][SZO] (α-diimine = (2,6-$^{i}Pr_2$-C_6H_3)N=CMeMeC=N(2,6-$^{i}Pr_2$-C_6H_3) and L = Et2O or MeCN) (Figure 2.2.5).[24] [(α-diimine)NiMeL][SZO] initiates the polymerization of ethylene with a similar activity and polymer properties as the homogeneous analogue [(α-diimine)NiMeL][BAr^{F}_4]. [(α-diimine)NiMeL][SZO] produces polymers with narrow polydispersities of 1.8-2.4. In the presence of 10-undecanoate and ethylene, [(α-diimine)NiMeL][SZO] incorporated up to 0.4 % of the polar monomer into polyethylene chain, though with a broader polydispersities of 4.2-5.2. [(α-diimine)NiMeL][SZO] is not compatible with methyl acrylate.

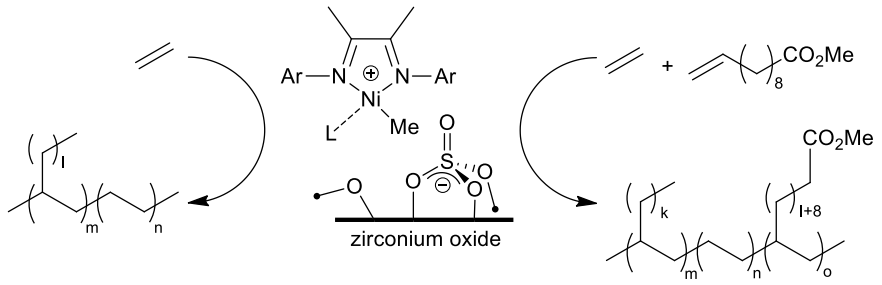

Figure 2.2.5. (α-diimine)NiMeL$^+$ catalyst supported on SZO$^-$ for the synthesis of branched polyethylene and polyethylene with 10-undecanoate incorporated at the ends of branches.

In this chapter, a bulky (α-diimine)$PdMe_2$ precursor is grafted onto SZO.[1] The catalyst is characterized by elemental analysis, FT-IR spectroscopy, and solid-state NMR spectroscopy. The (α-diimine)PdMe$^+$ cations on the surface react with ^{13}CO to form (α-diimine)PdMe(CO)$^+$. The catalyst initiates the polymerization of ethylene to form high molecular weight polyethylene and incorporates small amounts of MA into polymer chains with narrow polydispersities. Active site counting shows only 9.4 % of the Pd contained on the surface is active in polymerization reactions.

2.3 Results and discussion

2.3.1 Synthesis of partially dehydroxylated sulfated zirconium oxide (SZO)

$Zr(OH)_4$ was prepared by basifying an aqueous solution of zirconyl nitrate with an aqueous ammonia solution to a pH of ~ 8, ageing at 95 °C for 24 hours, and isolation of the precipitate by filtration. Sulfated zirconium oxide was prepared by soaking the $Zr(OH)_4$ with dilute sulfuric acid, and calcination in air at 600 °C. The calcined material was partially dehydroxylated under vacuum at 300 °C yielding sulfated zirconium oxide (SZO) (Scheme 2.3.1).[24] The FT-IR spectrum of SZO is shown in Figure 2.3.1. SZO was measured

by N_2 absorption and has a BET surface area of ~95 m^2/g. SZO reacts with excess Me_3SiCH_2Li to produce $SiMe_4$ which shows that SZO has a reactive surface -OH loading of 0.13 mmol g^{-1}.

Scheme 2.3.1. Synthesis of SZO

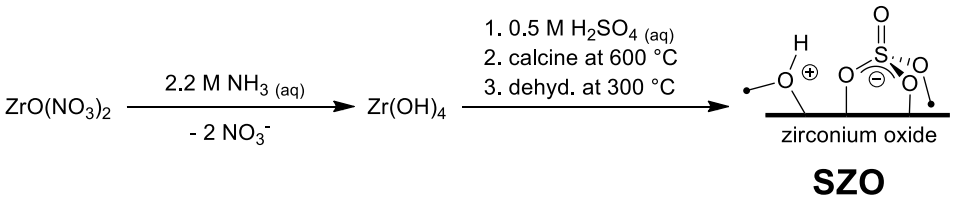

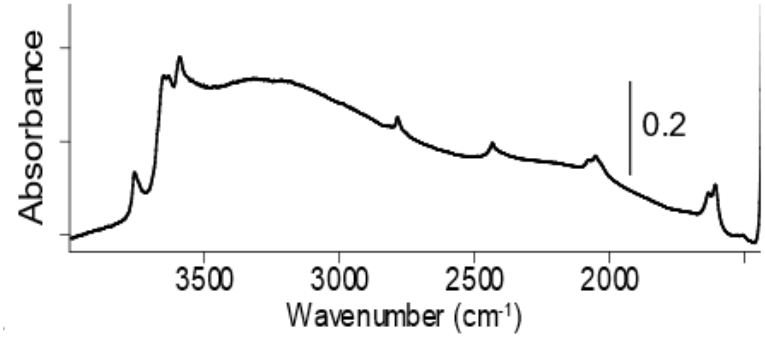

Figure 2.3.1. FT-IR spectrum of SZO (cm^{-1}).

2.3.2 Synthesis of [LPdMe][SZO]

$LPdMe_2$ (L = (2,6-(Ph_2CH)-4-MeC_6H_2)N=CMeMeC=N(2,6-(Ph_2CH)-4-MeC_6H_2)) reacts with SZO in a slurry of diethyl ether to form [LPdMe(OEt_2)][SZO] (**Pd1**), Scheme 2.3.2. Elemental analysis shows that **Pd1** contains 0.4 % Pd (0.039 mmol g^{-1}) and 0.11 % N (~2 N/Pd). Analysis of the volatiles shows that ~ 1.5 equivalents of methane per palladium is released during the reaction, suggesting that not all Pd sites contain a methyl

group. The FT-IR spectrum of **Pd1** contains sp^2 ν_{C-H}, sp^3 $\nu_{C-H,}$ and sp^2 $\nu_{C=C}$ stretches; **Pd1** also contains reduced ν_{O-H} stretches compared to SZO (Figure 2.3.2A). The solid-state ^{13}C CP-MAS NMR spectrum of **Pd1** contains signals at 185, 175, 140-129, 69, 52, 19, 13, and 11.5 ppm (Figure 2.3.2B). The signals at 185, 175, 140-129, 52, and 19 ppm are assigned to the N=**C**-Me, aromatic, **C**HPh_2, and **C**H_3-Ph signals from the ligand, respectively. The signals at 69, and 13 ppm are OEt_2 coordinated to palladium. The signal at 11.5 ppm is assigned to Pd-Me.

Scheme 2.3.2. Synthesis of **Pd1**

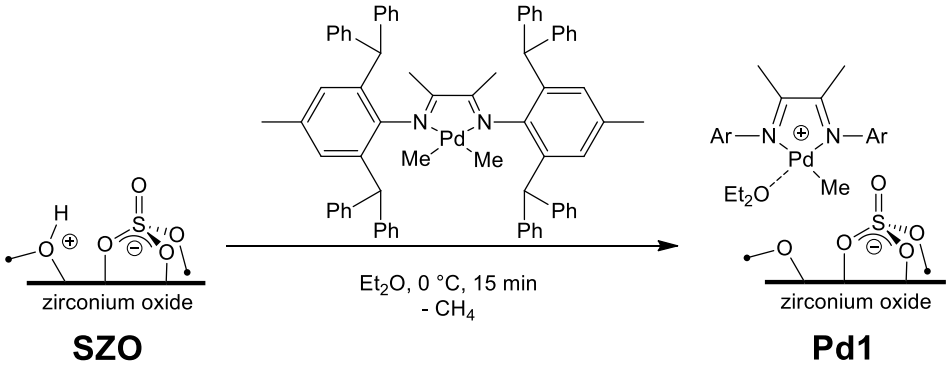

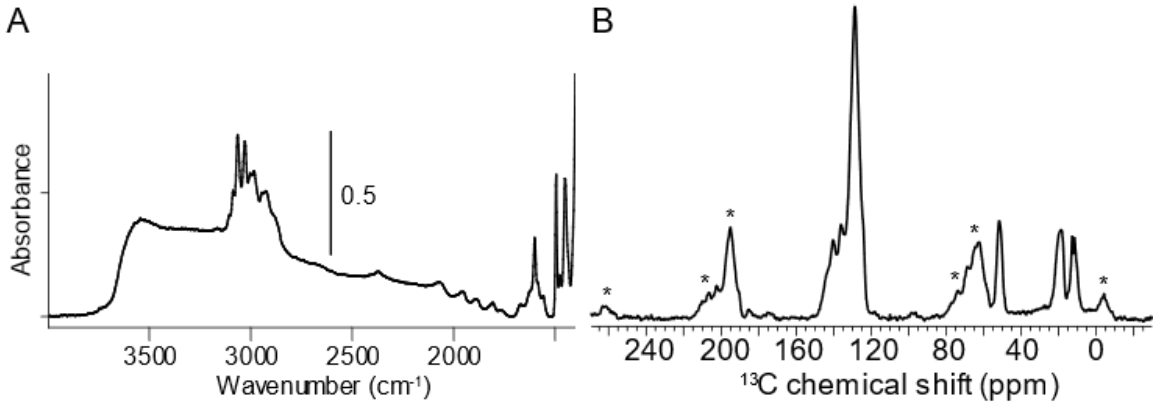

Figure 2.3.2. A) FT-IR spectrum of **Pd1**; and B) solid-state ^{13}C CP-MAS NMR spectrum of **Pd1**, * = spinning sidebands (ppm).

Pd1 reacts with ^{13}CO to form [LPdMe(^{13}CO)][SZO] (**Pd1-^{13}CO**), Scheme 2.3.3. The FT-IR spectrum of **Pd1-^{13}CO** contains a strong $\nu_{PdC=O}$ stretch at 2079 cm^{-1} (Figure 2.3.3A). Application of the harmonic oscillator approximation gives a calculated Pd-CO value of 2125 cm^{-1} for natural abundance CO, close to the $\nu_{C=O}$ stretch of [LPdMe(CO)][$B(C_6F_5)_4$] ($\nu_{C=O}$ = 2129 cm^{-1}) measured in a KBr pellet.[25] The ^{13}C CP-MAS NMR spectrum of **Pd1-^{13}CO** contains two new overlapping signals at 173 and 168 ppm for Pd-^{13}CO (Figure 2.3.3B), which is also similar to the $^{13}C\{^1H\}$ NMR signal for [LPdMe(CO)][$B(C_6F_5)_4$] in solution ($CDCl_3$, 172.5 ppm).[25] The NMR contains two different Pd-^{13}CO species, which is not surprising considering that not all the Pd has a methyl group based on methane quantification during the grafting reaction. The ^{13}C CP-MAS spectrum no longer contains signals for diethyl ether and the signal for Pd-Me shifts by 0.2 ppm (11.3 ppm), which supports that ^{13}CO displaces coordinated ether to form **Pd1-^{13}CO**.

Scheme 2.3.3. Reaction of **Pd1** with ^{13}CO

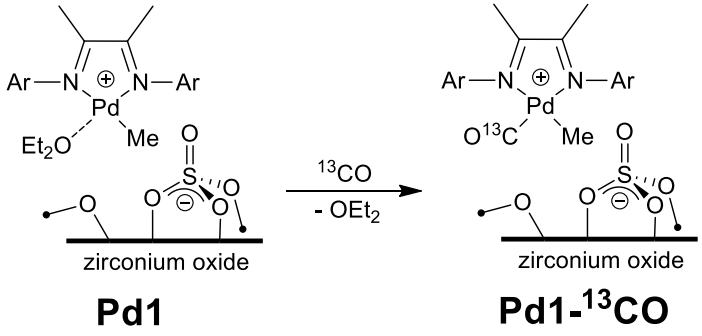

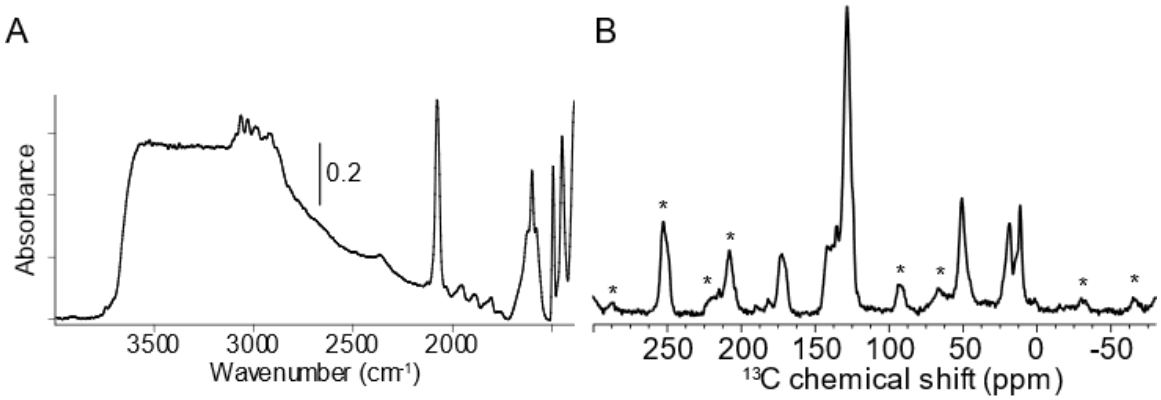

Figure 2.3.3. A) FT-IR spectrum of **Pd1-^{13}CO** (cm^{-1}); and B) solid-state ^{13}C CP-MAS MAS NMR spectrum of **Pd1-^{13}CO** (spinning at 12 kHz), * = spinning sidebands (ppm).

*2.3.3 Quantification of active sites on **Pd1** for ethylene polymerization*

The methane released during the synthesis of **Pd1** indicates that not all of the Pd has a methyl group, therefore not all of the Pd will be active for the polymerization of ethylene. Landis and coworkers reported a method for determining the percent of active zirconocene catalyst for the polymerization of 1-hexene by either quenching a polymerization reaction with MeOD or initiating the polymerization reaction with Zr-CD_3 and quenching the reaction natural abundance MeOH.[26] The active sites are quantified by

^{2}H NMR analysis of the polymer.[26] [LPdCD$_3$(OEt$_2$)][SZO] (**Pd1D**) was prepared with LPd(CD$_3$)$_2$ and SZO analogously to **Pd1** in order determine the quantity of active sites **Pd1** contains for the polymerization of ethylene. In a teflon-valved NMR tube, **Pd1D** was contacted with 1 atm of ethylene in a slurry of toluene to produce a small amount of polymer. The reaction was quenched with trifluoroacetic acid (TFA) and measured by ^{2}H NMR spectroscopy in the presence of an internal standard (Figure 2.3.4). Polymer chains terminated by -CD$_3$ or -CHD-(CH$_2$)$_n$-CHD$_2$ groups were observed in the NMR spectrum, Scheme 2.3.4 shows how these end groups form. The polymer deuterium content indicated that ~ 9.4 % of the Pd on Pd1 is active in the polymerization of ethylene.

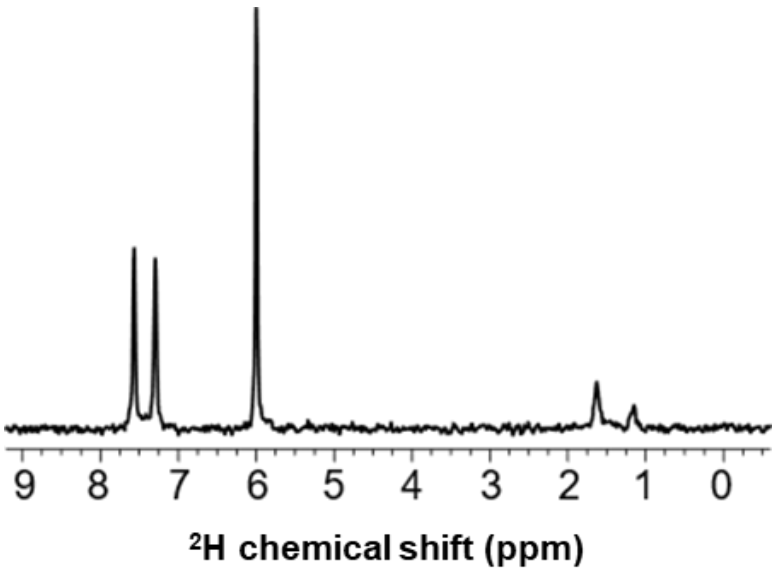

Figure 2.3.4. ^{2}H NMR spectrum of ^{2}H labeled homopolymer synthesized with **Pd1D** (d1=5s) with C$_2$D$_2$Cl$_4$ (6.0 ppm) as an internal standard (ppm). The signals at 7.57 and 7.29 ppm are natural abundance *o*-dichlorobenzene-d1.

Scheme 2.3.4. Formation of -CD_3 or -CHD-$(CH_2)_n$-CHD_2 polymer end groups with **Pd1D**

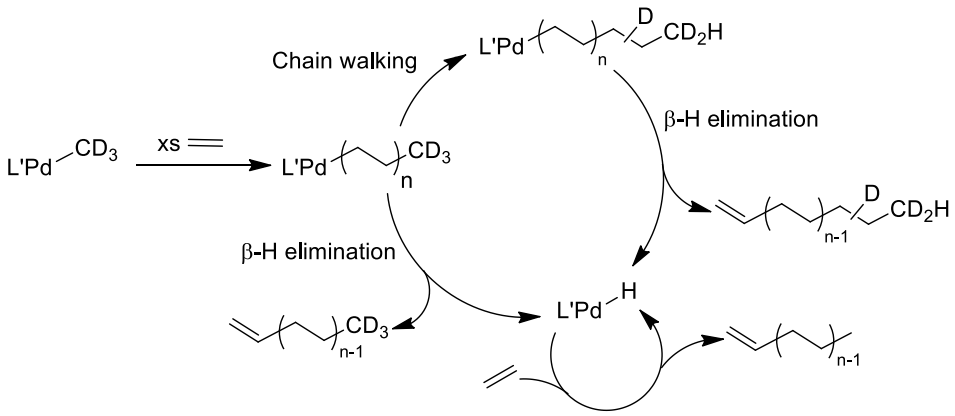

*2.3.4 Polymerization reactions with **Pd1***

The results of the polymerization reactions with **Pd1** are summarized in Table 2.1. **Pd1** initiates the polymerization of ethylene (150 psig) to produce polymers with low branching, high molecular weights, and narrow polydispersities (Scheme 2.3.5). **Pd1** at 25 °C has an activity of 879 kg_{PE} mol_{Pd}^{-1} hr^{-1} over one hour. The polymer has a Mn of 158 kg mol^{-1} and contains 44 branches per 1000 carbons. The polydispersity of the polymer is 1.4 indicating that the active sites on Pd1 are single-site (entry 1). At 40 °C, the activity increases to 1342 kg_{PE} mol_{Pd}^{-1} hr^{-1} and the molecular weight increases to 210 kg mol^{-1} (entry 2). The polydispersity (1.6) and branching (41/1000 carbons) of the polymer are similar to the polymer produced at 25 °C.

The activity at 60 and 80 °C decreases to 487 and 434 kg_{PE} mol_{Pd}^{-1} hr^{-1}, respectively (entries 3 and 4). The molecular weight of the polymer also drops below 100 kg mol^{-1} but the branching is maintained around 40 branches per carbon. At 60 °C, the polydispersity is still narrow (2.1). However, the polydispersity sharply increases to 3.9 at 80 °C, indicating

multi-site behavior. At 40 °C, **Pd1** steadily consumes ethylene over 15 hours but with reduced activity to 354 kg_{PE} mol_{Pd}^{-1} hr^{-1} (entry 5). This result suggests that Pd1 deactivates during polymerization. Homogeneous [LPdMe][$B(C_6F_5)_4$] (generated in-situ with $LPdMe_2$ and [$H(OEt_2)$][$B(C_6F_5)_4$]) has an activity similar to **Pd1** (1290 kg_{PE} mol_{Pd}^{-1} hr^{-1} at 40 °C assuming that all of the Pd is active, entry 6).

Scheme 2.3.5. Synthesis of polyethylene with **Pd1**

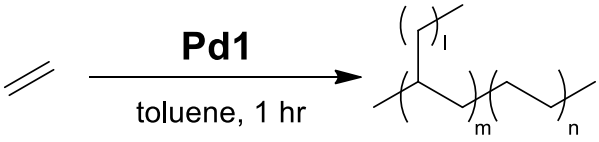

Table 2.1. Summary of the data for the polymerization of ethylene with **Pd1**.[a]

Entry	Catalyst	T (°C)	Activity (kg_{PE} mol^{-1} h^{-1})[b]	Mn (kg mol^{-1})[b]	Đ[c]	B[d]
1	**Pd1**	25	879	158	1.4	44
2	**Pd1**	40	1342	210	1.6	41
3	**Pd1**	60	487	93	2.1	41
4	**Pd1**	80	434	20	3.9	42
5[e]	**Pd1**	40	354	n.d.	n.d.	n.d.
6[f]	[LPdMe][$B(C_6F_5)_4$]	40	1290	n.d.	n.d.	n.d

a.) Polymerization conditions: catalyst loading = 0.07 μmol active Pd, 5 mL of toluene, 1 hour; b.) average of triplicate; c.) measured by GPC at 140 °C in trichlorobenzene; d.) number of branches /1000 C as determined by ^{1}H NMR spectroscopy in tetrachloroethane-d2 at 120 °C;[27] e.) activity after 15 hours; and f.) [LPdMe][$B(C_6F_5)_4$] prepared in situ under ethylene pressure, activity after 30 minutes.

A summary of the results for the copolymerization of MA and polyethylene are shown in Table 2.2. **Pd1,** under 80 psig of ethylene and 2 M MA in toluene, incorporates MA into polyethylene, Scheme 2.3.6, while maintaining a narrow polydispersity (Đ = 1.9) at 25 and 40 °C (entries 1 and 2). The presence of MA decreases polymerization activity to 5.0 and 14.9 kg_{PE} mol^{-1} h^{-1}. The decrease in activity is common to for cationic palladium polymerization catalysts because MA forms stable 6-membered chelates that inhibits formation of Pd(polymeryl)(ethylene)$^+$ intermediates necessary for chain growth. At 25 and 40 °C, **Pd1** incorporates 0.25 and 0.33 mol % MA into the polyethylene chain,

respectively. At 60 °C, **Pd1** also has an activity of 14.9 kg_{PE} mol^{-1} h^{-1} but incorporates more MA (0.46 mol %) with a polydispersity of 2.3. The decreased activities led to reduced molecular weights of the polymers ranging from 16 to 44 kg mol^{-1}.

Scheme 2.3.6. Scheme for the synthesis of MA incorporated polyethylene with **Pd1**

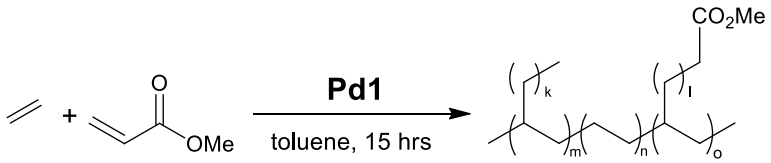

Table 2.2. Data for the incorporation of methyl acrylate into polyethylene with **Pd1**.[a]

Entry	T (°C)	% MA incorporation[b]	Activity (kg_{PE} mol^{-1} h^{-1})	Mn (kg mol^{-1})[c]	Đ[c]	B[d]
1	25	0.25	5.0	33	1.9	33
2	40	0.33	14.9	44	1.9	31
3	60	0.46	14.9	16	2.3	39

a.) polymerization conditions: 0.35 μmol active Pd, 5 mL of toluene, 15 hours, 2 M methyl acrylate; b.) mol % incorporation of the polar monomer; c). measured by GPC at 140 °C in trichlorobenzene; and d.) number of branches /1000 C as determined by ^{1}H NMR spectroscopy in tetrachloroethane-d2 at 120 °C.[27]

2.4 Conclusion

Pd1 contains Pd-Me active sites that initiate ethylene polymerization and copolymerize MA with polyethylene. The FT-IR, and solid-state ^{13}C NMR spectroscopic signatures of **Pd1** and **Pd1-^{13}CO** are similar to homogeneous analogues and support the well-defined structure of Pd1. However, deuterium labeling shows that only ~9.4 % of the Pd is active for polymerization. **Pd1** produces polyethylene with low branching, high molecular weights, and narrow polydispersities. **Pd1** incorporates up to 0.46 % of MA into polyethylene while maintaining narrow polydispersities.

2.5 Materials and methods

2.5.1 General considerations

All manipulations were performed under an inert atmosphere of dinitrogen or argon. C_6D_6 was dried over sodium/benzophenone, distilled under vacuum, and stored inside a glovebox. Solvents were purchased from Fisher Scientific and were dried by passing through a double-column J. C. Meyer solvent system and degassed before use. Dioxane, diethyl ether, and toluene were dried over sodium/benzophenone, degassed, and distilled under vacuum prior to use. Methyl acrylate was dried over CaH_2 and distilled under vacuum. All other commercially available reagents were used as received without purification. N,N'-bis(2,6-dibenzhydryl-4-methylphenyl)butane-2,3-diimine, (N,N'-bis(2,6-dibenzhydryl-4-methylphenyl)butane-2,3-diimine)$PdCl_2$, and $[H(OEt_2)][B(C_6F_5)_4]$ were prepared by reported procedures. The molecular starting materials (N,N'-bis(2,6-dibenzhydryl-4-methylphenyl)butane-2,3-diimine)$PdMe_2$ ($LPdMe_2$), and (N,N'-bis(2,6-dibenzhydryl-4-methylphenyl)butane-2,3-diimine)$Pd(CD_3)_2$ ($LPd(CD_3)_2$) were first synthesized by Dr. Hosein Tafazolian.[1]

Solution ^1H and ^{13}C NMR spectra were recorded on Bruker 300 or 600 MHz spectrometers. Solid state NMR spectra were recorded in 4 mm zirconia rotors spinning at 10 KHz at the magic angle. The probe was cooled to ca. -20 ^oC during sample spinning. FT-IR spectra were recorded as pressed pellets using a Bruker Alpha IR spectrometer in an argon-filled glovebox. Gas chromatography was carried out using Agilent 7820A GC system equipped with an KCl/Al_2O_3 column. Elemental analyses were carried out in Microanalysis Laboratory at University of Illinois Urbana-Champaign.

Polymerizations were performed in a Biotage Endeavor housed in a nitrogen-filled glovebox with eight parallel reactors and an overhead stirrer. Polymer grade ethylene 99.97% was purchased from Praxair and passed through a Chromatography Research Supplies column to remove traces of O_2 and H_2O. Polymer samples were analyzed by solution ^1H and $^{13}C\{^1H\}$ NMR in tetrachloroethane-d_2 at 120 ^oC. High-temperature GPC measurements were performed using an Agilent Pl-220 GPC/SEC system equipped with three (3) Waters 300mm X 7.8 mm Styragel HMW-6E Columns heated at 150° C in 1,2,4-Trichlorobenzene (TCB) stabilized with 2,6-di(tert-butyl)-4-methylphenol was used as the mobile phase at a flow rate of 1 mL min^{-1}. Columns and detectors were maintained at 150°C. Polymer concentrations were nominally 1 mg mL^{-1}.

2.5.2 Synthesis and characterization of SZO

SZO[24]: 70 g of zirconyl nitrate was dissolved in 420 ml of water and warmed to 65 °C. 280 ml of 2.2 M NH_4OH was added dropwise to the vigorously stirred solution over 1 h. After complete addition of NH_4OH, the pH of the white slurry was ~ 8.5. The slurry was heated to 95 °C for 24 h. The precipitate was filtered hot and collected. The white precipitate was dispersed in 700 ml of water and stirred for 30 minutes, filtered, and washed with 3 L of water. The white precipitate was dried at 120 °C for 24 h yielding 26.72 g $Zr(OH)_4$. 5 g of crushed $Zr(OH)_4$ was dispersed in 100 ml of 0.5 M sulfuric acid at room temperature. After 30 min, the solvent was poured off. The white solid was dispersed in 100 ml of water for 30 min, the H_2O decanted, and dried at 120 °C for 1 h. This material was calcined under air at 600 °C (5 °C/min) for 4 h and cooled to room temperature under

air. The material was dehydroxylated by heating to 300 °C (5 °C/min) under air for 3 hours and evacuated to 10^{-6} torr for 15 min to form SZO, which was stored in an argon-filled glovebox. Elemental analysis: 0.9% S. The surface area of SZO using this procedure is 98 m^2/g.

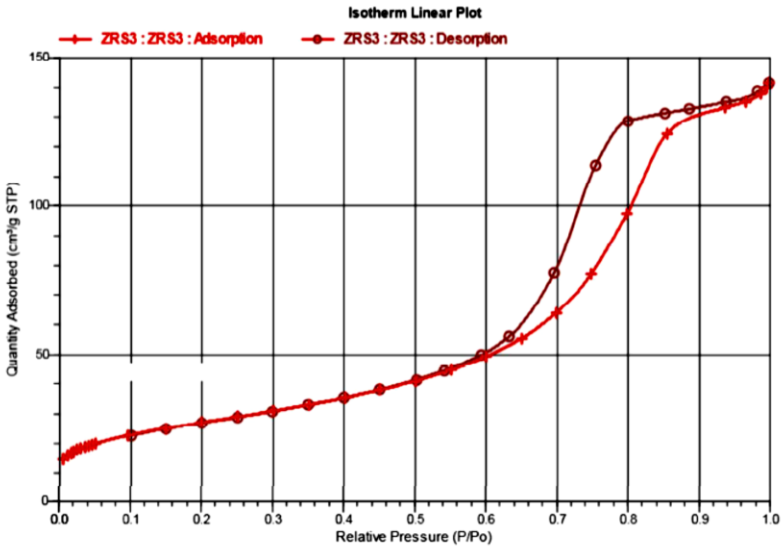

Figure 2.5.1. N_2 adsorption/desorption isotherm plot of SZO (BET surface area: 97.8 $m^2 g^{-1}$ and t-plot micropore volume: 0.000708 $cm^3 g^{-1}$).

-OH loading of SZO: 0.5 ml of benzene-d6 were added to SZO (100 mg) and $LiCH_2SiMe_3$ (10 mg) in a teflon-valved NMR tube. After 1 hour at room temperature, ferrocene (~15 mg) was added to the mixture as an internal standard. ^1H NMR spectra were recorded and the $SiMe_4$ was quantified by integration relative to ferrocene. These measurements were run in triplicate. The OH loading of SZO using this method is 0.133±0.007 mmol/g.

2.5.3 Synthesis of catalysts

Grafting $LPdMe_2$ onto SZO (**Pd1**): SZO (100−500 mg) and $LPdMe_2$ (0.5 equiv based on the 0.132 mmol OH/g SZO) were transferred to one arm of a double-Schlenk flask inside an argon-filled glovebox. Addition of more 2 before, or during, the grafting reaction does not result in higher palladium loadings. Diethyl ether (ca. 3−5 mL) was transferred under vacuum to the flask at 77 K. The mixture was warmed to 0 °C and gently stirred for 15 min. The brown solution was filtered to the other side of the double Schlenk. The solid was washed by condensing solvent from the other arm of the double Schlenk at 77 K, warming to room temperature and stirring for 2 min, and filtering the solvent back to the other side of the flask. This was repeated two times; the final washing was clear and colorless, indicating that all palladium on the SZO surface is chemisorbed onto the oxide surface. The volatiles were transferred to a 2 L flask at 77 K and allowed to equilibrate into the gas phase. Analysis of the gas phase by gas chromatography showed that methane (0.059 ± 0.006 mmol/g) evolved during the grafting reaction. Further details on gas quantification in grafting reactions are given in ref 11e. The orange solid was dried under vacuum (10−6 Torr) at room temperature and stored in an argon-filled glovebox at −20 °C. ^{13}C CP-MAS NMR (150.9 MHz): 184.7 (N=C-), 174.9 (N=C-), 140.3 (Ar.), 136.0 (Ar.), 128.7 (Ar.), 68.8 (Et_2O), 51.7 (-$CHPh_2$), 18.9 (2X p-CH_3), 18.9 (2X N=C-CH_3), 12.8 (Et_2O), 11.5 (Pd-CH_3). Elemental Analysis: Pd: 0.4%, C: 3.87%, H: 0.34%, N: 0.12%.

Grafting $LPd(CD_3)_2$ on SZO (**Pd1D**): Grafting conditions were identical to **Pd1**, replacing $LPdMe_2$ with $LPd(CD_3)_2$.

Pd1 + ^{13}CO (**Pd1*CO**): A 4 mm solid-state NMR rotor containing **Pd1** was contacted with excess ^{13}CO (~500 equiv/Pd) at room temperature for 1 hour. Excess ^{13}CO was removed by applying vacuum for 10 min. ^{13}C CP-MAS NMR (150.9 MHz): 191.6 (N=C-), 180.4 (N=C-), 172.4 (Pd-^{13}CO), 141.7 (Ar), 135.9 (Ar), 128.5 (Ar), 50.7 (-$CHPh_2$), 18.7 (p-CH_3), 18.7 (N=C-CH_3), 11.3 (Pd-CH_3).

*2.5.4 Quantification of active sites on **Pd1***

Quantification of Active Sites in **Pd1D**: A NMR tube containing a Teflon valve was loaded with **Pd1D** (106 mg, 4 μmol Pd-CD_3) and 0.5 mL of toluene. The toluene was degassed under high vacuum at −196 °C and the NMR tube was sealed under 1 atm of ethylene. After 16 h at room temperature ~0.1 mL of TFA was added to the NMR tube. Volatiles were removed under vacuum, and 0.5 mL of o-dichlorobenzene containing $C_2D_2Cl_4$ (1.9 μmol) was added to the NMR tube. ^2H NMR spectra were recorded at 120 °C. ^2H NMR (92.1 MHz): 6.00 (2.00D, $C_2D_2Cl_4$ standard), 1.63 (0.42 D), 1.15 (0.19 D). These integration values correspond to 0.38 μmol deuterium incorporation into the polymer under these conditions, indicating that 9.4% of the Pd-CD_3 sites are active for polymerization.

*2.5.5 Polymerization reactions with **Pd1***

Polymerization of ethylene with **Pd1**: In a Biotage Endeavor reactor, a 12 mL liner was charged with **Pd1** (20 mg, 0.75 μmol Pd, 0.07 μmol active Pd) and 5 mL of toluene. The reaction vessels were pressurized with ethylene to 150 psi and heated to the desired

reaction temperature(s). Polymerizations were conducted with ethylene on demand at 150 psi for 1 hour. The reaction vessel was vented and purged with nitrogen. Polymers were precipitated with 5% HCl in methanol (15 mL), filtered after 2 h, and dried under vacuum. All polymerizations were run in triplicate and the average activity for each temperature is reported in Table 2.1.

.

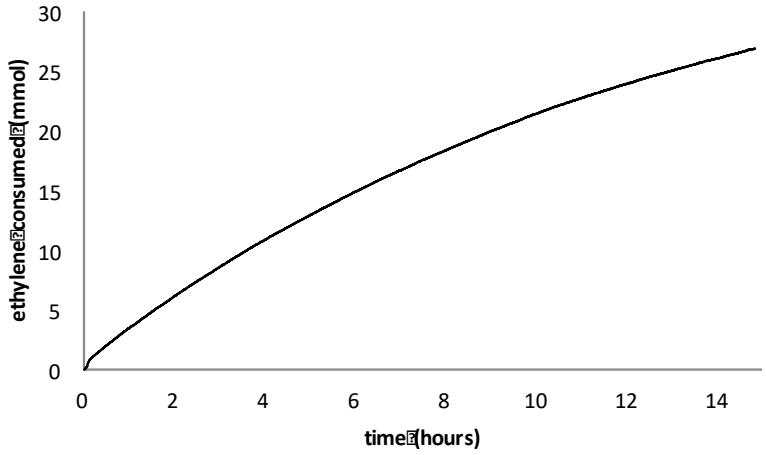

Figure 2.5.2. Ethylene consumption curve over 15 hours using **Pd1**.

Analysis of polymerization supernatants for Pd: Supernatants of two 15 hour homopolymerization runs were combined and the volatiles were removed en vacuo. The residue was treated with 40 ml 1 % HNO_3 (Trace metal) overnight, then filtered over a frit to remove insoluble particles. The filtrate was analyzed by AAS and found to not contain Pd levels above the detection limit of the instrument.

Incorporation of MA into polyethylene with **Pd1**: Copolymerization reactions with methyl acrylate were performed using a similar procedure, except for **Pd1** (100 mg, 3.7 μmol Pd, 0.3 μmol active catalyst), and 5 mL of 2 M methyl acrylate in toluene was used in these reactions. Ethylene pressure (80 psi) on demand was supplied to the reaction mixture for 15 h. The polymers were precipitated by the addition of 5% HCl in methanol (15 mL), filtered after 2 h, washed with 10 mL methanol (2×) to remove unreacted methyl acrylate, and dried under vacuum.

Polymerization of ethylene with [LPdMe][$B(C_6F_5)_4$]: In a Biotage Endeavor reactor, a 12 ml liner is charged with 0.3 ml of 1.2 mM $LPdMe_2$ (0.2 μmol) in toluene and diluted to 4.7 ml with toluene. The reaction vessels were pressurized to 150 psi (10 atm) and 0.3 ml of 1.2 mM [$(Et_2O)_2H$][$B(C_6F_5)_4$] (0.36 μmol, 1.8 eq.) in toluene were injected into the reaction. The reaction was then immediately heated to 40 °C. The reaction ran under constant pressure for 30 minutes. The reaction vessel was then vented and purged with nitrogen to remove ethylene from the system. Polymers were precipitated by addition of 15 ml of 5 % HCl in methanol solution, filtered after 2 hours then dried under vacuum. The reaction produced 129 mg of polymer giving an activity of 1290 $kg_{PE}\, mol_{Pd}^{-1}\, h^{-1}$.

2.5.6 NMR spectra of the polyethylene

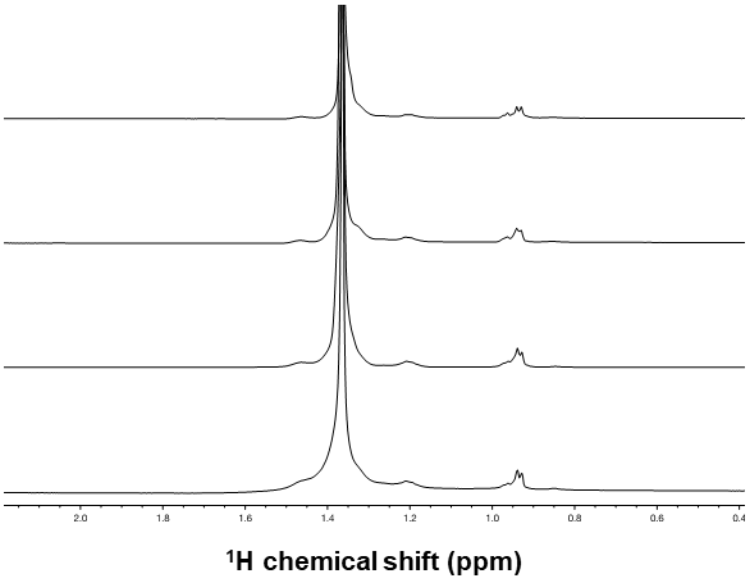

Figure 2.5.3. ^{1}H NMR spectra in ppm of homopolymers from Table 2.1 entries 1-4 from bottom to top.

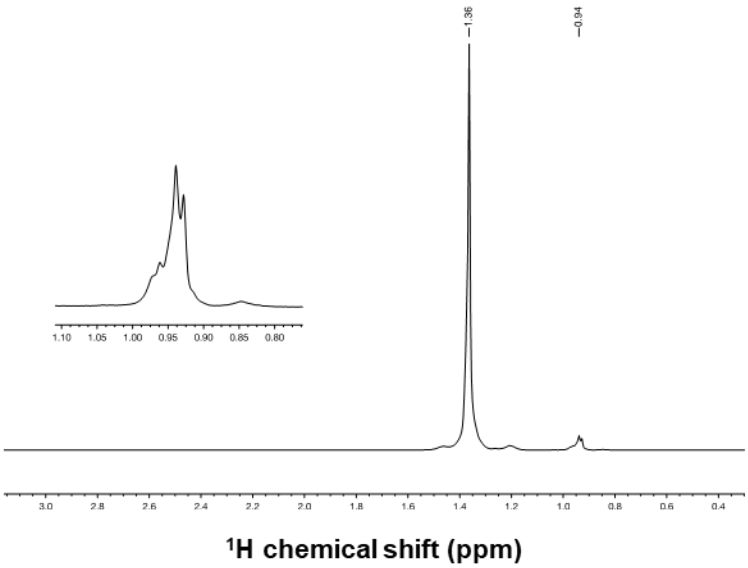

Figure 2.5.4. ^{1}H NMR spectrum of polyethylene produced by **Pd1** at 40 °C, inset is a zoom in on the region containing the signals for the ends of polymer branches.

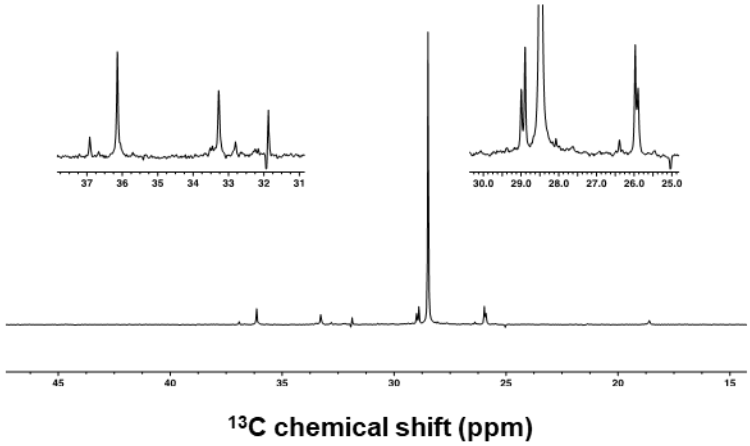

Figure 2.5.5. $^{13}C\{^{1}H\}$ NMR spectrum of polyethylene produced by **Pd1** at 40 °C (ppm), insets are zoom in on the polymer signals.

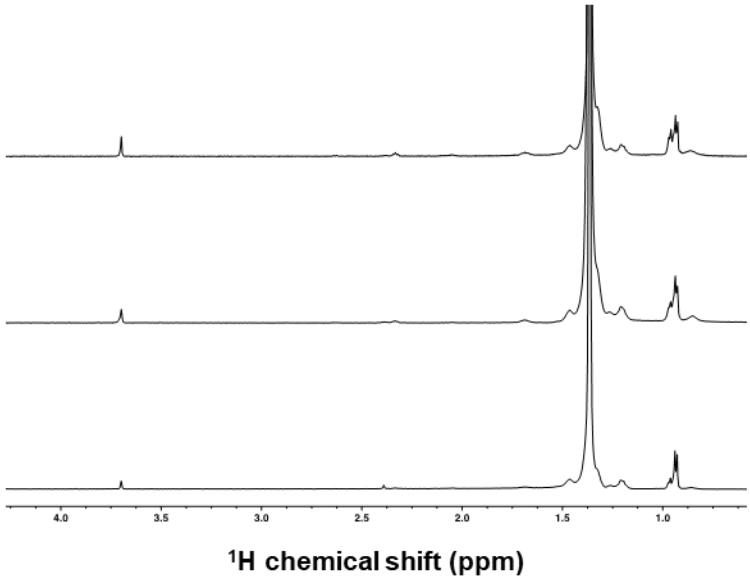

Figure 2.5.6. ^{1}H NMR spectra of copolymers from Table 2.2, entries 1-3 bottom to top (ppm).

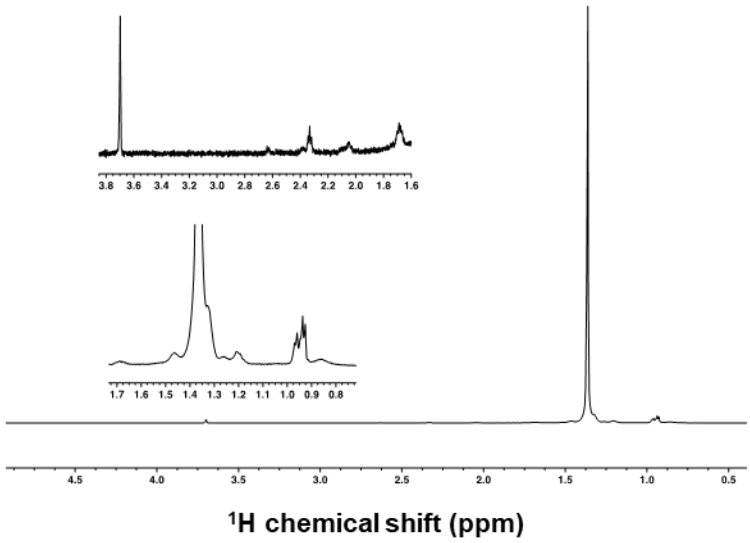

Figure 2.5.7. ^{1}H NMR spectrum of copolymer from entry 3, Table 2.2 (ppm). The left inset is a zoom in on the signals for the acrylates and the right inset is a zoom in on signals for the ends of polymer branches.

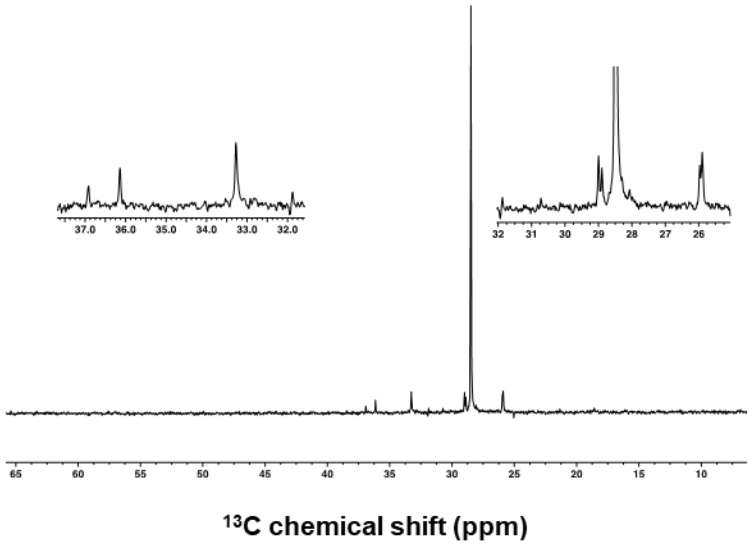

Figure 2.5.8. ^{13}C{^{1}H} NMR spectrum of copolymer from entry 3, Table 2.2 (ppm), insets are zoom in on the polymer signals.

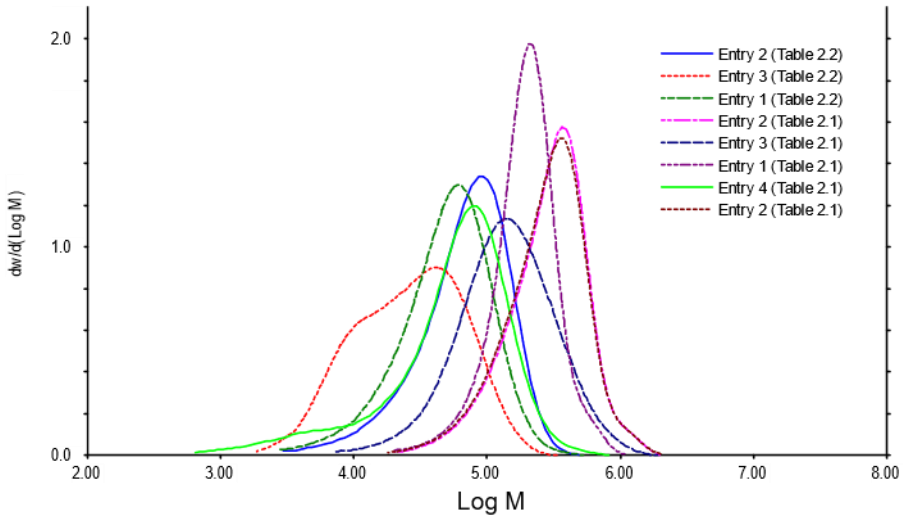

Figure 2.5.9. GPC data for all polymer samples.

2.6 References

(1) Culver, D. B.; Tafazolian, H.; Conley, M. P. A Bulky Pd(II) α-Diimine Catalyst Supported on Sulfated Zirconia for the Polymerization of Ethylene and Copolymerization of Ethylene and Methyl Acrylate. *Organometallics* **2018**, *37* (6), 1001–1006. https://doi.org/10.1021/acs.organomet.8b00016.

(2) Geyer, R.; Jambeck, J. R.; Law, K. L. Production, Use, and Fate of All Plastics Ever Made. *Sci. Adv.* **2017**, *3* (7), 1–5. https://doi.org/10.1126/sciadv.1700782.

(3) McDaniel, M. P. A Review of the Phillips Supported Chromium Catalyst and Its Commercial Use for Ethylene Polymerization. In *Advances in Catalysis*; Academic Press, 2010; Vol. 53, pp 123–606. https://doi.org/10.1016/S0360-0564(10)53003-7.

(4) Eisch, J. J. Fifty Years of Ziegler–Natta Polymerization: From Serendipity to Science. A Personal Account. *Organometallics* **2012**, *31* (14), 4917–4932. https://doi.org/10.1021/om300349x.

(5) Chen, C. Designing Catalysts for Olefin Polymerization and Copolymerization: Beyond Electronic and Steric Tuning. *Nat. Rev. Chem.* **2018**, *2* (5), 6–14. https://doi.org/10.1038/s41570-018-0003-0.

(6) Nakamura, A.; Ito, S.; Nozaki, K. Coordination-Insertion Copolymerization of Fundamental Polar Monomers. *Chem. Rev.* **2009**, *109*, 5215–5244. https://doi.org/10.1021/cr900079r.

(7) Johnson, L. K.; Mecking, S.; Brookhart, M. Copolymerization of Ethylene and Propylene with Functionalized Vinyl Monomers by Palladium(II) Catalysts. *J. Am. Chem. Soc.* **1996**, *118* (1), 267–268. https://doi.org/10.1021/ja953247i.

(8) Wang, F.; Chen, C. A Continuing Legend: The Brookhart-Type α-Diimine Nickel and Palladium Catalysts. *Polym. Chem.* **2019**, *10*, 2354–2369. https://doi.org/10.1039/c9py00226j.

(9) Tan, C.; Chen, C. Emerging Palladium and Nickel Catalysts for Copolymerization of Olefins with Polar Monomers. *Angew. Chemie Int. Ed.* **2019**, *58* (22), 7192–7200. https://doi.org/10.1002/anie.201814634.

(10) Drent, E.; Van Dijk, R.; Van Ginkel, R.; Van Oort, B.; Pugh, R. I. Palladium Catalysed Copolymerisation of Ethene with Alkylacrylates: Polar Comonomer Built into the Linear Polymer Chain. *Chem. Commun.* **2002**, 744–745. https://doi.org/10.1039/b111252j.

(11) Johnson, L. K.; Killian, C. M.; Brookhart, M. New Pd(II)- and Ni(II)-Based Catalysts for Polymerization of Ethylene and α-Olefins. *J. Am. Chem. Soc.* **1995**, *117* (23), 6414–6415. https://doi.org/10.1021/ja00128a054.

(12) Tempel, D. J.; Johnson, L. K.; Huff, R. L.; White, P. S.; Brookhart, M. Mechanistic Studies of Pd(II)-R-Diimine-Catalyzed Olefin Polymerizations 1. **2000**. https://doi.org/10.1021/ja000893v.

(13) Mecking, S.; Jonhnson, L. K.; Wang, L.; Brookhart, M. Mechanistic Studies of the Palladium-Catalyzed Copolymerization of Ethylene and R-Olefins with Methyl Acrylate. *J. Am. Chem. Soc.* **1998**, *120* (5), 888–899. https://doi.org/10.1021/ja964144i.

(14) Copéret, C.; Comas-Vives, A.; Conley, M. P.; Estes, D. P.; Fedorov, A.; Mougel, V.; Nagae, H.; Núnez-Zarur, F.; Zhizhko, P. A. Surface Organometallic and Coordination Chemistry toward Single-Site Heterogeneous Catalysts: Strategies, Methods, Structures, and Activities. *Chem. Rev.* **2016**, *116* (2), 323–421. https://doi.org/10.1021/acs.chemrev.5b00373.

(15) Hlatky, G. G. Heterogeneous Single-Site Catalysts for Olefin Polymerization. *Chem. Rev.* **2000**, *100* (4), 1347–1376. https://doi.org/10.1021/cr9902401.

(16) Severn, J. R.; Chadwick, J. C.; Duchateau, R.; Friederichs, N. "Bound but Not Gagged"-Immobilizing Single-Site a-Olefin Polymerization Catalysts. *Chem. Rev.* **2005**, *105* (11), 4073–4147. https://doi.org/10.1021/cr040670d.

(17) Stürzel, M.; Mihan, S.; Mülhaupt, R. From Multisite Polymerization Catalysis to Sustainable Materials and All-Polyolefin Composites. *Chem. Rev.* **2016**, *116* (3), 1398–1433. https://doi.org/10.1021/acs.chemrev.5b00310.

(18) Mackenzie, P. B.; Moody, L. S.; Killian, C. M.; Lavoie, G. G. Supported Group 8-10 Transition Metal Olefin Polymerization Catalysts., May 28, 2003.

(19) Schrekker, H. S.; Kotov, V.; Preishuber-Pflugl, P.; White, P.; Brookhart, M. Efficient Slurry-Phase Homopolymerization of Ethylene to Branched Polyethylenes Using α-Diimine Nickel(II) Catalysts Covalently Linked to Silica Supports. *Macromolecules* **2006**, *39* (19), 6341–6354. https://doi.org/10.1021/ma061032v.

(20) Preishuber-Pflugl, P.; Brookhart, M. Highly Active Supported Nickel Diimine Catalysts for Polymerization of Ethylene. *Macromolecules* **2002**, *35* (16), 6074–6076. https://doi.org/10.1021/ma020230t.

(21) Dorcier, A.; Merle, N.; Taoufik, M.; Bayard, F.; De Mallmann A., C. L.; Basset, J. M. Preparation of a Well-Defined Silica-Supported Nickel-Diimine Alkyl Complex - Application for the Gas-Phase Polymerization of Ethylene. *Organometallics* **2009**, *28* (7), 2173–2178. https://doi.org/10.1021/om800582x.

(22) Marks, T. J. Surface-Bound Metal Hydrocarbyls. Organometallic Connections Between Heterogeneous and Homogeneous Catalysis. *Acc. Chem. Res.* **1992**, *25* (2), 57–65. https://doi.org/10.1021/ar00014a001.

(23) Stalzer, M. M.; Delferro, M.; Marks, T. J. Supported Single-Site Organometallic Catalysts for the Synthesis of High-Performance Polyolefins. *Catal. Letters* **2015**, *145* (1), 3–14. https://doi.org/10.1007/s10562-014-1427-x.

(24) Tafazolian, H.; Culver, D. B.; Conley, M. P. A Well-Defined Ni(II) α-Diimine Catalyst Supported on Sulfated Zirconia for Polymerization Catalysis. *Organometallics* **2017**, *36* (13), 2385–2388. https://doi.org/10.1021/acs.organomet.7b00402.

(25) Dai, S.; Sui, X.; Chen, C. Highly Robust Palladium(II) α-Diimine Catalysts for Slow-Chain-Walking Polymerization of Ethylene and Copolymerization with Methyl Acrylate. *Angew. Chemie Int. Ed.* **2015**, *54* (34), 9948–9953. https://doi.org/10.1002/anie.201503708.

(26) Liu, Z.; Somsook, E.; Landis, C. R. A 2H-Labeling Scheme for Active-Site Counts in Metallocene-Catalyzed Alkene Polymerization. *J. Am. Chem. Soc.* **2001**, *123* (12), 2915–2916. https://doi.org/10.1021/ja0055918.

(27) Daugulis, O.; Brookhart, M.; White, P. S. Phosphinidine-Palladium Complexes for the Polymerization and Oligomerization of Ethylene. *Organometallics* **2002**, *21* (26), 5935–5943. https://doi.org/10.1021/om020631x.

Chapter 3 Formation of a Well-Defined Silylium-Like Surface Species Supported on Sulfated Zirconium Oxide[1]

3.1 Abstract

This chapter describes the reaction of allyltriisopropylsilane with sulfated zirconium oxide (SZO) to form [$^{i}Pr_3Si$][SZO], $^{i}Pr_3Si$-OZr≡, and SiO_x sites. The solid-state ^{29}Si NMR chemical shift of [$^{i}Pr_3Si$][SZO] is 53 ppm, which is downfield of $^{i}Pr_3SiOTf$ (41 ppm). The adsorption of Et_3PO to the surface forms [$^{i}Pr_3Si(OPEt_3)$][SZO] which has a $\Delta^{31}P$ NMR chemical shift similar to [$Et_3Si(OPEt_3)$][$B(C_6F_5)_4$], indicating that [$^{i}Pr_3Si$][SZO] is a strong Lewis acid. [$^{i}Pr_3Si$][SZO] initiates the hydrodefluorination of trifluorotoluene at 80 °C in the presence of Et_3SiH, producing up to 330 turnovers over 12 hours.

3.2 Introduction

Strong Lewis acid sites on oxide surfaces are important in heterogeneous catalysis.[2,3] For example, partially dehydroxylated alumina contains Lewis acidic Al sites on the surface that catalyze C-H bond activation and C-C bond formation.[4–8] Lewis acid sites in zeolites influence the Brønsted acidity of nearby hydroxyls in zeolites, which are implicated in several catalytic reactions.[9,10] High surface area $AlCl_xF_{3-x}$ (ACF) contains Lewis acid sites with acidities similar to the calculated gas phase fluoride ion affinity of SbF_5 and catalyzes Friedel-Craft coupling, dehydrohalogenation, and hydrodefluorination reactions.[11]

Silylium ions (R_3Si^+) are the silicon analogues of carbocations (R_3C^+) and are among the strongest known Lewis acids. Silanes tend to react with ≡M-OH sites on the

surface of oxides (such as silica and zeolites) to form inert ≡MO-SiR_3 sites.[12–16] Chapter 2 discussed the use of sulfated zirconium oxide (SZO) as a weakly coordinating anion for well-defined cationic organometallic catalysts. This chapter describes the reaction of allyltriisopropylsilane and SZO, which forms a well-defined silylium-like ion on the surface of SZO (Figure 3.2.1).

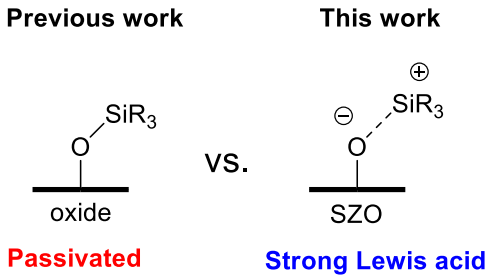

Figure 3.2.1. Silane passivated oxides (previous work) versus silylium-like ions supported on the surface of sulfated zirconium oxide (this work).

3.2.1 Properties of silylium ions

The challenges in isolating silylium ions are well documented.[17,18] This is related to silicon being larger, softer, and more electropositive than carbon. As a result, there are fewer examples of "free" silylium ions than carbocations. $[Mes_3Si^+][CHB_{11}Me_5Br_6^-]$ was the first characterized by x-ray crystallography.[19] The Mes_3Si^+ fragment contains a planar silicon with average C–Si–C bond angles of 120° (Figure 3.2.2A). Silylium-like ions that coordinate to weak Lewis bases (L = Et_3SiH, SO_2, toluene, or MeCN) to form $[R_3Si\text{-}L][WCA]$[20–23] or weakly coordinating anions (WCA = $CB_9H_5Br_5^-$, $CB_{11}H_6Cl_6^-$, or $CB_{11}H_6Cl_6^-$) to form $[R_3Si][WCA]$[20,24] are more common. Silylium-like ions contain average C–Si–C bond angles between 115 and 118°, indicating that the silicon is pyramidal

in these species. These values are smaller than the 120° for planar silicon, but larger than C–Si–C bond angles in more covalent R_3Si-X (X = -OR, OTf^- or ClO_4) compounds.

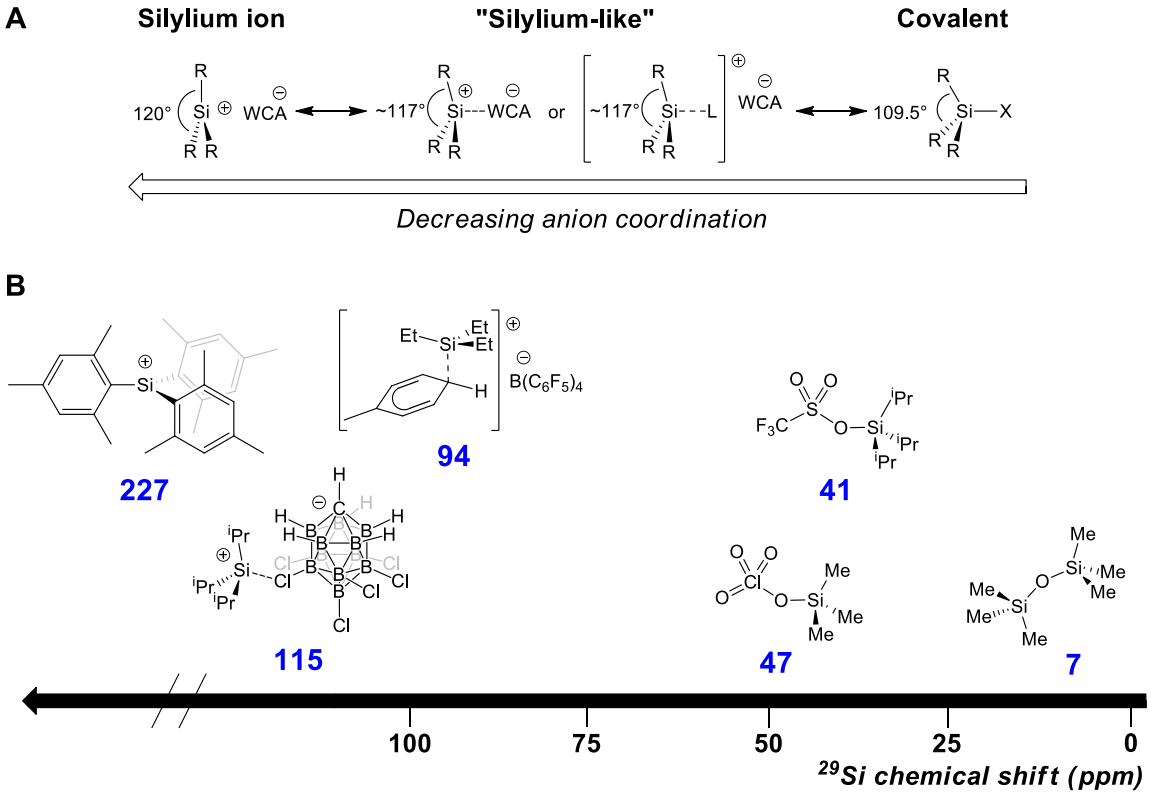

Figure 3.2.2. A) The R-Si-R bond angle increases as the anion becomes less coordinating and R_3Si-X becomes more ionic (L = ligand); and B) ^{29}Si NMR chemical shift scale for R_3Si-X, [R_3Si-L][WCA] and [R_3Si][WCA] compounds.

^{29}Si NMR chemical shifts are sensitive to the coordination environment around silicon. Representative examples of ^{29}Si NMR chemical shifts of R_3Si-X, [R_3Si-L][WCA], and [R_3Si][WCA] compounds are shown in Figure 3.2.2B. The ^{29}Si NMR chemical shift of $(Me_3Si)_2O$, a covalent R_3Si-X compound, is 7 ppm.[25] $R_3SiOClO_3$ and R_3SiOTf (R = alkyl) are mild Lewis acids and have ^{29}Si NMR chemical shifts that are downfield of

silylethers but upfield of silylium-like species.[26,27] Silylium-like ions [R_3Si-L][WCA] or [R_3Si][WCA] have more deshielded ^{29}Si NMR chemical shifts than R_3Si-X. For example, [Et_3Si(toluene)][$B(C_6F_5)_4$][28] and [$^iPr_3Si$][$CH_6B_{11}Cl_6$][29] have ^{29}Si NMR chemical shifts of 94 and 115 ppm in the solid-state, respectively. Free silylium [Mes_3Si][$CHB_{11}Me_5Br_6$] has a ^{29}Si NMR chemical shift of 226.7 ppm in the solid state.[19]

Silylium-like ions activate inert C-F bonds.[30–33] [Et_3Si][$CHB_{11}Cl_{11}$] abstracts a fluoride from fluorobenzene to yield an isolable phenyl cation,[34] which are reactive towards C-H bonds in alkanes to form alkylated products.[35] In the presence of excess R_3Si-H, incipient carbocations formed from C-F bond activation are quenched to form a C-H bond, a net hydrodefluorination (HDF) reaction (Figure 3.2.3A).[30–33] DFT studies of this reaction showed that the HDF reaction can be rationalized from fluoride ion affinity (FIA) and hydride ion affinity (HIA) of key intermediates.[36] The separated reactions and calculated enthalpies for the HDF of trifluorotoluene with triethylsilane are shown in Figure 3.2.3B. The calculated energy for $PhCF_3$ to form $PhCF_2^+$ and F^- is 205.5 kcal mol^{-1}. The driving force for this very endothermic reaction is the reaction of Et_3Si^+ with F^-, which has a calculated FIA of 217.4 kcal mol^{-1}. The HDF reaction is also driven by the very favorable HIA of $PhCF_2^+$ to form $PhCF_2H$ (HIA = -241.3 kcal mol^{-1}), and the modestly endothermic activation of the Si-H bond to form the silylium ion (HIA = 213.2 kcal mol^{-1}). These results show that the overall HDF reaction of $PhCF_3$ is thermodynamically favorable due to the strong C-H and Si-F bonds formed in this reaction.

A

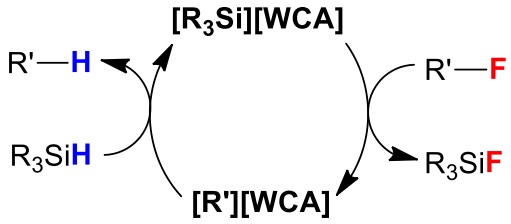

B

(1) $PhCF_3 \longrightarrow PhCF_2^+ + F^-$ ΔH = **FIA** = 205.5 kcal mol^{-1}

(2) $Et_3Si^+ + F^- \longrightarrow Et_3SiF$ ΔH = - **FIA** = - 217.4 kcal mol^{-1}

(3) $Et_3SiH \longrightarrow Et_3Si^+ + H^-$ ΔH = **HIA** = 213.2 kcal mol^{-1}

(4) $PhCF_2^+ + H^- \longrightarrow PhCF_2H$ ΔH = - **HIA** = - 241.3 kcal mol^{-1}

---

(5) $PhCF_3 + Et_3SiH \longrightarrow PhCF_2H + Et_3SiF$ ΔH_{HDF} = -40.0 kcal mol^{-1}

Figure 3.2.3. A) Catalytic HDF of C-F bonds with [R_3Si][WCA] in the presence of R_3SiH; and B) estimation of the overall reaction enthalpy (Hess's law) for the HDF of trifluorotoluene with triethylsilane using the calculated gas phase FIA and HIA of the $PhCF_2^+$ and Et_3Si^+ cation intermediates.

As the number of C-F bonds decreases the C-F activation becomes more favorable. For example, the calculated gas phase FIAs of $PhCHF^+$ and $PhCH_2^+$ (-196.5 and -186.9 kcal mol^{-1}, respectively) are lower than the FIA for $PhCF_2^+$. Therefore, in the HDF of trifluorotoluene the reaction ultimately forms toluene; $PhCHF_2$ or $PhCF_2H$ are not observed. Aryl cations and perfluorinated primary alkyl cations are less stable than benzyl cations making aryl fluorides and perfluro-alkanes more challenging to activate. The FIA for $C_6H_5^+$ and $CF_3CF_2^+$ have gas phase FIA calculated to be 241.2 and 272.4 kcal mol^{-1}, respectively. As a result, there are only a few silylium-like compounds that activate aryl fluorides or perfluoro-alkanes.[37]

Trifluorotoluene has been used to compare the reactivity of HDF catalysts (Figure 3.2.4). Et_3SiOTf does not react with trifluorotoluene at 110 °C for at least a week in the presence of excess Et_3SiH.[31] $[Et_3Si][B(C_6F_5)_4]$ initiates the HDF of trifluorotoluene in the presence of excess Et_3SiH to give 72 turnovers over 2 hours at room temperature.[38] Under these conditions the $B(C_6F_5)_4^-$ anion decomposes, which limits stability of this catalyst system. Carborane anions are more stable than $B(C_6F_5)_4^-$ and do not decompose under similar reaction conditions. This enhanced stability improves TON of trifluorotoluene HDF to give up to 2000 turnovers using $[Et_3Si][CHB_{11}Cl_{11}]$ at room temperature over 12 hours.[39,40]

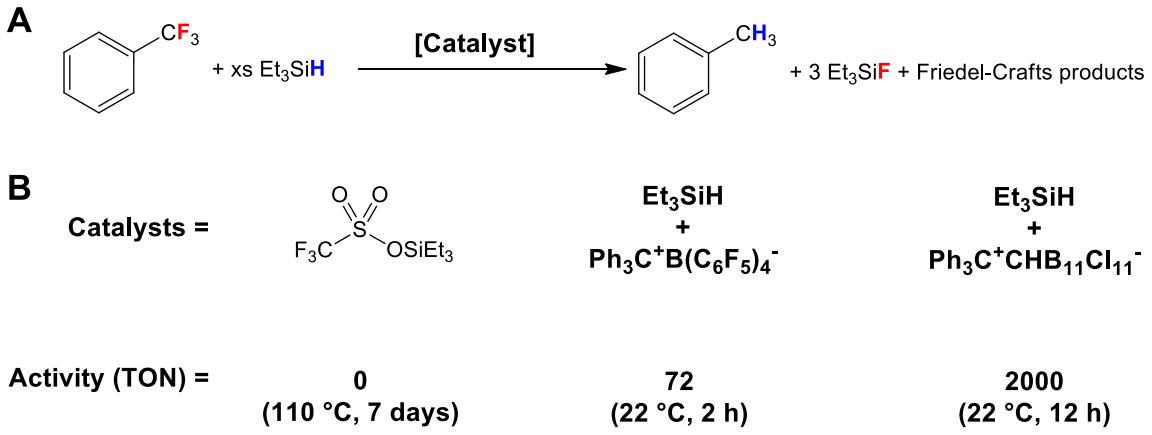

Figure 3.2.4. A) scheme for the catalytic HDF of trifluorotoluene and B) HDF activities of some homogeneous catalysts generated in-situ (reaction conditions shown in parenthesis).

This discussion shows there are several important features to consider when approaching the formation of R_3Si^+ like sites on oxide surfaces. A R_3Si^+ like surface species is expected to have a deshielded ^{29}Si NMR chemical shift and activate C-F bonds.

This chapter describes the reaction silanes with partially dehydroxylated silica, alumina, and SZO. Solid-state ^{29}Si NMR spectroscopy shows that silica and alumina contain R_3Si-O sites. SZO reacts with allyltriisopropylsilane to form silylium-like surface sites. These sites were characterized by solid-state ^{29}Si NMR spectroscopy and also by the Gutmann-Beckett method, both of which suggest that [$^{i}Pr_3Si$][SZO] are strong Lewis acid sites. [$^{i}Pr_3Si$][SZO] initiates the hydrodefluorination of trifluorotoluene and other substrates at elevated temperatures in the presence of excess Et_3SiH.[1]

3.3 Results and discussion

3.3.1 Synthesis and characterization of silane passivated silica

Silica contains surface -OH sites, and physisorbed water. Heating silica under vacuum results in removal of physisorbed water and partial dehydroxylation of the -OH sites. Silica partially dehydroxylated at 700 °C ($SiO_{2\text{-}700}$) is prepared by calcining Aerosil-200 (surface area = 200 m^2/g) in air, followed by dehydroxylation under vacuum at 700 °C (Scheme 3.3.1). $SiO_{2\text{-}700}$ contains 0.26 mmol -OH g^{-1}, most of which are isolated ≡SiOH sites, and a small number of geminal ≡$Si(OH)_2$ sites (~5-10 %).[41] An FT-IR spectrum of $SiO_{2\text{-}700}$ is shown in Figure 3.3.1.

Scheme 3.3.1. Synthesis of $SiO_{2\text{-}700}$.

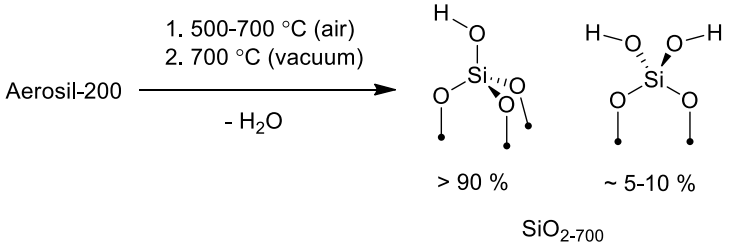

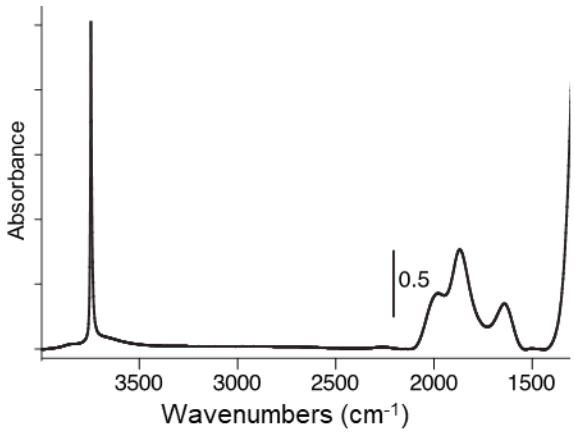

Figure 3.3.1. FT-IR spectrum of $SiO_{2\text{-}700}$ (cm^{-1}).

$SiO_{2\text{-}700}$ reacts with neat hexamethyldisilizane over 3 days to yield **Si1** (Scheme 3.3.2).[12] The FT-IR spectrum of **Si1** shows that the $\nu_{O\text{-}H}$ stretch decreases significantly, indicating that a majority of the ≡Si-OH were consumed in this reaction. New $\nu_{C\text{-}H}$ stretches for ≡Si-$OSiMe_3$ are also present in the FTIR spectrum of **Si1** (Figure 3.3.2A). The solid-state ^{29}Si CP-MAS NMR spectrum of **Si1,** shown in Figure 3.3.2B, contains signals at 14, 5 and -108 ppm. The peaks at 14 and 5 ppm are assigned to ≡SiO-$SiMe_3$ surface sites. The peak at -108 ppm is assigned to bulk SiO_2. The ^{29}Si chemical shifts for the surface trimethylsilyl sites (14 and 5 ppm) are similar to the chemical shifts of silyl ethers[25] and O-$SiMe_3$ sites on the surface of zeolite H-beta (^{29}Si NMR = 17 ppm; Si/Al = 37.5).[13]

Scheme 3.3.2. Synthesis of **Si1**

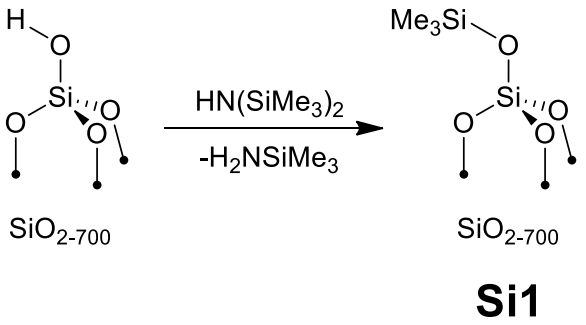

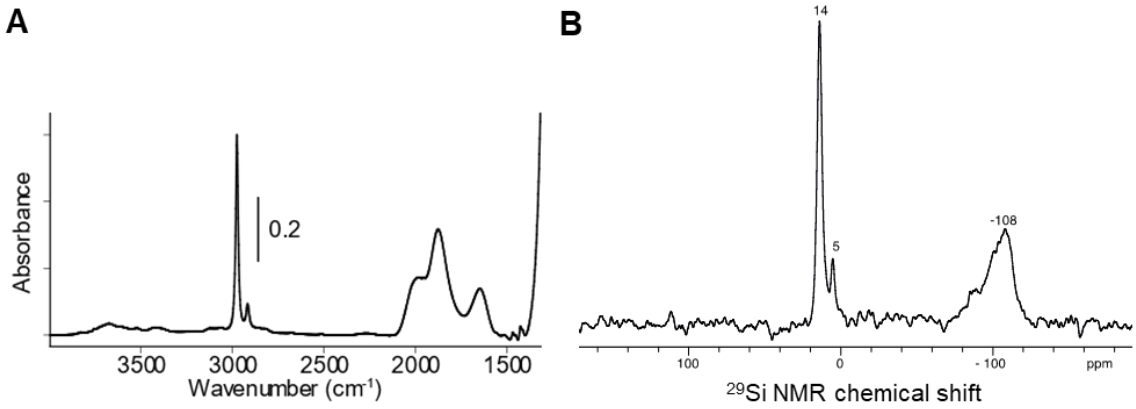

Figure 3.3.2. A) FT-IR spectrum of **Si1** (cm^{-1}); and B) solids-state ^{29}Si CP-MAS NMR spectrum of **Si1**.

3.3.2 Allyltriisopropylsilane grafted onto partially dehydroxylated alumina

High surface area γ-alumina (280 m^2/g) partially dehydroxylated at 600 °C ($Al_2O_{3\text{-}600}$) contains 0.93 mmol -OH g^{-1}. $Al_2O_{3\text{-}600}$ reacts with allyltriisopropylsilane to form **Si2** and 0.17 mmol/g of propene (18 % of the -OH), Figure 3.3.3A. The FT-IR spectrum of **Si2** shows a decrease in the $\nu_{O\text{-}H}$ stretches and the appearance of the expected sp^3 $\nu_{C\text{-}H}$ stretches

for ≡AlO-Si^{i}Pr$_3$ sites (Figure 3.3.3B). An sp^2 ν_{C-H} band is also observed and is assigned to physisorbed allyltriisopropylsilane on the surface. The ^{13}C CP-MAS NMR spectrum contains chemical shifts at 134, 111, 17 and 9.3 ppm (Figure 3.3.3C). The signals at 134 and 111 ppm are consistent with allyl ^{13}C chemical shifts which supports the presence of allyl groups on the surface of **Si2**. The signals at 17 and 9.3 ppm are assigned to overlapping isopropyl groups from ≡AlO-Si^{i}Pr$_3$ and physisorbed allyltriisopropylsilane. The ^{29}Si CP-MAS NMR spectrum of **Si2** contains signals at 1.4 and -5.2 ppm that are assigned to ≡AlO-Si^{i}Pr$_3$ and physisorbed allyltriisopropylsilane, respectively (Figure 3.3.3D). The ^{29}Si NMR chemical shift at 1.4 ppm is consistent with the formation of ≡AlO-Si^{i}Pr$_3$ sites.

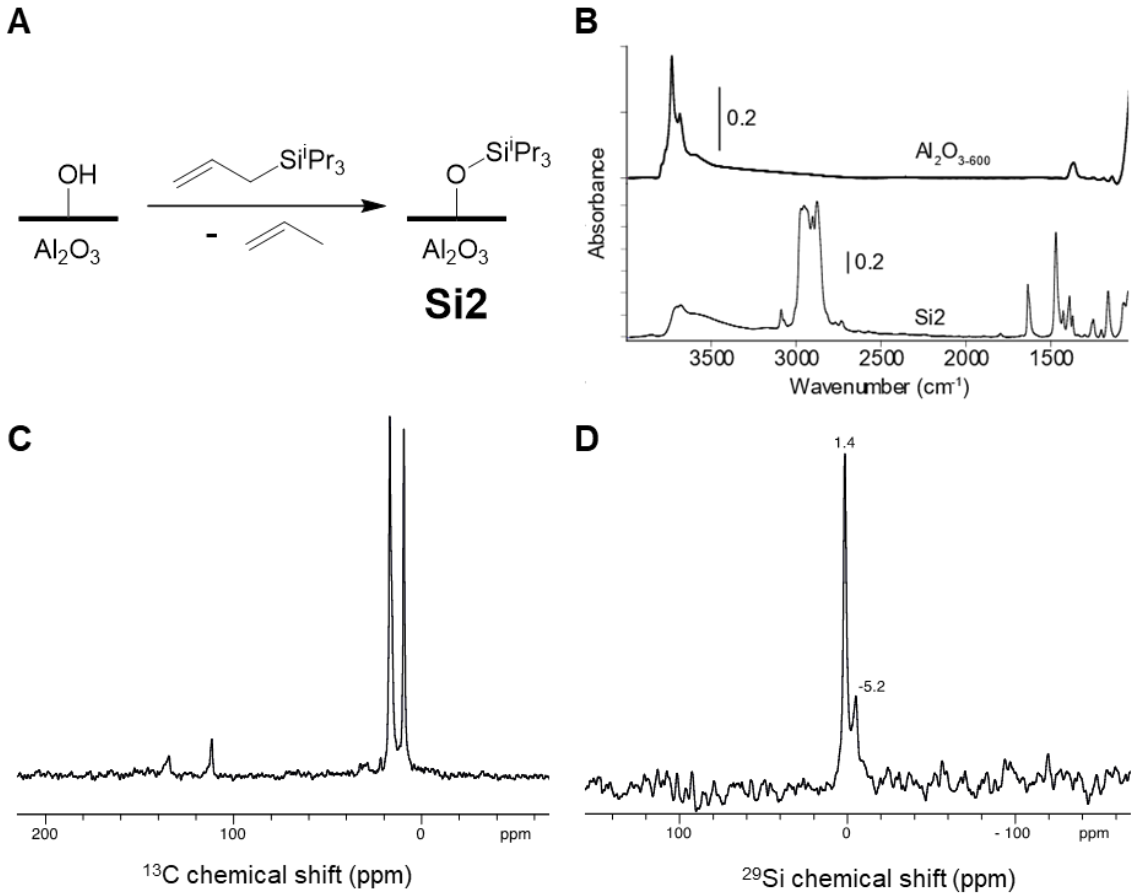

Figure 3.3.3. A) reaction scheme for the synthesis of **Si2**; and B) FT-IR spectrum of **Si2**. C) and D) Solid-state NMR spectra of **Si2**: C) ^{13}C CP-MAS; and D) ^{29}Si CP-MAS.

3.3.3 Synthesis and characterization of silylium-like ions on sulfated zirconium oxide

SZO (see chapter 2) reacts with allyltriisopropylsilane in a slurry of pentane to form **Si3** (Scheme 3.3.3). The reaction also forms 0.12 (±0.01) mmol g^{-1} of propene (~92 % of the surface -OH loading) and 0.041(±0.003) mmol g^{-1} of propane. The FT-IR spectrum of **Si3** shows that the ν_{O-H} bands have been partially consumed and new sp^3 ν_{C-H} stretches are present (Figure 3.3.4A). The ^{13}C CP-MAS of **Si3**, shown in Figure 3.3.4B, contains signals at 18 and 15 ppm for the isopropyl groups.

Scheme 3.3.3. Synthesis of **Si3**

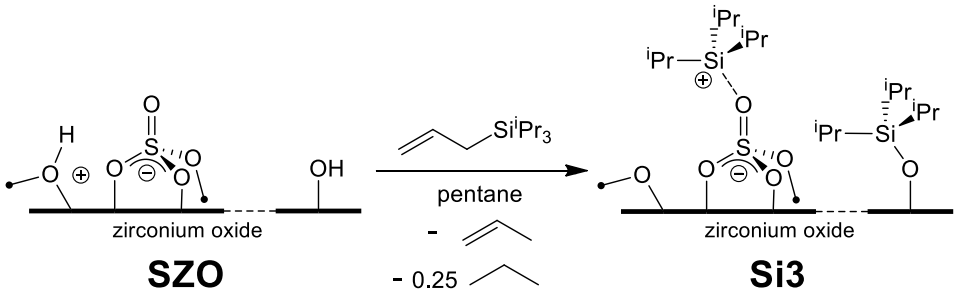

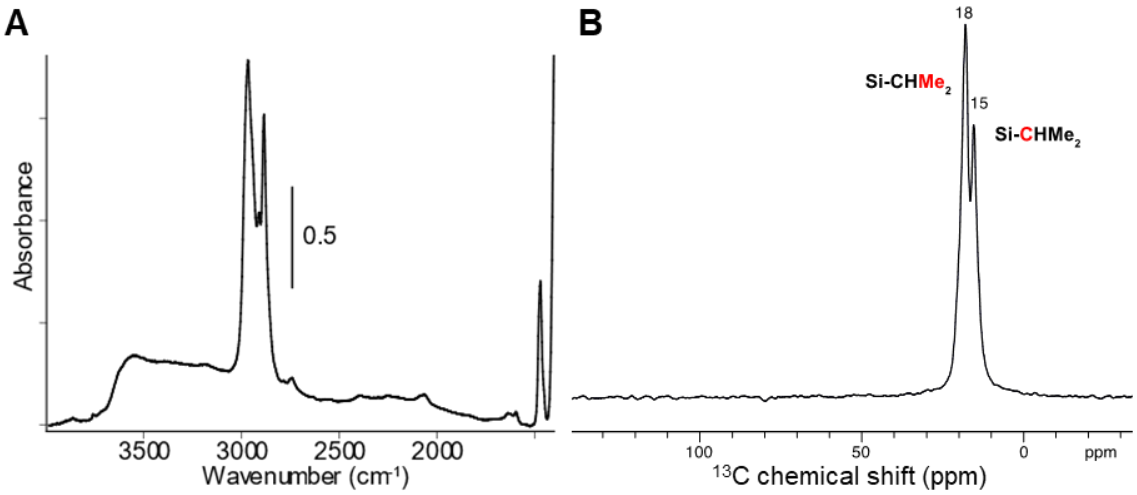

Figure 3.3.4. A) FT-IR spectrum of **Si3**; and B) solid-state ^{13}C CP-MAS NMR spectrum of **Si3**.

The ^{29}Si CP-MAS NMR spectrum of **Si3** contains signals at 53, 43, 4, and -100 ppm (Figure 3.3.5). The signal at -100 ppm is typical of SiO_x species on the surface of SZO, indicating that allyltriisopropylsilane reacts with SZO to form SiO_x, which likely accounts for the formation of propane in the reaction. The signal at 4 ppm is assigned to ≡ZrO-Si^{i}Pr$_3$ sites. The signals at 53 and 43 ppm are Lewis acidic [^{i}Pr$_3$Si][SZO] sites on **Si3**. These signals are more downfield than the ^{29}Si NMR chemical shifts of **Si1** and **Si2**.

The ^{29}Si NMR signals at 53 and 43 ppm are also more downfield than the ^{29}Si chemical shift of $^{i}Pr_3SiOTf$ (41.2 ppm),[26] suggesting that [$^{i}Pr_3Si$][SZO] sites may exhibit silylium-like behavior.

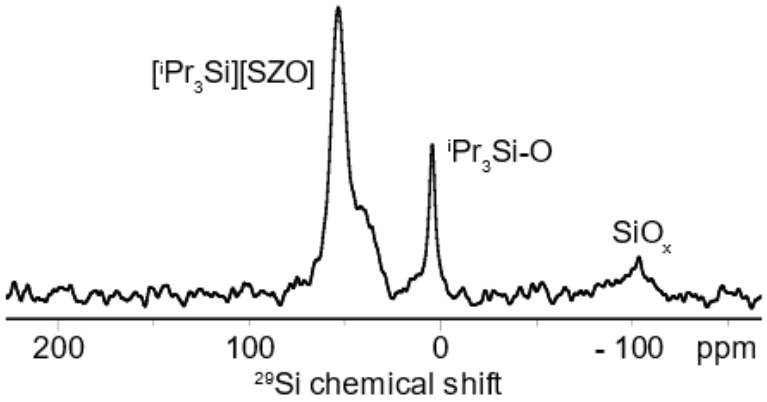

Figure 3.3.5. Solid-state ^{29}Si CP-MAS NMR spectrum of **Si3**.

*3.3.4 Examination of the Lewis acidity of **Si3** with Et_3PO*

Gutmann and Beckett studied the reaction of triaryl and trialkyl phosphine oxides ($R_3P=O$) with Lewis acids.[42,43] $R_3P=O$ forms adducts with Lewis acids (EX_n) to generate $R_3PO\rightarrow EX_n$. The adducts have downfield ^{31}P NMR chemical shifts with respect to free R3P=O, and the change in the ^{31}P NMR chemical shift ($\Delta\delta^{31}P$) correlates with Lewis acid strength. These trends also apply to measuring the acidity of a variety of solid acids.[44] A few $\Delta\delta^{31}P$ are shown in Table 3.1 for some selected Lewis acids. The coordination of Et_3PO to $B(C_6F_5)_3$ forms Et_3PO-$B(C_6F_5)_3$ which has a $\Delta^{31}P$ δ_{iso} of 30.6 ppm.[43] Perfluoro and perchloro bis-catechol silanes are neutral silicon Lewis acids and both have $\Delta\delta$ ^{31}P more deshielded than $B(C_6F_5)_3$.[45,46] This results suggests that halogenated *bis*(catechol)silanes

are stronger Lewis acids than $B(C_6F_5)_3$. $[Et_3Si(OPEt_3)][B(C_6F_5)_4]$ has a $\Delta\delta^{31}P$ of 42.2 ppm in C_6D_6;[47] larger than $B(C_6F_5)_3$ and $Si(cat^X)_2$.

Table 3.1. $\Delta\delta^{31}P$ NMR chemical shifts for a select Et_3PO-EXn adducts.

Entry	Lewis acid	$\Delta\delta^{31}P$ (ppm)[a]	Ref.
1	$B(C_6F_5)_3$	30.6	43
2	$Si(cat^{Cl})_2$	33.9	45
3	$Si(cat^{F})_2$	35.9	46
4	$[Et_3Si][B(C_6F_5)_4]$	42.2	47
5[b]	**Si3**	20 43	this work[1]

a) Measured in C_6D_6; and b) measured in the solid state.

Si3 reacts with Et_3PO in a slurry of pentane to form $[^iPr_3Si\text{-}OPEt_3][SZO]$ (**Si3P**), Scheme 3.3.4. The $^{31}P\{^1H\}$ solid-state NMR of **Si3P** contains signals at 93 and 70 ppm (Figure 3.3.6A). The presence of multiple signals in this spectrum is not surprising because there are different silicon sites present on **Si3** from the ^{29}Si NMR spectrum shown in Figure 3.3.5. The peak at 93 ppm has a $\Delta\delta^{31}P$ of 43 ppm, which is similar to $[Et_3Si(OPEt_3)][B(C_6F_5)_4]$ (42.2 ppm) and suggests that **Si3** may have silylium-like reactivity. The peak at 70 ppm has a $\Delta\delta^{31}P$ of 20 ppm, indicating that the sites is less Lewis

acidic. The solid-state ^{29}Si CP-MAS NMR spectrum of **Si3P** (Figure 3.3.6B) contains a new major signal at 25.5 ppm, indicating that Et_3PO is coordinates to the Lewis acidic silicon in [$^{i}Pr_3Si$][SZO].

Scheme 3.3.4. Reaction of **Si3** with Et_3PO

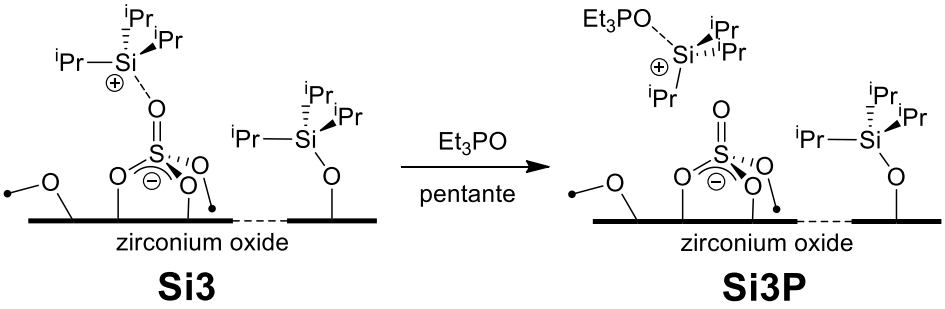

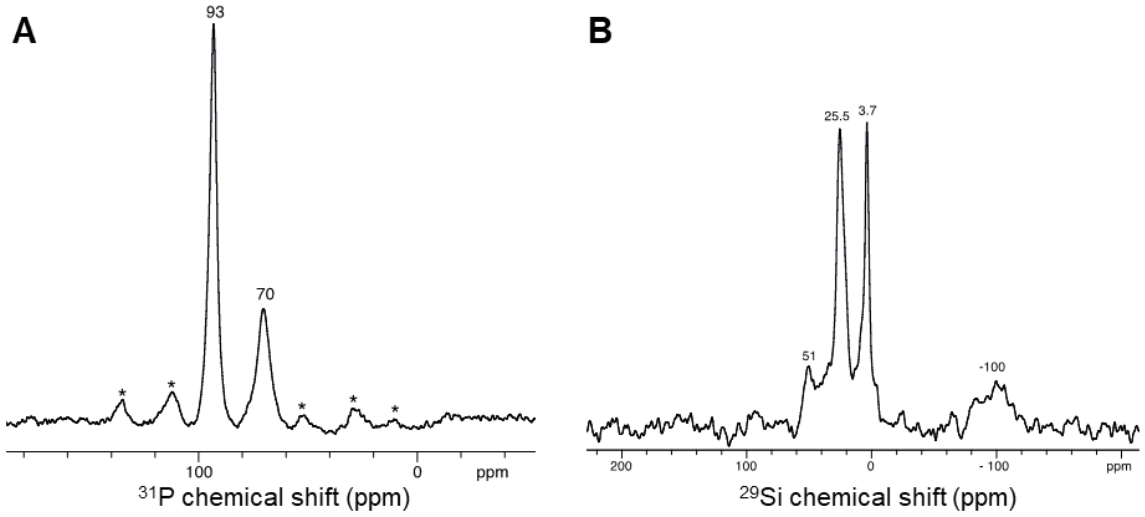

Figure 3.3.6. Solid-state NMR spectra of **Si3P**: A) ^{31}P MAS NMR spectrum, * = spinning sidebands; and B) ^{29}Si CP-MAS NMR spectrum.

*3.3.5 Hydrodefluorination of C-F bonds with **Si3***

Si3 initiates the HDF of trifluorotoluene (330 equiv/Si) in the presence of excess Et_3SiH at 80 °C, Scheme 3.3.5. This result, in addition to the deshielded ^{29}Si NMR chemical shift, indicates that some sites on **Si3** show silylium-like character. **Si3P** is inactive in the HDF of trifluorotoluene under these conditions, indicating that **Si3P** does not contain silylium-like sites.

Scheme 3.3.5. HDF of trifluorotoluene with **Si3**

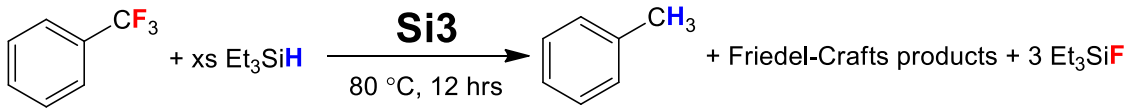

The solid-state NMR spectroscopy of **Si3** shows that multiple silicon sites are present, and some of these sites are not very Lewis acidic from Et_3PO adsorption studies. A poisoning study was conducted to determine the quantity of active sites in **Si3**. Titrated amounts of Et_3PO, the poison for this study because Si3P is inactive in HDF, are added to a known quantity of catalyst, then the catalytic reaction is initiated to determine the relative decrease in activity at a known poison loading. Plotting the poison:Si ratio versus catalytic activity should give a linear decrease in turnover, assuming the catalytic sites do not deactivate during the course of the experiment. Linear fitting of the data provides the quantity of active sites in this reaction, extrapolated to zero turnovers.[48] The TON versus equivalents of Et_3PO/Si plot is shown in Figure 3.3.7. The x-intercept of the plot, which

corresponds to TON = 0, corresponds to the quantity of active sites. This study showed that ~75 % of the silicon sites in Si3 are capable of initiating HDF of trifluorotoluene in **Si3**.

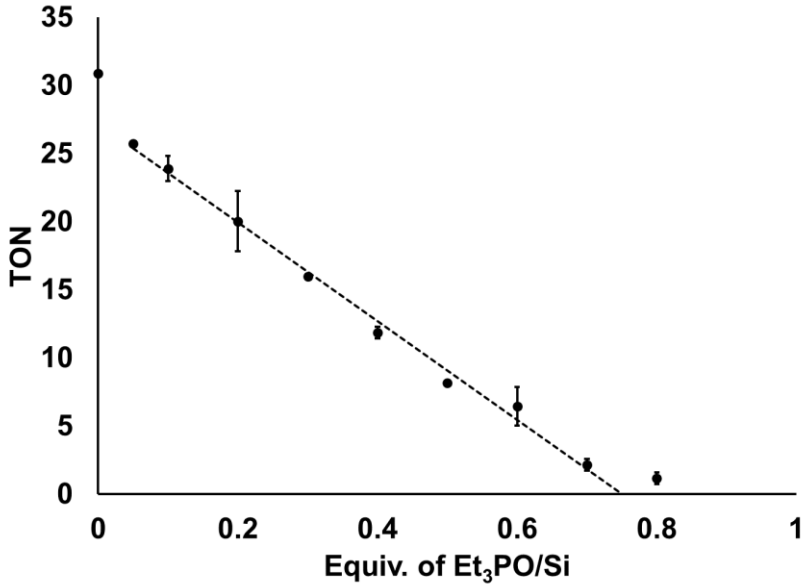

Figure 3.3.7. Data for the hydrodefluorination of trifluorotoluene with **Si3** in the presence of titrated quantities of Et_3PO. Each point is the average of a duplicate, the error bars indicate the difference between measurements, and the dashed line is the linear least squares regression of the data ($y = -36.2X + 27.2$, $R^2 = 0.994$).

Table 3.2 contains a summary of the HDF data using **Si3**. At 80 °C with a 0.13 % catalyst loading, **Si3** performs 330 turnovers in HDF of trifluorotoluene in 12 hours (entry 1). Representative $^{19}F\{^1H\}$ NMR spectra during the HDF of trifluorotoluene are shown in Figure 3.3.8A. The activity steadily decreases over ~ 12 hours at 42 % conversion of trifluorotoluene, indicating that the R_3Si^+ sites degrade during the HDF reaction over this time (Figure 3.3.8B). The yield of toluene was ~ 20 % of the theoretical yield based on the Et_3SiF suggesting that there is a significant amount of Friedel-Crafts side reactions that

occur. This behavior is typical of HDF reactions mediated by $[R_3Si][WCA]$.[39] Prior to this work, the only heterogeneous material for the HDF of trifluorotoluene was $AlCl_xF_y$ (ACF), which catalyzes 15 TON over 7 days in the presence of excess silane.[49]

Table 3.2 Summary of catalyzed hydrodefluorination reactions with **Si1-4**.[a]

Entry	Catalyst	Substrate	Cat. loading (%)[b]	t (h)	Conv. (%)	TON[c]
1	**Si3**	$C_6H_5CF_3$	0.13	12	42	330
2[d]	**Si3**	$C_6F_5CF_3$	0.82	504	76	93
3[e]	**Si3**	$C_{10}H_{15}F$	0.5	24	80	160
4[d]	**Si3**	$C_4F_9CHCH_2$	2.0	30	67	112
5	**Si4**	$C_6H_5CF_3$	0.13	4	22	180
6	**Si1**	$C_6H_5CF_3$	0.87[f]	24	0	0
7	**Si2**	$C_6H_5CF_3$	0.23[g]	12	0	0

a.) performed as neat solutions with ~1.1 equivalents of Et_3SiH per reactive C-F bond at 80 °C except where otherwise indicated; b.) reactive Si sites based on the poisoning study; c.) mol Et_3SiF/mol Si, quantified by ^{19}F NMR spectroscopy; d.) performed at 120 °C; e.) performed in cyclohexane at room temperature; f.) assuming all ≡SiOH react with HMDS to yield ≡SiO-$SiMe_3$ sites; and g.) based on the propene observed from the synthesis of **Si2**.

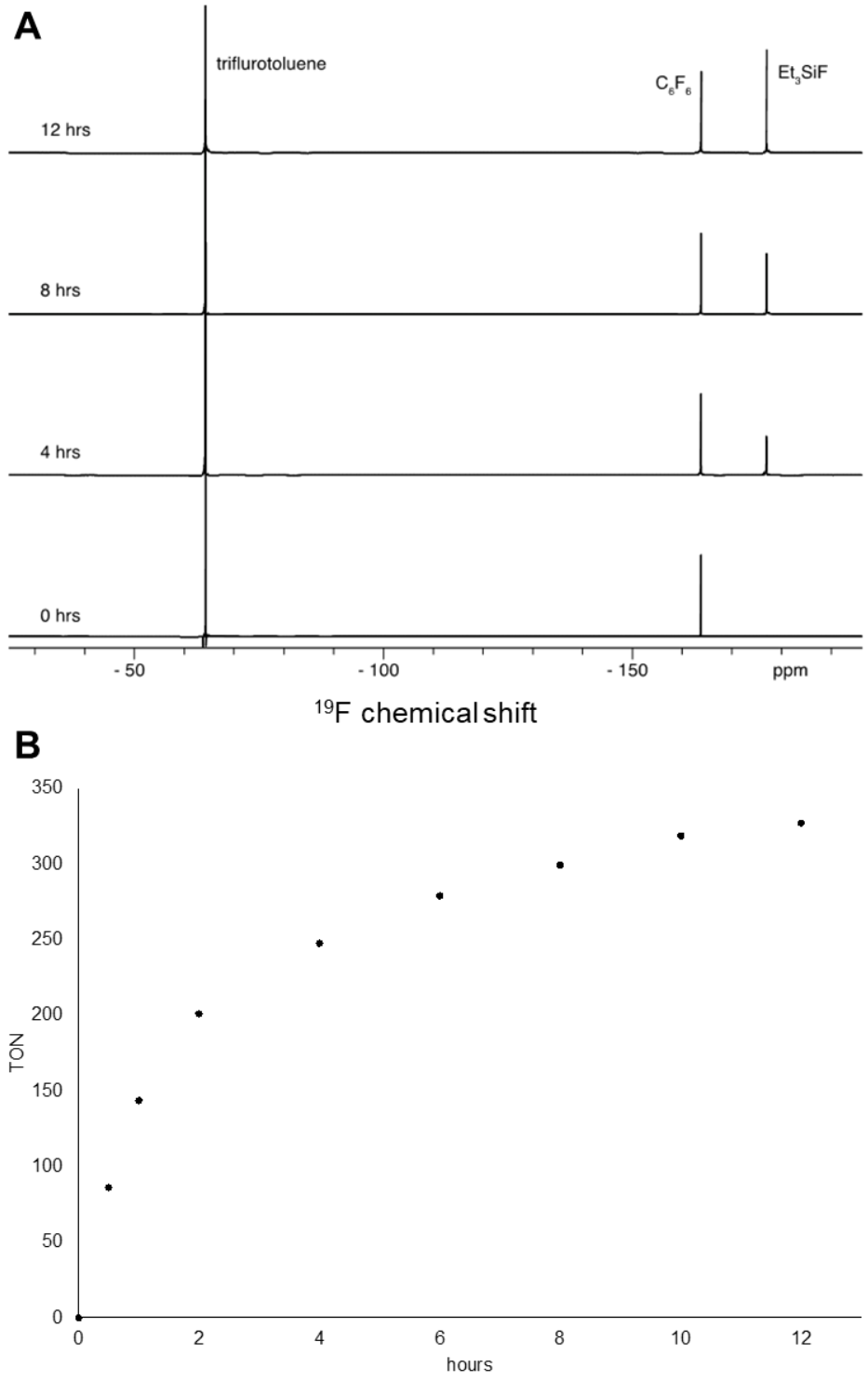

Figure 3.3.8. A) $^{19}F\{^{1}H\}$ NMR spectra of the HDF of trifluorotoluene with **Si3** over time and B) TON over time plot.

Si3 hydrodefluorinates octaflurotoluene at 120 °C to form pentafluorotoluene (TON = 93, 3 weeks, Table 3.2 Entry 2), though at much slower rates than trifluorotoluene. The $^{19}F\{^{1}H\}$ NMR spectra for the reaction show that 2,3,4,5,6-pentaflurotoluene cleanly grows in along with the Et_3SiF (Figure 3.3.9A). The sp^2 C-F bonds are not activated in this reaction. The TON versus time plot in Figure 3.3.9B shows that the activity is relatively linear over 3 weeks. This is contrary to trifluorotoluene where the activity slows down over 12 hours. This may suggest that the Friedel-Crafts side reactions during the hydrodefluorination of trifluorotoluene causes catalyst deactivation.[39]

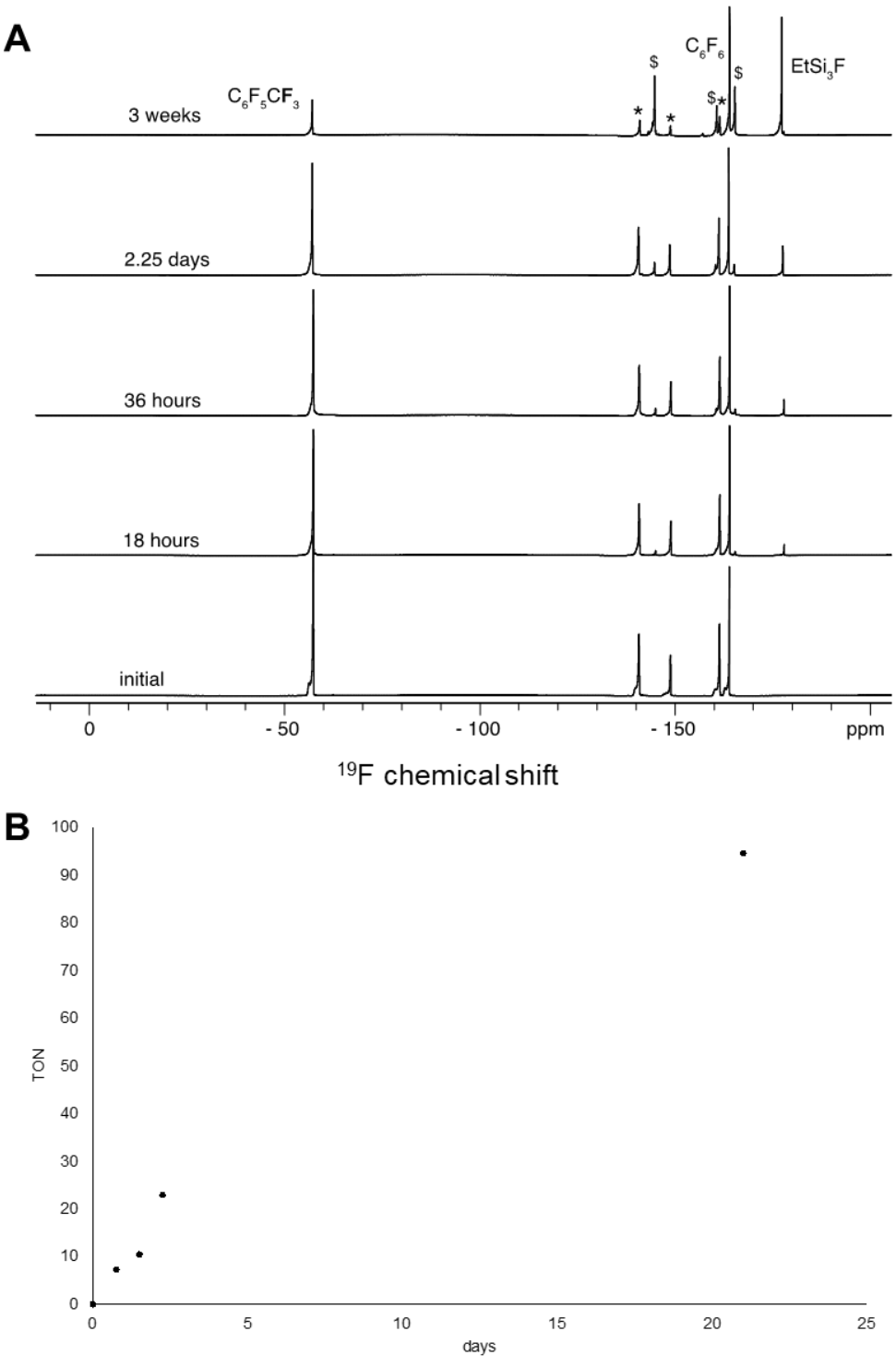

Figure 3.3.9. Data for the HDF of octafluorotoluene at 120 °C with **Si3** over time: A) $^{19}F\{^{1}H\}$ NMR spectra; * = starting material and $ = 2,3,4,5,6-pentaflurotoluene; and B) TON over time plot.

Si3 hydrodefluorinates 1-fluoroadamantane at room temperature to form adamantane (TON = 160, 24 h, Table 3.2 Entry 3). **Si3** also initiates HDF of 1H,1H,2H-perfluoro-1-hexene at 120 °C to give 112 TON in 30 hours (entry 4). The major product of the reaction is (Z)-$CH_3CHCFC_3F_7$. This reaction proceeds by allylic C-F bond activation to form the allyl cation intermediate, which is quenched by Et_3SiH at the least hindered position to give (Z)-$CH_3CHCFC_3F_7$ (Scheme 3.3.6). Similar to the HDF of octafluorotoluene, only the most activated allyl C-F bond in 1H,1H,2H-perfluoro-1-hexene is activated under these conditions. Attempts to hydrodefluorinate perfluorohexanes at 120 °C in the presence of excess Et_3SiH did not result in HDF products.

Scheme 3.3.6. Formation of (Z)-$CH_3CHCFC_3F_7$ from $CH_2CHCF_2C_3F_7$ using R_3Si^+ and Et_3SiH

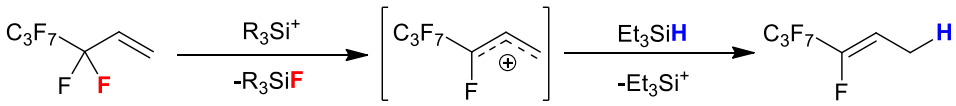

Et_3SiH reacts with SZO to form **Si4** (Scheme 3.3.7).[50] The FT-IR spectrum of **Si4** contains new ν_{C-H} bond stretches and the ν_{O-H} stretches are reduced (Figure 3.3.10A). There is also new broad ν_{Si-H} stretch at ~2200 cm^{-1} assigned to physisorbed triethylsilane. The solid-state ^{29}Si CP-MAS NMR spectrum of **Si4** contains signals at 57, 41, 18 and -108 ppm (Figure 3.3.10B). The chemical shifts are similar to the signals observed for **Si3**. The signal at 18 ppm is assigned to physisorbed Et_3SiH, and the signal at -108 ppm is assigned to SiOx species, respectively. The shifts at 57 and 41 ppm are assigned to electrophilic

[Et_3Si][SZO] sites. **Si4** reacts with Et_3PO (**Si4P**) and has a similar ^{31}P NMR spectrum to **Si3P**, Figure 3.3.11. The $\Delta\delta^{31}P$ for **Si4P** are 43 and 21 ppm, which are essentially the same as those in **Si3P**.

Scheme 3.3.7. Reaction of SZO with Et_3SiH

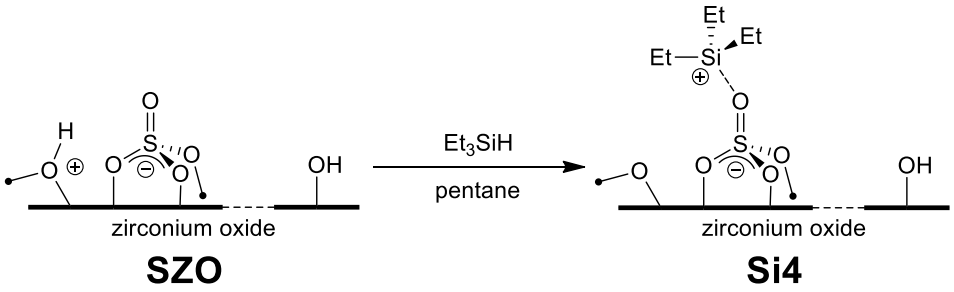

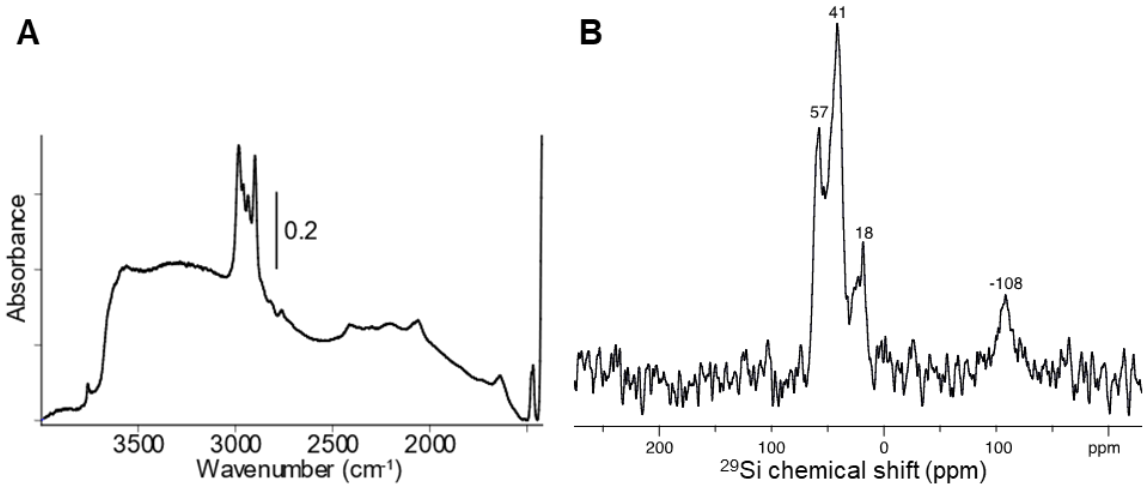

Figure 3.3.10. A) FT-IR spectrum of **Si4**; and B) solid-state ^{29}Si CP-MAS NMR spectrum of **Si4**.

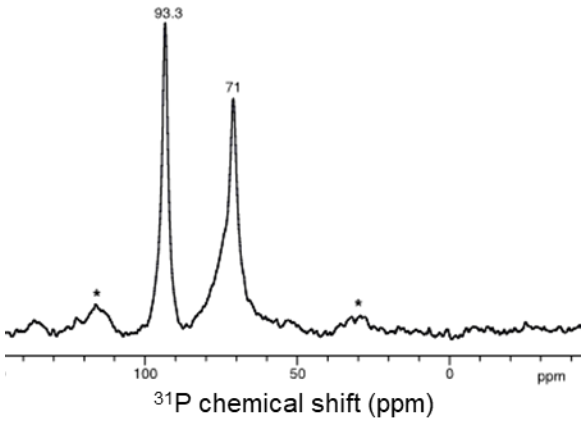

Figure 3.3.11. ^{31}P MAS NMR spectrum of **Si4** reacted with Et_3PO, * = spinning sidebands.

Si4 initiates the HDF of trifluorotoluene at 80 °C and performs 180 turnovers in the presence of Et_3SiH over 4 hours (entry 5). The reactivity of **Si4** stops in under 4 hours, Figure 3.3.12, indicating that Si4 deactivates faster tha **Si3**. **Si1** and **Si2** are unreactive for the HDF of trifluorotoluene, as expected based on the ^{29}Si NMR chemical shifts of **Si1** and **Si2**.

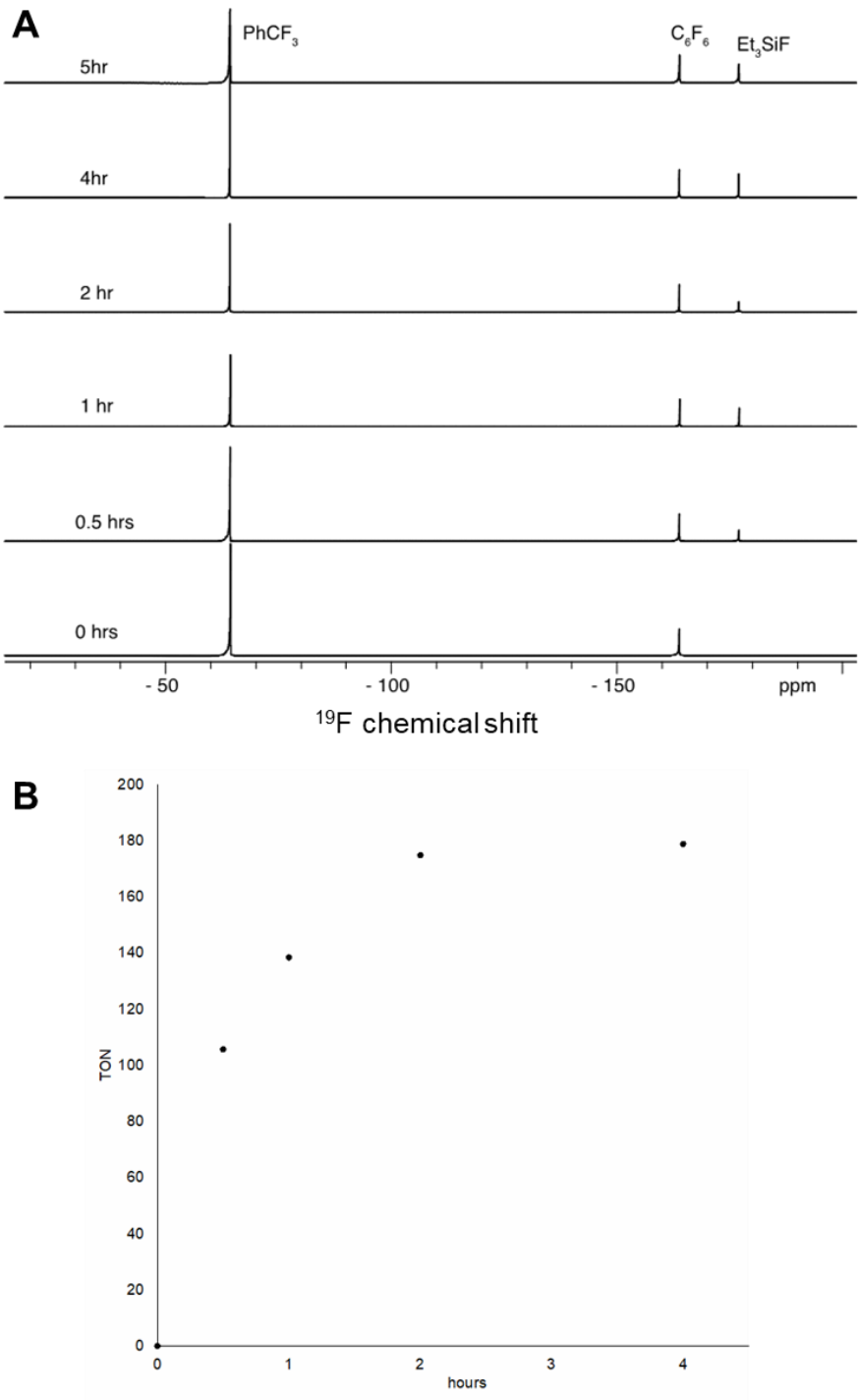

Figure 3.3.12. A) $^{19}F\{^{1}H\}$ NMR spectra of the HDF of trifluorotoluene with **Si4** over time and B) TON over time plot.

3.4 Conclusion

This study showed that SZO supports weakly coordinated silylium-like [$^{i}Pr_3Si$][SZO] surface sites that are more Lewis acidic than $^{i}Pr_3SiOTf$. [$^{i}Pr_3Si$][SZO] initiates HDF reactions of substrates containing activated C–F bonds in the presence of Et_3SiH at elevated temperatures. The NMR studies of **Si3** suggest that $[SZO]^-$ is not as weakly coordinating as $BAr^F_4^-$ or $CHB_{11}X_{11}^-$ ions, which is supported by the lower activity of [$^{i}Pr_3Si$][SZO] in HDF compared to [R_3Si-L][BAr^F_4] or [R_3Si][$CHB_{11}X_{11}$]. The design of a new heterogeneous WCA that coordinates weaker than $[SZO]^-$ is discussed in chapter 4 of this dissertation.

3.5 Materials and Methods

3.5.1 General considerations

All manipulations were performed under an inert atmosphere of nitrogen or argon using standard schlenk or high vacuum techniques. Grafting reactions were performed in flasks equipped with teflon valves that connect directly to high vacuum lines.[41] Deuterated solvents were purchased from Cambridge Isotope laboratories. Cyclohexane was dried over sodium/benzophenone, degassed, and distilled under vacuum. Pentane was dried over tetraglyme/sodium/benzophenone, degassed, and distilled under vacuum. Allyltriisopropylsilane was dried over 4 Å sieves and degassed under vacuum prior to use. Triethylsilane, hexamethyldisilazane (HMDS), trifluorotoluene, octaflurotoluene, hexafluorobenzene, perfluorohexanes, and 1H,1H,2H-perfluoro-1-hexene were dried over CaH_2 then vacuum distilled prior to use. Aerosil-200 was obtained from Degussa. $Al_2O_{3\text{-}600}$ was provided by the Chevron-Phillips Co. and used as received. Other commercially available reagents were used as received without any purification. Synthesis of SZO, and 1-fluoroadamantane (dried by sublimation) were synthesized as previously reported.[51,52]

FT-IR spectra were recorded as pressed pellets using a Bruker Alpha IR spectrometer in an argon-filled glovebox. Gas chromatography was carried out using Agilent 7820A GC system equipped with an Alumina/KCl column for gas phase measurements or on a HP-5 column for solution measurements. Scanning electron microscopy was performed by the Central Facility for Advanced Microscopy and Microanalysis at the University of California at Riverside on a NovaNanoSEM 450 under high vacuum with a TLD detector. Solution ^1H spectroscopy was carried out on an Avance

Bruker 300, an Avance Bruker NEO400, or an Avance Bruker 600. The ^{1}H spectra were referenced to the NMR solvent residual peak. Solution $^{19}F\{^{1}H\}$ spectroscopy was carried out on an Avance Bruker 300 (282 MHz) and the spectra were referenced to an internal standard of C_6F_6 (-163.9 ppm). For quantitative $^{19}F\{^{1}H\}$ NMR experiments, the relaxation delay was set to 10 seconds. Solid-state NMR spectra were recorded in 4 mm zirconia rotors at 8 – 12 KHz spinning at the magic angle at 14.1 T on an Avance Bruker NEO600 spectrometer equipped with a standard-bore magnet.

3.5.2 Synthesis of $SiO_{2\text{-}700}$

Synthesis of $SiO_{2\text{-}700}$: $SiO_{2\text{-}700}$ was prepared by suspending the silica in excess water and drying the slurry under static air at 120 °C in an oven until dry (usually overnight). The resulting monolith was crushed and sieved to give 250−425 μM size silica aggregates. This material was loaded into a quartz tube containing an adapter with a Teflon stopcock to attach to a high vacuum line, placed in a tube furnace, heated under static air at 500 °C (5 °C min^{-1}) for 4 h, and placed under vacuum on a diffusion pump vacuum line for 12 h. While under vacuum, the temperature was increased to 700 °C (5 °C min^{-1}) and its temperature maintained for 4 h. After this time, the Teflon stopcock was sealed, and the tube was cooled to ambient temperature. The partially dehydroxylated silica was stored in an Ar filled glovebox and contains 0.26 $mmol_{OH}\,g^{-1}$.

3.5.3 Characterization of $Al_2O_{3\text{-}600}$

Determination of $Al_2O_{3\text{-}600}$ OH loading[41]: in an argon filled glovebox Al_2O_3 (0.1 g) was loaded into a 3-neck round bottom which was fitted with a drop funnel, stopper, and a Schlenk adapter. The assembly was connected directly to a vacuum line. Diethyl ether (5 mL) was vacuum transferred into the flask at 77 K over the alumina. Excess MeMgBr (1.5 mL, 3 M in Et_2O) was added by syringe to the drop funnel under argon flow. The drop funnel was partially degassed to remove the argon but not Et_2O. The drop funnel was sealed under static vacuum then the bottom was opened to the round bottom containing the alumina. The reaction was stirred for 30 minutes then all of the volatiles were vacuum transferred to a 5 L flask. Measurement of the volatiles shows that 0.93 ($\pm$0.02) mmol/g of CH_4 was released.

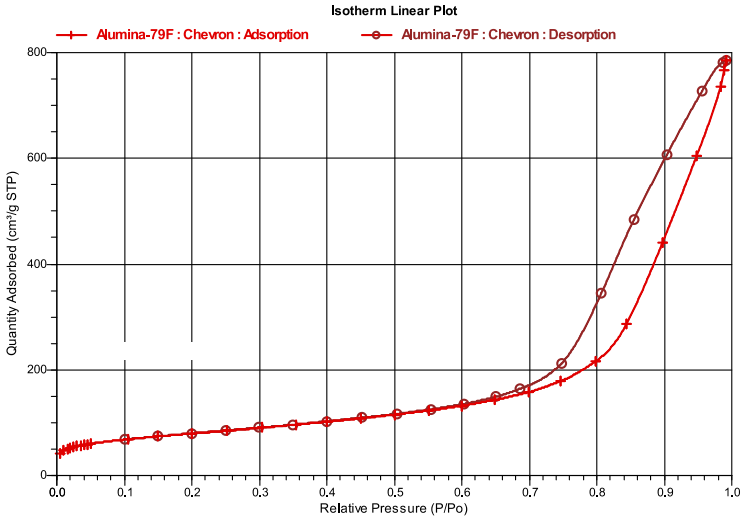

Figure 3.5.1. N_2 adsorption/desorption isotherm linear plot of $Al_2O_{3\text{-}600}$, surface area measurement: BET = 280 m^2/g.

*3.5.4 Synthesis and characterization of **Si1-4**.*

Passivation of $SiO_{2\text{-}700}$ with HMDS (**Si1**): The procedure was modified from reference 12. In a teflon-valved flask, HMDS (2 mL) was condensed over $SiO_{2\text{-}700}$ (500 mg) by vacuum transfer at 77 K. The wet solid was stirred for 3 days under static argon. The volatiles were removed en vacuo at room temperature for 3 hours and the dried solid was heated under dynamic vacuum (10^{-6} torr) at 300 °C for 4 hours. Solid-state NMR: ^{1}H NMR (600 MHz): 1.8, 1.3; $^{13}C\{^{1}H\}$ NMR (151 MHz): -1.1; $^{29}Si\{^{1}H\}$ NMR (119 MHz): 14, 5, and -108 ppm.

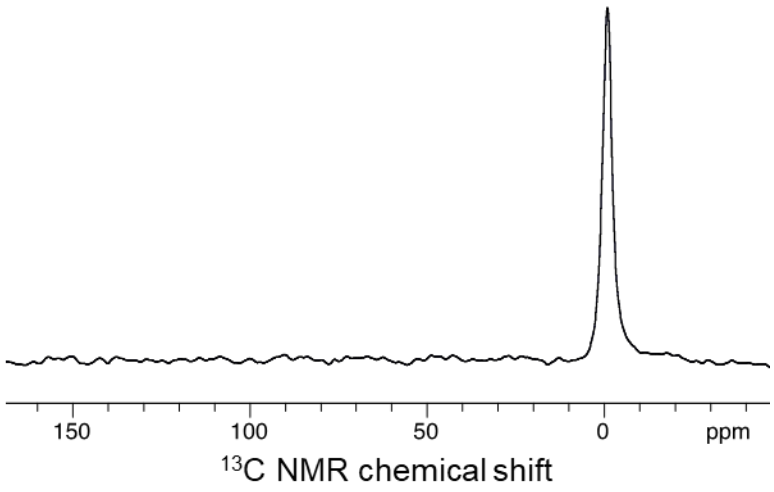

Figure 3.5.2. Solid-state ^{13}C CP-MAS NMR of **Si1** spinning at 8 kHz, 10k scans.

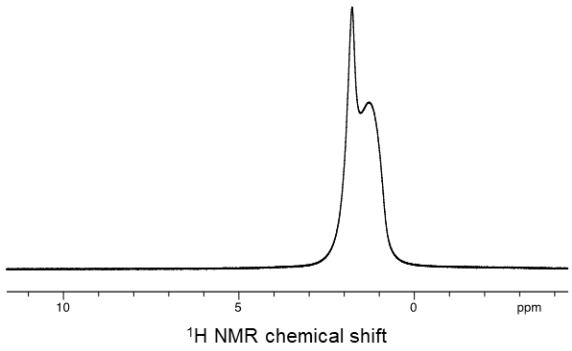

Figure 3.5.3. Solid-state ^{1}H MAS NMR of **Si1** spinning at 8 kHz, 64 scans.

Allyltriisopropylsilane + $Al_2O_{3\text{-}600}$ (**Si2**): allyltriisopropylsilane (0.12 ml, 0.5 mmol) was added to a slurry of cyclohexane (0.5 ml) and $Al_2O_{3\text{-}600}$ (0.1 g, 0.09 mmol OH) in a teflon – sealed NMR tube. The tube was sealed and allowed to react for 24 hours. The white solid was washed with pentane (4 X 1 ml) and dried under vacuum. The propene released was measured by vacuum transferring the volatiles to a new teflon – sealed NMR tube containing ferrocene as an internal standard. Propene: 0.17 mmol/g. Solid-state NMR: ^{1}H NMR (600 MHz): 6.5, 5.5, 1.7; ^{13}C{^{1}H} NMR (151 MHz): 134, 111, 17, 9.3; ^{29}Si{^{1}H} NMR (119 MHz): 1.4, -5.2 ppm.

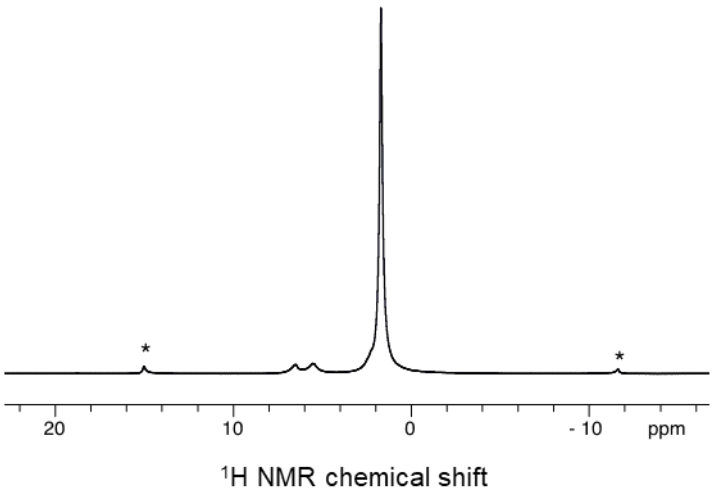

Figure 3.5.4. Solid-state ^{1}H MAS NMR spectrum of **Si2**, spinning at 10 kHz, 64 scans. * = spinning sidebands.

Allyltriisopropylsilane + SZO (**Si3**): To SZO (1 g, 0.13 mmol OH) in a teflon-valved flask, pentane (5 ml) was transferred under high vacuum (10^{-5} torr) to the flask at 77 K. The slurry was warmed to room temperature and allyltriisopropylsilane (0.16 mL, 0.7 mmol, 5 equiv.) was added by syringe under argon flow. The slurry was sealed and stirred at room temperature for 3 hours. The volatiles were transferred to a large teflon-valved flask under vaccum, and the yellow solid was washed by vacuum transferring in new pentane and removing it by cannula (3 X 5 ml). The solid was dried under high vacuum. Analysis of the volatiles by gas chromatography revealed 0.12(±0.01) mmol/g (92 % of OH loading) of propene and 0.041(±0.003) mmol/g (31 % of OH loading) of propane were made during the reaction.[53] Solid-state NMR: ^{1}H NMR (600 MHz): 0.7, 0.1; ^{13}C{^{1}H} NMR (151 MHz): 18, 15; ^{29}Si{^{1}H} NMR (119 MHz): 53, 43, 4, and –100 ppm.

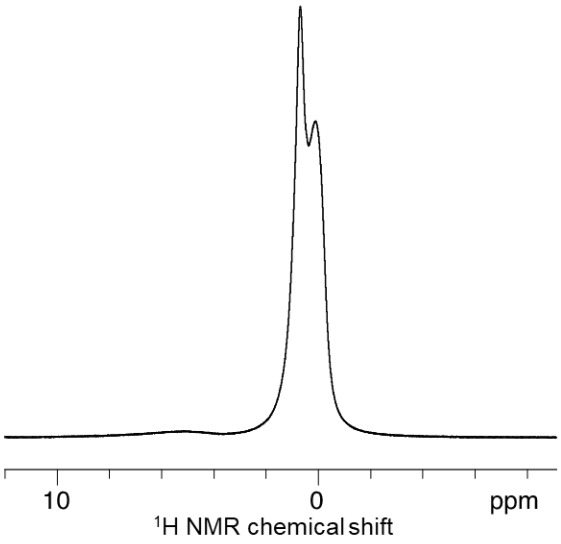

Figure 3.5.5. ^{1}H NMR spectrum of **Si3** spinning at 8 kHz, 128 scans.

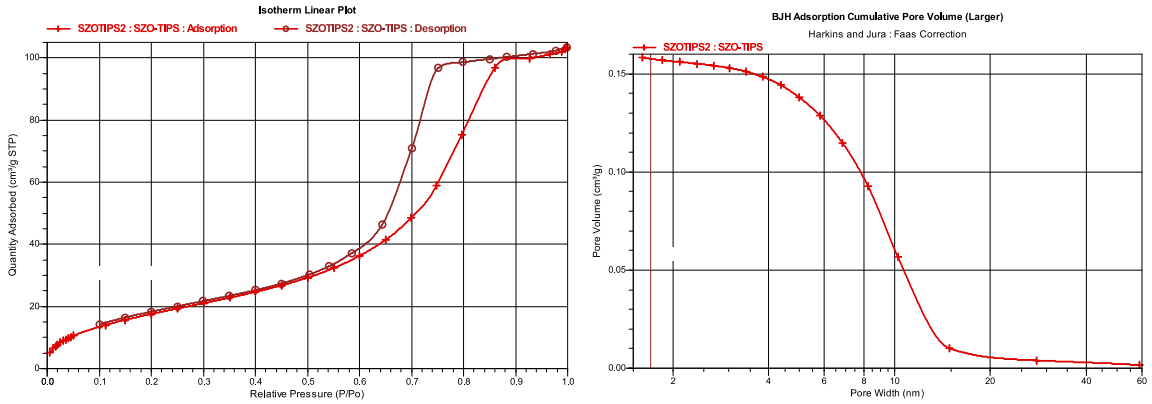

Figure 3.5.6. Left: N_2 adsorption/desorption isotherm linear plot for **Si3**, BET surface area = 69.16 m2/g. Right: BJH Adsorption plot for **Si3**. Cumulative volume of pores: 0.158 cm3/g (desorption: 0.159 cm3/g); average pore width: 7.37 nm (desorption: 6.42 nm).

*3.5.5 Reactions of **Si3** and **Si4** with Et_3PO*

Si3 + Et_3PO (**Si3P**): Pentane (0.5 ml) was condensed over 2.8 mg (22 μmol) of triethylphosphine oxide and 150 mg (21 μmol surface OH) of **Si3** at -196 °C. The slurry was stirred for 30 minutes at room temperature, then dried en vacuo. Solid-state NMR: ^{1}H NMR (600 MHz): 2.8; $^{13}C\{^{1}H\}$ NMR (151 MHz): 16, 12, 4.5; $^{29}Si\{^{1}H\}$ NMR (119 MHz): 51, 25.5, 3.7, –100; $^{31}P\{^{1}H\}$ NMR (243 MHz): 93, and 70 ppm.

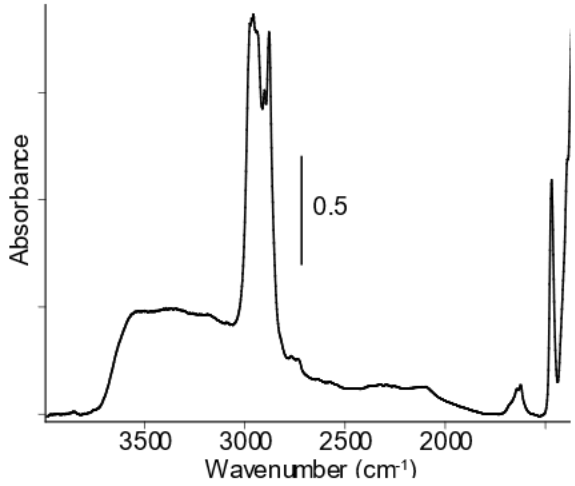

Figure 3.5.7. FT-IR spectrum of **Si3P**.

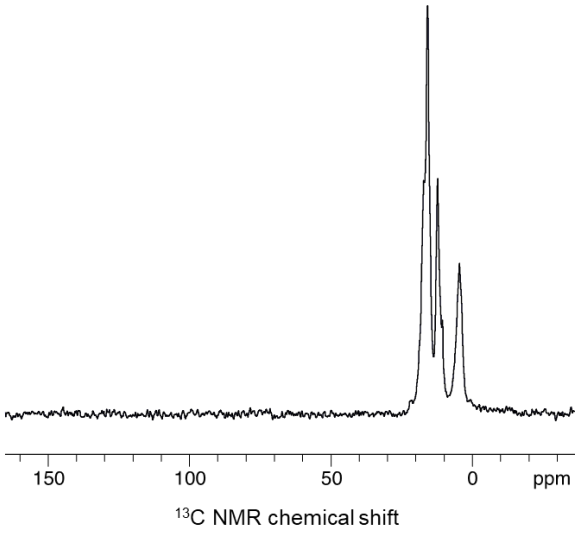

Figure 3.5.8. ^{13}C CP-MAS NMR spectrum of **Si3P**, spinning at 10 kHz.

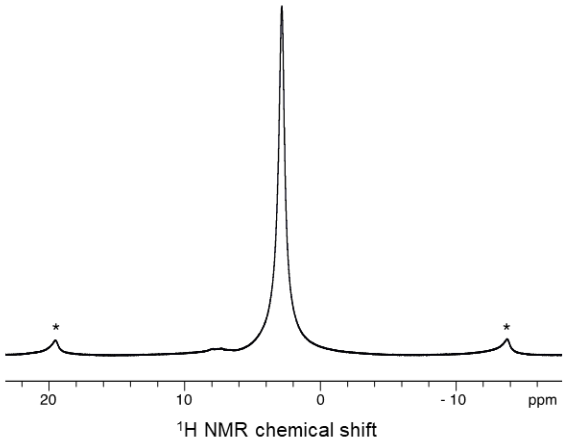

Figure 3.5.9. Solid-state ^{1}H NMR spectrum of **Si3P** spinning at 10 kHz, 64 scans.

Triethylsilane + SZO (**Si4**): In a N_2 filled glovebox, pentane (5 ml) was added to SZO (0.5 g) in a rotofloe, then 52 µl (0.33 mmol, 5 equiv. per surface OH) of triethylsilane were added by syringe. The slurry was sealed and stirred at room temperature overnight. The volatiles were transferred under vacuum for analysis by GC. The white solid was

washed by vacuum transferring in new pentane and removing it by cannula (3 X 5 ml). The solid was dried under high vacuum. Solid-state NMR: ^{1}H NMR (600 MHz): 3.7; ^{13}C{^{1}H} NMR (151 MHz): 6.1, 5.5; ^{29}Si{^{1}H} NMR (119 MHz): 57, 41, 18, and –108 ppm.

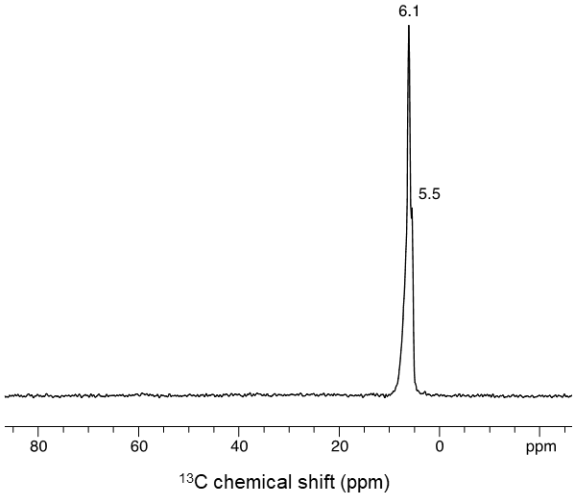

Figure 3.5.10. ^{13}C CP-MAS spectrum of **Si4**, spinning at 8 kHz, 20k scans.

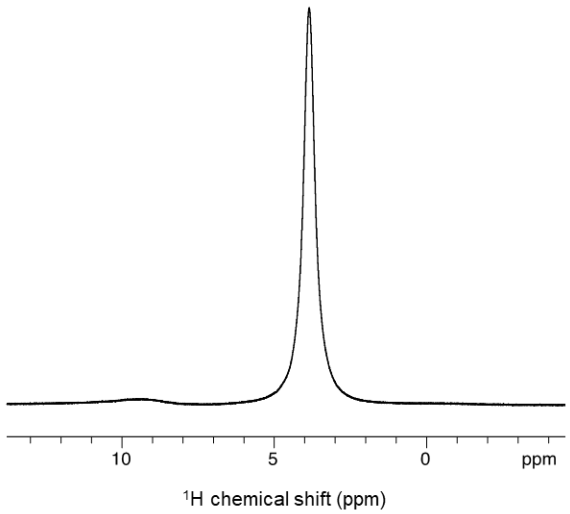

Figure 3.5.11. Solid-state ^{1}H NMR spectra of **Si4**, spinning at 8 kHz, 128 scans.

Si4 + Et_3PO (**Si4P**): Pentane (1 ml) was condensed over 2.8 mg (22 µmol) of triethylphosphine oxide and 150 mg (21 µmol surface OH) of **Si4** at -196 °C. The slurry was stirred for 30 minutes at room temperature, then dried en vacuo. Solid-state NMR: $^{31}P\{^1H\}$ NMR (243 MHz): 93.3, and 71 ppm.

*3.5.6 Catalytic HDF with **Si1-4***

Hydrodefluorination of trifluorotoluene: In a N_2 filled glovebox, **Si3** (20 mg, 2 µmol active Si) was loaded into a teflon sealed NMR tube. Trifluorotoluene (0.06 ml, 0.5 mmol), triethylsilane (0.25 ml, 1.6 mmol), and C_6F_6 (internal standard) were added to the solid and the NMR tube was sealed. The NMR tube was removed from the glovebox and the reaction was heated for 2 – 12 hours at 80 °C. The reaction was quenched by cooling to 0 °C and the solution was decanted away from the solid catalyst. The solution was analyzed by $^{19}F\{^1H\}$ NMR and GC to determine yields and TON. The same was repeated for **Si4** and SZO. For the attempts with **Si1** and **Si2** more material was used but the conditions were the same.

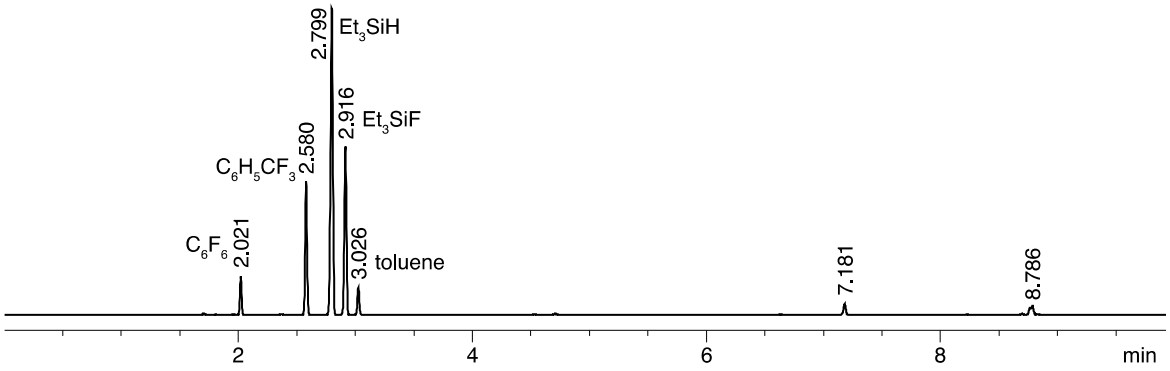

Figure 3.5.12. GC of HDF of trifluorotoluene with **Si3**.

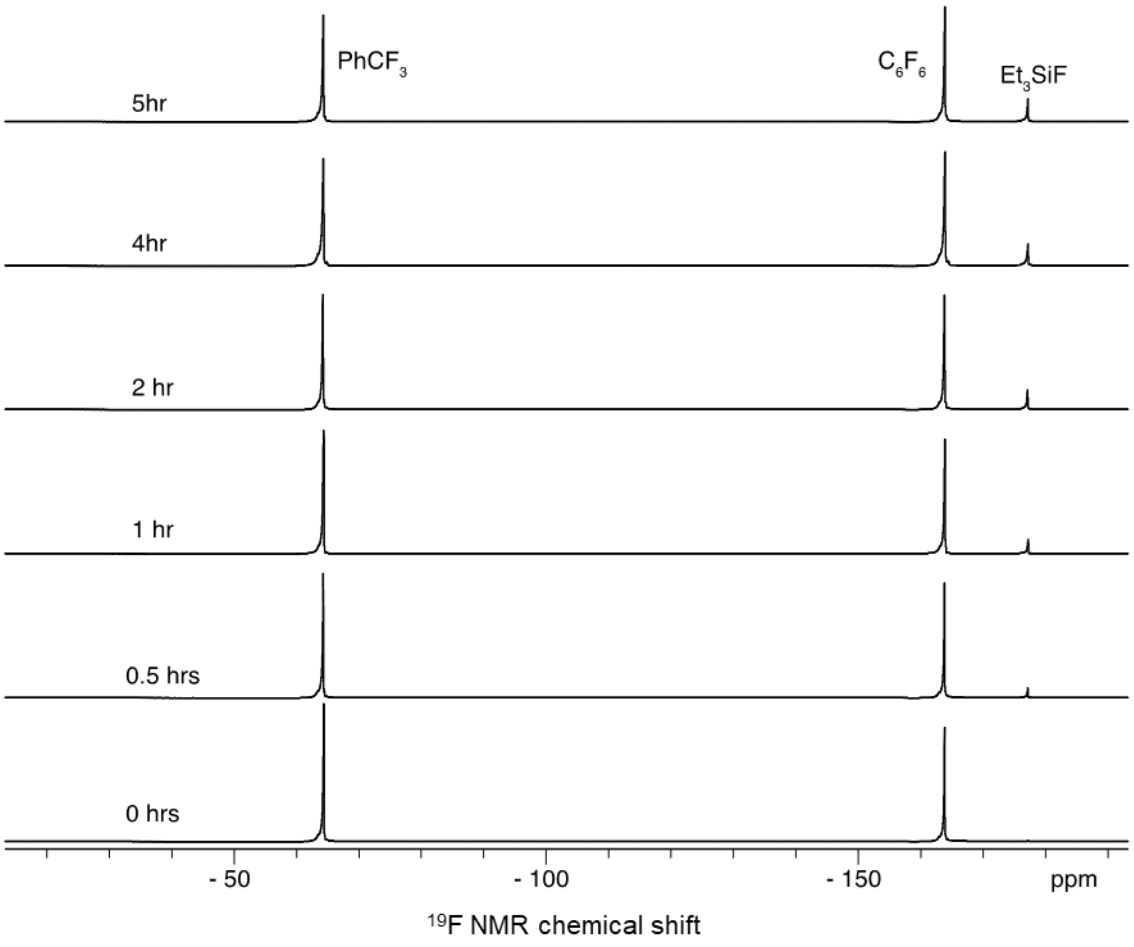

Figure 3.5.13. $^{19}F\{^{1}H\}$ NMR spectra of the HDF of trifluorotoluene with SZO over time.

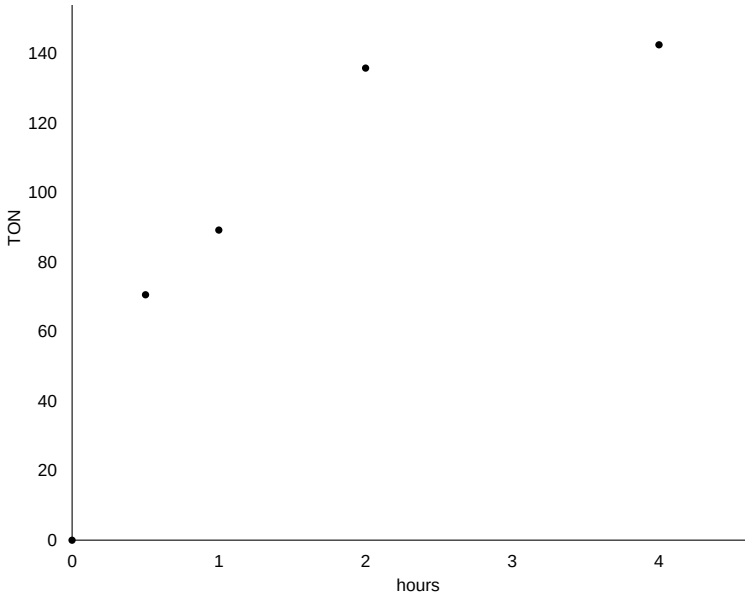

Figure 3.5.14. TON for trifluorotoluene HDF with SZO over time as measured by $^{19}F\{^{1}H\}$ NMR.

Hydrodefluorination of octafluorotoluene: In a N_2 filled glovebox, catalyst **Si3** (50 mg, 4.9 μmol active Si) was loaded into a teflon sealed NMR tube. Octafluorotoluene (0.03 ml, 0.2 mmol), triethylsilane (0.12 ml, 0.75 mmol), and C_6F_6 (internal standard) were added to the solid and the NMR tube was sealed. The NMR tube was removed from the glovebox and the reaction was heated for 3 weeks at 120 °C. The reaction was monitored by $^{19}F\{^{1}H\}$ NMR. After the reaction stopped, it was cooled to room temperature and the solution was decanted away from the solid catalyst. The solution was analyzed by GC.

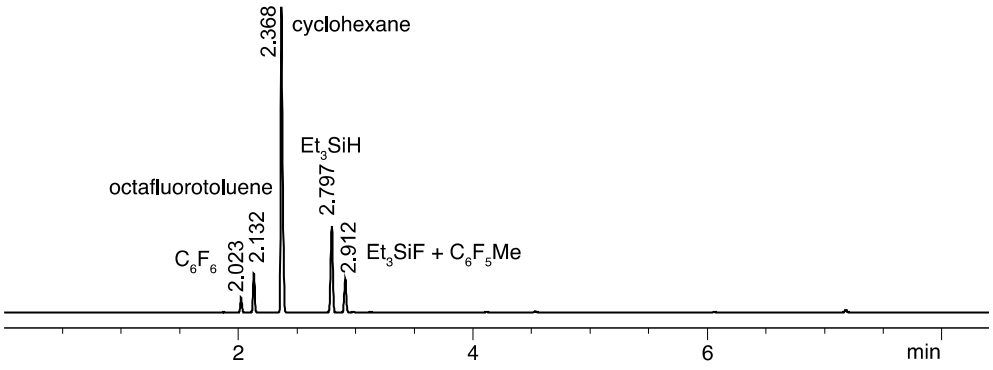

Figure 3.5.15. GC of the HDF of octafluorotoluene with **Si3**.

Hydrodefluorination of 1-fluoroadamantane: In a glovebox, catalyst **Si3** (20 mg, 2 µmol active Si) was loaded into a teflon sealed NMR tube. Fluoroadamantane (60 mg, 0.4 mmol), triethylsilane (0.07 ml, 0.44 mmol), C_6D_{12} (0.25 ml), and C_6F_6 (10 µl, 0.087 mmol) were added to the solid and the NMR tube was sealed. The NMR tube was removed from the glovebox and the reaction was monitored by $^{19}F\{^1H\}$ NMR while reacting at room temperature over 24 hours. The solution was analyzed by GC after the reaction.

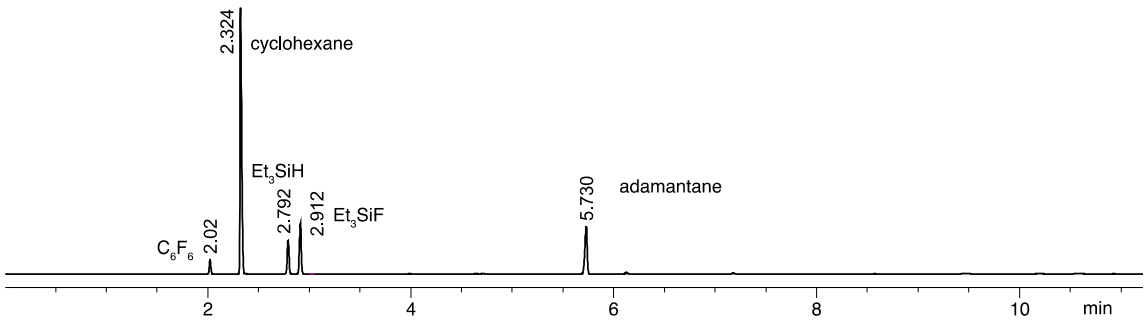

Figure 3.5.16. GC of the HDF of 1-fluoroadamantane with **Si3**.

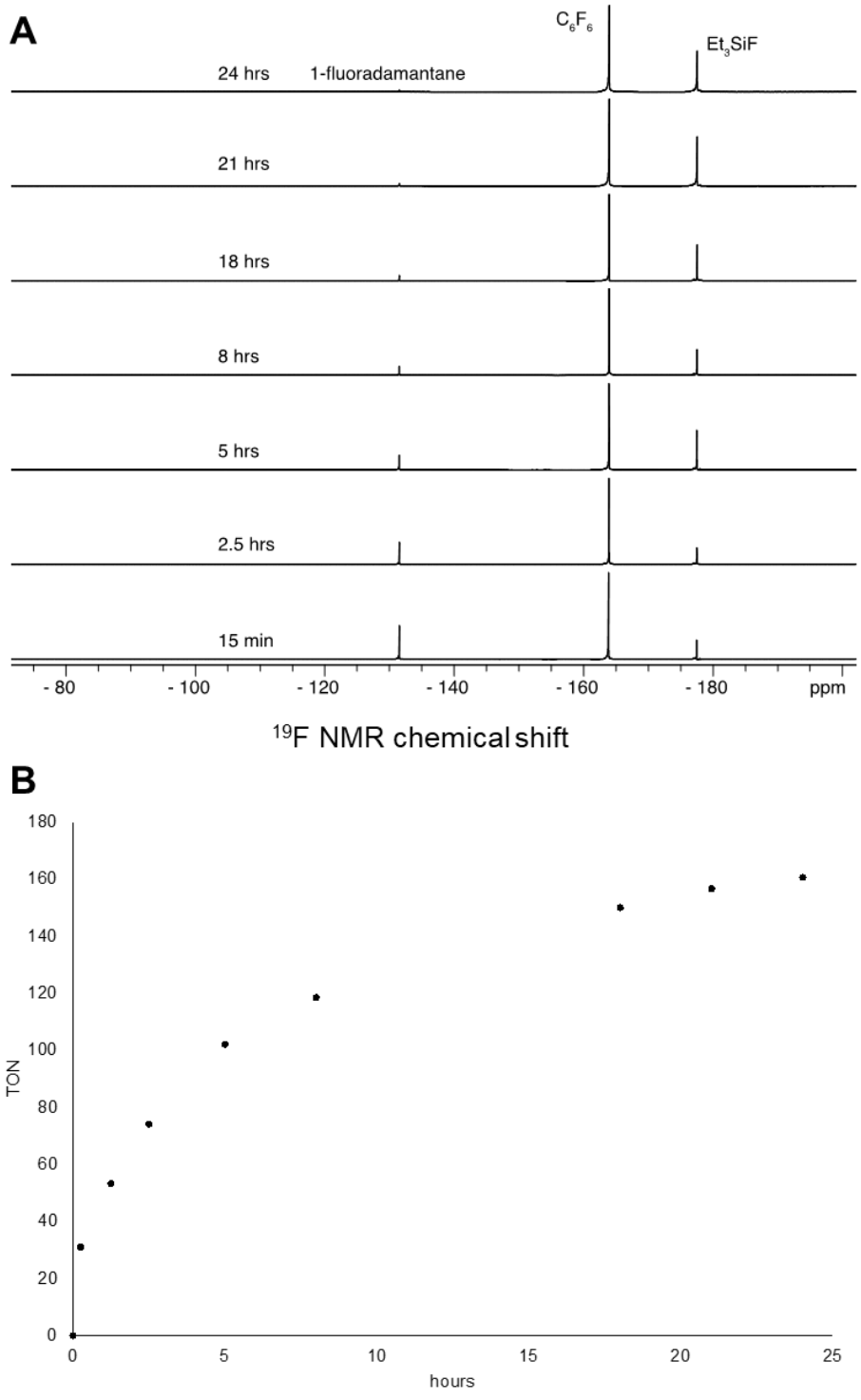

Figure 3.5.17. Data for the HDF of 1-fluoradamantane with **Si3** in the presence of excess Et_3SiH at room temperature: A) $^{19}F\{^1H\}$ NMR spectra over time; and B) TON over time plot.

Hydrodefluorination of 1H,1H,2H-perfluoro-1-hexene: In a N_2 filled glovebox, **Si3** (50 mg, 4.9 μmol active Si) was loaded into a teflon sealed NMR tube. 1H,1H,2H-perfluoro-1-hexene (0.04 ml, 0.24 mmol), triethylsilane (0.36 ml, 2 mmol), and C_6F_6 (internal standard) were added to the solid and the NMR tube was sealed. The NMR tube was removed from the glovebox and the reaction was heated for 36 hours at 120 °C. The reaction was monitored by $^{19}F\{^1H\}$ NMR. After the reaction stopped the solution was diluted in $CDCl_3$ and analyzed by ^1H NMR. The main product is (Z)-$CH_3CHCFCF_2CF_2CF_3$; ^1H NMR (C_6D_{12}, 600 MHz): 5.52 (dq, $^2J_{H-H}$ = 7.2 Hz, $^4J_{H-F}$ = 32.2 Hz, 1H), 1.72 (m,3H); $^{19}F\{^1H\}$ NMR (C_6D_{12}): -81.1 (3F), -118.5 (2F), -127.5 (2F), and -131.5 ppm (1H). This data matches previously reported NMR data.[54]

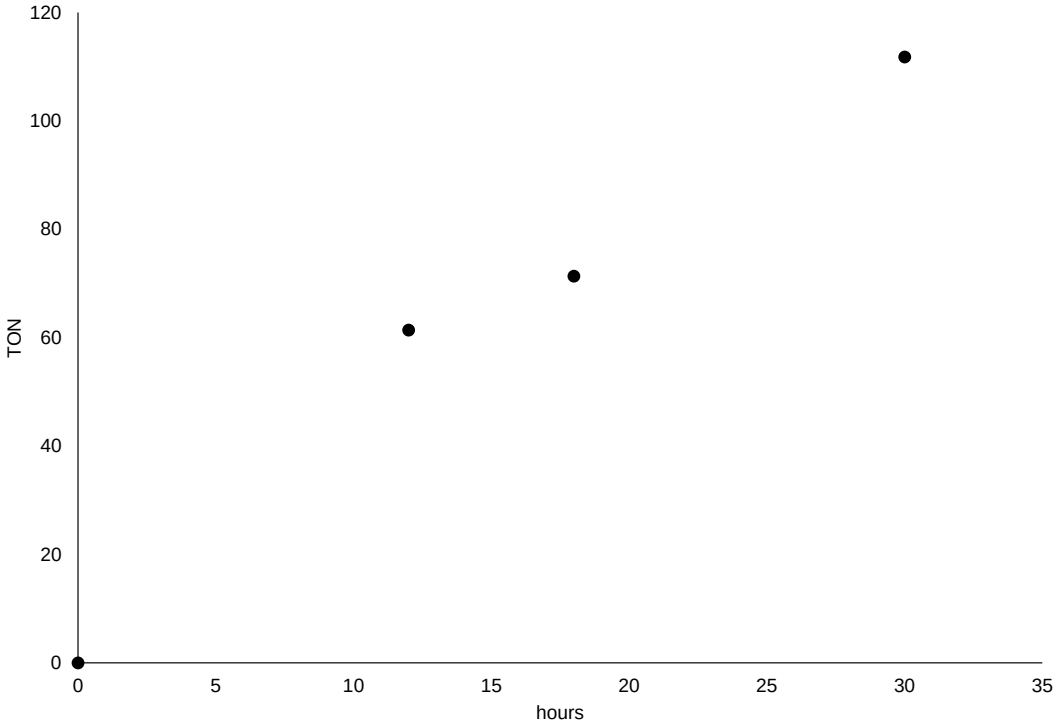

Figure 3.5.18. TON of the HDF of 1H,1H,2H-perfluoro-1-hexene with **Si3** over time.

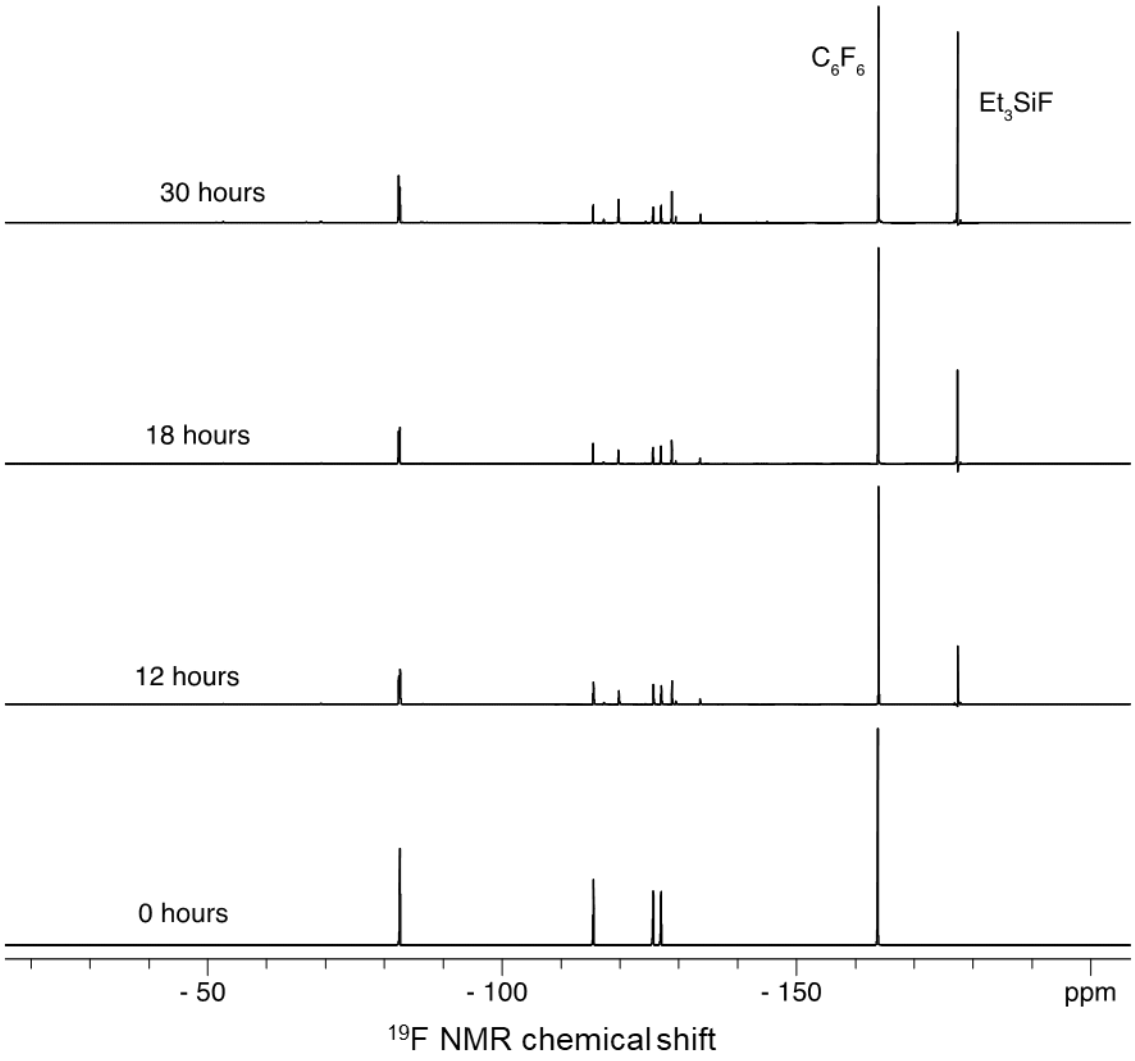

Figure 3.5.19. $^{19}F\{^{1}H\}$ NMR spectra of the HDF of 1H,1H,2H-perfluoro-1-hexene with **Si3** over time.

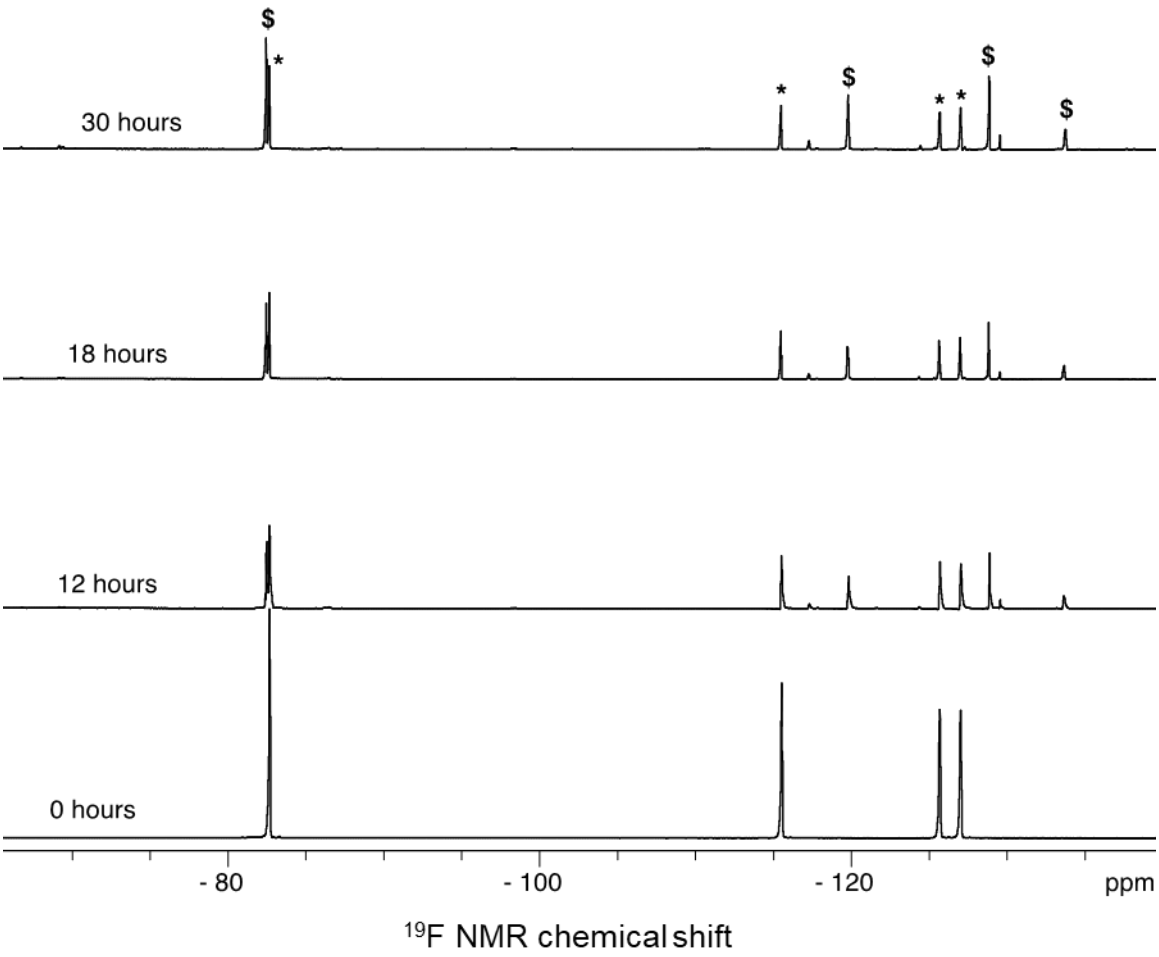

Figure 3.5.20. zoom in on the $^{19}F\{^{1}H\}$ NMR spectra of the HDF of 1H,1H,2H-perfluoro-1-hexene with **Si3** over time, * = starting material, and $ = (Z)-$CH_3CHCFC_3F_7$.

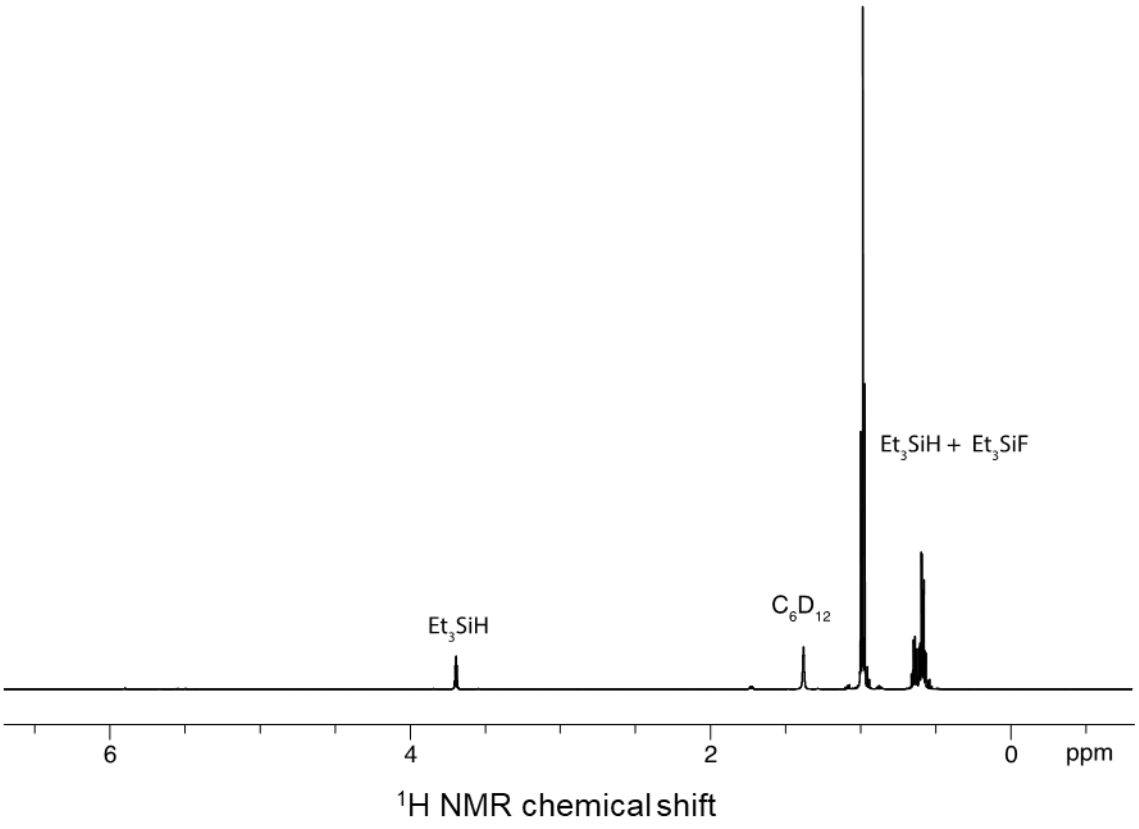

Figure 3.5.21. ^{1}H (600 MHz) NMR spectrum of the HDF of 1H,1H,2H-perfluoro-1-hexene with **Si3** diluted in C_6D_{12}.

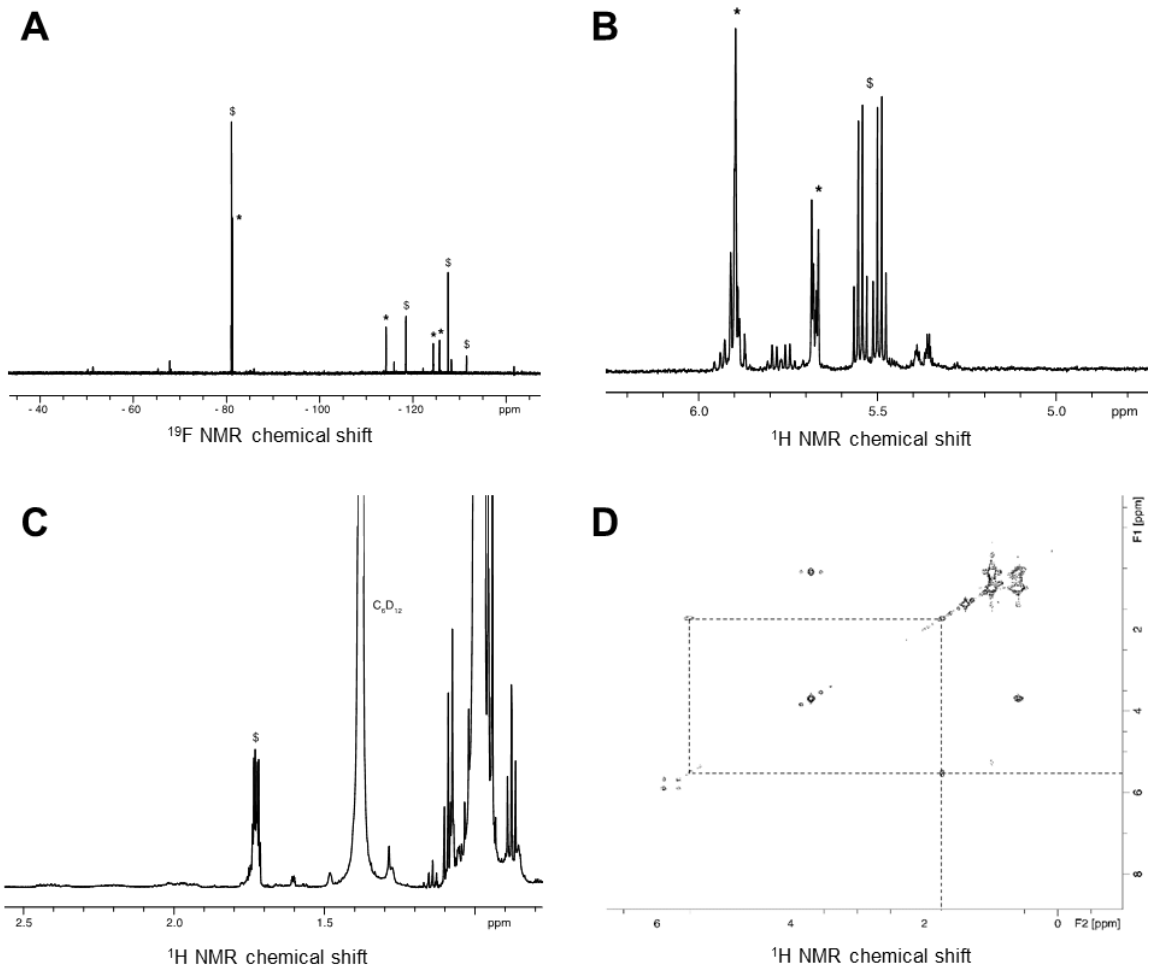

Figure 3.5.22. solution NMR spectra of the HDF of 1H,1H,2H-perfluoro-1-hexene with **Si3** diluted in C_6D_{12} (14.1 T): A) $^{19}F\{^1H\}$ NMR spectrum; B & C) zoomed in regions of the ^1H NMR spectrum, * = starting material, and $ = (Z)-$CH_3CHCFC_3F_7$; and D) ^1H-^1H COSY NMR spectrum of the., the dashed line highlights the product correlation between the olefin at 5.5 ppm and the methyl at 1.7 ppm.

Solid-state NMR measurements of **Si3** after HDF reaction: following the same procedure as above the reaction was scaled up by 7.5 times (150 mg of **1**, 0.45 ml of $PhCF_3$, and 1.9 ml of Et_3SiH). After heating at 80 °C for 18 hours, in a N_2 filled glovebox the solution was decanted off the solid then the yellow solid was washed with cyclohexane (3 X 2 ml) and dried under high vacuum (10^{-5} torr).

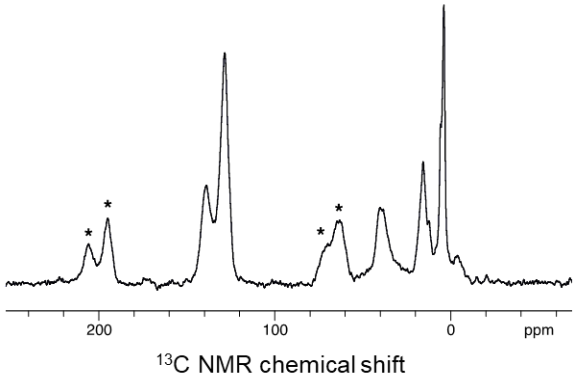

Figure 3.5.23. ^{13}C CP-MAS NMR spectrum of **Si3** after the HDF of trifluorotoluene, spinning at 10 kHz, 20k scans, * = spinning sidebands.

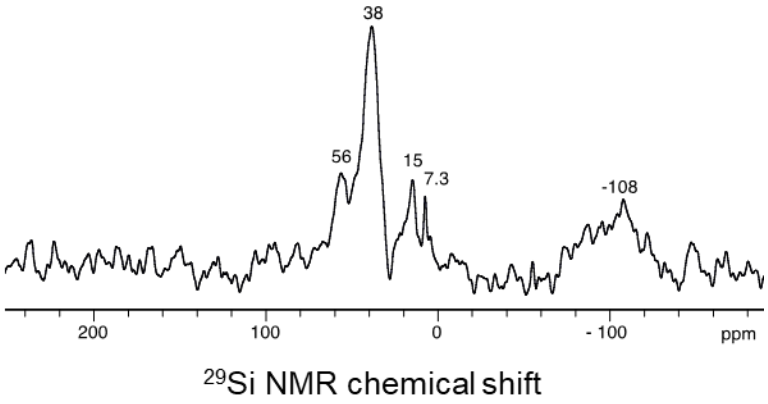

Figure 3.5.24. ^{29}Si CP-MAS NMR spectrum of **Si3** after the HDF of trifluorotoluene, spinning at 8 kHz, 40k scans.

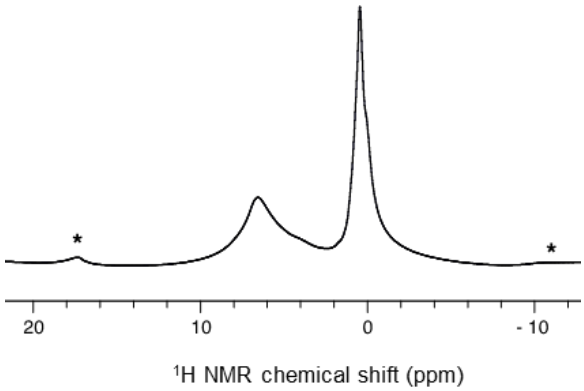

Figure 3.5.25. Solid-state ^{1}H NMR spectrum of **Si3** after the HDF of trifluorotoluene, spinning at 10 kHz, 64 scans, * = spinning sidebands.

3.5.7 Poisoning study

Poisoning study procedure: cyclohexane (0 – 0.1 ml) and a solution of 0.07 M Et_3PO in cyclohexane (0.1 - 0 ml) were added to catalyst **Si3** (50 mg, 7 µmol OH) in a teflon sealed NMR tube to a constant volume of 0.1 ml. The slurry was allowed to equilibrate for 30 min then triethylsilane (81 µl, 0.5 mmol), trifluorotoluene (19 µl, 0.15 mmol), and hexafluorobenzene (internal standard) were added to the slurry. The reaction was sealed and heated to 80 °C for 30 minues then quenched by cooling to 0 °C. The reactions were analyzed by $^{19}F\{^{1}H\}$ NMR (relaxation delay of 10 seconds). The short reaction time and the high catalyst loading (Si:C-F = 1:36) were used to reduce the possibility of Friedal-Craft side reactions affecting the HDF activity. Under these conditions catalyst **Si3** is active beyond 30 minutes. After 1 hour, in the absence of Et_3PO, catalyst **Si3** performs 45 turn overs, compared to 32 turn overs after 30 minutes.

3.6 References

(1) Culver, D. B.; Conley, M. P. Activation of C−F Bonds by Electrophilic Organosilicon Sites Supported on Sulfated Zirconia. *Angew. Chemie Int. Ed.* **2018**, *57* (45), 14902–14905. https://doi.org/10.1002/anie.201809199.

(2) Corma, A.; García, H. Lewis Acids: From Conventional Homogeneous to Green Homogeneous and Heterogeneous Catalysis. *Chem. Rev.* **2003**, *103* (11), 4307–4365. https://doi.org/10.1021/cr030680z.

(3) Román-Leshkov, Y.; Davis, M. E. Activation of Carbonyl-Containing Molecules with Solid Lewis Acids in Aqueous Media. *ACS Catal.* **2011**, *1* (11), 1566–1580. https://doi.org/10.1021/cs200411d.

(4) Wischert, R.; Copéret, C.; Delbecq, F.; Sautet, P. Dinitrogen: A Selective Probe for Tri-Coordinate Al "Defect" Sites on Alumina. *Chem. Commun.* **2011**, *47* (17), 4890–4892. https://doi.org/10.1039/c1cc10623f.

(5) Wischert, R.; Copéret, C.; Delbecq, F.; Sautet, P. Optimal Water Coverage on Alumina: A Key to Generate Lewis Acid-Base Pairs That Are Reactive Towards the C-H Bond Activation of Methane. *Angew. Chemie Int. Ed.* **2011**, *50* (14), 3202–3205. https://doi.org/10.1002/anie.201006794.

(6) Wischert, R.; Laurent, P.; Copéret, C.; Delbecq, F.; Sautet, P. Γ-Alumina: The Essential and Unexpected Role of Water for the Structure, Stability, and Reactivity of "Defect" Sites. *J. Am. Chem. Soc.* **2012**, *134* (35), 14430–14449. https://doi.org/10.1021/ja3042383.

(7) Comas Vives, A.; Schwarzwälder, M.; Copéret, C.; Sautet, P. Carbon−Carbon Bond Formation by Activation of CH3F on Alumina. *J. Phys. Chem. C* **2015**, *119* (13), 7156–7163. https://doi.org/10.1021/jp512598p.

(8) Comas-Vives, A.; Valla, M.; Copéret, C.; Sautet, P. Cooperativity between Al Sites Promotes Hydrogen Transfer and Carbon−Carbon Bond Formation upon Dimethyl Ether Activation on Alumina. *ACS Cent. Sci.* **2015**, *1* (6), 313–319. https://doi.org/10.1021/acscentsci.5b00226.

(9) Bhan, A.; Iglesia, E. A Link between Reactivity and Local Structure in Acid Catalysis on Zeolites. *Acc. Chem. Res.* **2008**, *41* (4), 559–567. https://doi.org/10.1021/ar700181t.

(10) Boronat, M.; Corma, A. Factors Controlling the Acidity of Zeolites. *Catal. Letters* **2015**, *145* (1), 162–172. https://doi.org/10.1007/s10562-014-1438-7.

(11) Krahl, T.; Kemnitz, E. Aluminium Fluoride-the Strongest Solid Lewis Acid: Structure and Reactivity. *Catal. Sci. Technol.* **2017**, *7* (4), 773–796. https://doi.org/10.1039/c6cy02369j.

(12) Zapilko, C.; Anwander, R. Size-Selective Surface Silylation of Cagelike Mesoporous Silica SBA-2 with Disilazane Reagents. *Chem. Mater.* **2006**, *18* (6), 1479–1482. https://doi.org/10.1021/cm0524345.

(13) Song, W.; Marcus, D. M.; Abubakar, S. M.; Jani, E.; Haw, J. F. Trimethylsilylation of Framework Brønsted Acid Sites in Microporous Zeolites and Silico-Aluminophosphates. *J. Am. Chem. Soc.* **2003**, *125* (46), 13964–13965. https://doi.org/10.1021/ja034541a.

(14) Conley, M. P.; Copéret, C.; Thieuleux, C. Mesostructured Hybrid Organic-Silica Materials: Ideal Supports for Well-Defined Heterogeneous Organometallic Catalysts. *ACS Catal.* **2014**, *4* (5), 1458–1469. https://doi.org/10.1021/cs500262t.

(15) Blümel, J. Reactions of Ethoxysilanes with Silica: A Solid-State NMR Study. *J. Am. Chem. Soc.* **1995**, *117* (7), 2112–2113. https://doi.org/10.1021/ja00112a033.

(16) Behringer, K. D.; Blümel, J. Reactions of Ethoxysilanes with Silica: A Solid-State NMR Study. *J. Liq. Chromatogr. Relat. Technol.* **1996**, *19* (17–18), 2753–2765. https://doi.org/10.1080/10826079608015108.

(17) Reed, C. A. The Silylium Ion Problem, R3Si+. Bridging Organic and Inorganic Chemistry. *Acc. Chem. Res.* **1998**, *31* (6), 325–332. https://doi.org/10.1021/ar960132q.

(18) Zuowei Xie, S. R.; Bau, R.; Benesi, A.; Reed, C. A. The Silylium Ion (R3Si+) Problem: Effect of Alkyl Substituents R. *Organometallics* **1995**, *14*, 3933–3941.

(19) Kim, K. C.; Reed, C. A.; Elliott, D. W.; Mueller, L. J.; Tham, F.; Lin, L.; Lambert, J. B. Crystallographic Evidence for a Free Silylium Ion. *Science* **2002**, *297* (5582), 825–827. https://doi.org/10.1126/science.1073540.

(20) Xie, Z.; Liston, D. J.; Jelínek, T.; Mitro, V.; Bau, R.; Reed, C. A. A New Weakly Coordinating Anion: Approaching the Silylium (Silicenium) Ion. *J. Chem. Soc. Chem. Commun.* **1993**, No. 4, 384–386. https://doi.org/10.1039/C39930000384.

(21) Hoffmann, S. P.; Kato, T.; Tham, F. S.; Reed, C. A. Novel Weak Coordination to Silylium Ions: Formation of Nearly Linear Si-H-Si Bonds. *Chem. Commun.* **2006**, No. 7, 767–769. https://doi.org/10.1039/b511344j.

(22) Nava, M.; Reed, C. A. Triethylsilyl Perfluoro-Tetraphenylborate, [Et3Si+][F20-BPh4-], a Widely Used Nonexistent Compound. *Organometallics* **2011**, *30* (17), 4798–4800. https://doi.org/10.1021/om200636u.

(23) Lambert, J. B.; Zhang, S.; Stern, C. L.; Huffman, J. C. Crystal Structure of a Silyl Cation with No Coordination to Anion and Distant Coordination to Solvent. *Science* **1993**, *260* (5116), 1917–1918. https://doi.org/10.1126/science.260.5116.1917.

(24) Xie, Z.; Manning, J.; Reed, R. W.; Mathur, R.; Boyd, P. D. W.; Benesi, A.; Reed, C. A. Approaching the Silylium (R3Si+) Ion: Trends with Hexahalo Cl, Br, I Carboranes as Counterions. *J. Am. Chem. Soc.* **1996**, *118* (12), 2922–2928. https://doi.org/10.1021/ja953211q.

(25) Scholl, R. L.; Maciel, G. E.; Musker, W. K. Silicon-29 Chemical Shifts of Organosilicon Compounds. *J. Am. Chem. Soc.* **1972**, *94* (18), 6376–6385. https://doi.org/10.1021/ja00773a021.

(26) Olah, G. A.; Laali, K.; Farooq, O. Organometallic Chemistry. 21. Silyl Trifluoromethanesulfonate (Triflate)-Boron Trichloride (Tribromide) Complexes. *Organometallics* **1984**, *3* (9), 1337–1340. https://doi.org/10.1021/om00087a003.

(27) Lambert, J. B.; Kania, L.; Zhang, S. Modern Approaches to Silylium Cations in Condensed Phase. *Chem. Rev.* **1995**, *95* (5), 1191–1201. https://doi.org/10.1021/cr00037a003.

(28) Lambert, J. B.; Zhang, S.; Ciro, S. M. Silyl Cations in the Solid and in Solution. *Organometallics* **1994**, *13* (6), 2430–2443. https://doi.org/10.1021/om00018a041.

(29) Reed, C. A. The Silylium Ion Problem, R3Si+. Bridging Organic and Inorganic Chemistry. *Acc. Chem. Res.* **1998**, *31* (6), 325–332. https://doi.org/10.1021/ar960132q.

(30) Reed, C. A. H+,CH3+, and R3Si+ Carborane Reagents: When Triflates Fail. *Acc. Chem. Res.* **2010**, *43* (1), 121–128. https://doi.org/10.1021/ar900159e.

(31) Klare, H. F. T.; Oestreich, M. Silylium Ions in Catalysis. *Dalt. Trans.* **2010**, *39* (39), 9176–9184. https://doi.org/10.1039/c003097j.

(32) Stahl, T.; Klare, H. F. T.; Oestreich, M. Main-Group Lewis Acids for C-F Bond Activation. *ACS Catal.* **2013**, *3* (7), 1578–1587. https://doi.org/10.1021/cs4003244.

(33) Engesser, T. A.; Lichtenthaler, M. R.; Schleep, M.; Krossing, I. Reactive P-Block Cations Stabilized by Weakly Coordinating Anions. *Chem. Soc. Rev.* **2016**, *45* (4), 789–899. https://doi.org/10.1039/C5CS00672D.

(34) Duttwyler, S.; Douvris, C.; Fackler, N. L. P.; Tham, F. S.; Reed, C. A.; Baldridge, K. K.; Siegel, J. S. C-F Activation of Fluorobenzene by Silylium Carboranes: Evidence for Incipient Phenyl Cation Reactivity. *Angew. Chemie - Int. Ed.* **2010**, *49* (41), 7519–7522. https://doi.org/10.1002/anie.201003762.

(35) Shao, B.; Bagdasarian, A. L.; Popov, S.; Nelson, H. M. Arylation of Hydrocarbons Enabled by Organosilicon Reagents and Weakly Coordinating Anions. *Science* **2017**, *355* (6332), 1403–1407. https://doi.org/10.1126/science.aam7975.

(36) Gusev, D. G.; Ozerov, O. V. Calculated Hydride and Fluoride Affinities of a Series of Carbenium and Silylium Cations in the Gas Phase and in C6H5Cl Solution. *Chem. - A Eur. J.* **2011**, *17* (2), 634–640. https://doi.org/10.1002/chem.201000696.

(37) Klare, H. F. T. Catalytic C-H Arylation of Unactivated C-H Bonds by Silylium Ion-Promoted C(Sp2)-F Bond Activation. *ACS Catal.* **2017**, *7* (10), 6999–7002. https://doi.org/10.1021/acscatal.7b02658.

(38) Scott, V. J.; Çelenligil-Çetin, R.; Ozerov, O. V. Room-Temperature Catalytic Hydrodefluorination of C(Sp3)-F Bonds. *J. Am. Chem. Soc.* **2005**, *127* (9), 2852–2853. https://doi.org/10.1021/ja0426138.

(39) Douvris, C.; Nagaraja, C. M.; Chen, C. H.; Foxman, B. M.; Ozerov, O. V. Hydrodefluorination and Other Hydrodehalogenation of Aliphatic Carbon-Halogen Bonds Using Silylium Catalysis. *J. Am. Chem. Soc.* **2010**, *132* (13), 4946–4953. https://doi.org/10.1021/ja100605m.

(40) Douvris, C.; Ozerov, O. V. Hydrodefluorination of Perfluoroalkyl Groups Using Silylium-Carborane Catalysts. *Science* **2008**, *321* (5893), 1188–1190. https://doi.org/10.1126/science.1159979.

(41) Copéret, C.; Comas-Vives, A.; Conley, M. P.; Estes, D. P.; Fedorov, A.; Mougel, V.; Nagae, H.; Núnez-Zarur, F.; Zhizhko, P. A. Surface Organometallic and Coordination Chemistry toward Single-Site Heterogeneous Catalysts: Strategies, Methods, Structures, and Activities. *Chem. Rev.* **2016**, *116* (2), 323–421. https://doi.org/10.1021/acs.chemrev.5b00373.

(42) Mayer, U.; Gutmann, V.; Gerger, W. The Acceptor Number - A Quantitative Empirical Parameter for the Electrophilic Properties of Solvents. *Monatshefte für Chemie* **1975**, *106* (6), 1235–1257. https://doi.org/10.1007/BF00913599.

(43) Beckett, M. A.; Brassington, D. S.; Coles, S. J.; Hursthouse, M. B. Lewis Acidity of Tris(Pentafluorophenyl) Borane: Crystal and Molecular Structure of B(C6F5)3·OPEt3. *Inorg. Chem. Commun.* **2000**, *3* (10), 530–533. https://doi.org/10.1016/S1387-7003(00)00129-5.

(44) Osegovic, J. P.; Drago, R. S. Measurement of the Global Acidity of Solid Acids by 31P MAS NMR of Chemisorbed Triethylphosphine Oxide. *J. Phys. Chem. B* **2000**, *104* (1), 147–154. https://doi.org/10.1021/jp992907t.

(45) Liberman-Martin, A. L.; Bergman, R. G.; Tilley, T. D. Lewis Acidity of Bis(Perfluorocatecholato)Silane: Aldehyde Hydrosilylation Catalyzed by a Neutral Silicon Compound. *J. Am. Chem. Soc.* **2015**, *137* (16), 5328–5331. https://doi.org/10.1021/jacs.5b02807.

(46) Maskey, R.; Schädler, M.; Legler, C.; Greb, L. Bis(Perchlorocatecholato)Silane—A Neutral Silicon Lewis Super Acid. *Angew. Chemie - Int. Ed.* **2018**, *57* (6), 1717–1720. https://doi.org/10.1002/anie.201712155.

(47) Großekappenberg, H.; Reißmann, M.; Schmidtmann, M.; Müller, T. Quantitative Assessment of the Lewis Acidity of Silylium Ions. *Organometallics* **2015**, *34* (20), 4952–4958. https://doi.org/10.1021/acs.organomet.5b00556.

(48) Crabtree, R. H. Deactivation in Homogeneous Transition Metal Catalysis: Causes, Avoidance, and Cure. *Chem. Rev.* **2015**, *115* (1), 127–150. https://doi.org/10.1021/cr5004375.

(49) Ahrens, M.; Scholz, G.; Braun, T.; Kemnitz, E. Catalytic Hydrodefluorination of Fluoromethanes at Room Temperature by Silylium-Ion-like Surface Species. *Angew. Chemie Int. Ed.* **2013**, *52* (20), 5328–5332. https://doi.org/10.1002/anie.201300608.

(50) Corey, E. J.; Cho, H.; Rücker, C.; Hua, D. H. Studies with Trialkylsilyltriflates: New Syntheses and Applications. *Tetrahedron Lett.* **1981**, *22* (36), 3455–3458. https://doi.org/10.1016/S0040-4039(01)81930-4.

(51) Tafazolian, H.; Culver, D. B.; Conley, M. P. A Well-Defined Ni(II) α-Diimine Catalyst Supported on Sulfated Zirconia for Polymerization Catalysis. *Organometallics* **2017**, *36* (13), 2385–2388. https://doi.org/10.1021/acs.organomet.7b00402.

(52) Williard, P. G.; Büchi, G. FLUORINATIONS WITH PYRIDINIUM POLYHYDROGEN FLUORIDE REAGENT : 1-FLUOROADAMANTANE. *Org. Synth.* **1988**, *6*, 225–227. https://doi.org/10.1002/0471264180.os058.13.

(53) Conley, M. P.; Rossini, A. J.; Comas-Vives, A.; Valla, M.; Casano, G.; Ouari, O.; Tordo, P.; Lesage, A.; Emsley, L.; Copéret, C. Silica-Surface Reorganization during Organotin Grafting Evidenced By119Sn DNP SENS: A Tandem Reaction of Gem-Silanols and Strained Siloxane Bridges. *Phys. Chem. Chem. Phys.* **2014**, *16* (33), 17822–17827. https://doi.org/10.1039/c4cp01973c.

(54) Kraft, B. M.; Jones, W. D. Mechanism of Vinylic and Allylic Carbon-Fluorine Bond Activation of Non-Perfluorinated Olefins Using Cp*2ZrH2. *J. Am. Chem. Soc.* **2002**, *124* (29), 8681–8689. https://doi.org/10.1021/ja0125568.

Chapter 4 PhF-Al(OC(CF_3)$_3$)$_3$ Activated Silica: Formation of Weak Ion-Pairs on a Silica surface[1]

4.1 Abstract

This chapter describes the reaction of PhF-Al(OC(CF_3)$_3$)$_3$ (a strong Lewis acid) and partially dehydroxylated silica to form ≡Si-O(H)-Al(OC(CF_3)$_3$)$_3$ sites. These sites were characterized by elemental analysis, FT-IR spectroscopy, and solid-state NMR spectroscopy. Contacting ≡Si-O(H)-Al(OC(CF_3)$_3$)$_3$ with Octyl$_3$N forms [Octyl$_3$NH][≡SiO-Al(OC(CF_3)$_3$)$_3$]. FT-IR measurements of the ν_{N-H} stretch show that the ≡SiO-Al(OC(CF_3)$_3$)$_3^-$ surface anion formed in this reaction is more weakly coordinating than FSO_3^- or ClO_4^- anions, but less weakly coordinating than $BAr^F{}_4^-$ or $CHB_{11}X_{11}^-$ anions. The reaction of ≡Si-O(H)-Al(OC(CF_3)$_3$)$_3$ with allyltriisopropylsilane forms [^{i}Pr$_3$Si][≡SiO-Al(OC(CF_3)$_3$)$_3$]. The isotropic ^{29}Si NMR chemical shift of [^{i}Pr$_3$Si][≡SiO-Al(OC(CF_3)$_3$)$_3$] is 70 ppm, which is 17 ppm more downfield than [^{i}Pr$_3$Si][SZO] (discussed in Chapter 3). This result indicates that ≡SiO-Al(OC(CF_3)$_3$)$_3^-$ is a weaker coordinating anion than the sulfate anions on SZO.

4.2 Introduction

Chapters 2 and 3 discussed the use of sulfated zirconium oxide (SZO) as a weakly coordinating anionic support for transition-metal and silylium-like ions. These studies showed that a palladium olefin polymerization catalyst has a similar activity to the homogeneous analogue with a B(C_6F_5)$_4^-$ anion, and that [^{i}Pr$_3$Si][SZO] is a strong silicon Lewis acid that activates C-F bonds. However, [^{i}Pr$_3$Si][SZO] is not as reactive towards C-

F bonds as [$^{i}Pr_3Si$][BAr^{F}_4] or [$^{i}Pr_3Si$][$CHB_{11}X_{11}$]. Solid state ^{29}Si NMR spectroscopy of [$^{i}Pr_3Si$][SZO] suggests that the sulfate anions on SZO coordinate stronger to the $^{i}Pr_3Si^{+}$ cation than $BAr^{F}_4{}^{-}$ or $CHB_{11}X_{11}{}^{-}$ anions.

The predominant physical property that regulates ion pairing to an anion (X^{-}) is the Brønsted acidity of the conjugate acid (HX). The weaker X^{-} coordinates to a cation the stronger the conjugate Brønsted acid HX. Therefore, the anion of a strong Brønsted acid on a surface should be a weakly coordinating anion (WCA) when deprotonated. The acidity of a Brønsted acid can be increased by coordination of a strong Lewis acid (LA) to form HX-LA. The classic example of this behavior is "magic acid", a combination of a strong Brønsted acid (FSO_3H) and a strong Lewis acid (SbF_5).[2] This concept is widely applicable to homogeneous Bronsted acids.[3]

Similar concepts apply to solid acids. Zeolites contain Brønsted acid sites that are a result of ≡Si-OH coordinated to nearby Al Lewis acid sites to form ≡Si-O(H)-Al≡ sites (Figure 4.2.1A).[4,5] Modification of the Lewis acid, such as $AlCl_3$ contacted silica, forms a complex mixture, but some of the sites form bridging silanols (≡Si-O(H)-Al(Cl_2)-O-Si≡, (Figure 4.2.1B) that are very strong Bronsted acids.[6] Well-defined strong acid sites are accessible through the reaction of $B(C_6F_5)_3$ with silanols on partially dehydroxylated silica in the presence of diethylphenylamine to form [Et_2PhNH][≡SiO-$B(C_6F_5)_3$] ion pairs, (Figure 4.2.1C).[7,8]

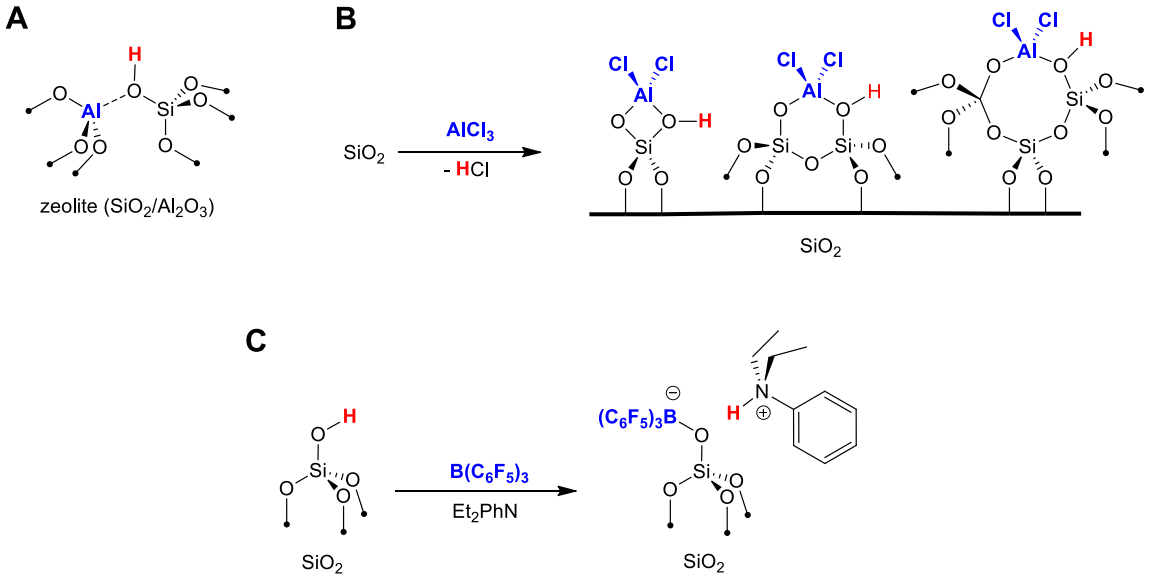

Figure 4.2.1. Simplified structure of ≡Si-O(H)-Al≡ sites in zeolites; B) proposed Brønsted sites present on $AlCl_3$ functionalized SiO_2; and C) functionalization of partially dehydroxylated SiO_2 with $B(C_6F_5)_3$.

This chapter describes the reaction of PhF-$Al(OC(CF_3)_3)_3$ with ≡Si-OH groups on silica partially dehydroxylated at 700 °C ($SiO_{2\text{-}700}$) to form ≡Si-O(H)-$Al(OC(CF_3)_3)_3$. This material was characterized by solid-state NMR and FT-IR spectroscopies, which show that these sites are strong Brønsted acids. The material reacts with trioctylamine or allyltriisopropylsilane to form heterogeneous ion pairs [$Octyl_3NH$][≡SiO-$Al(OC(CF_3)_3)_3$] or [$^iPr_3Si$][≡SiO-$Al(OC(CF_3)_3)_3$], respectively. Spectroscopic studies of these materials indicate that ≡SiO-$Al(OC(CF_3)_3)_3^-$ is a weakly coordinating anion.[1]

4.3 Results and discussion

*4.3.1 Synthesis and characterization of **AS1***

$SiO_{2\text{-}700}$ reacts with PhF-Al(OC(CF_3)$_3$)$_3$ in a slurry of perfluorohexanes to form ≡Si-O(H)-Al(OC(CF_3)$_3$)$_3$ (**AS1**) (Scheme 4.3.1). Elemental analysis showed that **AS1** contains 0.24 mmol/g of Al, indicating that ~ 92 % of the available surface hydroxyls coordinate to the Lewis acid. The FT-IR spectrum of **AS1** contains a $\nu_{O\text{-}H}$ stretch at 3743 cm^{-1} for unreacted ≡SiOH and a $\nu_{O\text{-}H}$ stretch at 3542 cm^{-1} for ≡Si-O(H)-Al(OC(CF_3)$_3$)$_3$. The red shift of the $\nu_{O\text{-}H}$ stretch is consistent with the coordination of the silanol to the Lewis acid (Figure 4.3.1A).[9] The FT-IR spectrum also contains sp^2 $\nu_{C\text{-}H}$ and $\nu_{C=C}$ stretches assigned to fluorobenzene physisorbed to the silica surface. $^{19}F\{^1H\}$ NMR measurements of **AS1** suspended in acetonitrile showed that there is 0.045 ± 0.004 mmol/g of fluorobenzene absorbed to the surface of **AS1**. The static solid-state ^{27}Al NMR spectrum of **AS1**, shown in Figure 4.3.1B, contains one signal with a chemical shift of 43 ppm, a C_Q of 14.6 MHz and an η of 0.23. The ^{27}Al NMR parameters are consistent with distorted tetrahedral symmetry at aluminum.[10,11] The ^1H MAS NMR spectrum of **AS1** contains signals at 7.1, 5.0, and 2.3 ppm. These signals are assigned to physisorbed fluorobenzene, ≡Si-O(H)-Al(OC(CF_3)$_3$)$_3$, and unreacted ≡Si-OH, respectively.

Scheme 4.3.1. Reaction of PhF-Al(OC(CF$_3$)$_3$)$_3$ with SiO$_{2\text{-}700}$

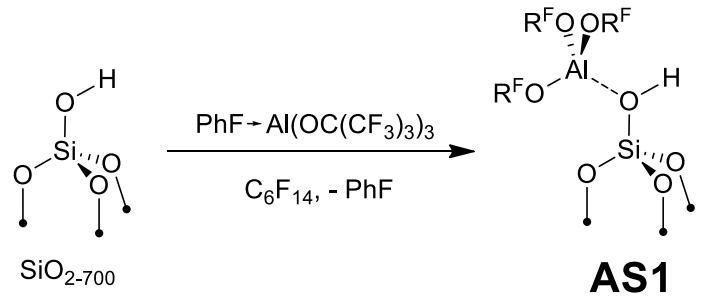

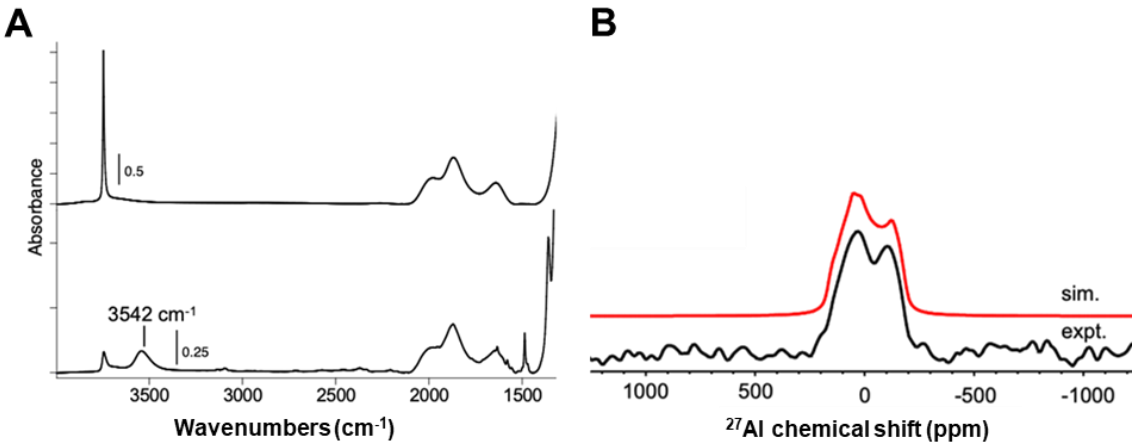

Figure 4.3.1 A) FT-IR spectra of SiO$_{2\text{-}700}$ (top) and **AS1** (bottom); and B) static ^{27}Al NMR of **AS1** (black) with simulation (red).

Dipolar coupling is the through space interaction of magnetic spins between two NMR active nuclei and is inversely proportional to the distance between NMR active spins ($1/r^3$). Resonance-Echo Saturation-Pulse Double-Resonance (RESPDOR) is a solid-state NMR experiment capable of measuring dipolar coupling of NMR active nuclei within close proximity (~5 Å).[12,13] In collaboration with the Rossini group at Iowa State University, RESPDOR experiments were acquired on **AS1**. The ^{1}H{^{27}Al} RESPDOR difference spectrum shown in Figure 4.3.2A contains a signal at 5.1 ppm. This result indicates that

the signal is close to Al in **AS1**, whereas the signals at 7.1 and 2.3 are far from Al, consistent with assignments from the ^{1}H MAS NMR spectrum of **AS1**. The dipolar dephasing plot in Figure 4.3.2B is constructed by varying the recoupling times in the pulse sequence of the RESPDOR experiment and fitting signal intensity data to extract a dipolar coupling constant. The fit of the data in Figure 4.3.2B gives a ^{1}H-^{27}Al dipolar coupling in the range of ~2.0-2.3 Hz which corresponds to a distance of ~2.4-2.5 Å between the acidic proton and the Al center. This assignment is further supported by the 2D ^{1}H{^{27}Al} D-RINEPT spectrum which shows that the ^{1}H signal at 5.1 ppm is close to an Al center with a C_Q of 15.7 MHz (Figure 4.5.5).

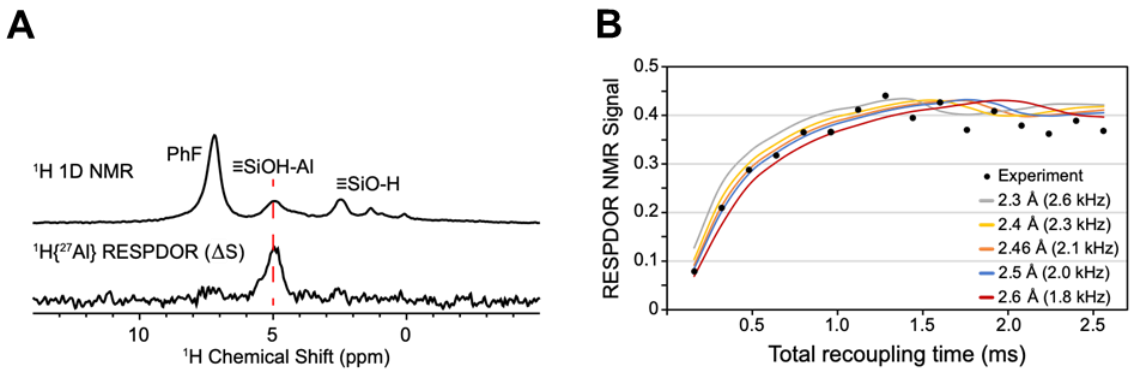

Figure 4.3.2. A) solid-state ^{1}H MAS NMR spectrum of **AS1** (top) and 1D projection of the ^{1}H{^{27}Al} RESPDOR NMR of **AS1**; and B) fit of RESPDOR dipolar dephasing curve to measure dipolar ^{1}H-^{27}Al dipolar coupling present in **AS1**, see the Materials and methods section for details.

4.3.2 Formation of [Octyl$_3$N-H][≡SiO-Al(OC(CF$_3$)$_3$)$_3$] to estimate the relative anion coordination strength

Measuring Brønsted acidity on solid acids usually involves the reaction of a solid acid with a sterically small base, such as pyridine or acetone, followed by FT-IR or NMR spectroscopy to determine acidity relative to other solids. However, the aluminum alkoxide in **AS1** desorbs from the silica surface in the presence of sterically small Lewis bases. Reed and coworkers showed that the ν_{N-H} stretch of [Oct$_3$NH][X] salts in CCl_4 solution is related to the gas phase acidity of HX, and the ability of X^- to behave as a weakly coordinating anion. [Oct$_3$NH][B(C$_6$F$_5$)$_4$] and [Oct$_3$NH][CHB$_{11}$X$_{11}$] ion pairs have more blue shifted ν_{N-H} stretches than [Oct$_3$NH][X] with more coordinating anions, such as ClO_4^- and FSO_3^-.[14]

AS1 reacts with trioctylamine in a pentane slurry to form [Octyl$_3$N-H][≡SiO-Al(OC(CF$_3$)$_3$)$_3$] (**AS2**), Scheme 4.3.2. Elemental analysis shows that **AS2** contains 0.63 % Al, indicating that minimal loss of the aluminum alkoxide occurs during this reaction. The static solid-state ^{27}Al NMR spectrum of **AS2** contains a new signal with a chemical shift of 45.6 ppm and a C_Q of 6.7 MHz (Figure 4.3.3B). The significant decrease of the ^{27}Al C_Q from 14.6 (**AS1**) to 6.7 MHz indicates that the Al center is more tetrahedrally symmetric. The FT-IR spectrum of **AS2** contains a ν_{N-H} stretch at 3070 cm^{-1}, as well as, sp^3 ν_{C-H} stretches for the n-Octyl groups (Figure 4.3.3A).

Scheme 4.3.2. Reaction of **AS1** with (n-octyl)$_3$N

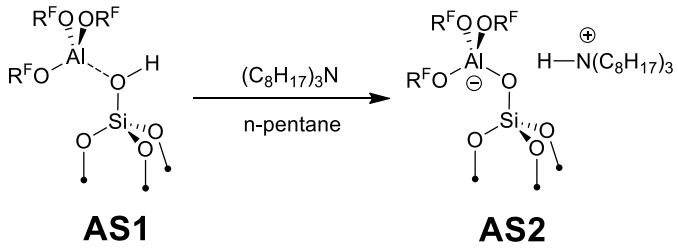

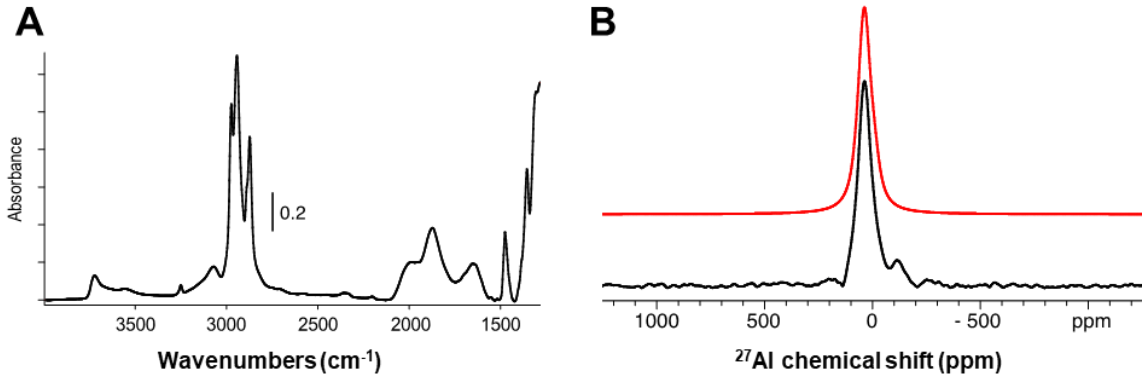

Figure 4.3.3. A) FT-IR spectrum of **AS2** (cm^{-1}); and B) static ^{27}Al NMR spectrum of **AS2** (black) and simulation of the [Octyl$_3$NH][≡Si-OAl(OC(CF$_3$)$_3$)$_3$] sites (red).

Table 4.1 contains $\nu_{N\text{-}H}$ stretches of **AS2** and select [Oct$_3$NH][X] salts measured in CCl_4 solution.[14] The $\nu_{N\text{-}H}$ stretch of **AS2** is more blue shifted than than $SO_3CF_3^-$, SO_3F^-, and ClO_4^- anions (entries 1-3), indicating that [≡SiO-Al(OC(CF$_3$)$_3$)$_3$]$^-$ is more weakly coordinating than these anions. However, the $\nu_{N\text{-}H}$ stretch of **AS2** indicates that [≡SiO-Al(OC(CF$_3$)$_3$)$_3$]$^-$ is more coordinating than $CHB_{11}X_{11}^-$ and $B(C_6F_5)_4^-$ anions (entries 5-8).

Table 4.1. $\nu_{N\text{-}H}$ stretch frequencies for several [Octyl$_3$N-H][X] ion pairs.

Entry	Anion	$\nu_{N\text{-}H}$ (cm^{-1})[a]
1	SO_3CF_3	2939
2	SO_3F	2953
3	ClO_4	3049
4	$\equiv SiO\text{-}Al(OC(CF_3)_3)_3$[b]	3070
5	$[CH_5B_{11}I_6]$	3097
6	$[CH_5B_{11}Br_6]$	3125
7	$[CHB_{11}Cl_{11}]$	3163
8	$B(C_6F_5)_4$	3223

a.) from reference 14; and b.) this work.

4.3.3 Support of a silylium-like ion on the $\equiv SiO\text{-}Al(OC(CF_3)_3)_3^-$ anion

AS1 reacts with allyltriisopropylsilane in a pentane slurry to form **AS3**, Scheme 4.3.3. Propene or propane were not observed in this reaction. However, ^{1}H NMR measurements of pentane washings were consistent with the formation of propene oligomers during the synthesis of **AS3**. This is likely a result of propene reacting with $\equiv$Si-O(H)-Al(OC(CF$_3$)$_3$)$_3$ during the reaction prior to formation of **AS3**, which is supported by control experiment of **AS1** with propene. The FT-IR spectrum of **AS3** shows that most $\equiv$Si-O(H)-Al(OC(CF$_3$)$_3$)$_3$ sites were consumed in this reaction and that new sp^3 $\nu_{C\text{-}H}$ stretches appear (Figure 4.3.4A). The ^{13}C CP-MAS NMR spectrum of **AS3** contains signals at 121, 78, 15, and 12 ppm assigned to AlOC(**C**F$_3$)$_3$, AlO**C**(CF$_3$)$_3$, Si-CH(**C**H$_3$)$_2$ and Si-**C**H(CH$_3$)$_2$, respectively (Figure 4.3.4B). The static ^{27}Al solid state NMR spectrum has one

signal with a chemical shift of 33 ppm and a C_Q of 13 MHz (Figure 4.3.4C). The C_Q for **AS3** is lower than the C_Q for **AS1** (14.6 MHz), but higher than the C_Q for **AS2** (6.7 Hz). The ^{29}Si CP-MAS NMR spectrum of **AS3** contains signals at 70, 4, and -105 ppm that are assigned to [^{i}Pr$_3$Si][≡SiO-Al(OC(CF$_3$)$_3$)$_3$], ≡SiO-Si^{i}Pr$_3$, and bulk SiO_2, respectively (Figure 4.3.4D).

Scheme 4.3.3. Synthesis of [^{i}Pr$_3$Si][≡SiO-Al(OC(CF$_3$)$_3$)$_3$]

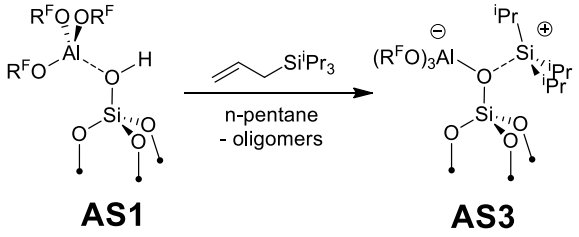

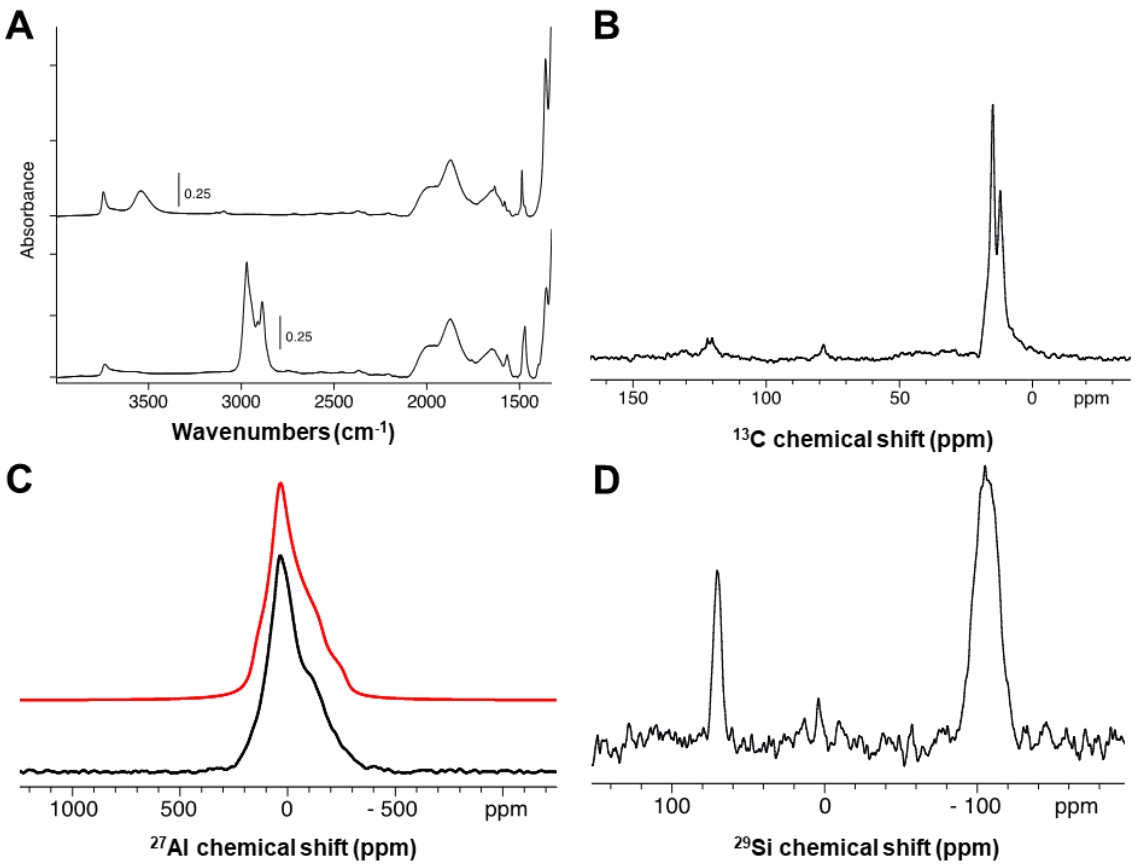

Figure 4.3.4. Characterization data for **AS3**: A) FT-IR spectra (cm^{-1}) of **AS1** (top) and **AS3** (bottom); B) ^{13}C CP-MAS NMR spectrum; C) static ^{27}Al solid state NMR spectrum; and D) ^{29}Si CP-MAS NMR spectrum.

Figure 4.3.5 shows the ^{29}Si NMR chemical shift values for R_3Si-X (red) and heterogeneous R_3Si-oxide (blue) compounds. In R_3Si-X the ^{29}Si NMR chemical shift appears near 0 ppm, such as silyl ethers or silyl halides. Silylium-like ions with weakly coordinating carboranes have ^{29}Si NMR chemical shifts over 100 ppm. Silylium-like ions coordinate to weak Lewis bases (such as R_3SiH, SO_2, or toluene) and these compounds have chemical shifts between ~50-100 ppm.[15,16] Me_3Si- groups on silica and zeolites have chemical shifts similar to silyl ethers. The silylium-like surface ion [$^{i}Pr_3Si$][SZO], from

chapter 3, coordinates to sulfate anions on SZO and has a chemical shift of 53 ppm.[17] The ^{29}Si NMR chemical shift of [^{i}Pr$_3$Si][≡SiO-Al(OC(CF$_3$)$_3$)$_3$] is 17 ppm more downfield than [^{i}Pr$_3$Si][SZO]. This is consistent with [≡SiO-Al(OC(CF$_3$)$_3$)$_3$]$^-$ behaving as a weaker coordinating anion than sulfate anions on [SZO]$^-$. However, the chemical shift of [^{i}Pr$_3$Si][≡SiO-Al(OC(CF$_3$)$_3$)$_3$] is lower than silylium-like ions with weakly coordinated [CHB$_{11}$X$_{11}$]$^-$ counter anions and lies within the range of silylium-like ions coordinated to a weak Lewis base.

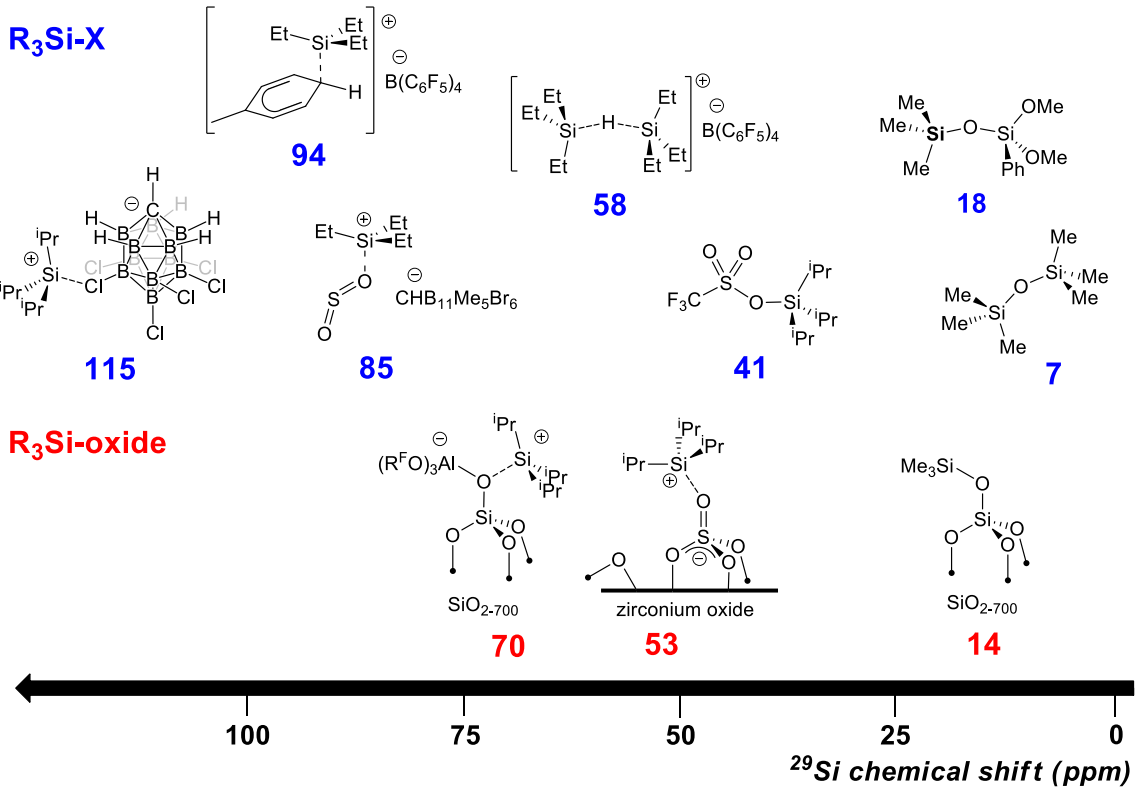

Figure 4.3.5. Examples of ^{29}Si NMR chemical shifts of soluble R$_3$SiX (blue) and R$_3$Si-oxide materials from chapter 3 and this work (red).

Silylium-like ions initiate the hydrodefluorination (HDF) of C-F bonds (refer to chapter 3 for discussion). In a slurry of cyclohexane at 0 °C in the presence of excess Et_3SiH, **AS3** initiates the HDF of 1-fluoroadamantane, Scheme 4.3.4. Under these conditions **AS3** performs 18 turn overs in 2 hours. The solution $^{19}F\{^1H\}$ NMR spectrum following HDF of 1-fluoroadamantane contains signals for $HOC(CF_3)_3)_3$ and $Al(OC(CF_3)_3)_3$, indicating that **AS3** decomposes during the reaction. PhF-$Al(OC(CF_3)_3)_3$ does not form HDF products in the presence of 1-fluoroadamantane and Et_3SiH under similar conditions.

Scheme 4.3.4 HDF of 1-fluoroadamantane with **AS3**

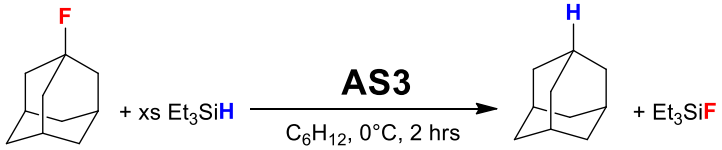

4.4 Conclusion

This study showed that PhF-$Al(OC(CF_3)_3$ reacts with silanols on $SiO_{2\text{-}700}$ to form ≡Si-O(H)-$Al(OC(CF_3)_3)_3$. The $\nu_{N\text{-}H}$ stretch of [$Octyl_3N$-H][≡SiO-$Al(OC(CF_3)_3)_3$] indicates that [≡SiO-$Al(OC(CF_3)_3)_3]^-$ coordinates weaker than ClO_4^- and FSO_3^- ions but is more coordinating than carborane or $B(C_6F_5)_4^-$ ions. The ^{29}Si NMR chemical shift of [$^iPr_3Si$][≡SiO-$Al(OC(CF_3)_3)_3$] also supports that [≡SiO-$Al(OC(CF_3)_3)_3]^-$ anion is weakly coordinating. However, [≡SiO-$Al(OC(CF_3)_3)_3]^-$ forms stronger ion pairs than carborane or $B(C_6F_5)_4^-$ ions.

4.5 Materials and Methods

4.5.1 General considerations

All manipulations were performed under an inert atmosphere of nitrogen or argon using standard schlenk or high vacuum techniques. Grafting reactions were performed in flasks equipped with teflon valves that connect directly to high vacuum lines.[18] Cyclohexane-D12, chloroform-D, benzene-D6, acetonitrile-D3, and methylene chloride-D2 were purchased from Cambridge Isotope laboratories. Benzene and cyclohexane were dried over sodium/benzophenone, degassed, and distilled under vacuum. Pentane was dried over tetraglyme/sodium/benzophenone, degassed, and distilled under vacuum. Allyltriisopropylsilane was dried over 4 Å sieves and degassed under vacuum prior to use. Triethylsilane, trioctylamine, hexafluorobenzene, and perfluorohexane were dried over CaH_2 then vacuum distilled just prior to use. $SiO_{2\text{-}700}$ was prepared as described in chapter 3 of this dissertation. Other commercially available reagents were used as received without any purification. Synthesis of PhF-Al$[OC(CF_3)_3]_3$, and 1-fluoroadamantane (dried by sublimation) were synthesized as previously reported.[19,20]

FT-IR spectra were recorded as pressed pellets using a Bruker Alpha IR spectrometer in an argon-filled glovebox. Gas chromatography was carried out using Agilent 7820A GC system equipped with an Alumina/KCl column for gas phase measurements or on a HP-5 column for solution measurements. Aluminum elemental analyses were carried out by digesting solid samples in dilute nitric acid and measuring the samples at the University of California, Riverside Environmental Sciences Research Laboratory (ESRL) on a Perkin – Elmer Optima 7300DV ICP – OES. Fluorine, and CHN

analyses were performed by the microanalysis laboratory at the University of Illinios, Urbana-Champagne.

Solution ^{1}H spectroscopy was carried out on an Avance Bruker 300, an Avance Bruker NEO400, or an Avance Bruker 600. The ^{1}H spectra were referenced to the NMR solvent residual peak. Solution $^{19}F\{^{1}H\}$ spectroscopy was carried out on an Avance Bruker 300 (282 MHz) and the spectra were referenced to an internal standard of C_6F_6 (-163.9 ppm). For quantitative $^{19}F\{^{1}H\}$ NMR experiments, the relaxation delay was set to 10 seconds. Solid state NMR spectra at UC Riverside were recorded in 4 mm zirconia rotors at 8 – 12 KHz spinning at the magic angle at 14.1 T on an Avance Bruker NEO600 spectrometer equipped with a standard-bore magnet. ^{27}Al simulations were performed using the simulation software SOLA from Topspin 4.0.2. Solid state ^{19}F MAS NMR at the California Institute of Technology were recorded at 11.7 T in a 4 mm rotor spinning at 10 kHz on an Avance Bruker 500.

Solid-state NMR experiments at 9.4 T at Iowa State University were performed on a Bruker Avance III HD spectrometer equipped with wide-bore magnet. Experiments were performed at an MAS frequency (ν_{rot}) of 25 kHz using a 2.5 mm triple-resonance probe. 1D ^{1}H NMR spectra were acquired using the DEPTH pulse sequence[21] comprising of a 90° excitation pulse and followed by two successive 180° pulses for background suppression at 100 kHz radiofrequency (RF) field.

The $^{1}H\{^{27}Al\}$ RESPDOR[12,13] experiment was performed with the $SR4_1^2$ dipolar recoupling sequence[22] on the ^{1}H channel applied with a radiofrequency (RF) field of twice the MAS frequency ($2 \times \nu_{rot}$). The saturation pulse was applied on the ^{27}Al channel at 80

kHz RF field with a duration of 60 μs (1.5 × τ_{rot}, $\tau_{rot} = 1/\nu_{rot}$). The experiment was performed in an interleaved manner where a control dataset is obtained without the pulse on the ^{27}Al channel for every recoupling duration. Numerical simulations of ^{1}H-^{27}Al RESPDOR were performed with SIMPSON *v*4.2.1[23–25]. The ^{1}H{^{27}Al} RESPDOR curve shown in the main text compares $\Delta S/S_0$ with numerical simulations performed with a saturation factor (*f*) =0.55 and different ^{1}H-^{27}Al dipolar coupling constants/inter-nuclear distances. The curve corresponding to a ^{1}H-^{27}Al distance of 2.46 Å shows the best agreement with experiment, consistent with the DFT calculated structure of **AS1D**. Numerical simulations were performed in SIMPSON with the start operator set to I_{1x} and the detect operator set to I_{1p}. Powder averaging was performed using the 'rep320' crystallite orientation file comprising of 320 (α, β) pairs. 16 γ angles were used. An ideal ^{1}H 180° pulse was used, whereas the ^{27}Al saturation pulse used an 80 kHz RF field and a duration of 60 μs (1.5 × τ_{rot}) to mimic experimental conditions. The ^{27}Al C_Q and η were set to 15.2 MHz and 0.0, respectively. The relative orientations (Euler angles) of the ^{27}Al quadrupole and CSA tensors and the ^{1}H-^{27}Al dipole vector were set according to the DFT optimized structure of **AS1D**.

The proton detected ^{27}Al→^{1}H D-RINEPT experiment[26,27] was performed with a 0.1 s recycle delay, 4096 scans, 100 kHz indirect spectral width and 92 t_1 increments. The STATES-TPPI procedure was used to achieve sign discrimination and obtain absorptive peaks in the indirect dimension. Rotor synchronized $SR4_1^2$ dipolar recoupling was applied on the ^{1}H channel with RF set to 2 × ν_{rot}. 4 μs central transition (CT) selective 90° pulses were applied on the ^{27}Al channel. RAPT pulses[28] were applied on the ^{27}Al channel prior to

the D-RINEPT transfer step using 38 μs frequency switched WURST (wideband, uniform rate, smooth truncation) pulses separated by a 2 μs delays at 31 kHz RF field.

All solid-state NMR were processed using Topspin *v*3.6.1. ^{27}Al analytical simulations were performed using ssNake v1.1.[29]

*4.5.2 Synthesis and characterization of **AS1-3***

Table 4.2. ^{27}Al simulation parameters for **AS1-3**.[a]

Material	δ_{iso} (ppm)	Ω (ppm)	κ	C_Q (MHz)	η	α	β	γ
AS1	43.2	196	-0.41	14.6	0.23	60	34	75
AS1[b]	43.0	227	-0.96	14.6	0.20	60	35	75
AS2	45.6	90	-0.22	6.7	0.47	332	15	173
AS3	33	118	-0.14	13.0	0.85	0	33	0

a.) taken from simulations of the static spectra in the Results and discussion; and b.) taken from the simulation of the MAS spectrum in Figure 4.5.4.

Synthesis of **AS1**: $SiO_{2\text{-}700}$ (2 g, 0.52 mmol OH) and PhF-Al[$OC(CF_3)_3)_3$] (480 mg, 0.58 mmol) were transferred to one arm of a double-Schlenk flask inside an argon-filled glovebox. Perfluorohexane (ca. 10 ml) was transferred under vacuum to the flask at 77 K. The mixture was warmed to room temperature and gently stirred for two hours. The clear solution was filtered to the other side of the double Schlenk. The remaining solid was

washed by condensing solvent from the other arm of the double Schlenk at 77 K, warming to room temperature, stirring for 2 minutes, and filtering the solvent back to the other side of the flask. This was repeated two times. The solid was dried under diffusion pump vacuum for 1 hour. The white material was stored in a glovebox freezer at -20 °C. FT-IR: $\nu_{O\text{-}H}$ = 3743 (≡Si–O**H**) and 3542 (≡Si–O**H**---Al(OR^F)$_3$) cm^{-1}. Solid state NMR: ^{1}H MAS NMR (600 MHz): 7.1 (PhF), 4.9 (≡Si–O**H**---Al(OR^F)$_3$), 2.3 (≡Si–O**H**); ^{19}F MAS NMR (470 MHz): -78.5 (AlOC(C**F**$_3$)$_3$), -134 (Ph**F**); ^{13}C{^{1}H} MAS NMR (151 MHz): 121 (q, $^1J_{C\text{-}F}$: 277 Hz, --OC(**C**F$_3$)$_3$), 78 (-O**C**(CF$_3$)$_3$); ^{29}Si{^{1}H} NMR (119 MHz): -95 (≡**Si**–OH---Al(OR^F)$_3$) and -104 (**Si**O$_2$) ppm. Elemental analysis: 0.64 % Al, 2.52 % C, and 7.61 % F.

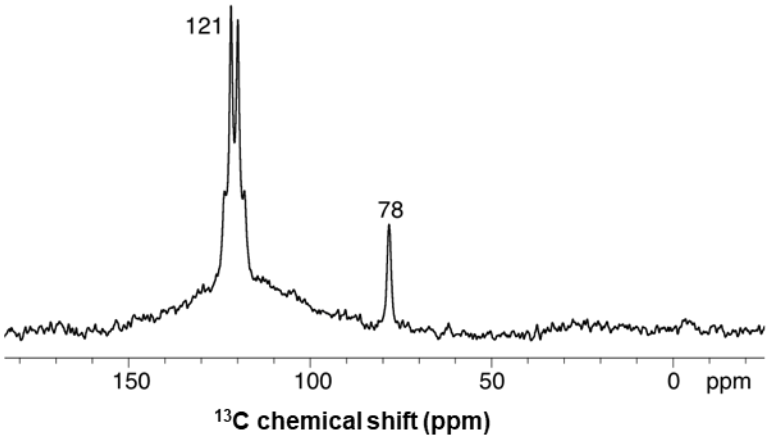

Figure 4.5.1. ^{13}C{^{1}H} HP-DEC MAS NMR spectrum of **AS1** spinning at 10 kHz, relaxation delay of 3 seconds (the broad peak centered around 120 ppm is rotor background).

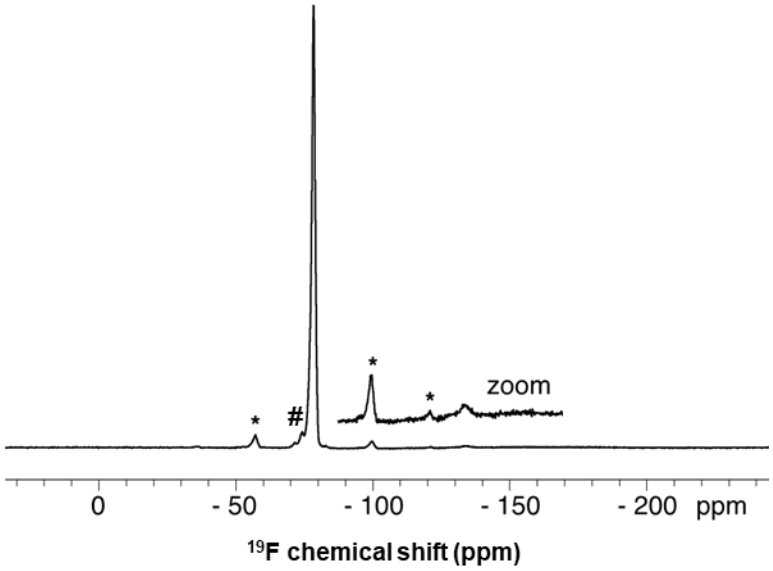

Figure 4.5.2. ^{19}F NMR spectrum of **AS1** spinning at 10 kHz, * = spinning sideband. The zoom contains the signal for PhF at -134 ppm, # = $HOC(CF_3)_3$ due to thermal decomposition.

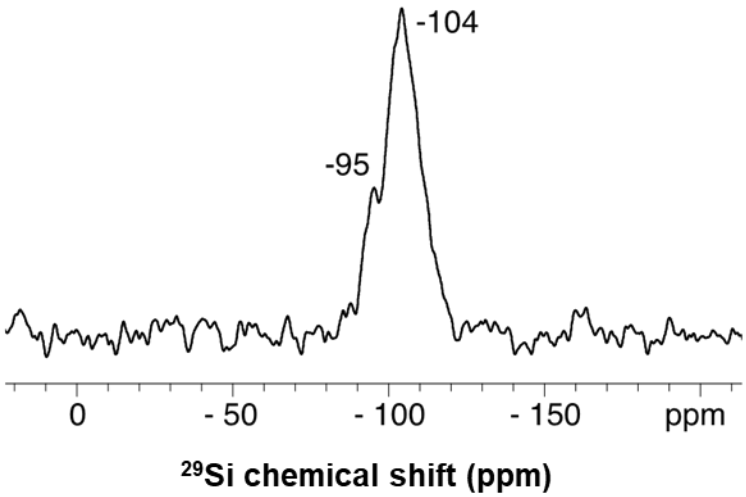

Figure 4.5.3. ^{29}Si CP-MAS NMR spectrum of **AS1** spinning at 8 kHz.

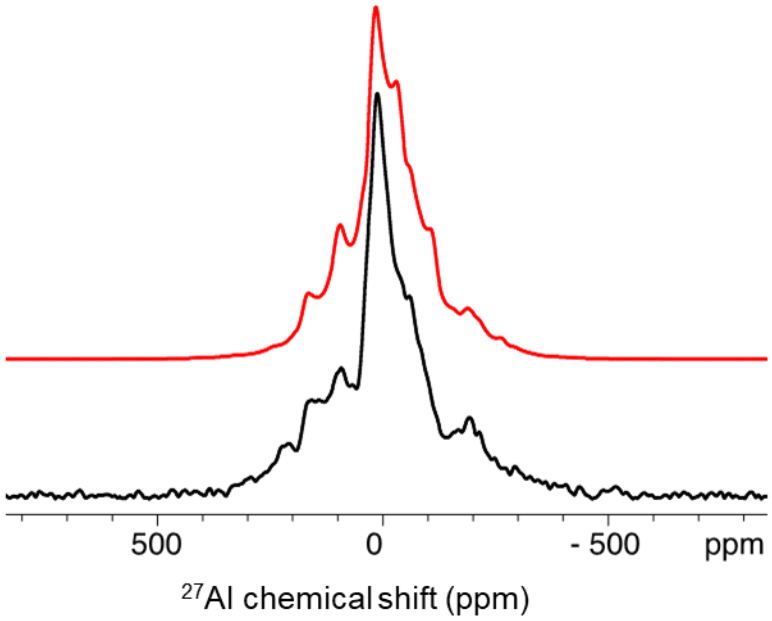

Figure 4.5.4. ^{27}Al{^{1}H} MAS NMR spectrum of **AS1** spinning at 12 kHz (black) and simulation (red).

Full description for the ^{1}H{^{27}Al} RESPDOR from Figure 4.3.2: Plot comparing ^{1}H{^{27}Al} RESPDOR experimental and numerically simulated dephasing intensities as a function of total $SR4_1^2$ recoupling time. Comparison of experimental $\Delta S/S_0$ RESPDOR curves with numerical simulations performed with different saturation factor (*f*) for a fixed ^{1}H-^{27}Al dipolar coupling constant of 2.1 kHz (2.46 Å ^{1}H-^{27}Al distance). The saturation factor f was applied as a scaling factor to the calculated RESPDOR curves ($f \times \Delta S/S_0$) to account for incomplete saturation of ^{27}Al satellite transitions and/or additional ^{1}H signal intensity attributed to ^{1}H spins that are isolated from ^{27}Al.[13]

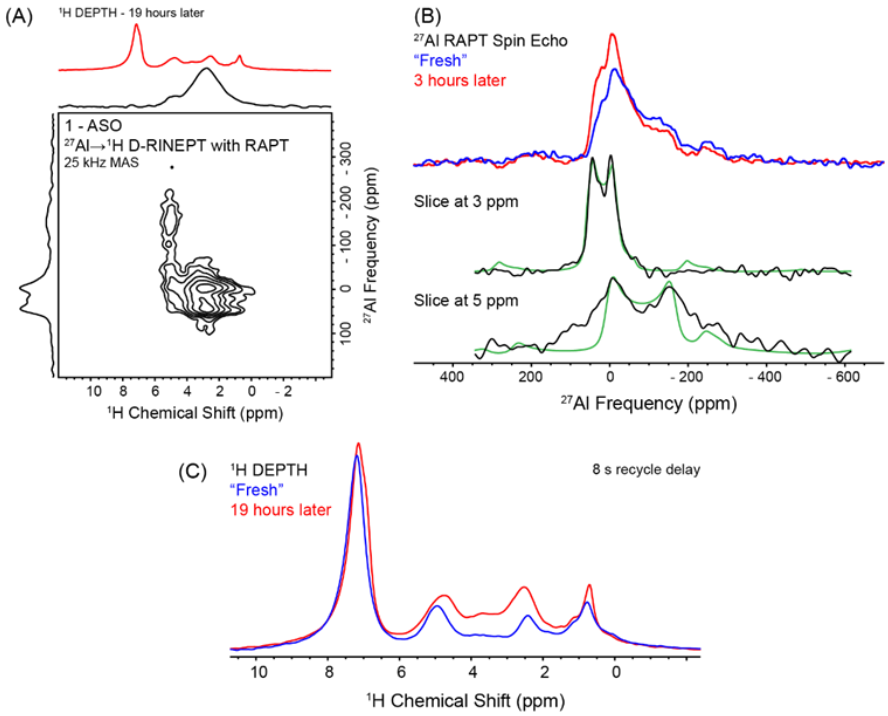

Figure 4.5.5. (A) 2D ^{27}Al→^{1}H RAPT D-RINEPT spectrum acquired with the $SR4_1^2$ dipolar recoupling sequence at 25 kHz MAS and 9.4 T (20.5 hours experiment time). (B) Comparison of ^{27}Al RAPT spin echo spectra, ^{27}Al slices (black) extracted from the 2D D-RINEPT spectrum at ^{1}H chemical shifts of 3 and 5 ppm and simulated spectra (green). The RAPT spin echo spectra shown were acquired one after the other. (C) Comparison of 1D ^{1}H DEPTH spectra acquired initially and 19 hours later. During this time, the rotor was spinning under N_2 gas. The 2D ^{27}Al→^{1}H D-RINEPT spectrum shows that the acidic proton at 5.0 ppm correlates with a broad ^{27}Al NMR signal at 50 ppm (C_Q = 15.7 MHz), which is assigned to **AS1**. The observed C_Q of this site is consistent with the 14.1 T measurements shown in Table S1. The INEPT spectrum also shows an intense correlation between a ^{1}H NMR signal at 3.0 ppm and a sharper ^{27}Al NMR signal at 73 ppm (C_Q = 10.0 MHz). This signal is assigned to a higher symmetry ^{27}Al species that forms during the course of sample rotation, most likely because of partial hydrolysis of **AS1** in the imperfectly sealed 2.5 mm rotors. Consistent with this interpretation, the ^{1}H DEPTH spectrum of **AS1** obtained immediately at the start of MAS experiments ("fresh") and after 19 hours of continuous MAS ("19 hours later") shows a clear increase in total ^{1}H integrated signal intensity, suggesting ingress of water into the rotor. The ^{27}Al RAPT spin echo spectrum of the "fresh" sample was obtained immediately after starting MAS, however, acquisition of the spectrum required ca. 3 hours, during which partial hydrolysis likely occurred (Figure S6B). A second ^{27}Al spin echo spectrum was then obtained ("3 hours later") and the intensity of the broad ^{27}Al signal was observed to decrease slightly, while the narrower ^{27}Al signal increased slightly. All of these observations are again consistent with partial hydrolysis of **AS1** in the rotor.

Stability of **AS1** in common solvents: **AS1** (50 mg) was loaded into a teflon – valved NMR tube then solvent (0.5 mL) was vacuum transferred over the solid. The $^{19}F\{^{1}H\}$ NMR spectra were recorded 1 hour after solvent addition. In all solvents tested solvent - $Al[OC(CF_3)_3]_3$ and $HOC(CF_3)_3$ were observed leaching off of the surface, except in the cased of cyclohexane.

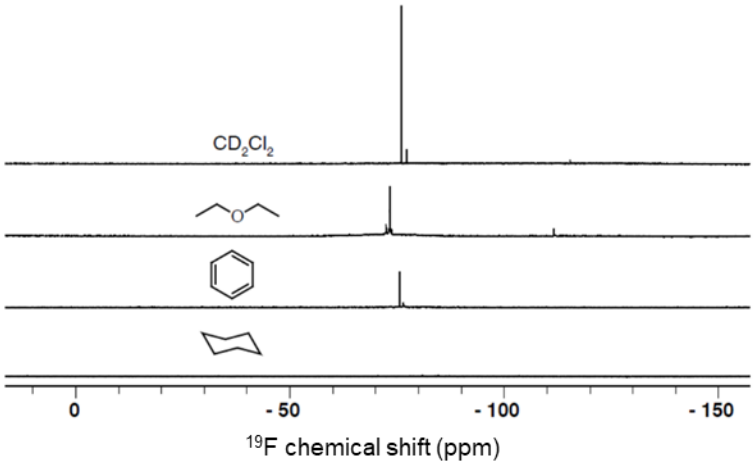

Figure 4.5.6. $^{19}F\{^{1}H\}$ NMR of **AS1** suspended in the indicated solvents.

Leaching experiment: **AS1** (200 mg) was placed in a teflon – valved flask then acetonitrile (2 mL) was transferred to the flask under vacuum at -196 °C. The slurry was stirred at room temperature for 30 minutes. The solution was canulae transferred under argon flow into a clean teflon – valved flask. The remaining solid was dried under vacuum for 1 hour at room temperature. In a glovebox, hexafluorobenzene (10 µL, 86 µmol) was added to the acetonitrile solution then the solution was transferred to an NMR tube and examined by $^{19}F\{^{1}H\}$ solution NMR with perfluorobenzene (-164 ppm) as an internal

standard. From this experiment **AS1** contains 0.045 ± 0.004 mmol/g of PhF (-114 ppm). Signals for $Al(OR^F)_3$ (-76 ppm) and HOR^F (-73 ppm) are also present in this spectrum. The presence of these signals in the ^{19}F NMR spectrum indicate that the bridging silanol sites in **AS1** are not stable in the presence of MeCN. Desorption of $Al(OR^F)_3$ occurs in the presence of MeCN, and an unknown decomposition to form HOR^F occurs under these conditions.

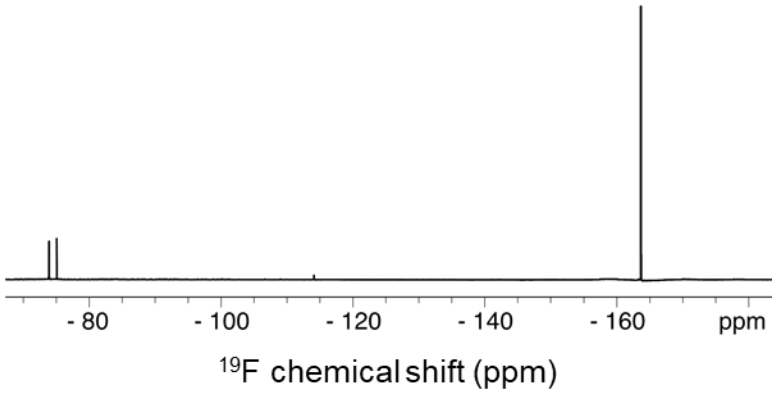

Figure 4.5.7. $^{19}F\{^1H\}$ NMR spectrum from the leaching experiment.

AS1 + n-octyl$_3$N (**AS2**): **AS1** (200 mg, 0.05 mmol ≡Si–OH---$Al(OR^F)_3$) was loaded into a teflon – valved flask. Pentane (2 ml) was vacuum transferred to the solid at -196 °C using a high vacuum line. In a N_2 filled glovebox, trioctylamine (12 µL, 0.03 mmol) was added to the slurry. The reaction was gently stirred for 30 minutes then the solution was removed by cannula under argon flow. The solid was washed 2 X more by vacuum transferring in more pentane (2 mL) then removing solvent by cannula again. The cream-colored solid was dried under vacuum. FT-IR: ν_{NH} = 3070 cm^{-1}. Solid state NMR: ^1H NMR

(600 MHz): 7.1 (PhF), 1.0 (n-octyl), 0.7 (n-octyl); ^{19}F MAS NMR (470 MHz): -77 (AlOC(C**F**$_3$)$_3$); ^{13}C{^{1}H} NMR (151 MHz): 121 (q, $^1J_{C\text{-}F}$: 277 Hz, -OC(**C**F$_3$)$_3$), 79 (-O**C**(CF$_3$)$_3$), 55 (n-octyl), 53 (n-octyl), 31 (n-octyl), 29 (n-octyl), 26 (n-octyl), 22.5 (n-octyl), 12 (n-octyl); ^{29}Si{^{1}H} NMR (119 MHz): -105 (SiO_2) ppm. Elemental analysis: 0.63 % Al, 0.26 % N, 5.83 % C and 6.5 F %.

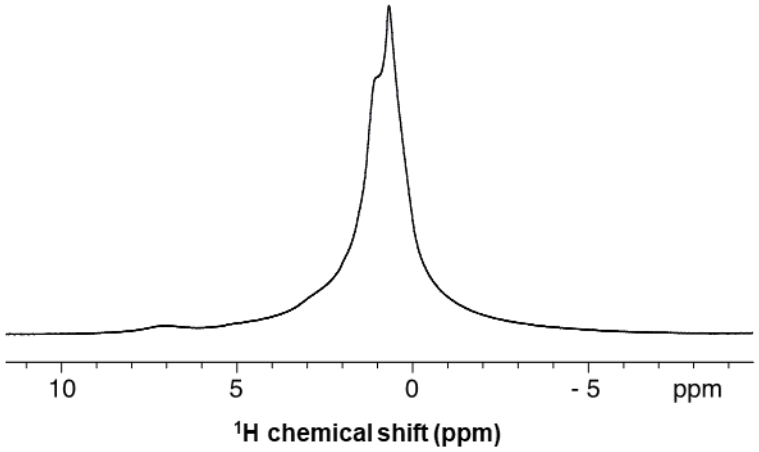

Figure 4.5.8. Solid-state ^{1}H MAS NMR spectrum of AS3, spinning at 10 kHz.

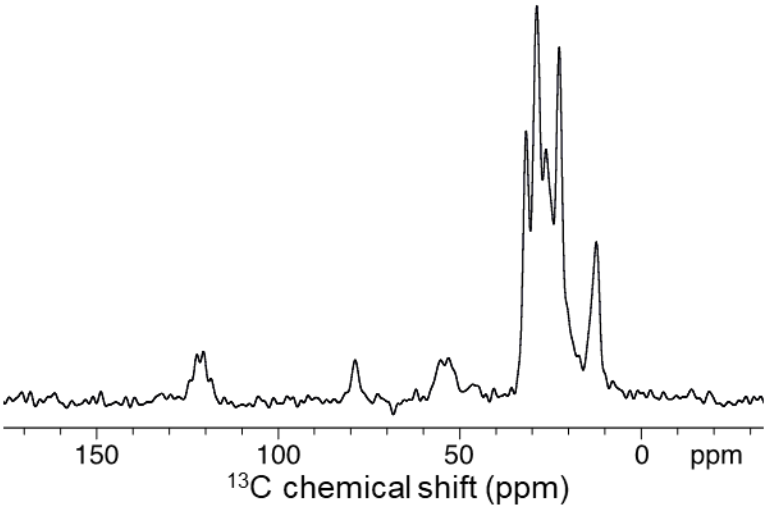

Figure 4.5.9. ^{13}C CP-MAS NMR spectra of **AS2**, spinning at 10 kHz.

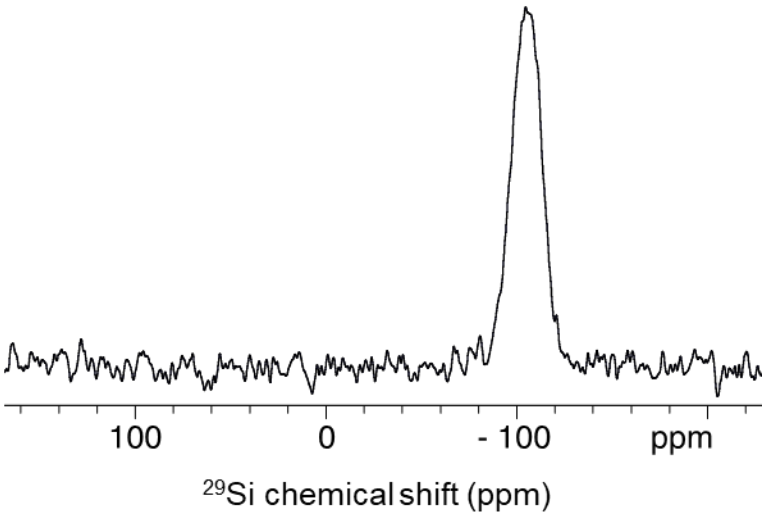

Figure 4.5.10. ^{29}Si CP-MAS NMR spectrum of **AS2**, spinning at 8 kHz.

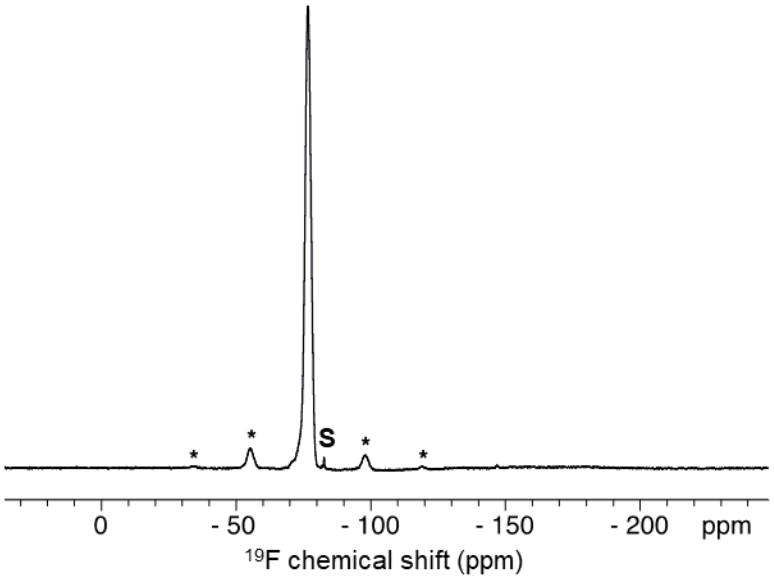

Figure 4.5.11. ^{19}F NMR spectrum of **AS2**, spinning at 10 kHz, * = spinning sideband. S = unknown impurity.

Synthesis of **AS3**: **AS1** (1 g, 0.24 mmol ≡Si–OH---Al(OR^F)$_3$) was loaded into a teflon – valved flask and evacuated under diffusion pump vacuum. Pentane (~5 mL) was transferred to the flask at -196 °C. The slurry was warmed up to 0 °C and allyltriisopropylsilane (0.06 mL, 0.26 mmol) was added by syringe under the flow of argon. The slurry was stirred at 0 °C for 2 hours. The solution was decanted by cannula, washed with freshly distilled pentane (2 x 5 mL). The solid was dried under diffusion pump vacuum to give a cream colored solid **AS3**. The solution NMR of the washings after ca. 90 % of the pentane was allowed to evaporate shows that a mixture of oligomers derived from cationic oligomerization of propene forms under these conditions (Figure 4.5.12). Solid state NMR: ^{1}H NMR (600 MHz): 7.0 (PhF), 0.88 (^{i}Pr); ^{19}F MAS NMR (470 MHz): -78 (-OC(C**F**$_3$)$_3$); ^{13}C{^{1}H} NMR (151 MHz): 121 (-OC(**C**F$_3$)$_3$), 78 (-O**C**(CF$_3$)$_3$), 15

(SiCH(**C**H_3)$_2$), 12 (Si**C**H(CH$_3$)$_2$); ^{29}Si{^{1}H} NMR (119 MHz): 70 (≡Si–O**Si**^{i}Pr$_3$---Al(OR^F)$_3$), 4 (≡Si–O**Si**^{i}Pr$_3$) and -105 (**Si**O_2) ppm. Elemental analysis: 0.65 % Al, 4.24 % C, 0.47 % H and 4.5 F %.

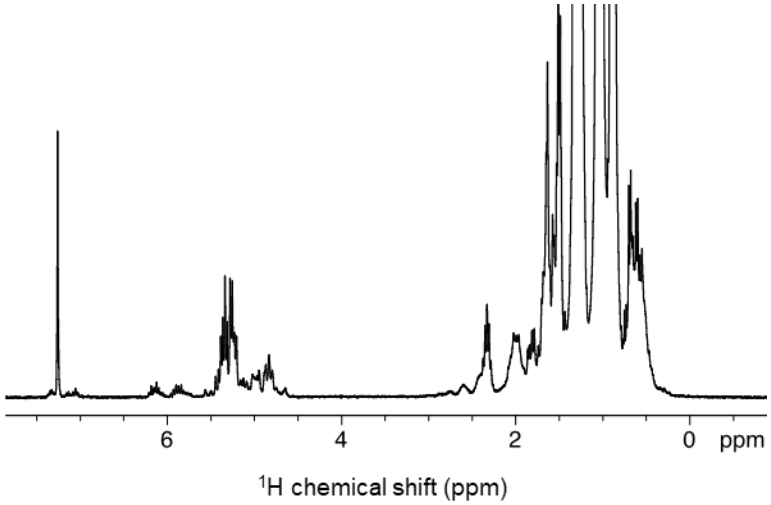

Figure 4.5.12. ^{1}H NMR spectrum of the washings after the synthesis of **AS3** in $CDCl_3$.

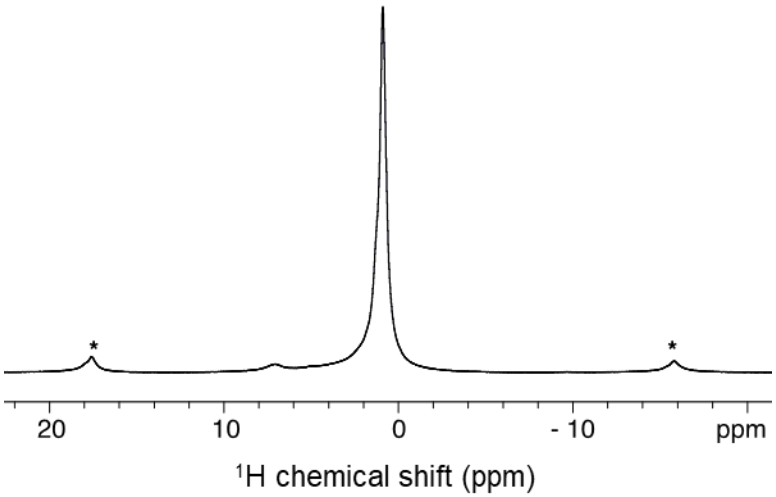

Figure 4.5.13. ^{1}H NMR spectrum of **AS3** spinning at 10 kHz, * = spinning sidebands.

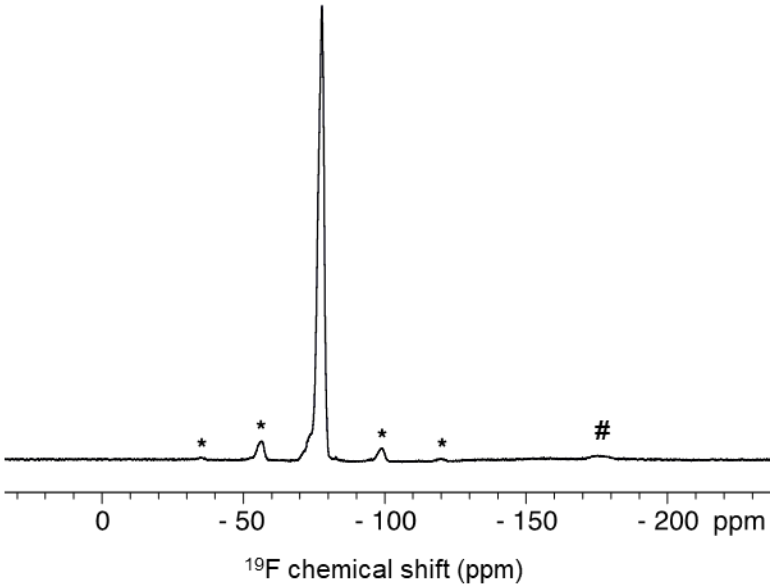

Figure 4.5.14. ^{19}F NMR spectrum of **AS3** spinning at 10 kHz, * = spinning sideband. # = $^{i}Pr_3SiF$ due to thermal decomposition.

Hydrodefluorination of 1-adamantylfluoride with **AS3**: **AS3** (20 mg, 4.8 μmol of Al) and 1-adamantylfluoride (40 mg, 0.26 mmol) were loaded into a teflon-valved flask then it was connected to a vacuum line. The flask evacuated, cooled to 0 °C, and cyclohexane (2 mL) and triethylsilane (0.05 mL, 0.31 mmol) were added by syringe. The reaction was stirred at 0 °C for 2 hours. The reaction was monitored by taking aliquots of the solution phase and measuring the $^{19}F\{^{1}H\}$ NMR in air. Under these conditions, 0.086 mmol Et_3SiF forms, giving a TON of 18.

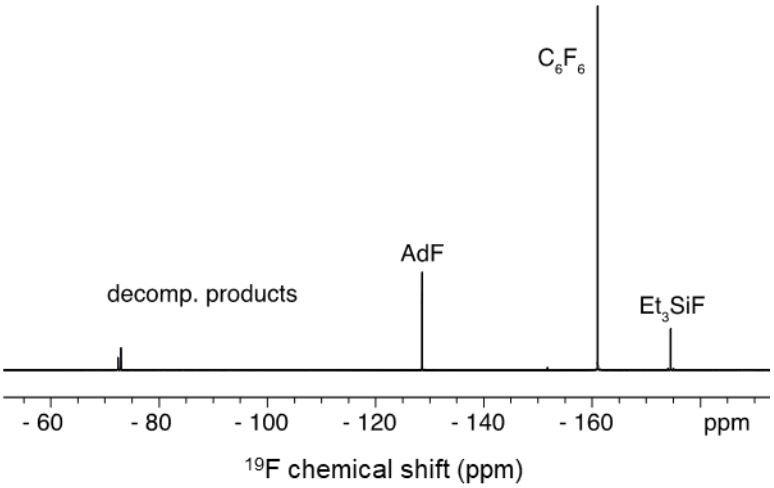

Figure 4.5.15 $^{19}F\{^{1}H\}$ NMR spectrum of the HDF of 1-adamantylfluoride with **AS3**.

4.6 References

(1) Culver, D. B.; Venkatesh, A.; Huynh, W.; Rossini, A. J.; Conley, M. P. Al(ORF)3 (RF = C(CF3)3) Activated Silica: A Well-Defined Weakly Coordinating Surface Anion. *Chem. Sci.* **2020**, *11* (6), 1510–1517. https://doi.org/10.1039/c9sc05904k.

(2) Olah, G. A.; Surya Prakash, G. K.; Molnr, R.; Sommer, J. Superacid Chemistry. In *Superacid Chemistry*; Wiley, 2008; pp 1–34. https://doi.org/10.1002/9780470421604.

(3) Yamamoto, H.; Futatsugi, K. "Designer Acids": Combined Acid Catalysis for Asymmetric Synthesis. *Angew. Chemie - Int. Ed.* **2005**, *44* (13), 1924–1942. https://doi.org/10.1002/anie.200460394.

(4) Bhan, A.; Iglesia, E. A Link between Reactivity and Local Structure in Acid Catalysis on Zeolites. *Acc. Chem. Res.* **2008**, *41* (4), 559–567. https://doi.org/10.1021/ar700181t.

(5) Boronat, M.; Corma, A. Factors Controlling the Acidity of Zeolites. *Catal. Letters* **2015**, *145* (1), 162–172. https://doi.org/10.1007/s10562-014-1438-7.

(6) Xu, T.; Kob, N.; Drago, R. S.; Nicholas, J. B.; Haw, J. F. A Solid Acid Catalyst at the Threshold of Superacid Strength: NMR, Calorimetry, and Density Functional Theory Studies of Silica-Supported Aluminum Chloride. *J. Am. Chem. Soc.* **1997**, *119* (50), 12231–12239. https://doi.org/10.1021/ja970850n.

(7) Walzer, J. F. Supported Ionic Catalyst Composition. US5643847A, June 7, 1995.

(8) Millot, N.; Santini, C. C.; Lefebvre, F.; Basset, J. M. Surface Organometallic Chemistry: A Route to Well-Defined Boron Heterogeneous Co-Catalyst for Olefin Polymerisation. *Comptes Rendus Chim.* **2004**, *7* (8–9), 725–736. https://doi.org/10.1016/j.crci.2004.03.011.

(9) Kraft, A.; Beck, J.; Steinfeld, G.; Scherer, H.; Himmel, D.; Krossing, I. Synthesis and Application of Strong Brønsted Acids Generated from the Lewis Acid Al(ORF)3 and an Alcohol. *Organometallics* **2012**, *31* (21), 7485–7491. https://doi.org/10.1021/om300776a.

(10) Haouas, M.; Taulelle, F.; Martineau, C. Recent Advances in Application of 27Al NMR Spectroscopy to Materials Science. *Prog. Nucl. Magn. Reson. Spectrosc.* **2016**, *94–95*, 11–36. https://doi.org/10.1016/j.pnmrs.2016.01.003.

(11) Ashbrook, S. E.; Sneddon, S. New Methods and Applications in Solid-State NMR Spectroscopy of Quadrupolar Nuclei. *J. Am. Chem. Soc.* **2014**, *136* (44), 15440–15456. https://doi.org/10.1021/ja504734p.

(12) Gan, Z. Measuring Multiple Carbon-Nitrogen Distances in Natural Abundant Solids Using R-RESPDOR NMR. *Chem. Commun.* **2006**, No. 45, 4712–4714. https://doi.org/10.1039/b611447d.

(13) Chen, L.; Wang, Q.; Hu, B.; Lafon, O.; Trébosc, J.; Deng, F.; Amoureux, J. P. Measurement of Hetero-Nuclear Distances Using a Symmetry-Based Pulse Sequence in Solid-State NMR. *Phys. Chem. Chem. Phys.* **2010**, *12* (32), 9395–9405. https://doi.org/10.1039/b926546e.

(14) Stoyanov, E. S.; Kim, K. C.; Reed, C. A. An Infrared VNH Scale for Weakly Basic Anions. Implications for Single-Molecule Acidity and Superacidity. *J. Am. Chem. Soc.* **2006**, *128* (26), 8500–8508. https://doi.org/10.1021/ja060714v.

(15) Lambert, J. B.; Zhang, S.; Ciro, S. M. Silyl Cations in the Solid and in Solution. *Organometallics* **1994**, *13* (6), 2430–2443. https://doi.org/10.1021/om00018a041.

(16) Hoffmann, S. P.; Kato, T.; Tham, F. S.; Reed, C. A. Novel Weak Coordination to Silylium Ions: Formation of Nearly Linear Si-H-Si Bonds. *Chem. Commun.* **2006**, No. 7, 767–769. https://doi.org/10.1039/b511344j.

(17) Culver, D. B.; Conley, M. P. Activation of C−F Bonds by Electrophilic Organosilicon Sites Supported on Sulfated Zirconia. *Angew. Chemie Int. Ed.* **2018**, *57* (45), 14902–14905. https://doi.org/10.1002/anie.201809199.

(18) Copéret, C.; Comas-Vives, A.; Conley, M. P.; Estes, D. P.; Fedorov, A.; Mougel, V.; Nagae, H.; Núnez-Zarur, F.; Zhizhko, P. A. Surface Organometallic and Coordination Chemistry toward Single-Site Heterogeneous Catalysts: Strategies, Methods, Structures, and Activities. *Chem. Rev.* **2016**, *116* (2), 323–421. https://doi.org/10.1021/acs.chemrev.5b00373.

(19) Müller, L. O.; Himmel, D.; Stauffer, J.; Steinfeld, G.; Slattery, J.; Santiso-Quiñones, G.; Brecht, V.; Krossing, I. Simple Access to the Non-Oxidizing Lewis Superacid PhF→Al(ORF)3(RF= C(CF3)3). *Angew. Chemie - Int. Ed.* **2008**, *47* (40), 7659–7663. https://doi.org/10.1002/anie.200800783.

(20) Williard, P. G.; Büchi, G. FLUORINATIONS WITH PYRIDINIUM POLYHYDROGEN FLUORIDE REAGENT : 1-FLUOROADAMANTANE. *Org. Synth.* **1988**, *6*, 225–227. https://doi.org/10.1002/0471264180.os058.13.

(21) Cory, D. G.; Ritchey, W. M. Suppression of Signals from the Probe in Bloch Decay Spectra. *J. Magn. Reson.* **1988**, *80* (1), 128–132. https://doi.org/10.1016/0022-2364(88)90064-9.

(22) Brinkmann, A.; Kentgens, A. P. M. Proton-Selective 17O-1H Distance Measurements in Fast Magic-Angle-Spinning Solid-State NMR Spectroscopy for the Determination of Hydrogen Bond Lengths. *J. Am. Chem. Soc.* **2006**, *128* (46), 14758–14759. https://doi.org/10.1021/ja065415k.

(23) Bak, M.; Rasmussen, J. T.; Nielsen, N. C. SIMPSON: A General Simulation Program for Solid-State NMR Spectroscopy. *J. Magn. Reson.* **2000**, *147* (2), 296–330. https://doi.org/10.1006/jmre.2000.2179.

(24) Tošner, Z.; Andersen, R.; Stevensson, B.; Edén, M.; Nielsen, N. C.; Vosegaard, T. Computer-Intensive Simulation of Solid-State NMR Experiments Using SIMPSON. *J. Magn. Reson.* **2014**, *246*, 79–93. https://doi.org/10.1016/j.jmr.2014.07.002.

(25) Tošner, Z.; Vosegaard, T.; Kehlet, C.; Khaneja, N.; Glaser, S. J.; Nielsen, N. C. Optimal Control in NMR Spectroscopy: Numerical Implementation in SIMPSON. *J. Magn. Reson.* **2009**, *197* (2), 120–134. https://doi.org/10.1016/j.jmr.2008.11.020.

(26) Trebosc, J.; Hu, B.; Amoureux, J. P.; Gan, Z. Through-Space R3-HETCOR Experiments between Spin-1/2 and Half-Integer Quadrupolar Nuclei in Solid-State NMR. *J. Magn. Reson.* **2007**, *186* (2), 220–227. https://doi.org/10.1016/j.jmr.2007.02.015.

(27) Venkatesh, A.; Hanrahan, M. P.; Rossini, A. J. Proton Detection of MAS Solid-State NMR Spectra of Half-Integer Quadrupolar Nuclei. *Solid State Nucl. Magn. Reson.* **2017**, *84*, 171–181. https://doi.org/10.1016/j.ssnmr.2017.03.005.

(28) Yao, Z.; Kwak, H. T.; Sakellariou, D.; Emsley, L.; Grandinetti, P. J. Sensitivity Enhancement of the Central Transition NMR Signal of Quadrupolar Nuclei under Magic-Angle Spinning. *Chem. Phys. Lett.* **2000**, *327* (1–2), 85–90. https://doi.org/10.1016/S0009-2614(00)00805-8.

(29) van Meerten, S. G. J.; Franssen, W. M. J.; Kentgens, A. P. M. SsNake: A Cross-Platform Open-Source NMR Data Processing and Fitting Application. *J. Magn. Reson.* **2019**, *301*, 56–66. https://doi.org/10.1016/j.jmr.2019.02.006.

Chapter 5 Determination of the Active Site Structure in a Ziegler-Natta Type Polymerization Catalyst

5.1 Abstract

The combination of $Cp^b_2ZrCl_2$, Al^iBu_3 (TIBA), and alumina partially dehydroxylated at 600 °C ($Al_2O_{3\text{-}600}$) produces high molecular weight polyethylene. In this complex catalyst system TIBA plays several roles. $Al_2O_{3\text{-}600}$ reacts with TIBA to form $\equiv AlO\text{-}Al(R_2)\text{-}O(Al\equiv)_2$ (R = H or ^{i}Bu, **TA**), which passivates surface -OH present on $Al_2O_{3\text{-}600}$. TIBA also reacts with $Cp^b_2ZrCl_2$ to form a mixture of $Cp^b_2ZrH_2(HAl^iBu_2)(Al^iBu_3)$ (**2**) and $Cp^b_2ZrH_2(HAl^iBu_2)(ClAl^iBu_2)_2$ (**3**); the former species is critical to form active sites in this catalyst. **TA** reacts with mixtures of $Cp^b_2ZrCl_2$ and excess TIBA to form **ZH1TA**. This catalyst polymerizes ethylene with a similar activity to $Cp^b_2ZrCl_2$, TIBA, and $Al_2O_{3\text{-}600}$ mixtures combined *in-situ*. **ZH1TA** reacts with *cis*-1,2-dichloroethylene to form vinyl chloride, implicating $Cp^b_2Zr\text{-}H^+$ as active sites in this material. Model studies using $[Cp^b_2ZrH_2]_2$ and **TA** form **ZH2TA**, and using $[Cp^b_2ZrD_2]_2$ and **TA** forms **ZD2TA**, which are also active in polymerization reactions. The reaction of **ZD2TA** with *cis*-1,2-dichloroethylene show that ~24 % of the $Zr\text{-}D^+$ sites are active in olefin insertion reactions. Solid-state ^2H NMR spectroscopy of deuterium labeled **ZD2TA** confirm that $[Cp^b_2ZrD][DAl\equiv]$ active sites are present in this material.

5.2 Introduction

The Ziegler-Natta (ZN) catalyst is a combination of $TiCl_4$ and AlR_3 supported on $MgCl_2$ for the synthesis of high molecular weight polyethylene and isotactic polypropylene

(Figure 5.2.1). These catalysts are very important because they polymerize ethylene to high density polymer products that were not accessible using traditional radical polymerization methods available at the time. The ZN catalysts are also more active than $CrOx/SiO_2$ catalysts,[1] which also produce high density polyethylene and were discovered a few years before the work of Ziegler and Natta. Ziegler-Natta (ZN) catalysts currently account for roughly half of the polyethylene produced in industry.[2,3]

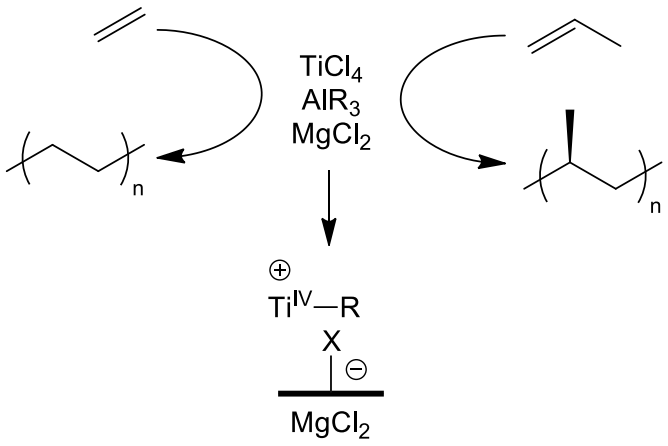

Figure 5.2.1. Classic ZN catalyst for the synthesis of polyethylene and isotactic polypropylene, and a general structure of the proposed Ti(IV)-R^+ cation active site.

ZN catalysts evolved into a diverse class of catalysts that typically consist of a group IV metal precursor, an activator, and a support.[3] Early transition metal halides and metallocenes are common precursors to active sites in ZN type catalysts. Alkyl-aluminums,[4] partially hydrolyzed alkyl aluminums,[5] and oxides are commonly used activators for ZN catalysts.[6] ZN catalysts produce polymers with broad molecular weight distributions, indicating a distribution of active sites are present in these catalysts. A further

complication is the unknown quantity of active sites in ZN catalysts. A common assumption is that only a few percent of the metal sites are active in polymerization reactions. The active site structure is unknown, but is postulated to be a Ti(IV)-R^+ cation on the $MgCl_2$ surface shown in Figure 5.2.1.[7]

Many of the insights into that support the formation of a Ti(IV)-R^+ cation as a potential active site in ZN catalysts are derived from studies of organometallic complexes in solution. The reaction of Cp_2TiCl_2 with Et_2AlCl in solution is proposed to form $[Cp_2TiEt][AlCl_3Et]$, and is active in the polymerization of ethylene (Scheme 5.2.1).[8] Addition of water to related systems results in significantly higher polymerization activity,[9] which was later serendipitously discovered by Sinn and Kaminsky to be the potent methylaluminoxane (MAO) activator for metallocene based polymerization catalysis.[10] Activation of zirconocenes with MAO are complicated because the structure of MAO is unknown, and large Al:Zr ratios are usually present in catalytically active metallocenes.[10,11] The active site is likely contains a Zr-Me^+ cation based on solid-state NMR measurements of Cp_2ZrMe_2/MAO mixtures.[12]

Scheme 5.2.1. Activation of Cp_2TiCl_2 with Et_2AlCl for the polymerization of ethylene.

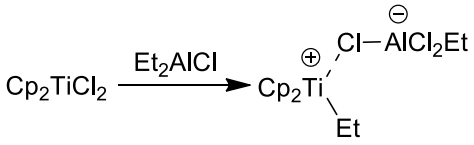

Jordan and coworkers isolated and crystallographically characterized $[Cp_2ZrMe(THF)][BPh_4]$ from the reaction of Cp_2ZrMe_2 with $AgBPh_4$ (Scheme 5.2.2).[13,14]

[$Cp_2ZrMe(THF)$][BPh_4] rapidly polymerizes ethylene, supporting the hypotheses above that cationic metallocenes are active in ethylene polymerization reactions. Hlatky, Turner, and Eckman reported the activation of $Cp^*_2ZrMe_2$ with [Bu_3NH][BPh_4] to form base free [Cp^*ZrMe][BPh_4], methane and Bu_3N.[15] The also reported the first use of a carborane counter anion for the isolation of Zr-Me^+ cations from the reaction of $C_2B_9H_{13}$ via protonolysis of Cp^*ZrMe_2 to form [Cp^*ZrMe][$C_2B_9H_{12}$] and methane.[15]

Scheme 5.2.2. Cp_2ZrMe_2 activation pathways

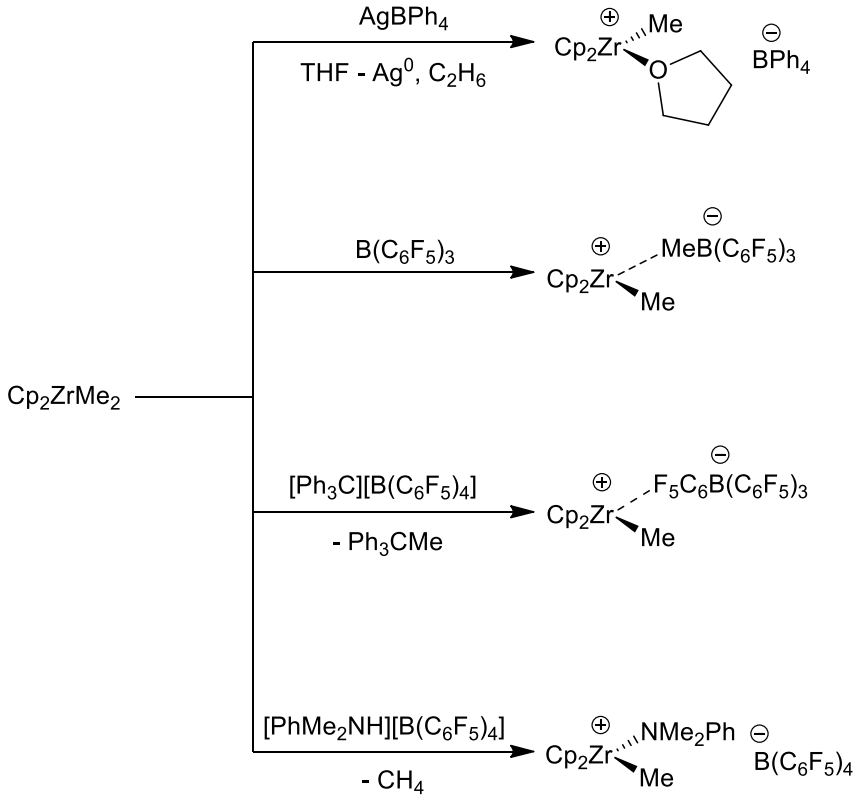

Several zirconocene cations have been isolated with derivatives of $XB(C_6F_5)_3^-$ anions and are also very active polymerization catalysts.[4,11,16,17] Scheme 5.2.2 shows

several pathways for the activation of Cp_2ZrMe_2 to form $[Cp_2ZrMe][XB(C_6F_5)_3]$ (X = Me, or C_6F_5) catalysts. Marks and coworkers reported the reaction of Cp_2ZrMe_2 with $B(C_6F_5)_3$ forming base free $[Cp_2ZrMe][MeB(C_6F_5)_3]$, which initiates the polymerization of ethylene and propylene.[18] Cp_2ZrMe_2 can also be activated by $[Ph_3C][B(C_6F_5)_4]$ forming $[Cp_2ZrMe][B(C_6F_5)_4]$ that polymerizes ethylene with a similar activity to $[Cp_2ZrMe][MeB(C_6F_5)_3]$.[16,19] $[Et_2PhNH][B(C_6F_5)_4]$ is a similarly common activator, the reaction of Cp_2ZrMe_2 forms $[Cp_2ZrMe(NEt_2Ph)][B(C_6F_5)_4]$.[11]

The generally accepted mechanism for the polymerization is shown in Figure 5.2.2. Coordination of ethylene to $[Cp_2ZrMe][WCA]$ forms $Cp_2ZrMe(ethylene)^+$ that undergoes near barrierless migratory insertion[20] to form $ZrCH_2CH_2Me^+$, which contains a β-agostic interaction.[21] Repetition of ethylene coordination and migratory insertion propagates chain growth in $ZrCH_2CH_2P^+$ until β-hydride elimination (chain termination) to form polymers with an olefinic end-group. In the presence of large excess organoaluminum, which is common in MAO activated catalysts, chain transfer to aluminum can also occur.[22]

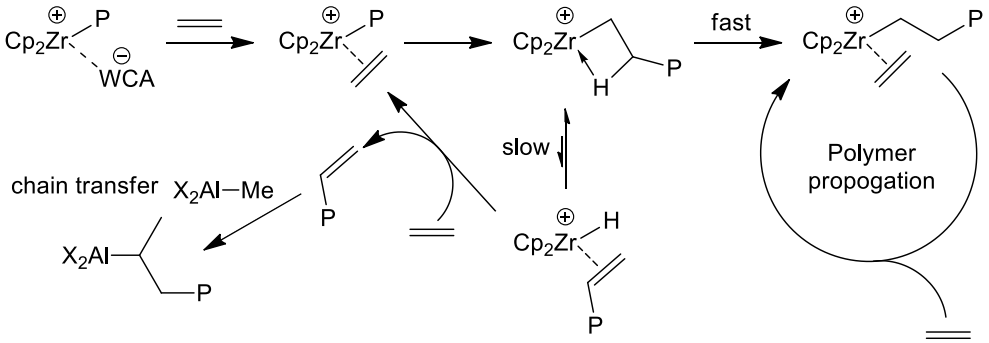

Figure 5.2.2. Mechanism for the polymerization of ethylene with $[Cp_2Zr\text{-}P][WCA]$ (P = polymer chain), WCA is omitted after the 1st step for simplicity.

These studies show that isolable M-R^+ coordinate olefins and propagate polymer growth through insertion reactions. The ZN catalyst is more complicated because metal halides react with the trialkylaluminum to form the M-R bond *in-situ*. For example, Cp_2ZrCl_2 reacts with excess Al_2Me_6 to form $Cp_2ZrMeCl$ and $(Me_2AlCl)_2$ (Figure 5.2.3A).[23] Subsequent alkylation or ionization does not occur in this reaction. Isolable $[Cp_2ZrMe][B(C_6F_5)_4]$ reacts with $AlMe_3$ to form $[Cp_2ZrMe_2AlMe_2][B(C_6F_5)_4]$, a likely resting state when the $AlMe_3$ concentration is high (Figure 5.2.3B).[4,24] Cp_2ZrCl_2 reacts with excess diisobutylaluminum hydride (iBu_2AlH) to form $Cp_2ZrH_2(HAl^iBu_2)(ClAl^iBu_2)_2$ (Figure 5.2.3C).[25] This reaction probably occurs through exchange of both Zr-Cl to form Zr-H that are trapped by $ClAl^iBu_2$ to form the reaction product. The addition of $[Ph_3C][B(C_6F_5)_4]$ to this mixture forms a $[Cp_2ZrH(HAl^iBu_2)_2][B(C_6F_5)_4]$ ion pair.[26]

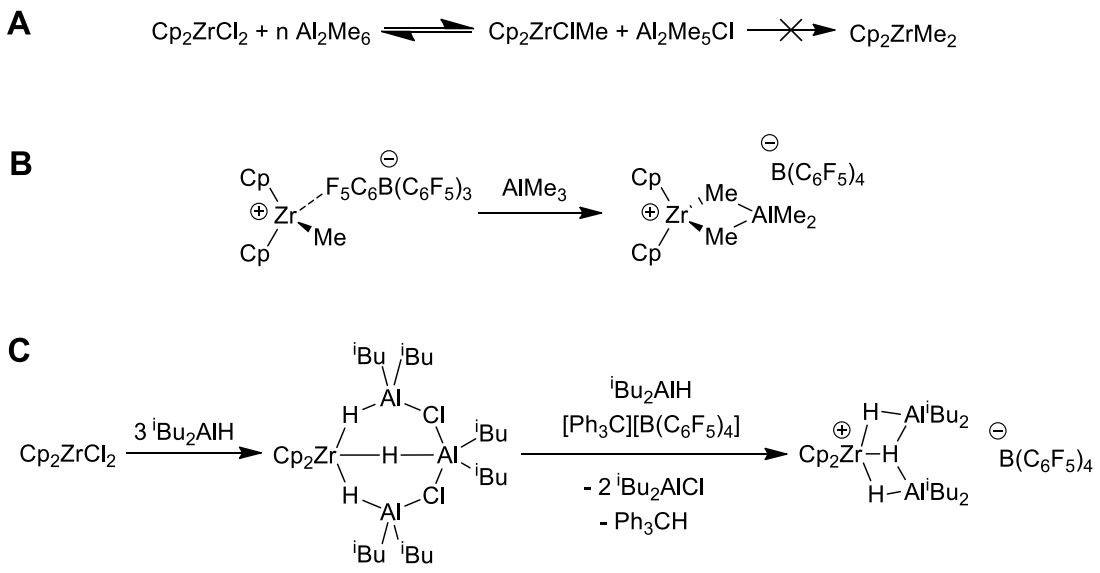

Figure 5.2.3. A) reaction of Cp_2ZrCl_2 with Al_2Me_6; B) reaction of $[Cp_2ZrMe][B(C_6F_5)_4]$ with Al_2Me_6; and C) reaction of Cp_2ZrCl_2 with iBu_2AlH and $[Ph_3C][B(C_6F_5)_4]$.

Further complicating understanding of active sites in ZN catalysts is the high surface area support that interacts with the metallocene precatalyst, alkylaluminum, and products formed from these reactants. Most studies have focused on reactions of pre-formed organometallics with surfaces, these studies are described in Chapter 1. In the context of ZN catalysts, the reaction of $Cp^*_2ThMe_2$ with anhydrous $MgCl_2$ forms $[Cp^*_2ThMe][Me\text{-}MgCl_n]$ (Scheme 5.2.3),[27] and is similar to the products of organometallics with strong Lewis acids shown in Scheme 5.2.2. This result suggests that strong Lewis sites are probably necessary in ZN catalysts to form organometallic ion-pairs.

Scheme 5.2.3. reaction of $Cp^*_2ThMe_2$ with $MgCl_2$

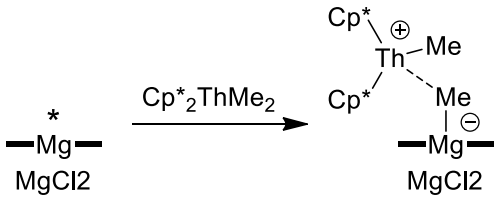

This chapter studies the ternary $Cp^b_2ZrCl_2/Al^iBu_3/Al_2O_3$ catalyst for the polymerization of ethylene. This catalyst produces polymers with narrow molecular weight distributions, indicating that these catalysts are single-site.[28] Solution phase experiments show that excess TIBA used in these catalyst mixtures is necessary to form neutral Zr-H species that react with TIBA functionalized alumina to form small quantities of $Zr\text{-}H^+$ sites. The related model catalyst prepared from $[Cp^b_2ZrD_2]_2/Al^iBu_3/Al_2O_3$ was characterized by ^2H MAS NMR studies, which show that a $Zr\text{-}D^+$ site is formed in this material. Active site

titrations using *cis*-1,2-dichloroethylene show that ~24 % of the sites in the model system sites are active in olefin insertion reactions.

5.3 Results and discussion

5.3.1 Experimental design

Though the ternary $Cp^b{}_2ZrCl_2/Al^iBu_3/Al_2O_3$ catalyst is single-site, this mixture is expected to be complex because of the competing surface and solution chemistry that can happen in this mixture. The $Cp^b{}_2ZrCl_2$ (Cp^b = n-butylcyclopentadienyl) precatalyst was chosen for this study because this zirconocene is very active in polymerization reactions in the presence of suitable activators, and this complex is soluble in hydrocarbon solvents common in heterogeneous polymerization processes. Typical $Cp^b{}_2ZrCl_2/Al^iBu_3/Al_2O_3$ mixtures contain an excess of Al^iBu_3 (TIBA) (Zr:Al = 1:12), suggesting that $Cp^b{}_2ZrCl_2$ (**1**) reacts with excess TIBA to form Zr-R (R = iBu or H) intermediates (Scheme 5.3.1).

Scheme 5.3.1. Reaction of **1** with excess Al^iBu_3 for the formation of Zr-R intermediates

$$Cp^b{}_2ZrCl_2 \xrightarrow{12\ Al^iBu_3} [Cp^b{}_2ZrR_2]\ (R = H \text{ or } {}^iBu)$$

TIBA is also expected to react with hydroxyls on the surface alumina partially dehydroxylated at 600 °C ($Al_2O_{3\text{-}600}$). The role of these organoaluminum species in catalyst formation is not clear, but they may alkylate Zr-Cl species or activate Zr-R species similar to partially hydrolyzed alkylaluminum activators.[11] Finally, partially dehydroxylated alumina contains strong Lewis sites that are known to activate Th-Me[29–31] and Zr-R[32,33]

containing complexes, which may be important in the formation of active sties in this catalyst system.

The formation of Zr-H complexes was observed in the study of $Cp^b_2ZrCl_2$ and TIBA mixtures in solution, implicating that Zr-H may be the reactive precursor to the formation of catalytic sites in $Cp^b_2ZrCl_2$/TIBA/$Al_2O_{3\text{-}600}$. Studies of the reaction between TIBA and $Al_2O_{3\text{-}600}$ showed that the reaction forms high symmetry ≡AlO-Al(R_2)-O(Al≡)$_2$ (R = ^{i}Bu or H) sites on the surface. Polymerization reactions indicate that the formation of a solution Zr-H precursor and surface ≡AlO-Al(R_2)-O(Al≡)$_2$ sites are critical to the formation of active sites. In the absence of TIBA, $Al_2O_{3\text{-}600}$ reacts with Zr-H to form inactive surface species. Mechanistic studies show that [Cp^b_2ZrH][HAl≡] is formed under catalytic conditions (Scheme 5.3.2).

Scheme 5.3.2. Proposed active structure for the ZN type catalyst: $Cp^b_2ZrCl_2$/TIBA/$Al_2O_{3\text{-}600}$ (R = H or ^{i}Bu)

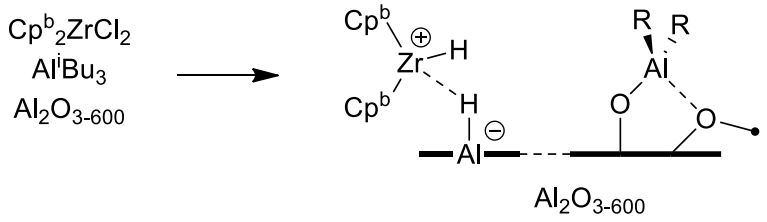

5.3.2 Solution NMR studies

1 reacts with 12 equivalents of TIBA to form $Cp^b{}_2ZrH_2(HAl^iBu_2)(Al^iBu_3)$ (**2**), $Cp^b{}_2ZrH_2(HAl^iBu_2)(ClAl^iBu_2)_2$ (**3**), Al^iBu_2H, Al^iBu_2Cl, and isobutene upon mixing at room temperature (Scheme 5.3.3), denoted as **1**/TIBA. The ^1H NMR signals of this mixture are broad at room temperature, but sharpen in methylcyclohexane-d_{14} at -40 °C (Figure 5.3.1). The ^1H NMR spectrum of $Cp^b{}_2ZrH_2(HAl^iBu_2)(ClAl^iBu_2)_2$ under these condition is similar to those reported previously.[25] The key ^1H NMR signals for $Cp^b{}_2ZrH_2(HAl^iBu_2)(Al^iBu_3)$ are 6.24, 5.78, 5.73, and 5.68 ppm for the Cp-H, indicating C_s symmetry and at 0.98, -1.32, and -1.72 ppm for the bridging Zr-H-Al.

Scheme 5.3.3. Reaction of **1** with 12 equivalents of TIBA (**1**/TIBA)

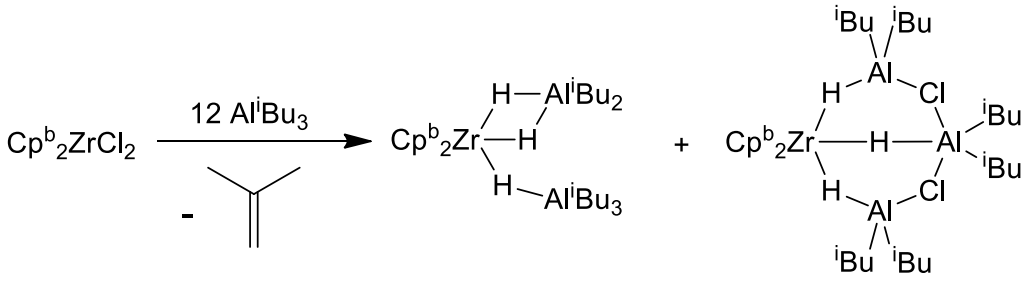

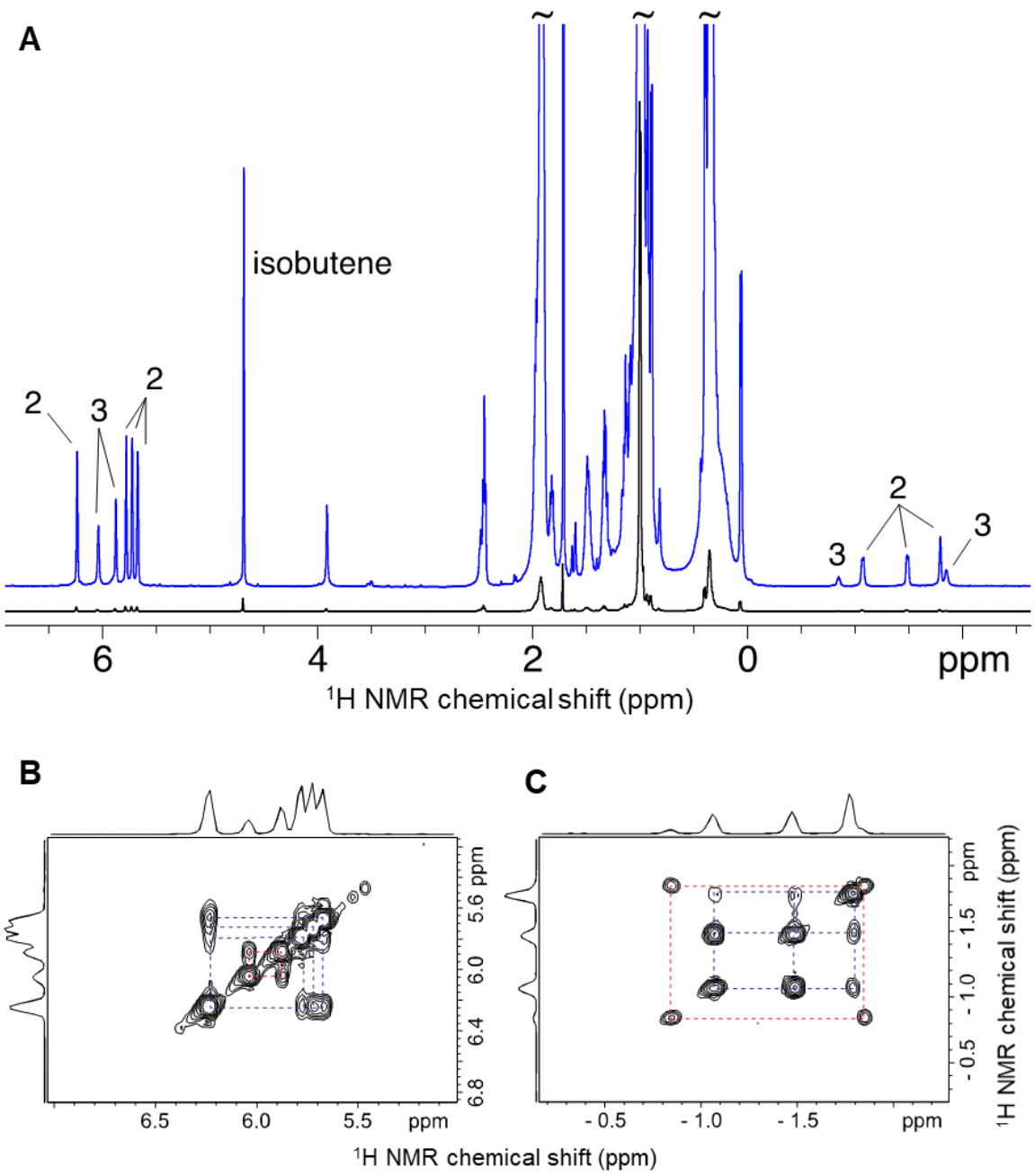

Figure 5.3.1. NMR spectra of **1**/TIBA in methylcyclohexane-*d14* at -40 °C: A) ^{1}H NMR spectrum (black), 10 X zoom (blue); B and C) zoom in on the Cp-H and Zr-H-Al regions of the ^{1}H-^{1}H COSY NMR spectrum (full spectrum in the Materials and methods section).

$Cp^b_2ZrH_2(HAl^iBu_2)(Al^iBu_3)$ was synthesized independently in solution from $[Cp^b_2ZrH_2]_2$ (**4**) in the presence of two equivalents of AlH^iBu_2 and two equivalents of TIBA, resulting in the formation of **2** (Scheme 5.3.4). The ^1H NMR spectrum of **2** (generated in-situ from **4**, Al^iBu_2H and Al^iBu_3) in methylcyclohexane-*d14* at -40 °C is shown in Figure 5.3.2 and are consistent with the assignments for **2** in **1**/TIBA.

Scheme 5.3.4. Formation of **2**

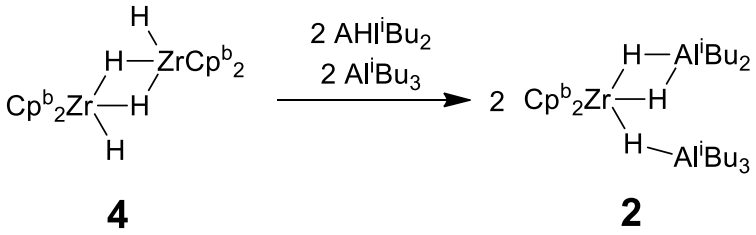

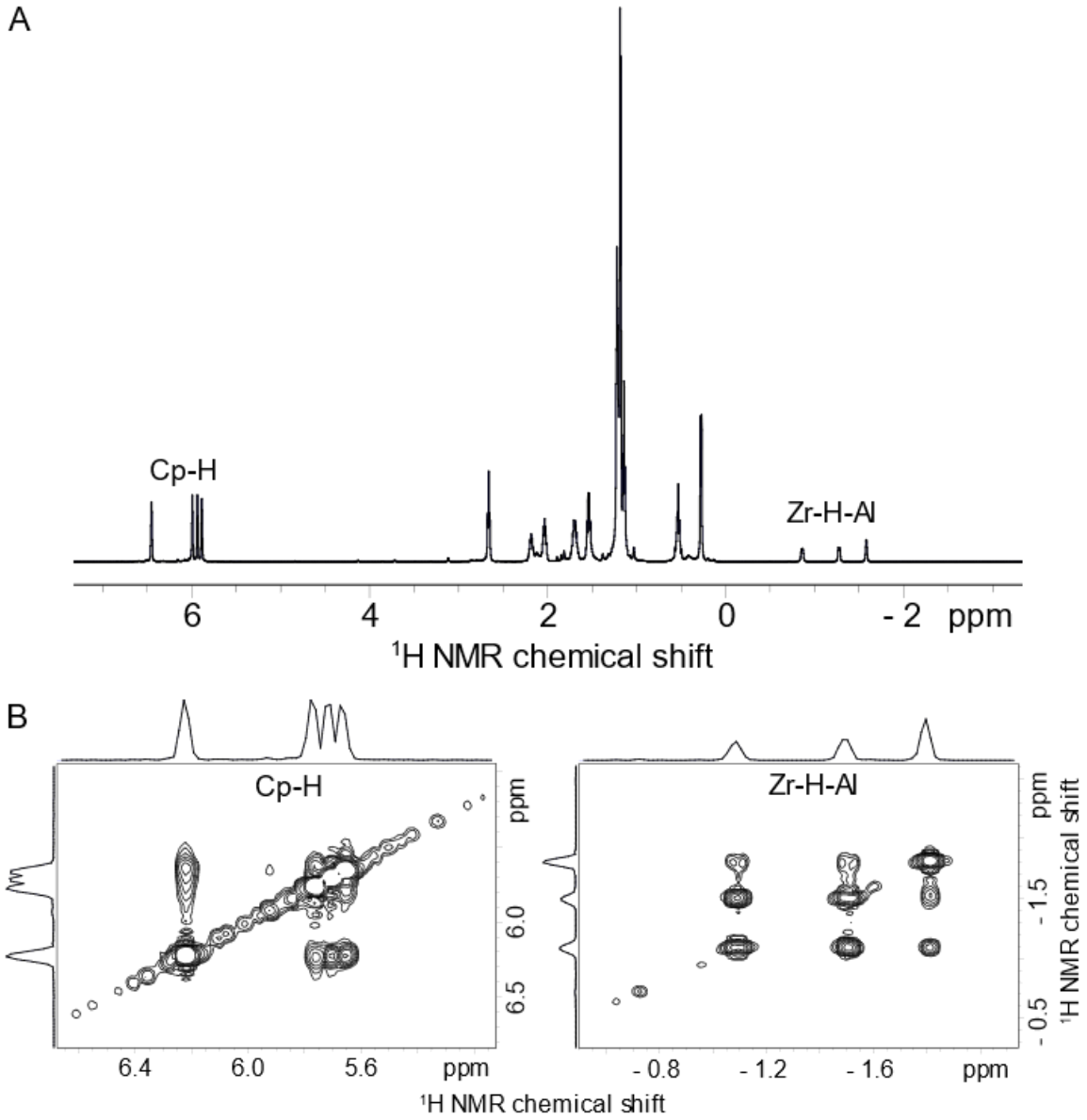

Figure 5.3.2. NMR spectra of **2** in methylcyclohexane-*d14* at -40 °C: A) ^{1}H; and B) zoom in on the Cp-H and Zr-H-Al portions of the ^{1}H-^{1}H COSY (full spectrum in the Materials and methods section).

1/TIBA (Zr:Al = 1:12) contains a 4:1 ratio of **2**:**3** at -40 °C in methylcyclohexane-d_{14}. Warming a cyclohexane-d_{12} solution of this mixture to 10 °C shows that the ratio of **2**:**3** increases to ~9:1. This result indicates that at higher temperatures, **1**/TIBA mixtures

(Zr:Al = 1:12) favor formation of **2**. The ratio of **2**:**3** at room temperature is difficult to measure due to the broad ^{1}H NMR line shapes of this mixture. The ratio of **2**:**3** formed in this reaction is dependent on the reaction stoichiometry. **1** reacts with 7 equivalents of TIBA to form a 3:2 mixture of **2**:**3** from ^{1}H NMR measurements in toluene-*d*$_8$ ate -40 °C. Decreasing the Zr/Al stoichiometry to two results in incomplete conversion of **1** and a 1:1 ratio of **2**:**3** in ~20 % yield of each product. This reaction also forms an unidentified zirconocene product tentatively assigned to Cp^b_2ZrHCl or $Cp^b_2Zr^iBuCl$ in 20 % yield.

The fast reaction between **1** and TIBA is rationalized based on the steps shown in Scheme 5.3.5. A Zr-Cl in **1** exchanges with an Al-^{i}Bu group to form $ClAl^iBu_2$ and Zr-^{i}Bu that undergoes β-H elimination to form Zr-H and isobutene. At high TIBA concentrations this reaction is exhaustive, eventually resulting in the formation of a $Cp^b_2ZrH_2$ intermediate, which is trapped by excess TIBA and HAl^iBu_2. The formation of HAl^iBu_2 probably results from reactions of Zr-H intermediates with $ClAl^iBu_2$ that forms in this reaction, or from thermal decomposition of TIBA under the reaction conditions.[34]

Scheme 5.3.5. Proposed reaction pathways for the formation of **2** and **3**

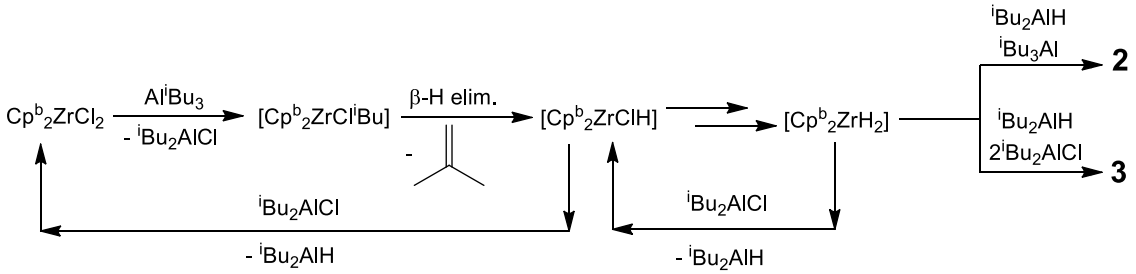

*5.3.3 Generation of TIBA/Alumina (**TA**)*

TIBA reacts with oxides rapidly with -OH groups on oxide surfaces. Previous studies showed that partially dehydroxylated silica forms different surface species depending on the conditions of the reaction. In hexane or pentane slurries, silica reacts with TIBA to form mixed species that open siloxane bridges and embed the aluminum into the silica framework (Scheme 5.3.6).[35,36] However, if the reaction is performed in diethyl ether, well-defined (≡SiO)-Al^{i}Bu(OEt$_2$) forms. This reaction occurs by protonolysis of one Al-^{i}Bu in TIBA by surface silanols to form isobutane, followed by alkyl transfer to the surface to form the product (Scheme 5.3.6).[36,37]

Scheme 5.3.6. Reactions of TIBA with silica in hexane or Et$_2$O

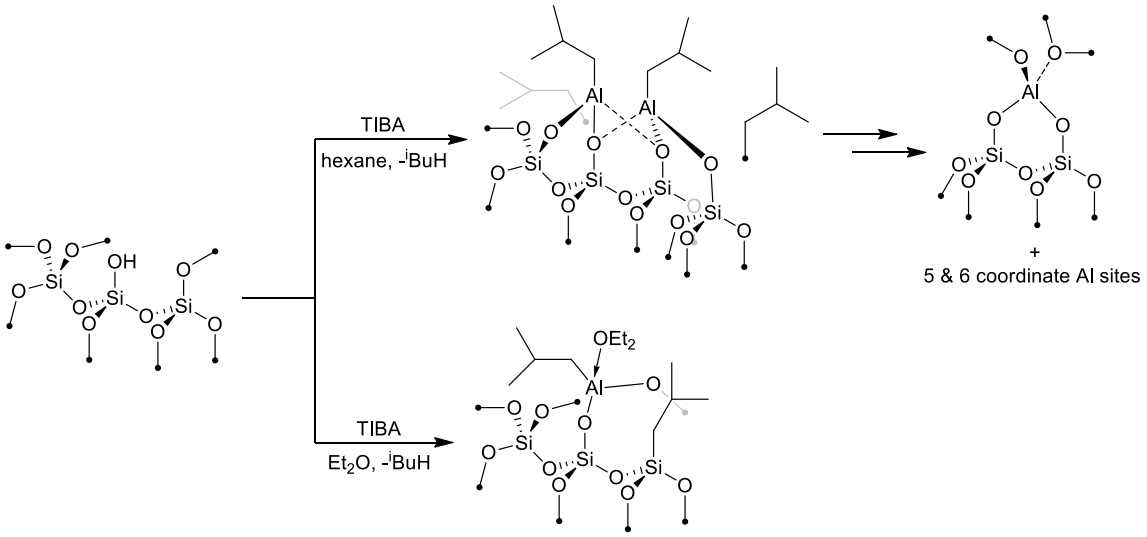

Alumina treated at 600 °C ($Al_2O_{3\text{-}600}$) contacted with excess MeMgBr contains 0.93 mmol g^{-1} of -OH sites from quantification of methane (chapter 3). A typical $Cp^{b}_2ZrCl_2$/TIBA/$Al_2O_{3\text{-}600}$ catalyst mixture (Zr:Al = 12) contains ~2 equivalents of TIBA

per surface -OH group. In pentane, a mixture of $Al_2O_{3\text{-}600}$ and two equivalents of TIBA forms 0.56 mmol g^{-1} of isobutane and 0.054 mmol g^{-1} of isobutene, indicating that ~60 % of the -OH groups on alumina react with TIBA (Scheme 5.3.7). The material (**TA**) formed during this reaction contains surface ≡AlO-Al(R_2)-O(Al≡)$_2$ sites, where R is an ^{i}Bu or H. The static $^{1}H \rightarrow ^{27}Al$ CP NMR spectrum of this material contains one signal at 58 ppm with a quadrupolar coupling constant (C_Q) of 8.8 MHz (Figure 5.3.3A). A ^{1}H-^{27}Al DHMQC experiment correlates ^{1}H and ^{27}Al nuclei through space (dipolar), indicating that only signals for aluminum and protons close to one another will be detected in this experiment. The results of this experiment are shown in Figure 5.3.3B, and show that the ^{27}Al signal in the static 1D CP NMR spectrum correlates to protons at 0.8 ppm, which is the expected for ^{1}H NMR chemical shift of Al–CH_2 group. Extracting a 1D slice from this experiment, and simulation of the NMR parameters also agree with the static 1D ^{27}Al NMR experiment. The chemical shift and small C_Q value for **TA** are consistent with a high symmetry organoaluminum surface species, shown as a tetrahedral site in Scheme 5.3.7.

Scheme 5.3.7. Synthesis of **TA** (R = H or ^{i}Bu)

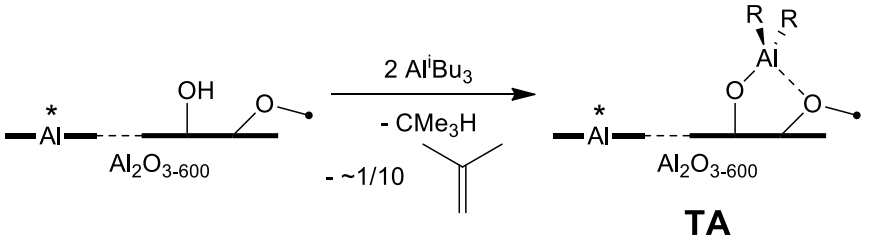

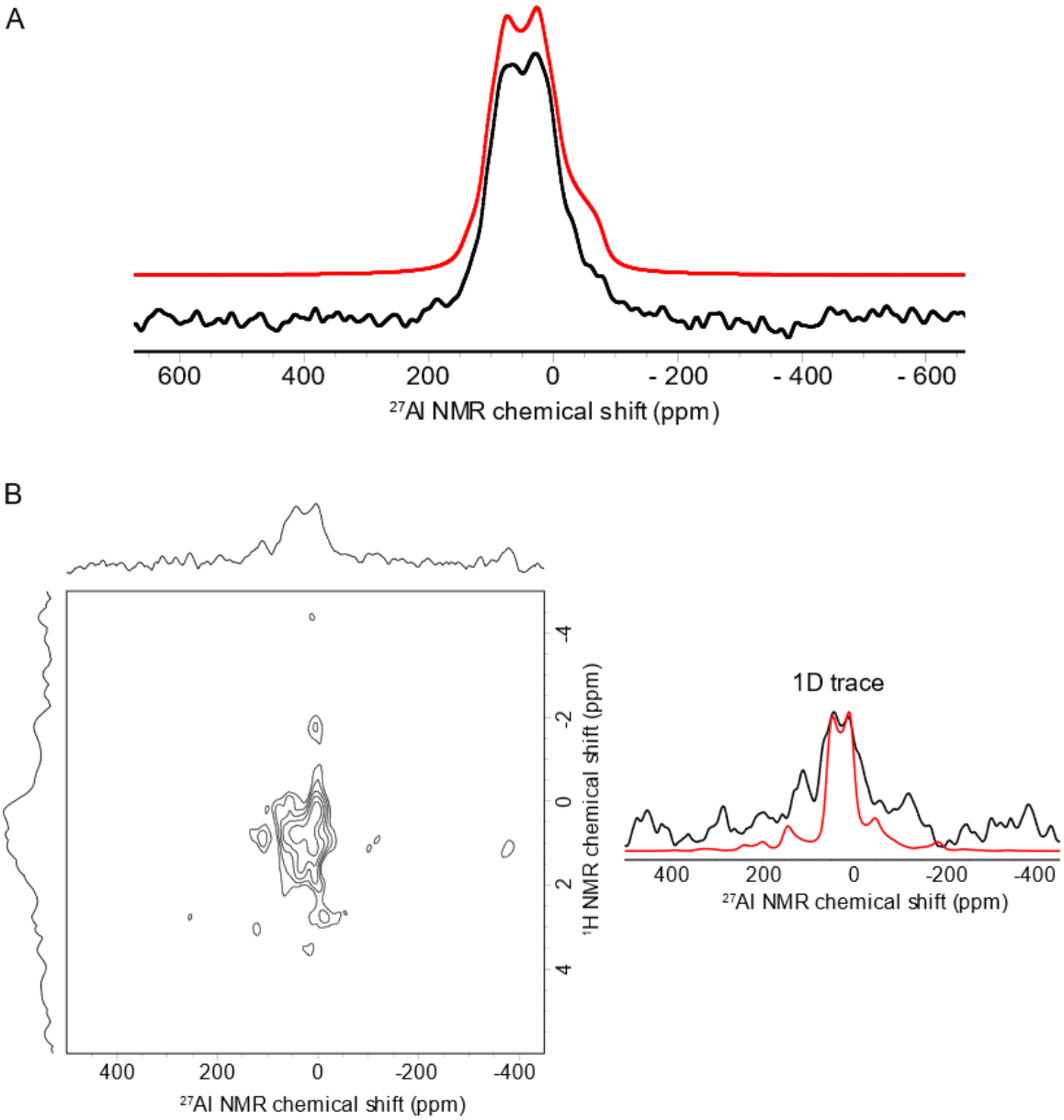

Figure 5.3.3. A) static $^{1}H \rightarrow ^{27}Al$ CP NMR spectrum of **TA** (experimental = black, red = simulation); and B) MAS 2D ^{1}H-^{27}Al DHMQC of **TA**, ^{27}Al trace with simulation (red) shown on the right.

5.3.4 Polymerization of ethylene

Table 5.1 contains a summary of the polymerization of ethylene with various combinations of zirconium precursors, TIBA, and alumina (Scheme 5.3.8). **1**/TIBA/$Al_2O_{3\text{-}600}$, formed *in-situ* by mixing TIBA with **1** followed by $Al_2O_{3\text{-}600}$, forms 58 g of polyethylene per gram of $Al_2O_{3\text{-}600}$ (entry 1). The polymer has a high molecular weight of 90.8 kg mol^{-1} and a polydispersity of 4.25. Polymerization with **1**/TIBA in the presence of **TA** shows similar activity and produces polymer with a similar M_n and polydispersity (entry 2), suggesting **TA** is an important component in this catalyst.

Scheme 5.3.8. Polymerization of ethylene

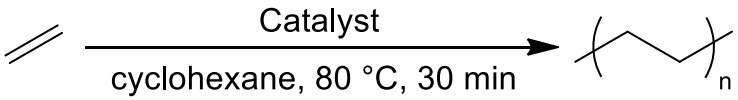

Table 5.1. Polymerization of ethylene activities.[a]

Entry	Solid material	*in-situ* precursor[b]	Zr loading[c]	Activity ($g_{PE}\ g_{cat}^{-1}\ h^{-1}$)	Mn[d]	Đ[d]
1	$Al_2O_{3\text{-}600}$	**1**/TIBA	150	58	90.8	4.25
2	**TA**	**1**/TIBA	150	46	73.3	4.13
3	**1/TA**	---	N.D.	0.1	N.D.	N.D.
4	**1/TA**	TIBA	N.D.	1	23.3	67
5	**ZH2A**	---	98.9	trace[e]	N.D.	N.D.
6	**ZH1TA**	---	0.65	55	160.7	2.37
7	**ZH2TA**	---	7.6	92	145.7	2.75
8	**ZH3TA**	---	0.33	37	189.5	2.55
9	**TA**	**3**	150	trace[e]	N.D.	N.D.
10	---	**1**/TIBA	150	0.0	---	---
11	---	**4**/TIBA	150	0.0	---	---
12	---	**2**	150	0.0	---	---

a.) 10-20 mg solid material, cyclohexane (2 mL), 300 psi ethylene provided on demand at 80 °C, activities are reported as averages of 2 runs; b.) *in-situ* during the polymerization (12 equivalents of TIBA/Zr where indicated); c.) μmol g^{-1}; d.) determined by GPC in trichlorobenzene at 150 °C (Mn = kg mol^{-1}); and e.) less than 0.1 $g_{PE}\ g_{cat}^{-1}\ h^{-1}$.

Contacting **TA** with **1**, followed by successive washings with pentane to remove excess **1** forming **1/TA**, is essentially inactive in the ethylene polymerization (0.1 $g_{PE}\ g_{cat}^{-1}\ h^{-1}$, entry 3). This result indicates that **TA** is not capable of activating **1** to form active catalysts. The addition of excess TIBA to **1/TA** during ethylene polymerization results in low activity (1 $g_{PE}\ g_{cat}^{-1}\ h^{-1}$, entry 4), and the polymer has a very broad molecular weight

distribution (D = 67) indicative of multi-site behavior. These results indicate that formation the of Zr-H species discussed above are important in forming the active site in this catalyst. $[Cp^b_2ZrH_2]_2$ reacts with Al_2O_3-$_{600}$ to form **ZH2A** (Scheme 5.3.9, see experimental section for characterization). **ZH2A** contains 99 μmol g^{-1} of zirconium, corresponding to ~ 10 % of the -OH loading on Al_2O_{3-600}, but also produces only a trace amounts of polymer (entry 5). This result indicates that reaction of Zr-H with -OH groups on alumina is not a productive path to form active sites in this catalyst.

Scheme 5.3.9. Reaction of **4** with Al_2O_{3-600}

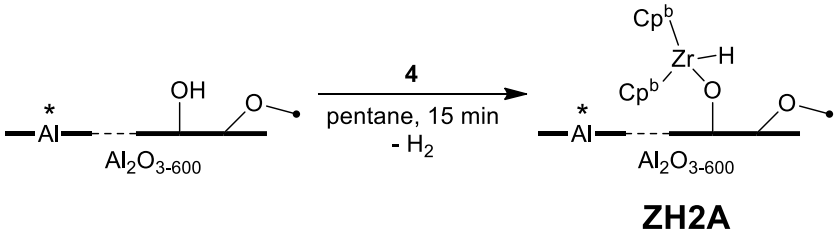

ZH2A

The polymerization results thus far suggest that **2** or **3** react with **TA** to form active sites in **1**/TIBA/Al_2O_{3-600}. **1**/TIBA contains at > 9:1 mixture of **2**:**3** at room temperature and reacts with **TA** to form **ZH1TA** after successive pentane washings to remove excess TIBA, $ClAl^iBu_2$, and zirconium from the material. Elemental analysis of **ZH1TA** reveals that the material contains 0.65 μmol g^{-1} of zirconium, a far lower loading than **ZH2A**, corresponding to ~0.0014 Zr-H sites nm^{-2}. This value is far lower than the ~ 1.2 ≡AlO-Al(R_2)-O(Al≡)$_2$ sites nm^{-2}, corresponding to a rough Zr:Al surface coverage of ~1:860. **ZH1TA** produces polymer with a similar activity a **1**/TIBA/Al_2O_{3-600} (55 g_{PE} g_{cat}^{-1} h^{-1}), but with narrow a polymer dispersity (Đ) of 2.37 (entry 6), indicating that **ZH1TA** is a single-

site catalyst. Polymerizations with **ZH1TA** do not contain excess TIBA, suggesting that the broader molecular weight distributions in **1**/TIBA/alumina are a result of chain transfer to aluminum during polymerization reactions.

4 reacts with **TA** to form **ZH2TA** and has a Zr loading of 7.6 μmol g^{-1}, corresponding to ~0.016 Zr-H sites nm^{-2} (Zr:Al surface coverage of 1:74). This is still significantly lower than the quantity of ≡AlO-Al(R_2)-O(Al≡)$_2$ sites, but ~ 12 times higher than the Zr loading of **ZH1TA**. **ZH2TA** exhibits the best activity per gram of material (92 g_{PE} g_{cat}^{-1} h^{-1}), produces polymer with an Mn of 145.7 kg mol^{-1} and a D of 2.75 (entry 7). *In-situ* generated **2** reacts with **TA** to form **ZH3TA**. Elemental analysis of **ZH3TA** shows that the Zr loading is the lowest of the model catalysts (0.0030 %, 0.33 μmol g^{-1}, ~0.0007 Zr-H sites nm^{-2}), corresponding to (Zr:Al surface coverage of 1:1700). **ZH3TA** has a lower activity per gram of material (37 g_{PE} g_{cat}^{-1} h^{-1}), attributed to the lower zirconium loading. However, **ZH3TA** produces polyethylene with the highest molecular weight (Mn = 189.5 kg mol^{-1}) with a polydispersity (2.55) similar to the polymer produced by **ZH1TA** (entry 8).

1/TIBA contains ~10 % **3** at 10 °C in cyclohexane-d_{12}. **1** reacts with 3 equivalents of HAliBu$_2$ to form **3** as the exclusive product in solution.[25] Mixtures of **TA** and **3** at typical [Zr] (1.5 mM) results in trace amounts of polymer (entry 9). Mixtures of zirconocene and alkylaluminums are generally not active in the absence of a support. The homogeneous mixtures zirconocene and alkylaluminum with compositions of **1**/TIBA, **4**/TIBA, and **2** do not initiate the polymerization of ethylene in the absence of a support (entries 10-12).

The polymerization data indicates that all three components in **1**/TIBA/$Al_2O_{3\text{-}600}$ are necessary for active site formation. Catalysts prepared from **2** and **TA** produce polymers with narrow molecular weight distributions that show the active species are nearly single site. The activities of these catalysts differ slightly, which is due to zirconium loading. Activities expressed from molar zirconium loading show that **ZH3TA** (5610 kg_{PE} mol_{Zr}^{-1} h^{-1} atm^{-1}) > **ZH1TA** (4230 kg_{PE} mol_{Zr}^{-1} h^{-1} atm^{-1}) > **ZH2TA** (605 kg_{PE} mol_{Zr}^{-1} h^{-1} atm^{-1}). These values are greater than the activity for **1**/TIBA/$Al_2O_{3\text{-}600}$ (19 kg_{PE} mol_{Zr}^{-1} h^{-1} atm^{-1}), and are close to activities for **1** activated with MAO (5330 kg_{PE} mol_{Zr}^{-1} h^{-1} atm^{-1}).[38]

These results relate to previous studies of organometallics with alumina. Cp_2ZrMe_2 to alumina partially dehydroxylated at 500 °C ($Al_2O_{3\text{-}500}$) to form neutral $Cp_2Zr(Me)\text{-}OAl\equiv$ and ionic $[Cp_2ZrMe][MeAl\equiv]$ surface species (Figure 5.3.4A).[32] This material polymerizes ethylene (3 kg_{PE} mol_{Zr}^{-1} h^{-1} atm^{-1}), but is far less active than **1**/TIBA/$Al_2O_{3\text{-}600}$ or Cp_2ZrMe_2 activated by MAO (1925 kg_{PE} mol_{Zr}^{-1} h^{-1} atm^{-1}) because the minor $[Cp_2ZrMe][MeAl\equiv]$ species is the active site in polymerization reactions.[33]

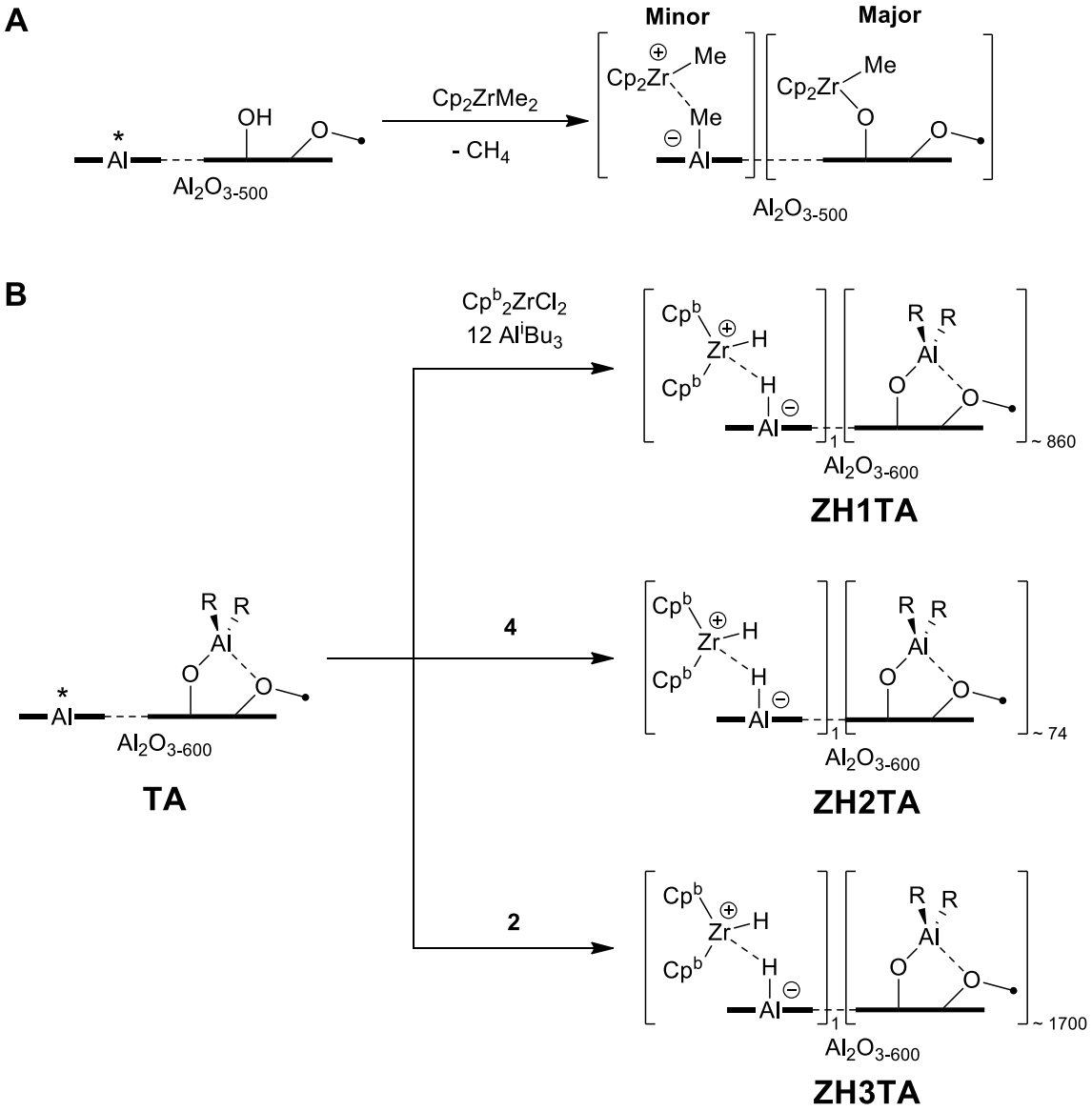

Figure 5.3.4. A) Reaction of Cp_2ZrMe_2 with $Al_2O_{3\text{-}500}$; and B) formation of **ZH1TA**, **ZH2TA**, and **ZH3TA**.

The difference in the catalyst **1**/TIBA/$Al_2O_{3\text{-}600}$ is that excess TIBA passivates -OH groups, preventing reactions of these sites with Zr-H species formed in solution. This results in very low Zr-loadings in the catalysts described here, but significantly higher polymerization activities. This result is clear from reactions of ≡AlO-Al(R_2)-O(Al≡)$_2$ sites

and **1**, which is inactive in polymerization, and by the negligible activity of $Cp^b_2Zr(H)$-OAl≡ in **ZH2A**. Taken together, these results suggest that Zr-H, **2** or **4**, react with **TA** to form $[Cp^b_2ZrH][HAl\equiv]$ (Figure 5.3.4B), and is the active site in **1**/TIBA/$Al_2O_{3\text{-}600}$.

5.3.5 Active site counting with cis-1,2-dichloroethylene

Vinyl halides (VX) react with cationic zirconocenes through olefin insertion and β-chloride elimination.[39–41] For example, [rac-(EBI)ZrMe][$MeBAr^F_3$] reacts with vinyl chloride (**VC**) forming [rac-(EBI)ZrCl][$MeBAr^F_3$] and propene (Figure 5.3.5A),[39,40] and Cp_2ZrHCl reacts with vinyl fluoride (**VF**) to form Cp_2ZrFCl and ethylene (Figure 5.3.5B).[41] Neutral zirconocenes are slower in these reactions than cationic zirconocenes. This reaction is an ideal active site probe because the product Zr-Cl cannot insert olefins and suggests that this reaction may be used to quantify active sites in **1**/TIBA/$Al_2O_{3\text{-}600}$.

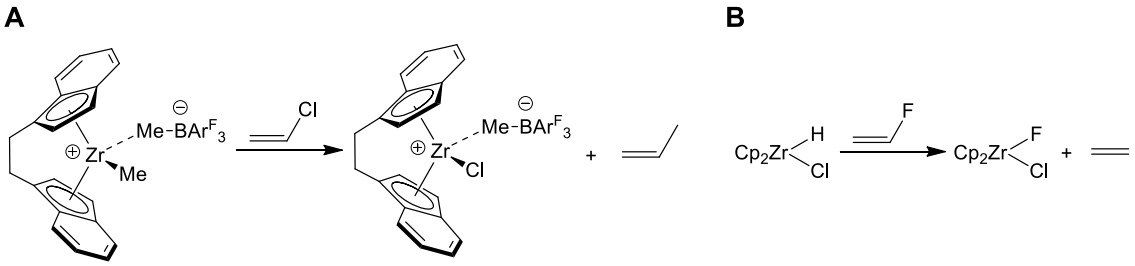

Figure 5.3.5. A) reaction of rac-(EBI)Zr$Me^+MeBAr^F_3{}^-$ with **VC**, and B) reaction of Cp_2ZrHCl with **VF**.

ZHITA reacts with *cis*-1,2-dichlorethylene (**VC2**) to form vinyl chloride (0.40 (1) μmol g^{-1}), ethylene (0.04 (1) μmol g^{-1}), isobutene (0.70 (1) μmol g^{-1}), and isobutane (8.8 (6) μmol g^{-1}). Isobutane and isobutene also from in reactions of **TA** with **VC2** in similar

yields, suggesting these products are likely a result of a background reaction. Vinyl chloride formation is a result of Zr-H species on the **TA** surface that form by olefin insertion of **VC2** and β-chloride elimination to form a Zr-Cl site (Scheme 5.3.10). The small amount of ethylene forms from reactions of a Zr-H with vinyl chloride. Chloro-methyl-pentene is not observed in this reaction, indicating that Zr-^{i}Bu^{+} are not present on **ZH1TA**.

Scheme 5.3.10. Reaction of surface Zr-H^{+} species with **VC2**

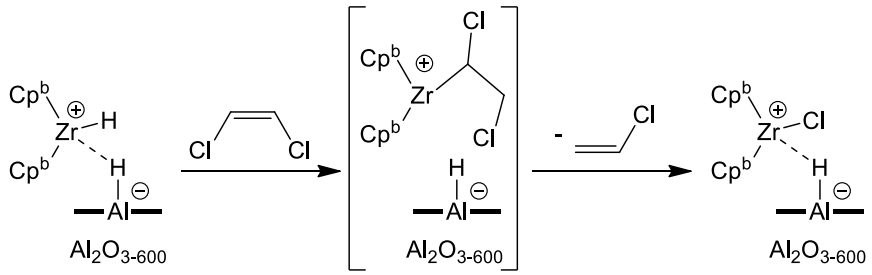

Table 5.2 contains volatile data for the reaction of **VC2** with the isolated materials. Unpassivated $Al_2O_{3\text{-}600}$ reacts with **VC2** to form significantly less vinyl chloride and ethylene (total 0.09 μmol g^{-1}, entry 1).[42] **TA** also forms **VC** (0.19 μmol/g), isobutene (1.7 μmol/g) and isobutene (11 μmol g^{-1}, entry 2). **ZH2TA** reacts with **VC2** to form 3.9 μmol g^{-1} of **VC** and ethylene (entry 4), significantly more than **ZH1TA** and **TA**. **ZH3TA** reacts with **VC2** to form 0.72 μmol g^{-1} of **VC** and ethylene (entry 5), which is higher than the Zr loading of **ZH3TA**. **ZH2A** produces 2.9 μmol g^{-1} of **VC** and ethylene (entry 6).

Table 5.2. Quantification of the products from the reaction of *cis*-1,2-dichloroethylene with the solid materials and catalysts.[a]

Entry	Material	Zr loading	Ethylene	**VC**[b]	Isobutene	Isobutane
1	$Al_2O_{3\text{-}600}$	---	0.07 (1)	0.02 (2)	---	---
2	**TA**	---	0.0	0.19 (5)	1.7 (3)	11 (2)
3	**ZH1TA**	0.65	0.04 (1)	0.40 (1)	0.70 (1)	8.8 (6)
4	**ZH2TA**	7.6	0.30 (1)	3.6 (1)	2.1 (1)	14 (3)
5	**ZH3TA**	0.33	0.02 (1)	0.70 (1)	1.8 (4)	16 (2)
6	**ZH2A**	98.9	0.10 (1)	2.8 (2)	---	---

a.) all values in μmol g^{-1}, errors shown in parentheses; and b.) **VC** = vinyl chloride.

Interpretation of the results in Table 5.2 are complicated by the cross reactivity of **VC2** with **TA** and $Al_2O_{3\text{-}600}$. Deuterium labeling can confirm how much **VC** and ethylene are produced by tracking D-labeled **VC** formed in this reaction. The reaction of $[Cp^b2ZrD_2]_2$ (>99 % D) with **TA** forms **ZD2TA**. The D-loading in **ZD2TA** is 62 % D, indicating that Zr-H/Zr-D exchange occurs during this reaction; the origin of this exchange is unclear. **ZD2TA** reacts with **VC2** to form *cis*-D-vinylchloride, *trans*-D-vinylchloride, unlabeled vinyl chloride and ethylene (Scheme 5.3.11). An expansion of the olefinic region of the ^{1}H NMR spectrum of the reaction products is shown in Figure 5.3.6. Based on the relative ^{1}H NMR integrations the amount of deuterated vinyl chloride generated in this reaction is 1.8 μmol g^{-1} (recalculated from 1.1 μmol g^{-1} accounting for the 62 % D). Based

on the and the Zr loading and D-labelling efficiency in **ZD2TA**, 24% of the Zr-D^+ sites in **ZD2TA** are active in this reaction.

Scheme 5.3.11. Reaction of **ZD2TA** with **VC2**

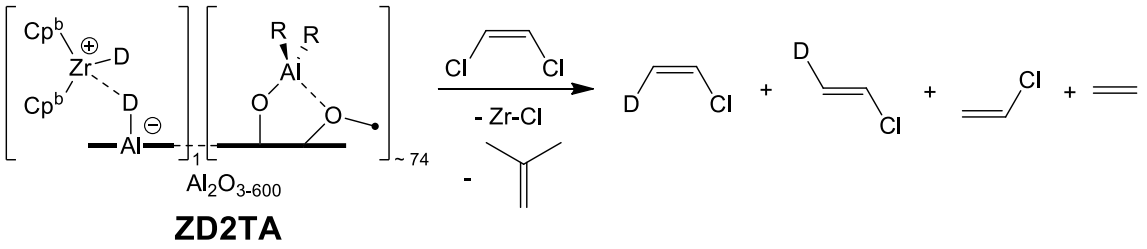

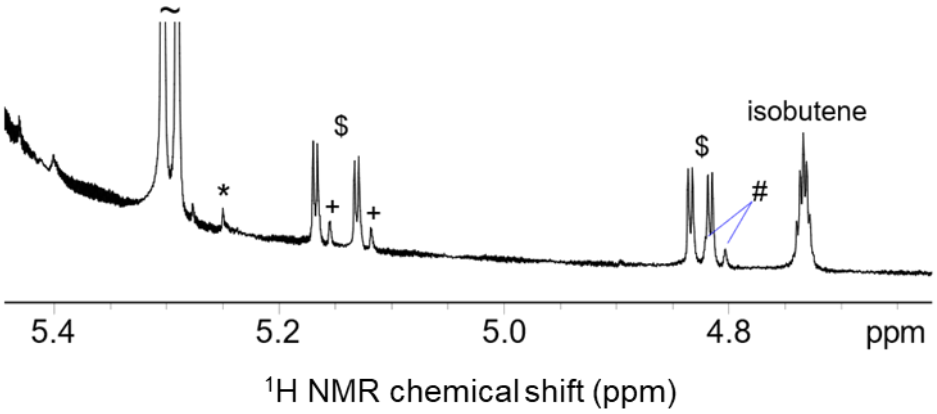

Figure 5.3.6. zoom in on the ^{1}H NMR spectrum of the volatiles from the reaction of **ZD2TA** with **VC2**. $ = **VC**, * = ethylene, + = *cis*-D-**VC**, and # = *trans*-D-**VC**. For full spectrum please refer to Figure 5.5.18 in the Materials and methods section of this chapter.

The formation of unlabeled **VC** and isobutene in this reaction can be rationalized by the steps shown in Scheme 5.3.12. Insertion of **VC2** into the Zr-D^+, followed by β-chloride elimination forms deuterated **VC** and a Zr-Cl^+. As mentioned above, ~74 ≡AlO-Al(R_2)-O(Al≡)$_2$ sites are present per Zr site. Alkylation of the Zr-Cl^+ with a nearby ≡AlO-

$Al(R_2)$-$O(Al\equiv)_2$ would form a Zr-$^{i}Bu^{+}$, that following β-H elimination would form a new Zr-H^{+} that can insert **VC2** and eliminate unlabeled **VC**. This would result in an expected ratio of unlabeled **VC**:isobutene of 1:1, experimental ratio of 1.3:1. The experimental ratio is 1:1 when corrected for the 62 % D-labeling in **ZD2TA**.

Scheme 5.3.12. Reaction of **VC2** with **ZD2TA** and regeneration by a nearby Al-^{i}Bu

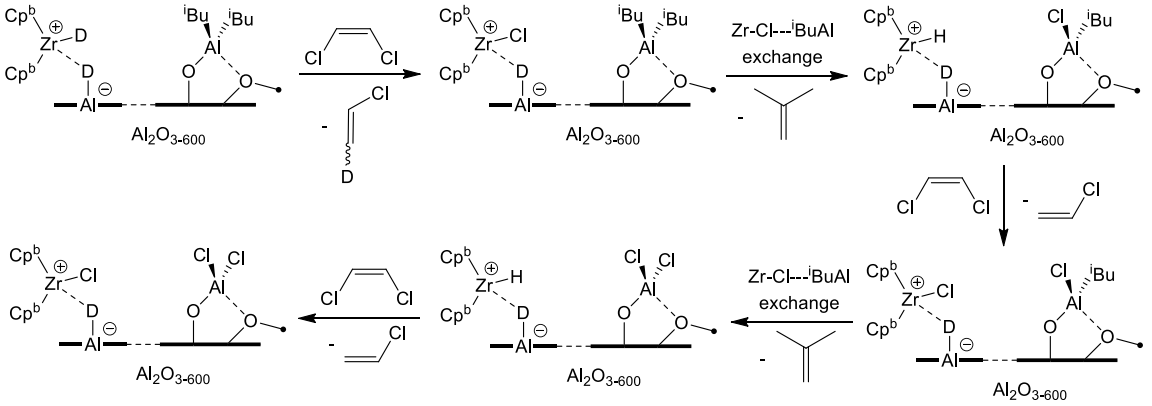

5.3.6 Characterization of the active site

The FT-IR spectra of **TA, ZH1TA**, **ZH2TA**, and **ZH3TA** are shown in Figure 5.3.7, and are essentially identical. The solid-state ^{13}C CP-MAS NMR spectra are also essentially identical, except for **ZH2TA** that contains weak broad signals for Cp carbons and a signal at 12 ppm assigned to the methyl end group of the Cp^{b} ligand (Figure 5.3.8). These results are not surprising because of the very high surface coverage of ≡AlO-$Al(R_2)$-$O(Al\equiv)_2$ groups relative to Zr from elemental analysis data.

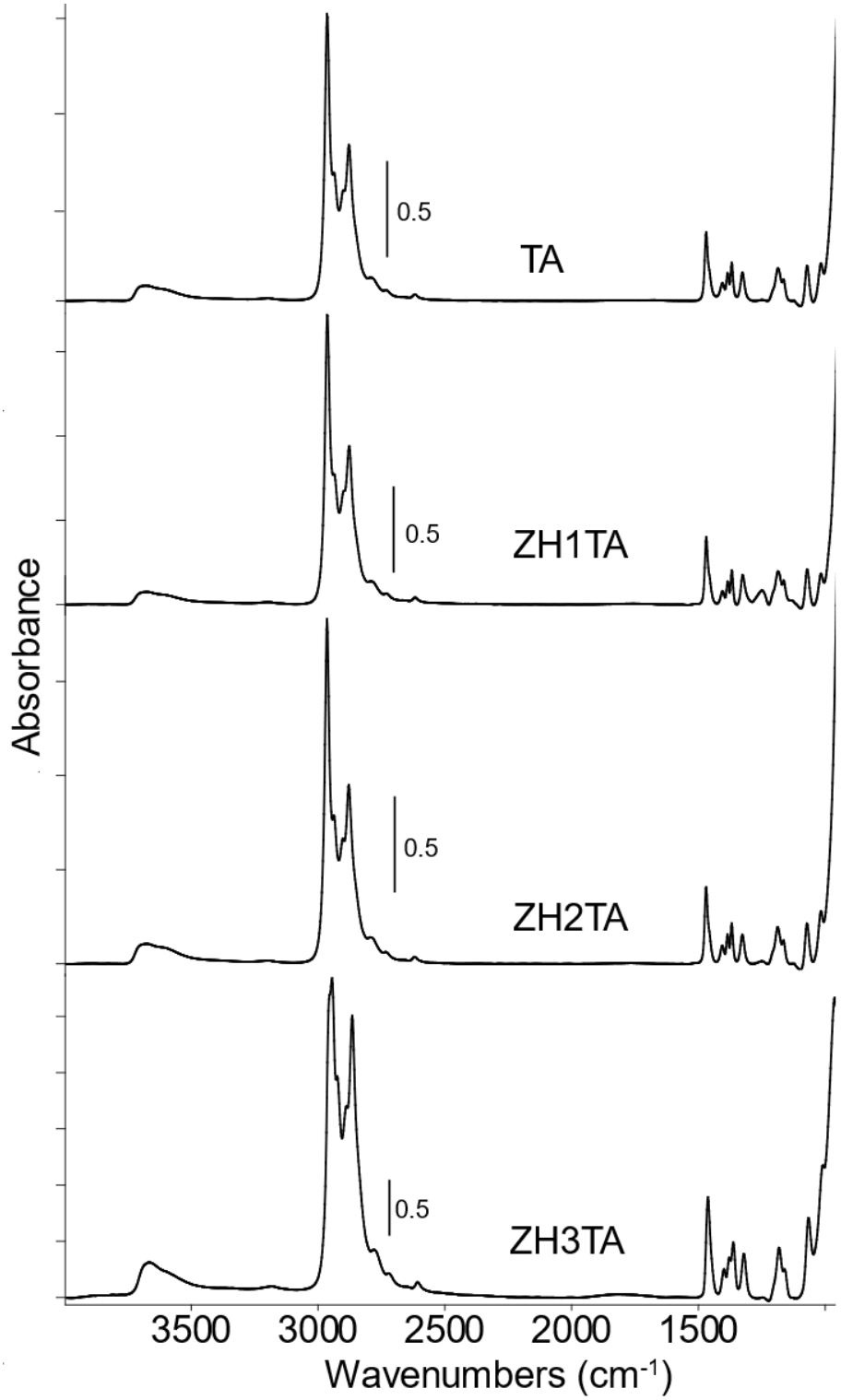

Figure 5.3.7. FT-IR spectra of **TA**, **ZH1TA**, **ZH2TA**, and **ZH3TA**.

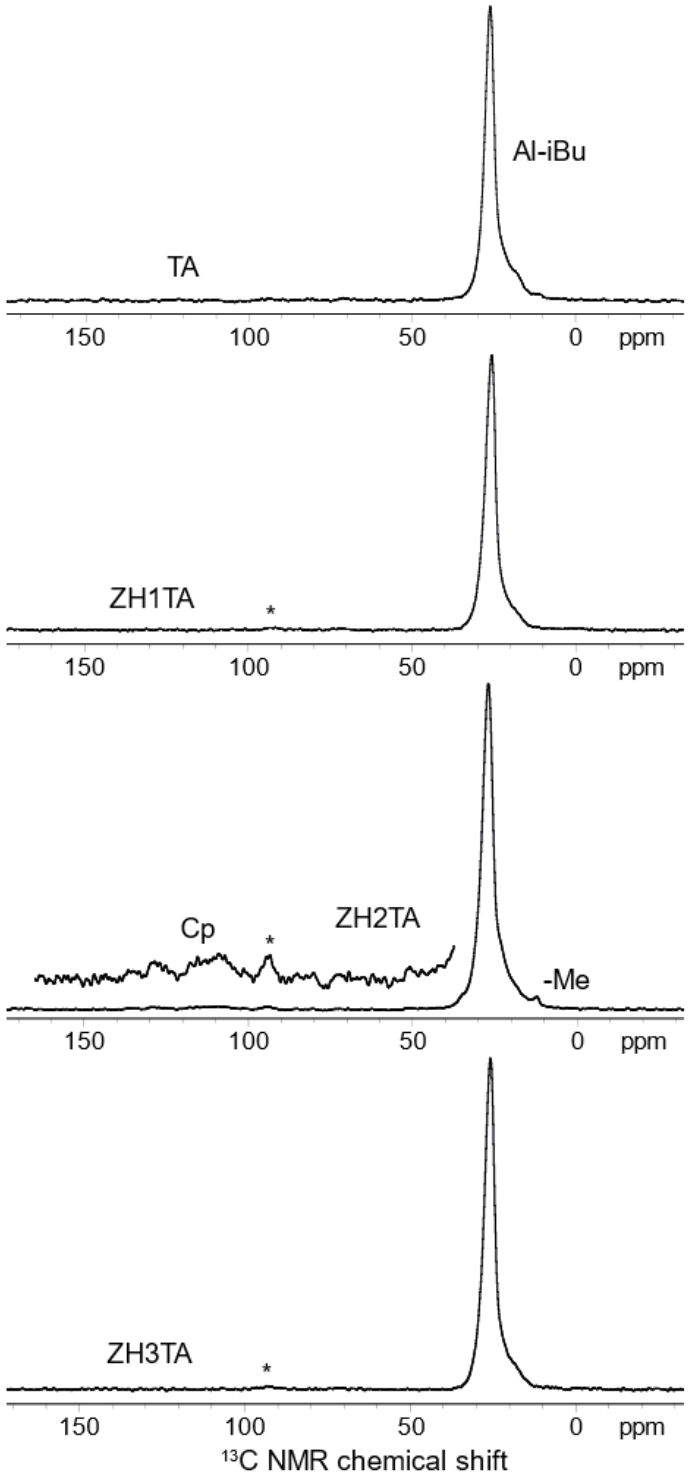

Figure 5.3.8. Solid-state ^{13}C CP-MAS NMR spectra of **TA**, **ZH1TA**, **ZH2TA**, and **ZH3TA** (* = spinning sideband).

The detection of the Zr-H^+ by solid-state ^{1}H NMR spectroscopy would be ideal but challenging. Dipolar ^{1}H-^{1}H coupling is large (~111 kHz), which broadens ^{1}H NMR signals. For these catalysts, the situation is further complicated by the very low surface coverage of Zr-H compared to ≡AlO-Al(R_2)-O(Al≡)$_2$. Therefore, the only signals observed spinning at 10 kHz are the Al-^{i}Bu protons (shown in the Materials and methods). Faster spinning speeds (50 kHz) are similarly uninformative.

*5.3.7 Solid State ^{2}H NMR studies of **ZD2TA** and relationship to molecular Zr-D complexes*

Deuterium is quadrupolar (spin = 1). Solid-state NMR of quadrupolar nuclei spectra are characterized by broad powder patterns that are affected by the symmetry and electronic structure of the ^{2}H nucleus. The shape of the NMR powder pattern is defined by the interaction of the nuclear electric quadrupole moment (eQ), and the electric field gradient (EFG) tensor V (equation 5.3.1). The three principal components of the EFG tensor are V_{33}, V_{22}, and V_{11}. V_{33} is the largest component followed by V_{22}, and V_{11}. The two parameters that can be measured by solid-state NMR are the quadrupolar coupling constant (C_Q) and the asymmetry parameter (η). The C_Q is defined by equation 5.3.2, where e is the fundamental charge, Q is the nuclear quadrupole moment, and h is Plank's constant. The asymmetry parameter (η) is defined by equation 5.3.3 and is between 0 and 1. The C_Q affects the overall linewidth, and can span several hundred kHz of spectral width, and η affects the shape of the signal.

Equation 5.3.1.

$$\boldsymbol{V} = \begin{vmatrix} V_{11} & 0 & 0 \\ 0 & V_{22} & 0 \\ 0 & 0 & V_{33} \end{vmatrix}$$

Equation 5.3.2.

$$C_Q = \frac{e^2 Q V_{33}}{h}$$

Equation 5.3.3.

$$\eta = \frac{V_{11} - V_{22}}{V_{33}}$$

C_Q in ^{2}H NMR is sensitive to X-D bond length and the charge of X.[43] The higher the charge at X or the shorter the X-D bond length the larger the C_Q. For example, C_Q of ^{2}H ranges from 33 kHz for Li-D to 354 kHz for D-F.[43] The symmetry at ^{2}H affects η. Linear X-^{2}H fragments have an η of 0.0, whereas nonlinear bridging X-^{2}H-X fragments have an η greater than zero. There are a limited number of metal deuterides that have been measured by solid-state ^{2}H NMR spectroscopy that have C_Q from 30 to 110 kHz, and follow trends in η mentioned above.[44–49] ^{2}H NMR in the solid state is also very sensitive to dynamics, which results in averaging of C_Q values.

Solid-state ^{2}H NMR experiments are performed under MAS or static conditions. An example of a static ^{2}H NMR spectrum of $[Cp_2ZrD_2]_2$ is shown in Figure 5.3.9.[45] This spectrum shows a typical ^{2}H NMR line shape. Static ^{2}H NMR experiments are plagued by

long acquisition times, for example the spectrum in Figure 5.3.9 took ~ 18 hours to collect (relaxation delay 20 s, 3286 scans). Under MAS conditions the signal narrows and the signal to noise increases, reducing the required acquisition period (for reference the spectra of the molecular complexes in this study took roughly 5-20 minutes to acquire). MAS produces spinning sidebands that dissipate from the isotropic signal, the intensity and shape of the spinning sidebands are sensitive to C_Q and η.

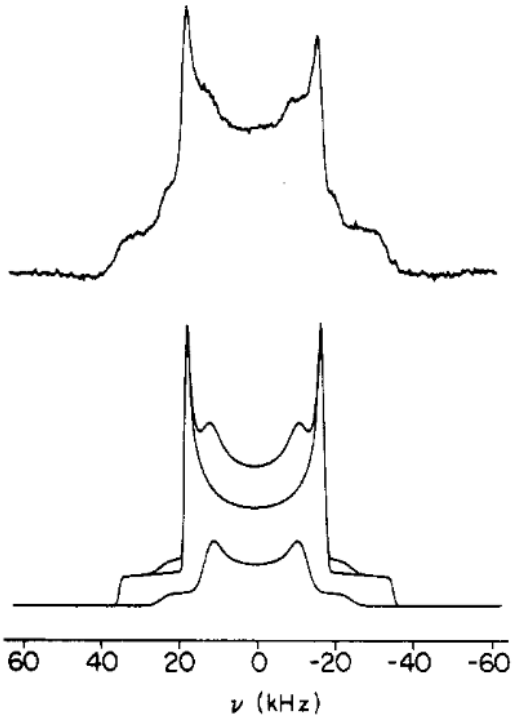

Figure 5.3.9. Static solid-state ^2H NMR of $[Cp_2ZrD_2]_2$ (top) and simulations (bottom). Reprinted (adapted) with permission from Inorganic Chemistry. Copyright (1987) American Chemical Society.[45]

Table 5.3 contains solid-state ^{2}H NMR parameters for several molecules and materials studied here. Li[DAl(O^{t}Bu)$_3$] is a molecular model for the proposed [D-Al≡] surface sites. The ^{2}H MAS NMR spectrum of Li[DAl(O^{t}Bu)$_3$] is shown in Figure 5.3.10A and contains a ^{2}H NMR signal at 4.1 with a C_Q of 61 kHz and an η of 0.0. $[Cp_2ZrD_2]_2$,[45] and $[Cp^b{}_2ZrD_2]_2$ contain bridging Zr-D-Zr and terminal Zr-D. For $[Cp_2ZrD_2]_2$, the Zr-D-Zr has a C_Q of 33 kHz and the Zr-D has a C_Q of 47 kHz (chemical shifts not reported, Figure 5.3.9).[45] The η for the terminal Zr-D is 0.0 but the bridged Zr-D-Zr is bent and has an η of 0.1, as expected based on the above discussion. The solid-state MAS ^{2}H spectrum of $[Cp^b{}_2ZrD_2]_2$ (**4D**) follows a similar trend; the terminal Zr-D has a C_Q of 50 kHz and an η of 0 and the Zr-D-Zr has a smaller C_Q of 44 kHz and an η of 0.3 (Figure 5.3.10B).

Table 5.3. ^{2}H solid state NMR simulation parameters.

Entry	Compound	^{2}H δ_{iso} (ppm)	C_Q (kHz)	η	Assignment
1	$LiAlD_4$[a]	---	72	N.A.	Al-D
2	$Li[DAl(OtBu)_3]$	4.1	61	0.0	Al-D
3	$[Cp_2ZrD_2]_2$[b]	---	33	0.1	Zr-D-Zr
		---	47	0.0	Zr-D
4	$[Cp^b{}_2ZrD_2]_2$	-3.3	44	0.3	Zr-D-Zr
		5.3	50	0.0	Zr-D
5	$Cp^*{}_2ZrD_2$	2.0	20	0.1	Cp-*Me*
		8.0	44	0.0	Zr-D
6	**ZD2A**	3.7	47	0.0	$Cp^b{}_2Zr(D)$-OAl≡
7	$[Cp^*{}_2ZrD][DB(C_6F_5)_3]$	1.0	21	0.0	Cp-*Me*
		4.0	116	0.2	B-D
		9.5	121	0.0	Zr-D
8	**ZD2TA**	2.0	30	0.1	Al-^{i}Bu[c]
		5.0	49	0.1	Zr-D or Al-D
		7.5	133	0.3	$[Cp^b{}_2ZrD][DAl≡]$

a.) From reference 44; b.) from reference 45; and c.) natural abundance from ≡AlO-Al(R_2)-O(Al≡)$_2$ (R = H or ^{i}Bu).

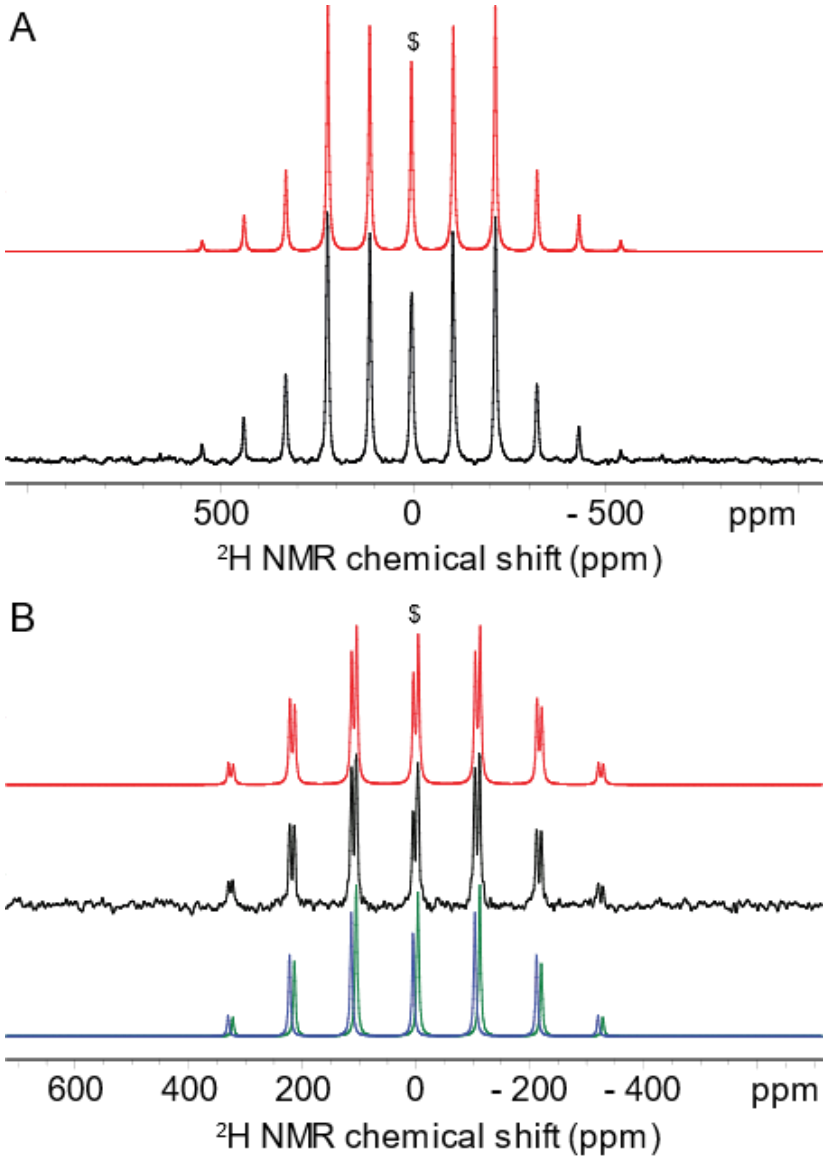

Figure 5.3.10. solid-state ^{2}H (92 MHz) NMR spectra spinning at 10 kHz: $ = isotropic chemical shift, black = experimental, red = simulated spectrum, and blue/green = separate site simulations. A) $LiAlD(O^{t}Bu)_3$; and B) **4D**.

$Cp^*_2ZrD_2$ is monomeric.[50] The ^2H MAS NMR spectrum of $Cp^*_2ZrD_2$ is shown in Figure 5.3.11A and contains a signal at 8.0 ppm for the Zr-D with a C_Q of 44 kHz. The η for this signal is zero, as expected for a terminal Zr-D. This spectrum also contains a signal at 2.0 ppm from partially deuterated Cp-*Me* that are a result of the synthesis of $Cp^*_2ZrD_2$ from $Cp^*_2ZrH_2$ and D_2. The partially deuterated Cp-*Me* have a C_Q of 20 kHz, much smaller than a static sp^3 hybridized C-D (~175 kHz) due to fast rotation of the C-C bond. The ^2H MAS NMR spectrum of **ZD2A**, prepared from the reaction of $[Cp^b_2ZrD_2]_2$ with $Al_2O_{3\text{-}600}$, contains a signal at 3.7 ppm, with a C_Q of 47 kHz and an η of 0.0, Figure 5.3.11B. These representative examples show that neutral zirconocene deuterides have C_Qs between ~ 33-50 kHz (entries 3-6).

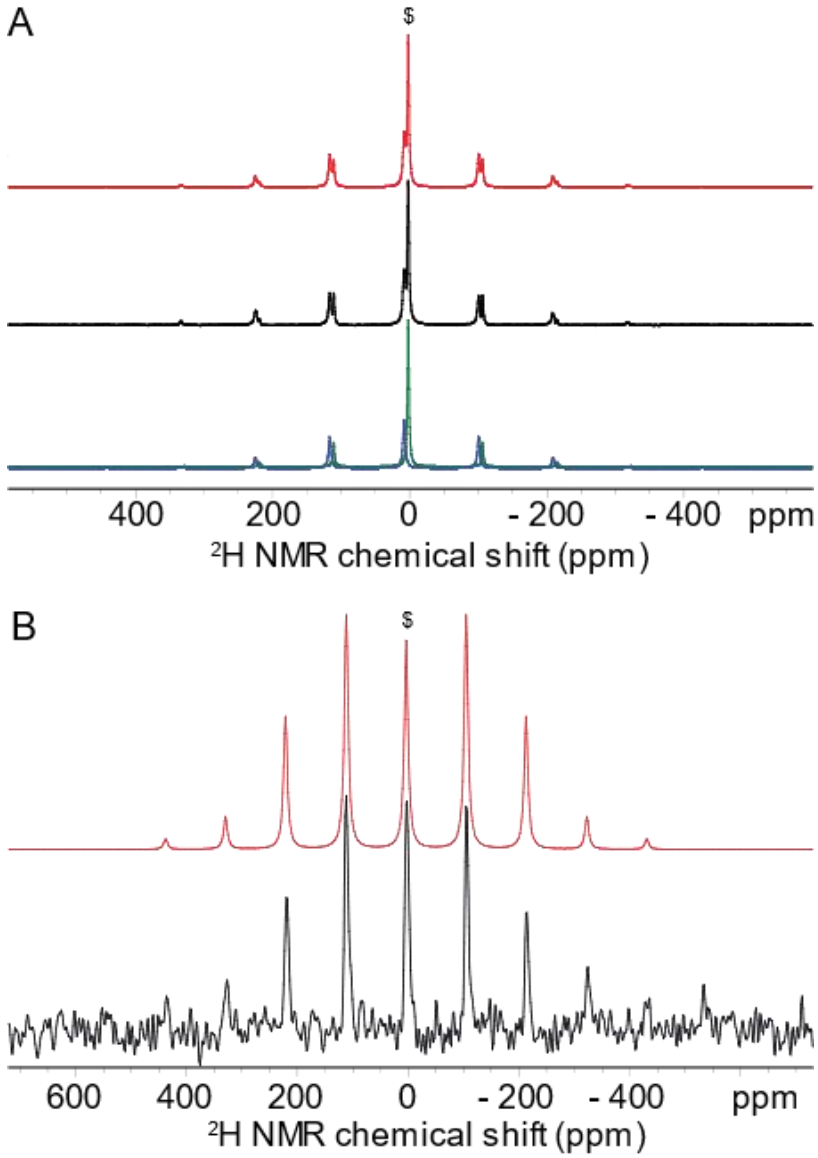

Figure 5.3.11. Solid-state ^{2}H (92 MHz) NMR spectra spinning at 10 kHz: $ = isotropic chemical shift, black = experimental, red = simulated spectrum, and blue/green = separate site simulations. A) $Cp^{*}_{2}ZrD_{2}$ (61 MHz); and B) **ZD2A**.

The arguments mentioned above indicate that Zr-D$^+$ cations will have larger C_Q than a neutral Zr-D species. [Cp$^*_2$ZrD][DB(C_6F_5)$_3$] was synthesized analogous to the synthesis of [Cp$^*_2$ZrH][HB(C_6F_5)$_3$].[51] The MAS ^{2}H NMR spectrum for [Cp$^*_2$ZrD][DB(C_6F_5)$_3$] contains three signals at 9.5, 4.0, and 1.0 ppm for the Zr-D, B-D, and C-D respectively (Figure 5.3.12). The C-D has a C_Q of 21 which is essentially the same as for Cp$^*_2$ZrD$_2$. The B-D has a C_Q of 116 kHz, similar to the Cq for D$_3$B-NMe$_3$ (105 kHz).[43] The Zr-D has a C_Q of 121 kHz and an η of 0.0. The C_Q is significantly larger than the C_Q for the neutral Zr-D complexes (33-50 kHz).

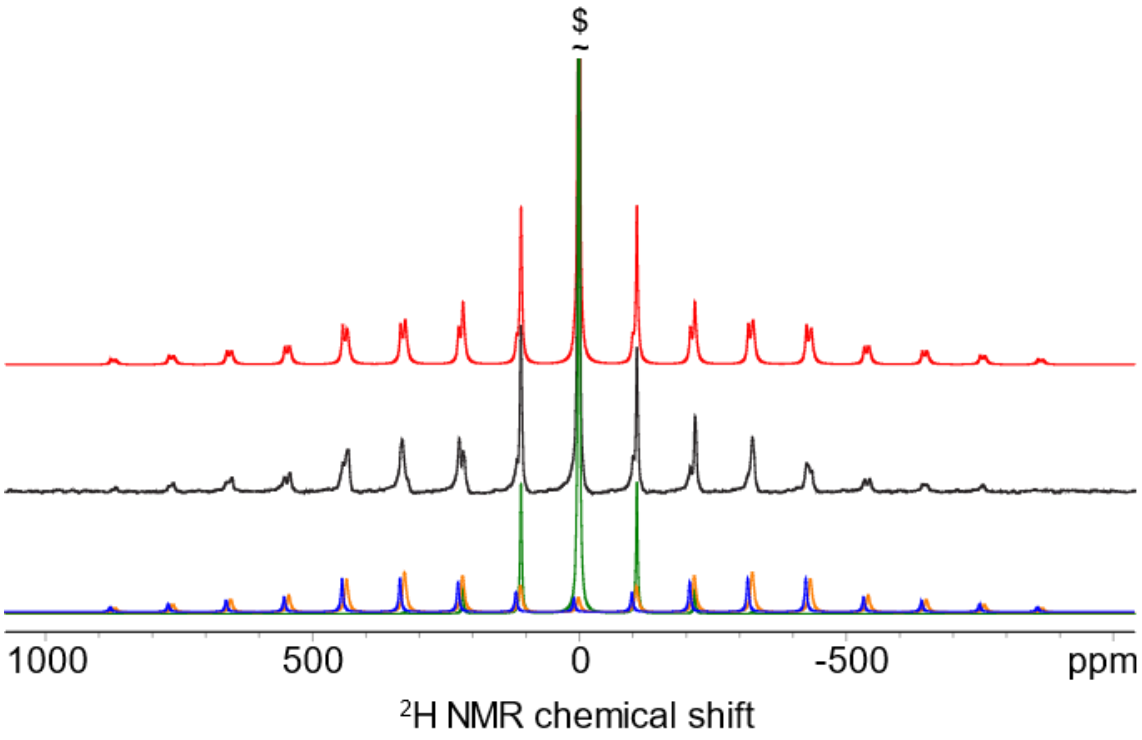

Figure 5.3.12. ^{2}H solid state NMR of [Cp*$_2$ZrD][DB(C_6F_5)$_3$] spinning at 10kHz, $ = isotropic chemical shift, Black = experimental, red = total simulation, and orange/blue/green = individual site simulations spectra.

The solid-state ^{2}H NMR spectrum of **ZD2TA** is shown in Figure 5.3.13. The spectrum contains three signals at 7.5 (major), 5.0 (minor), and 2.0 ppm. The signal at 2.0 ppm is relatively narrow, has a C_Q of 30 kHz and is assigned to dynamic natural abundance ^{2}H in ≡AlO-Al(R_2)-O(Al≡)$_2$. The low intensity signal at 5.0 ppm has a C_Q of 49 kHz and is either a neutral $Cp^b{}_2$Zr(D)-OAl≡ or surface Al-D species. The broad signal at 7.5 ppm is assigned to [$Cp^b{}_2$ZrD][DAl≡] and has a C_Q of 133 kHz with an η of 0.3. The large C_Q is similar to the C_Q of [$Cp^*{}_2$ZrD][DB(C_6F_5)$_3$] (121 kHz for Zr-D) which supports the assignment of a $Cp^b{}_2ZrD^+$ cationic species. However, η is 0.3 suggesting that the Zr-D is bridging with aluminum, such as the Zr-D-Al^+ site shown in Scheme 5.3.13. The ^{2}H MAS NMR also lacks a signal for the ≡Al-D^- anion, expected to have a C_Q similar to Li[DAl(O^tBu)$_3$] (61 kHz, entry 2).

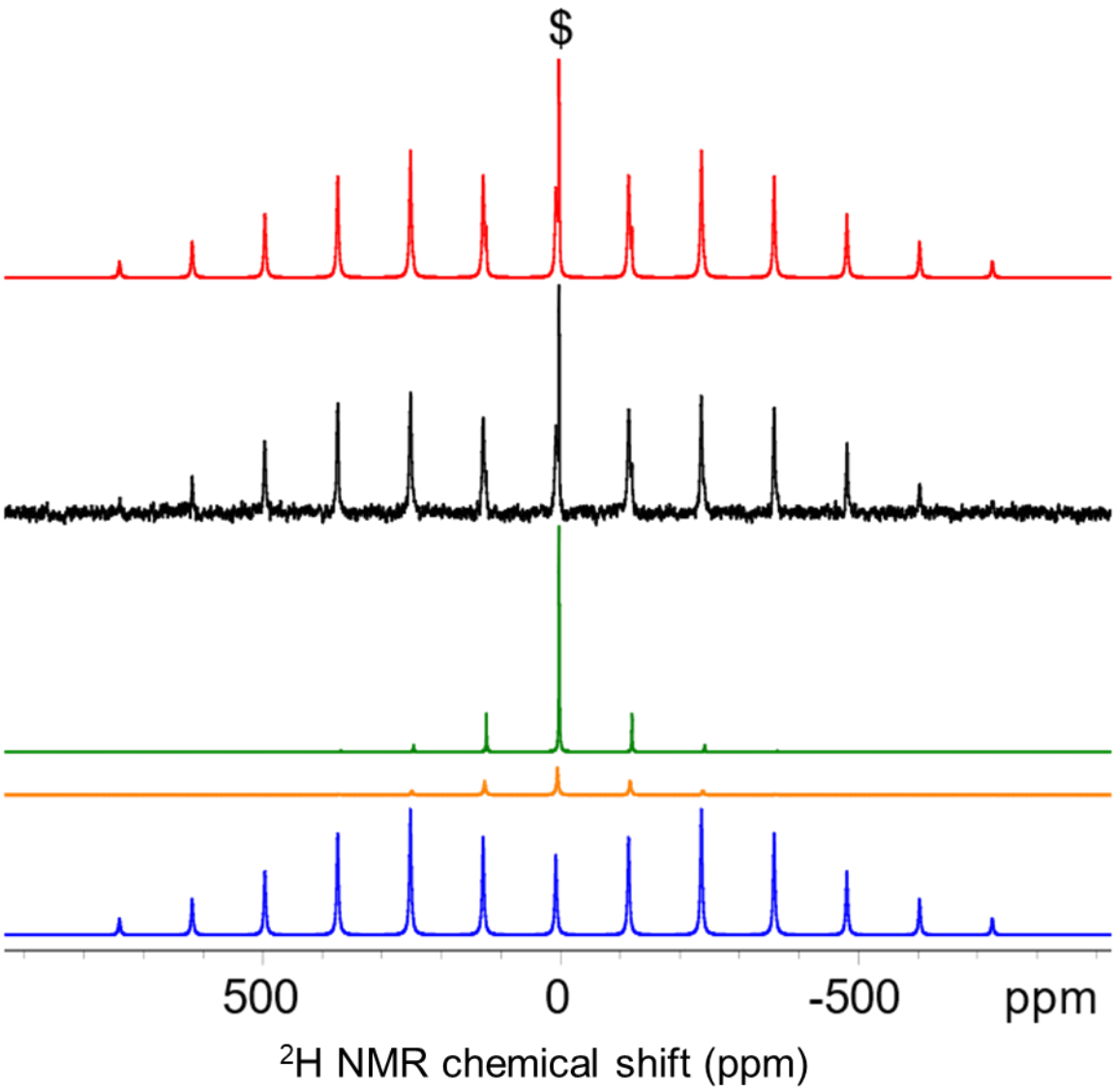

Figure 5.3.13. Solid-state ^{2}H (123 MHz) NMR spectrum of **ZD2TA** spinning at 15 kHz (black), combined simulation (red), and separate simulations (green = **TA** or Al-D, orange = $Cp^{b}_{2}Zr(D)$-OAl≡ or Al-D, and blue = $[Cp^{b}_{2}ZrD][DAl\equiv]$).

As mentioned above, ^{2}H NMR in the solid state is sensitive to dynamics, which averages the C_Q for the ^{2}H nuclei involved in the dynamic process. A reasonable dynamic process that accounts for this behavior is shown in Scheme 5.3.13. In the slow exchange limit **ZD2TA** is expected to contain a Zr-D$^+$ and an Al-D$^-$, and the ^{2}H NMR spectrum would contain two signals for these species. In the fast exchange limit the ^{2}H NMR signal the Zr-D$^+$ and the Al-D$^-$ sites exchange and one signal with an average of the C_Q values for the Zr-D$^+$ and an Al-D$^-$ is obtained. Low temperature ^{2}H MAS NMR experiments are expected to distinguish these exchange pathways, which is in progress.

Scheme 5.3.13. Proposed exchange process in **ZD2TA**

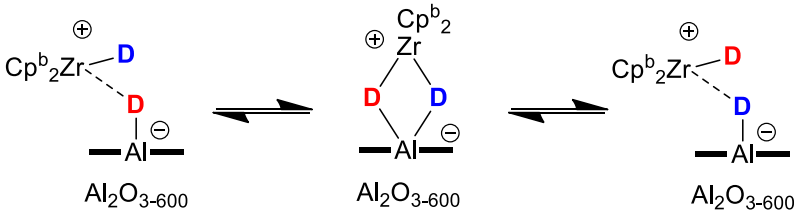

5.3.8 Discussion of the results

This study shows the complexity in this catalyst system, and the necessity to combine solution and solid-state techniques. An important feature of this catalyst is the multiple roles played by TIBA (Scheme 5.3.14). TIBA passivates the surface -OH of sites of Al_2O_{3-600} to form ≡AlO-Al(R_2)-O(Al≡)$_2$, rendering them unreactive and promotes formation of zirconium hydrides with Lewis sites. In solution, TIBA is in sufficient excess to also react with **1** to form Cp$^b_2$ZrH_2(HAl^{i}Bu_2)(Al^{i}Bu_3) (**2**), the active precursor in polymerization reactions. These results demonstrate the need for a large excess of TIBA,

and also show that TIBA is not just a scavenger of minor impurities in polymerization reactions.

Scheme 5.3.14. The solution and solid state reactions that form the active catalyst

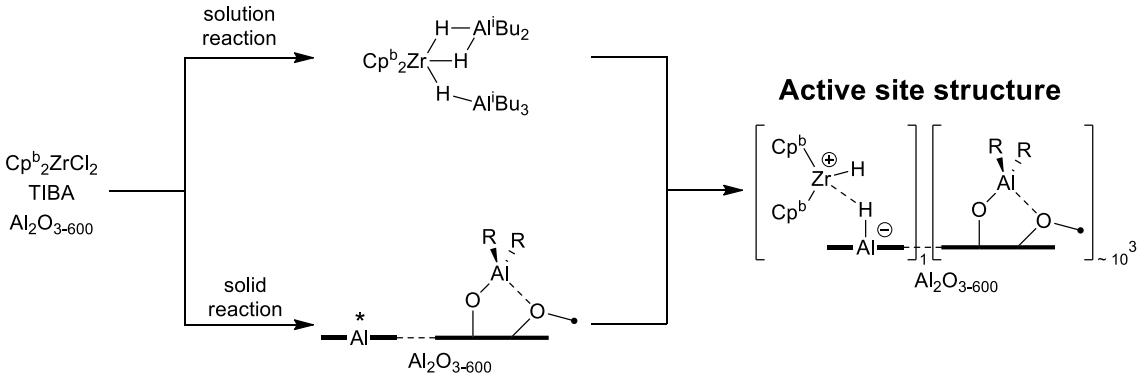

Solution studies of Cp_2ZrR_2 with silver salts,[13] Lewis acidic activators,[11] or MAO with Cp_2ZrMe_2,[12] show that the active site Ziegler-Natta catalysts contain Zr(IV)-R^+ (R = H or alkyl) cations. This study confirms that deduction for **1**/TIBA/$Al_2O_{3\text{-}600}$. A reasonable hypothesis is that an alkylaluminum functionalized alumina would be similar to MAO and would activate the zirconocene dichloride to form similar species. Polymerization activity shows this is not the case. A series of solution NMR studies showed that TIBA form Zr-H from **1**, and polymerization reactions showed that Zr-H are necessary for activity prior to contact with **TA** to form active Zr-H^+ active sites.

Mixtures of zirconocene dialkyls and dehydroxylated alumina in the absence of TIBA form mostly inactive neutral species and only a small quantity of active Zr-R^+ sites. The active sites in these materials are thought to form through alkyl abstraction to form [Cp_2ZrR][RAl≡]. The passivation of the -OH sites by TIBA to form ≡AlO-Al(R_2)-O(Al≡)$_2$

prevents reactions of **2** with -OH sites on alumina, and ~24 % of the Zr-H^+ sites are formed by hydride abstraction in **ZD2TA**. **ZH1TA** and **ZH3TA** contain over an order of magnitude less Zr-H than **ZH2TA** and produce nearly ten times the amount of polyethylene per Zr center. This suggests that **ZH1TA** and **ZH3TA** contain a higher percentage of active sites than **ZH2TA**. The solid-state deuterium NMR spectroscopy of **ZD2TA** and related neutral and cationic zirconium deuterides shows that contains cationic Zr-D^+ sites are present in this material, assigned to the proposed $Cp^b_2Zr(D)_2Al\equiv$ active sites. These sites are dynamic at room temperature, Zr-D and Al-D are exchanging, cooling this system down should slow down the exchange and allow for the observation of the separate ion pair $[Cp^b_2ZrD][DAl\equiv]$. These studies show that a catalyst that mimics industrial polymerization ZN catalysts follows similar reactivity trends as those formed in solution.

5.4 Conclusion

The combination of $Cp^b_2ZrCl_2$, TIBA, and $Al_2O_{3\text{-}600}$ forms an active polymerization catalyst that rivals MAO activated metallocenes. Solutions of **1** react with excess TIBA to form a mixture of **2** (major) and **3** (minor), and control experiments show that only **2** forms active sites in this catalyst. TIBA also reacts with $Al_2O_{3\text{-}600}$ to form **TA** that contains passivated $\equiv AlO\text{-}Al(R_2)\text{-}O(Al\equiv)_2$ species and restricts reactions of **2** with -OH sites on alumina to form inactive $Cp^b_2Zr(D)\text{-}OAl\equiv$ species. Zirconocene hydrides react with **TA** to form $[Cp^b_2ZrH][HAl\equiv]$ sites that are very active for ethylene polymerization.

Deuterium labeling and solid-state ^2H NMR spectroscopy confirm the presence of $[Cp^b_2ZrD][DAl\equiv]$, which follows trends in C_Q from ^2H MAS NMR measurement of Zr-D

organometallic complexes. **VC2** studies showed that the $[Cp^b{}_2ZrH][HAl\equiv]$ active site loading is low but a significant portion of the surface bound Zr. The combination of the experimental results support that the Zr active site in the $Cp^b{}_2ZrCl_2/TIBA/Al_2O_{3\text{-}600}$ catalyst is $[Cp^b{}_2ZrH][HAl\equiv]$. This is the first example of characterization of a catalytically active site in an industrial Ziegler Natta type catalyst.

5.5 Materials and methods

5.5.1 General considerations

All manipulations were performed under an inert atmosphere of argon or nitrogen either on a high vacuum Schlenk line or in a glovebox.[52] Benzene-d6, methylcyclohexane-d14, toluene-d8 and cyclohexane-d12 were purchased from Cambridge Isotope laboratories. Benzene-d6, methylcyclohexane-d14, toluene-d8 and cyclohexane-d12 were dried over sodium/benzophenone, distilled under vacuum and stored inside a glovebox. All other solvents were purchased from Fisher Scientific. Cyclohexane and n-pentane were dried over sodium/benzophenone, degassed and distilled under vacuum. Tetrahydrofuran and n-pentane for precursor synthesis were dried by passing through a double-column J. C. Meyer solvent system and degassed before use. Triisobutylaluminum (1 M in hexanes) and bis(n-butyl-cyclopentadienyl)zirconium dichloride ($Cp^b{}_2ZrCl_2$) were purchased from Sigma Aldrich. Diisobutylaluminum hydride was purchased from Fisher Scientific. $Cp^b{}_2ZrCl_2$ was dried by storage over molecular sieves in a pentane solution followed by recrystallization at 0 °C. *Cis*-1,2-dichloroethylene was dried over CaH_2 and degassed under vacuum. All other commercially available reagents were used as received without any purification. $Li[AlH(O^tBu)_3]$, $Li[AlD(O^tBu)_3]$, $Cp^*{}_2ZrD_2$ and $[Cp^*{}_2ZrD][DB(C_6F_5)_3]$ were synthesized by published procedures.[51,53,54] Partially dehydroxylated Al_2O_3 was provided by Chevron – Phillips Co. and was utilized without modification (see chapter 3).

Solution NMR spectroscopy was carried out on an Avance Bruker 300 [^1H (300 MHz)], an Avance NEO Bruker 400 [^1H (400 MHz), and ^2H (61 MHz)], or an Avance Bruker 600 [^1H (600 MHz), $^{13}C\{^1H\}$ (151 MHz), and ^2H (92 MHz)]; the spectra were

referenced to the NMR solvent residual peak. Solid-state NMR spectroscopy was carried out on an Avance Bruker Neo600 [^{1}H (600 MHz), ^{13}C{^{1}H} (151 MHz), and ^{2}H (92 MHz)] using a 4 mm 2-channel BBO probe and referenced to external standards. Other ^{2}H NMR solid state NMR experiments were performed at the University of California, Santa Barbara on an Avance 800 using a 3.2 mm HX double resonance MAS probe at 123 MHz for ^{2}H. Solid-state ^{2}H NMR simulations were performed in Topspin using the sola program. Reaction volatiles were analyzed by an Agilent 7820 GC fitted with a KCl/Al_2O_3 or a PLOTQ column, and a flame ionization detector. Elemental analysis for $[Cp^b_2ZrH_2]_2$ were performed at the University of California at Berkeley. All other elemental analyses were performed at the Mikroanalytisches Labor Pascher in Germany. GPC measurements were measured by the Chevron – Phillips Co.

5.5.2 Molecular precursors synthesis

Scheme 5.5.1. Synthesis of **4**

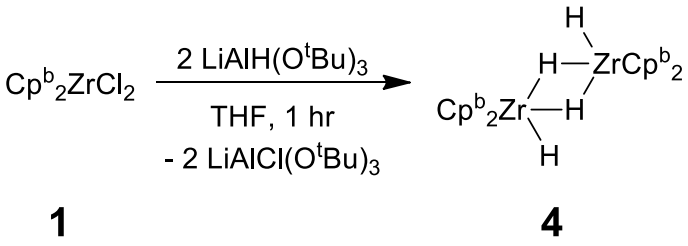

1 **4**

$[Cp^b_2ZrH_2]_2$ (**4**): $Cp^b_2ZrCl_2$ (1 g, 2.5 mmol) and $LiAlH(O^tBu)_3$ (1.5 g, 5.9 mmol) were loaded into a 250 mL teflon – valved flask then THF (50 mL) was vacuum transferred in at -196 °C. The solution was allowed to slowly warm up to room temperature. The clear reaction solution was stirred at room temperature for 30 minutes (total of ca. 1 hour). The

THF was removed en vacuo. The white residue was dissolved in pentane, filtered and recrystallized at – 20 °C. The fluffy white crystals are isolated by filtration and dried en vacuo giving $[Cp^b{}_2ZrH_2]_2$ in a 54 % yield (446 mg). Elemental analysis: Expected: 64.41 C, 8.41 H, Found: 64.26 C, 8.35 H. ^{1}H NMR (C_6D_6, 600 MHz): 6.15 (dd, $^2J_{H\text{-}H}$ = 2.55 Hz, 4 H, CpH), 5.73 (dd, $^2J_{H\text{-}H}$ = 2.55 Hz, 4 H, CpH), 5.39 (dd, $^2J_{H\text{-}H}$ = 2.55 Hz, 4 H, CpH), 5.28 (dd, $^2J_{H\text{-}H}$ = 2.55 Hz, 4 H, CpH), 4.12 (t, $^1J_{H\text{-}H}$ = 7.4 Hz, 2 H, ZrH), 2.57 (m, $^2J_{H\text{-}H}$ = 7.6 Hz, 8 H, Cp$C\mathbf{H}_2$), 1.58 (m, 8 H, $CpCH_2C\mathbf{H}_2CH_2CH_3$), 1.33 (m, 8 H, $CpCH_2CH_2C\mathbf{H}_2CH_3$), 0.91 (t, $^2J_{H\text{-}H}$ = 7.3 Hz, 12 H, $CpCH_2CH_2CH_2C\mathbf{H}_3$), and -2.78 (t, $^1J_{H\text{-}H}$ = 7.4 Hz, 2 H, Zr-H-Zr); $^{13}C\{^1H\}$ NMR (C_6D_6, 151 MHz): 125.6 (s, Cp), 104.1 (s, Cp), 104.3 (s, Cp), 102.9 (s, Cp), 99.3 (s, Cp), 34.6 (s, $CpCH_2\mathbf{C}H_2CH_2CH_3$), 31.4 (s, Cp$\mathbf{C}H_2$), 23.0 (s, $CpCH_2CH_2\mathbf{C}H_2CH_3$), and 14.2 (s, $CpCH_2CH_2CH_2\mathbf{C}H_3$) ppm.

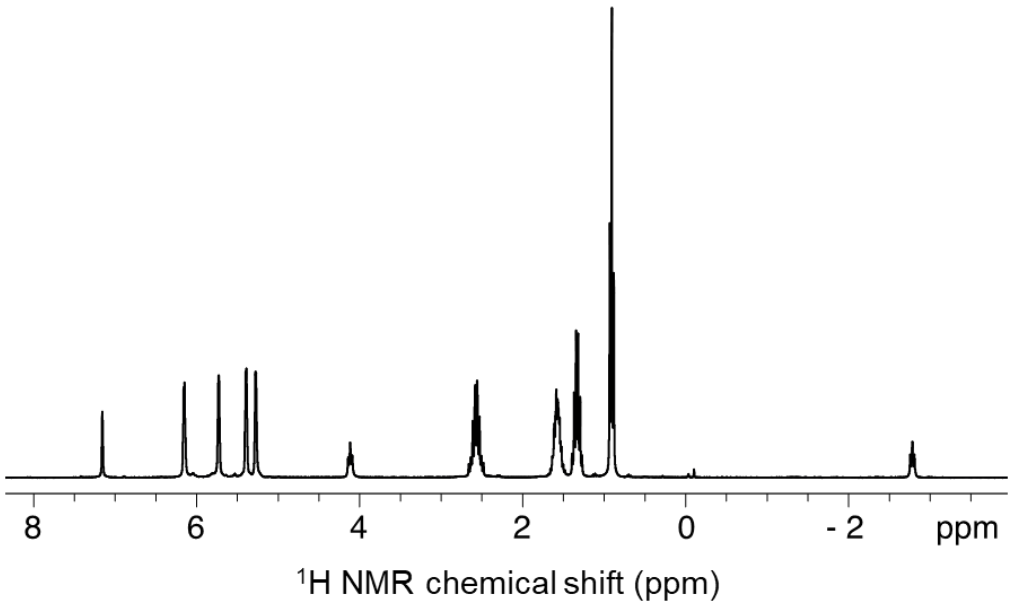

Figure 5.5.1. ^{1}H NMR spectrum of **4** in benzene-d6.

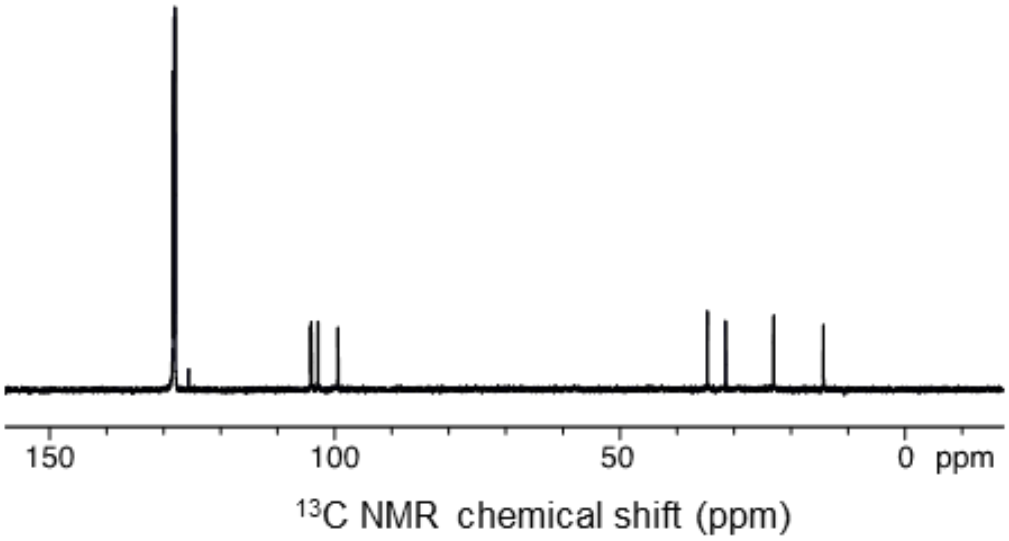

Figure 5.5.2. $^{13}C\{^{1}H\}$ NMR spectrum of **4** in benzene-d6.

Scheme 5.5.2. Synthesis of **4D**

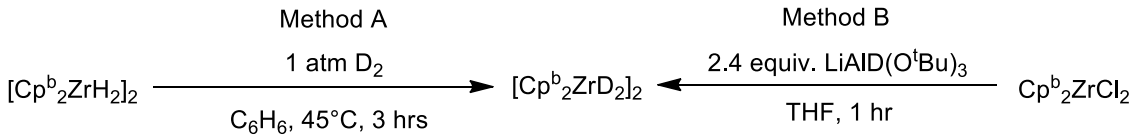

$[Cp^{b}{}_{2}ZrD_{2}]_{2}$ (**4D**): Method A: $[Cp^{b}{}_{2}ZrH_{2}]_{2}$ (50 mg, 0.15 mmol) was loaded into a teflon valved flask and dissolved in benzene (5 mL). Then the flask was filled with D_2 (1 atm) and heated at 45 °C for 3 hours. Removal of the benzene en vacuo then extraction with pentane and recrystallization resulted in $Cp^{b}{}_{2}ZrD_{2}$ in a 30 % yield (15 mg). Integration of the remaining Zr-H versus the Cp^{b} in ^{1}H nmr reveals there is an 88 % incorporation of Zr-D. Method B: prepare similarly to **4** but with $LiAlD(O^{t}Bu)_3$ (>99 % D). ^{1}H NMR (C_6D_6, 600 MHz): 6.15 (dd, $^{2}J_{H\text{-}H}$ = 2.55 Hz, 2 H, CpH), 5.73 (dd, $^{2}J_{H\text{-}H}$ = 2.55 Hz, 2 H, CpH), 5.39 (dd, $^{2}J_{H\text{-}H}$ = 2.55 Hz, 2 H, CpH), 5.28 (dd, $^{2}J_{H\text{-}H}$ = 2.55 Hz, 2 H, CpH), 2.56 (t, $^{2}J_{H\text{-}H}$ =

7.6 Hz, 2 H, $CpCH_2$), 2.57 (m, 8 H, $CpCH_2$), 1.58 (m, 4 H, $CpCH_2C\mathbf{H}_2CH_2CH_3$), 1.33 (m, 4 H, $CpCH_2CH_2C\mathbf{H}_2CH_3$), 0.91 (t, $^2J_{H\text{-}H}$ = 7.3 Hz, 6 H, $CpCH_2CH_2CH_2C\mathbf{H}_3$); ^{2}H NMR ($C_6H_6$, 61 MHz):6.2 (s, 1 D, Cp), 5.4 (s, 1 D, Cp), 4.1 (s, 1 D, Zr-D) , and -2.9 (s, 1 D, Zr-D-Zr) ppm.

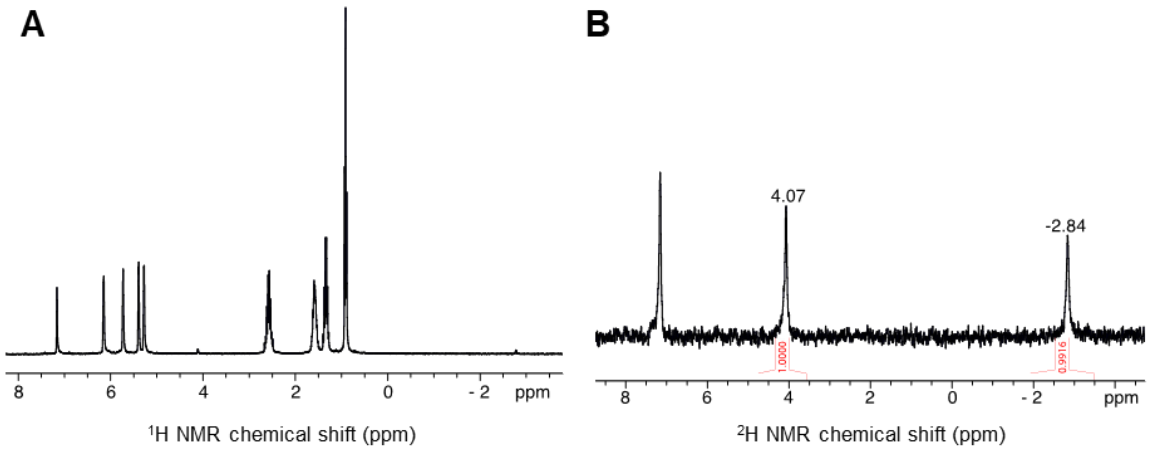

Figure 5.5.3. NMR spectra of $[Cp^b{}_2ZrD_2]_2$ (**4D**) in C_6H_6: A) ^{1}H; and B) ^{2}H.

*5.5.3 Synthesis and characterization of **TA**, **ZH1TA**, **ZH2TA**, **ZH3TA**, and **ZH2A***

$Al_2O_{3\text{-}600}$ + Al^iBu_3 (**TA**): $Al_2O_{3\text{-}600}$ (1 g, 0.93 mmol OH) was loaded into a double schlenk and attached to a high vacuum line. Under a flow of argon, 1.8 ml of 1 M TIBA (350 mg, 1.8 mmol) in hexanes was added by syringe at room temperature to the opposite arm. The double schlenk was degassed and approximately half of the solvent was removed from the TIBA mixture. Then pentane (10 ml) was condensed over the TIBA at -196 °C. The double schlenk was sealed and the TIBA/pentane solution was warmed up to room temperature then transferred to the solid through the dividing frit. The slurry was stirred at room temperature for 5 minutes. The solid was then washed 3 times. The white solid was

stored at -20 °C in an argon filled glovebox. Analysis of the volatiles by GC shows 0.56 mmol/g of isobutane and 0.054 mmol/g of isobutene is released during the reaction. Solid state NMR: ^{1}H (600 MHz): 0.7 (^{i}Bu); and $^{13}C\{^{1}H\}$ (151 MHz): 34-15 (^{i}Bu) ppm.

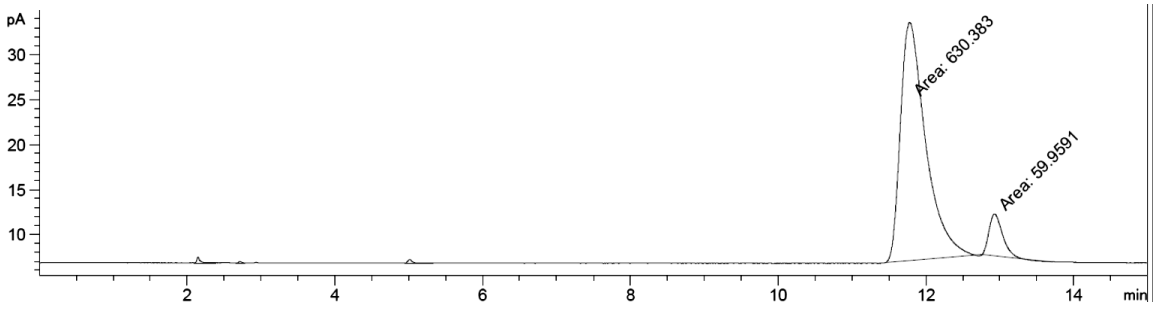

Figure 5.5.4. Sample GC of the volatiles from the grafting of TIBA with $Al_2O_{3\text{-}600}$.

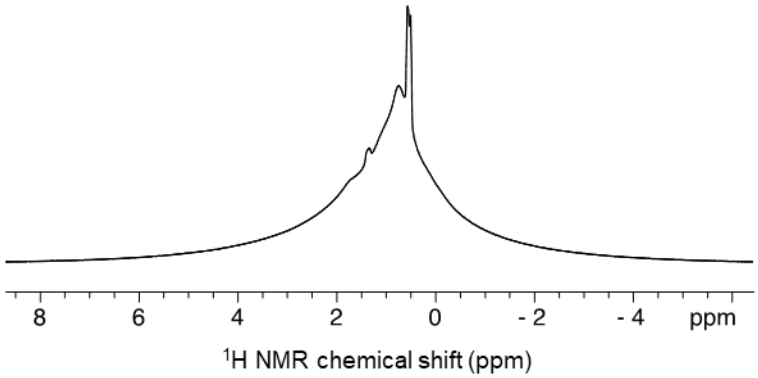

Figure 5.5.5. Solid-state ^{1}H NMR of **TA** spinning at 10 kHz.

ZH1TA: **TA** (1 g) was loaded into a double schlenk then a stock solution of $Cp^{b}_{2}ZrCl_2$/TIBA (61 mg, 0.15 mmol Zr/1.8 mmol TIBA) in pentane (20 mL) was added by syringe to the opposite arm of the double schlenk. The reaction flask was degassed, and the solution was transferred to the solid at -196 °C. The slurry was allowed to warm up to

room temperature and stirred for a total of 15 minutes. The solid was washed 5 times then the volatiles were transferred to a 5 L flask for analysis. The white solid was stored at -20 °C in an argon filled glovebox freezer. Method 2: the same procedure as in method 1 except 20 mg (0.05 mmol) of $Cp^b{}_2ZrCl_2$ and 0.6 mL (0.6 mmol) of TIBA (1 M in hexanes) were used. Elemental analysis for **ZH1TA**: Found Zr 0.0059 %, C 7.06 %, H 1.36 %. Solid state NMR: ^{1}H (600 MHz): 0.9 (^{i}Bu); and $^{13}C\{^1H\}$ (151 MHz): 34-15 (^{i}Bu) ppm.

ZH2TA: Method 1: **TA** (1 g) and $Cp^b{}_2ZrH_2$ (50 mg, 0.15 mmol) were loaded into a double schlenk in an argon filled glovebox. The double schlenk was removed from the glovebox then connected to a high vacuum line. Pentane (20 mL) was condensed over the solids by vacuum transfer at -196 °C. The reaction was allowed to warm up to room temperature and stirred for 15 minutes. The solid was washed 4 times then the volatiles were removed en vacuo. The cream-colored solid was stored at -30 °C in an argon filled glovebox freezer. Method 2: the same procedure as in method 1 except 17 mg (0.025 mmol) was used of $[Cp^b{}_2ZrH_2]_2$ instead of 50 mg. In both methods excess $[Cp^b{}_2ZrH_2]_2$ was observed in the washings. Elemental analysis for **ZH2TA**: Found Zr 0.069 %, C 1.24 %, H 6.50 %. Solid state NMR: ^{1}H (600 MHz): 0.5; $^{13}C\{^1H\}$ (151 MHz): 130-109 (Cp), 34-15 (^{i}Bu), and 12 ($Cp(CH_2)_3CH_3$) ppm. **ZD2TA** was prepared analogously with method 1 with **4D**. Monitoring the reaction by solution ^{1}H NMR in cyclohexane-d12 showed that ~38 % of the unreacted **4D** converted to **4** via H/D exchange with an unknown source after 15 minutes.

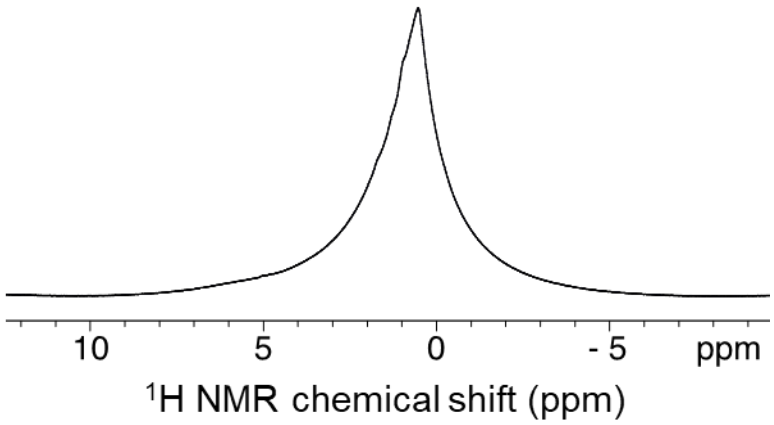

Figure 5.5.6. ^{1}H MAS NMR spectrum of **ZH2TA** spinning at 10 kHz.

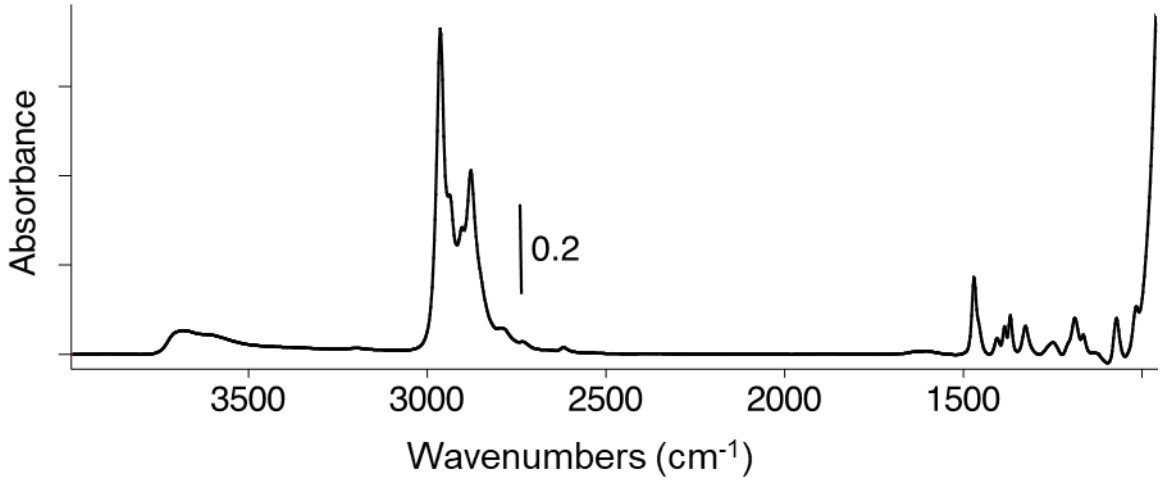

Figure 5.5.7. FT-IR spectrum of **ZD2TA**.

ZH3TA: **TA** (1 g) was loaded into a double schlenk then a stock solution of 2 ($[Cp^b{}_2ZrH_2]_2$ (17 mg, 0.025 mmol), diisobutylaluminum hydride (8.9 µL, 0.05 mmol), and Triisobutylaluminum (12.5 µL, 0.05 mmol)) in pentane (20 mL) was added by syringe to the opposite arm of the double schlenk. The reaction flask was degassed, and the solution was transferred to the solid at -196 °C. The slurry was allowed to warm up to room

temperature and stirred for a total of 15 minutes. The solid was washed 5 times then the solid was dried en vacuo. The white solid was stored at -20 °C in an argon filled glovebox freezer. Elemental analysis for ZH3TA: Found Zr 0.0030 %, C 6.64 %, H 1.30 %. Solid state NMR: ^{1}H (600 MHz): 0.7; ^{13}C{^{1}H} (151 MHz): and 34-15 (^{i}Bu) ppm.

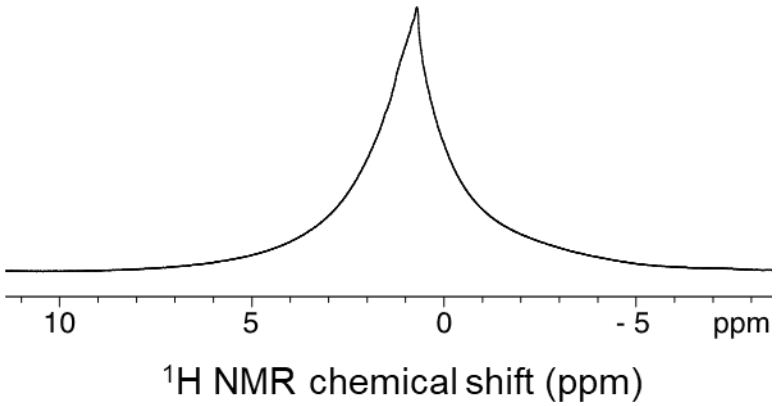

Figure 5.5.8. Solid-state ^{1}H MAS NMR spectrum of **ZH3TA** spinning at 10 kHz.

ZH2A: Al_2O_3 (0.5 g) and $[Cp^{b}{}_2ZrH_2]_2$ (50 mg, 0.75 mmol) were loaded into a double schlenk in an argon filled glovebox. The double schlenk was removed from the glovebox then connected to a high vacuum line. Pentane (20 mL) was condensed over the solids by vacuum transfer at -196 °C. The reaction was allowed to warm up to room temperature and stirred for 15 minutes. The solid was washed 4 times then the volatiles were removed en vacuo. The cream-colored solid was stored at -30 °C in an argon filled glovebox freezer. Elemental analysis for ZH2A: Found Zr 0.90 %, C 1.94 %, H 0.36 %. Solid state NMR: ^{1}H (600 MHz): 6.0 (Cp**H**), 2.0-0.7 (Cp(C**H**$_2$)$_3$C**H**$_3$); ^{13}C{^{1}H} (151 MHz):

135-97 (Cp), 33 (Cp(**C**H_2)$_3$$CH_3$), 29 (Cp(**C**$H_2$)$_3$$CH_3$), 22 (Cp(**C**$H_2$)$_3$$CH_3$) and 12 (Cp($CH_2$)$_3$**C**$H_3$) ppm. **ZD2A** was prepared in a similar manner with [$Cp^b{}_2ZrD_2$]$_2$.

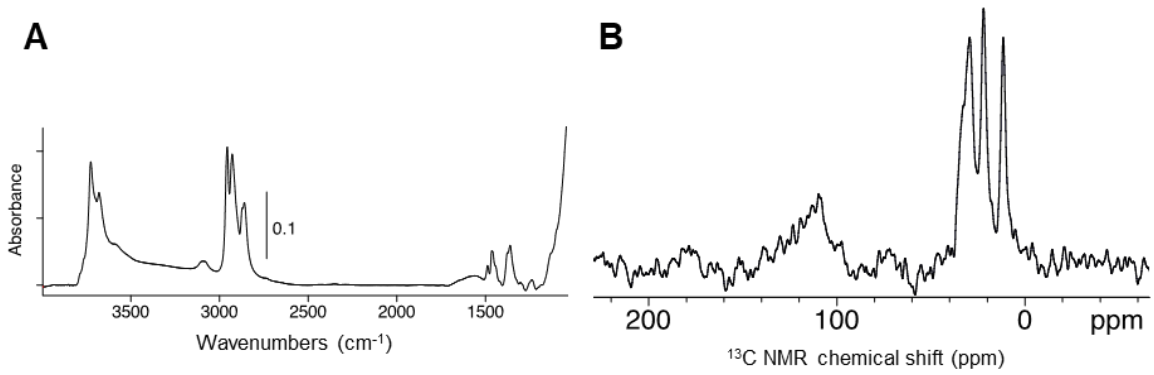

Figure 5.5.9. A) FT-IR spectrum of **ZH2A**; and B) solid-state ^{13}C CP-MAS NMR spectrum of **ZH2A**.

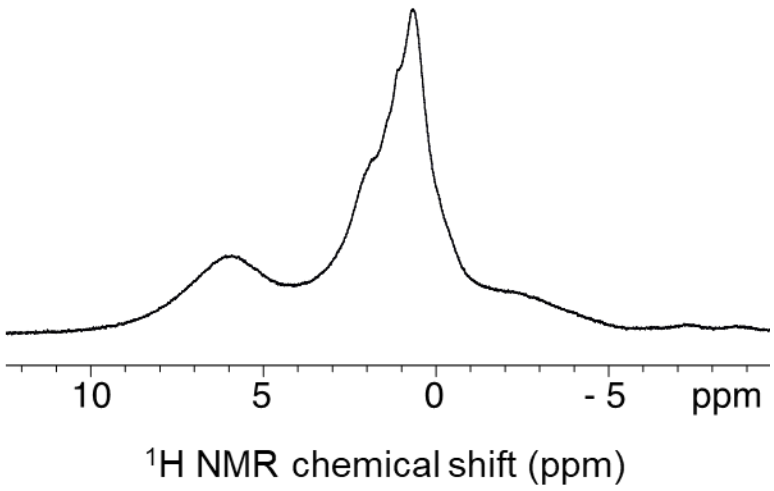

Figure 5.5.10. Solid-state ^1H MAS NMR spectrum of **ZH2A** spinning at 10 kHz.

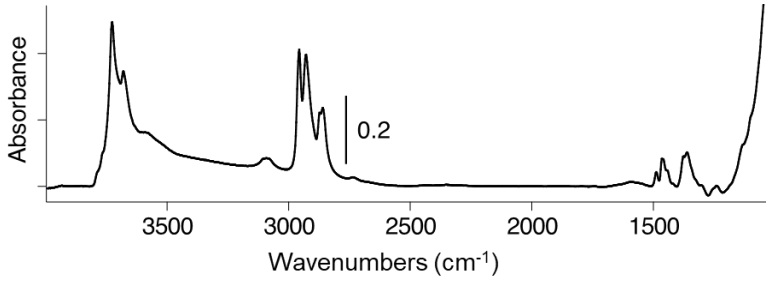

Figure 5.5.11. FTIR spectrum of **ZD2A**.

5.5.4 Polymerization of ethylene

Procedure: in an 8 – well parallel reactor, material (10 – 20 mg) was loaded into each well then cyclohexane (2 mL) was added to each well. The pressure reactor was sealed then pressurized with 300 psi (20 atm) of ethylene, heated to 80 °C and stirred at 1000 rpm for 30 minutes. For polymerizations in the presence of in-situ zirconium precursor and TIBA, the precursor and TIBA were combined in situ (1:12 Zr:TIBA and 150 µmol Zr g_{solid}^{-1}) in a solution of cyclohexane (2 mL) then added to the solid directly before the introduction of ethylene. The reaction was stopped by venting the ethylene pressure and purging the system with nitrogen. The polymers were dried en-vacuo prior to weighing to remove excess cyclohexane.

5.5.5 Active site counting with cis-1,2-dichloroethylene

Table 5.4. GC calibration data for methane.[a]

Entry	P (torr)	CH_4 area
1	1	98 (±5)[b]
2	2	290 (±17)
3	10	1610 (±5)
4	20	3026 (±136)

a.) Samples were prepared by measuring the pressure with a monometer in a 500 mL flask then partially backfilling the flask with nitrogen; and b.) measured after ca. half of the pressure was removed from the 2 torr sample.

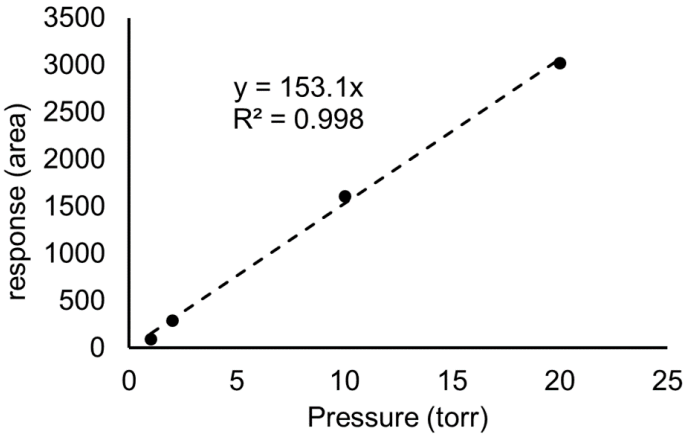

Figure 5.5.12. Response vs pressure plot for CH_4 with linear regression fit.

Reaction of solids with *cis*-1,2-dichloroethylene: solid materials (200-500 mg) were exposed to excess cis-1,2-dichlorethylene (**VC2**) (ca. 0.3 mmol) in a sealed flask for 2 hours. The flask was partially back filled with nitrogen and the gas phase was analyzed by GC, representative gas chromatographs are shown below.

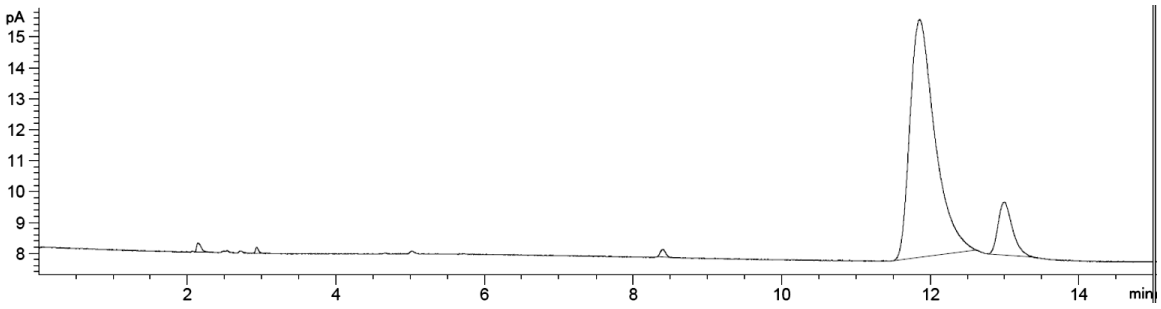

Figure 5.5.13. GC of **TA** + cis-dichloroethylene.

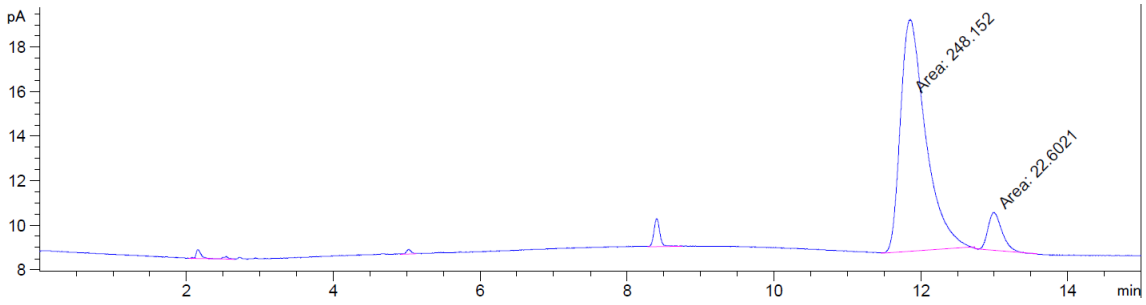

Figure 5.5.14. GC of **ZH1TA** + cis-dichloroethylene.

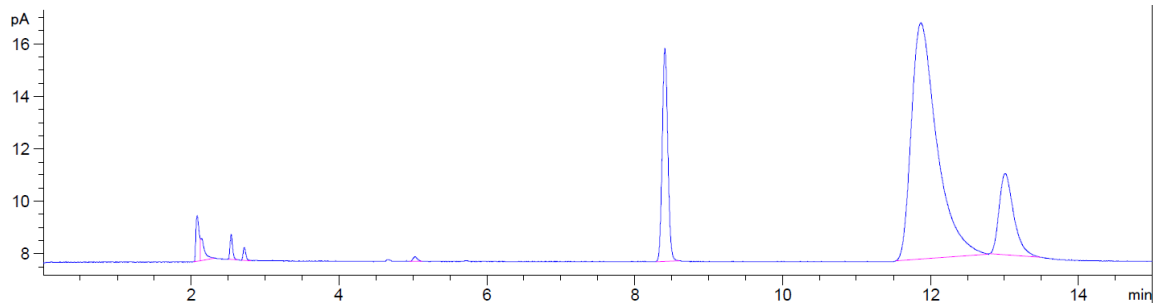

Figure 5.5.15. GC of **ZH2TA** + cis-dichloroethylene.

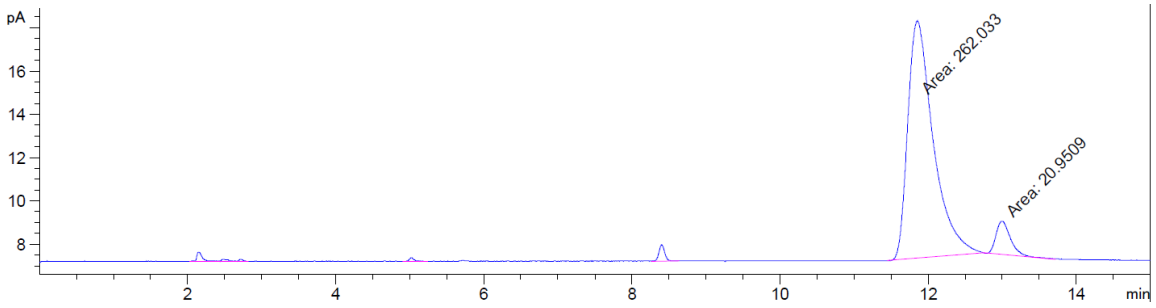

Figure 5.5.16. GC of **ZH3TA** + cis-dichloroethylene.

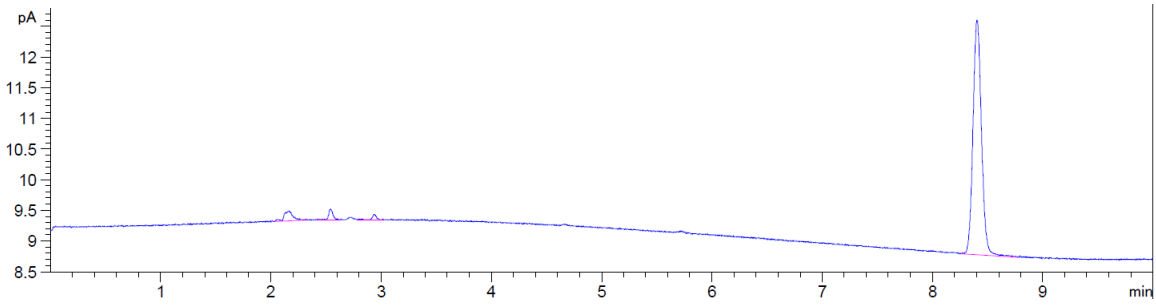

Figure 5.5.17. GC of **ZH2A** + cis-dichloroethylene.

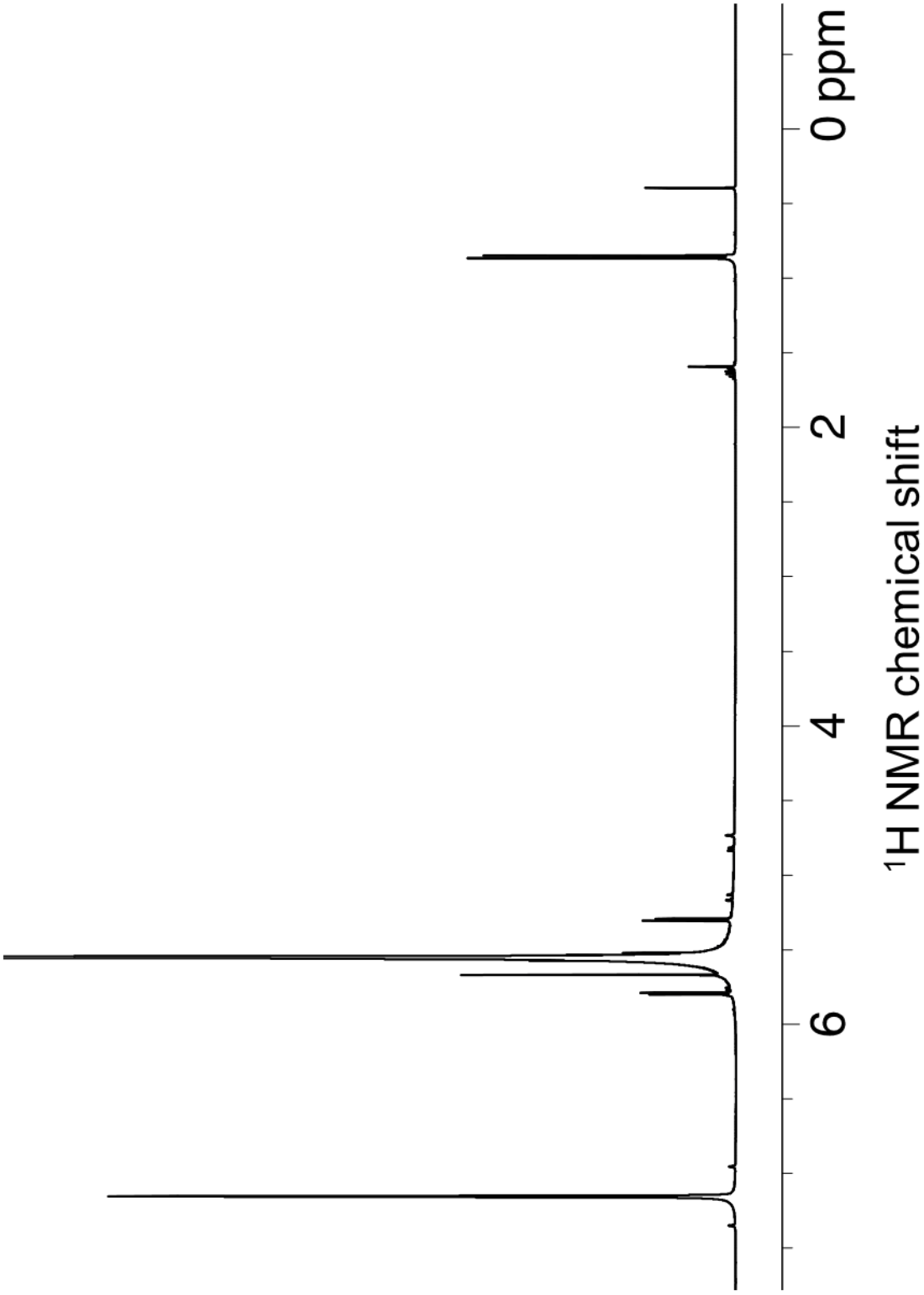

Figure 5.5.18. ^{1}H NMR of the volatiles from the reaction of **ZD2TA** with **VC2**.

5.5.6 Solution NMR data zirconocene and alkylaluminum mixtures

Table 5.5. ^{1}H NMR assignments for the Cp^{b} ligand and M-H for **2**, and **5**.

Complex	ligand δ^{1}H (ppm)[a]	Assignment	M-H δ^{1}H (ppm)[b]	Assignment
2[c]	6.21 (bs, 2H)	Cp**H**	-0.98 (bs, 1H)	$^{i}Bu_2Al$-**H**-Zr
	5.77 (bs, 2H)	Cp**H**	-1.31 (bs, 1H)	$^{i}Bu_2Al$-**H**-Zr
	5.76 (bs, 2H)	Cp**H**	-1.72 (bs, 1H)	$^{i}Bu_3Al$-**H**-Zr
	5.71 (bs, 2H)	Cp**H**		
	2.46 (t, 7.7, 4H)	Cp$C\mathbf{H}_2CH_2CH_2CH_3$		
	1.50 (m, 4H)	$CpCH_2C\mathbf{H}_2CH_2CH_3$		
	1.33 (q, 7.5, 4H)	$CpCH_2CH_2C\mathbf{H}_2CH_3$		
	0.92 (t, 7.3, 6H)	$CpCH_2CH_2CH_2C\mathbf{H}_3$		
2[d]	6.22 (bs, 2H)	Cp**H**	-1.09 (bd, 8.4, 1H)	$^{i}Bu_2Al$-**H**-Zr
	5.76 (bs, 2H)	Cp**H**	-1.50 (bd, 8.4, 1H)	$^{i}Bu_2Al$-**H**-Zr
	5.70 (bs, 2H)	Cp**H**	-1.81 (bs, 1H)	$^{i}Bu_3Al$-**H**-Zr
	5.66 (bs, 2H)	Cp**H**		
	2.43 (t, 7.5, 4H)	Cp$C\mathbf{H}_2CH_2CH_2CH_3$		
	1.46 (m, 4H,)	$CpCH_2C\mathbf{H}_2CH_2CH_3$		
	1.31 (m, 4H)	$CpCH_2CH_2C\mathbf{H}_2CH_3$		
	0.91 (t, 7.4, 6H)	$CpCH_2CH_2CH_2C\mathbf{H}_3$		

Table 5.5. continued.

Complex	ligand δ^1H (ppm)[a]	Assignment	M-H δ^1H (ppm)[a]	Assignment
5[e]	5.73 (bs, 2H)	Cp**H**	3.21 (bs, 1H)	Zr-**H**
	5.56 (bs, 2H)	Cp**H**	-1.59 (bs, 1H)	$^{i}Bu_2Al$-**H**-Zr
	5.41 (bs, 2H)	Cp**H**	-2.48 (bs, 1H)	$^{i}Bu_2Al$-**H**-Zr
	5.30 (bs, 2H)	Cp**H**		
	2.42 (bt, 4H)	$CpC\mathbf{H}_2CH_2CH_2CH_3$		
	1.44 (m, 4H)	$CpCH_2C\mathbf{H}_2CH_2CH_3$		
	1.26 (m, 4H)	$CpCH_2CH_2C\mathbf{H}_2CH_3$		
	0.91 (t, 7.1, 6H)	$CpCH_2CH_2CH_2C\mathbf{H}_3$		

a.) splitting pattern, $^2J_{H\text{-}H}$ and ratio shown in parenthesis; b.) splitting pattern, $^1J_{H\text{-}H}$ and ratio shown in parenthesis; c.) cyclohexane-d12 at 10 °C; d.) methylcyclohexane-d14 at -40 °C; and e.) toluene-d8 at -40 °C.

Table 5.6. ^{1}H NMR assignments for the Cp-H of the Cp^{b} ligand and M-H from the reactions of **1** or **4** with ^{i}Bu$_3$Al at -40 °C.

Mixture[a]	CpH δ^{1}H (ppm)[b]	Assignment	M-H δ^{1}H (ppm)[b]	Assignment
1 + 2TIBA[d]	6.18 (bs, 2H)	**2** (Cp**H**)	-0.74 (bs, 1H)	**3** (^{i}Bu$_2$Al-**H**-Zr)
(2:1:1)	6.13 (bs, 2H)	**x** (Cp**H**)	-0.84 (bd, 8, 1H)	**2** (^{i}Bu$_2$Al-**H**-Zr)
	5.83 (bs, 10H)	**3**+**1** (Cp**H**)	-1.44 (bd, 8, 1H)	**2** (^{i}Bu$_2$Al-**H**-Zr)
	5.74 (bs, 2H)	**2** (Cp**H**)	-1.84 (bs, 1H)	**2** (^{i}Bu$_3$Al-**H**-Zr)
	5.62 (bs, 8H)	**1** (Cp**H**)	-1.89 (bs, 2H)	**3** (^{i}Bu$_2$ClAl-**H**-Zr)
	5.57 (bs, 2H)	**2** (Cp**H**)		
	5.53(bs, 2H)	**2** (Cp**H**)		
	5.50(bs, 2H)	**3** (Cp**H**)		
	5.48(bs, 2H)	**x** (Cp**H**)		
	5.44(bs, 2H)	**x** (Cp**H**)		
	5.26(bs, 2H)	**x** (Cp**H**)		
1 + 7TIBA [d]	6.17 (bs, 2H)	**2** (Cp**H**)	-0.77 (bs, 0.65H)	**3** (^{i}Bu$_2$Al-**H**-Zr)
(0:3:2)	5.81 (bs, 3H)	**3** (Cp**H**)	-0.87 (bd, 8, 1H)	**2** (^{i}Bu$_2$Al-**H**-Zr)
	5.56 (bs, 2H)	**3** (Cp**H**)	-1.45 (bd, 8, 1H)	**2** (^{i}Bu$_2$Al-**H**-Zr)
	5.53 (bs, 2H)	**2** (Cp**H**)	-1.85 (bs, 1H)	**2** (^{i}Bu$_3$Al-**H**-Zr)
	5.48 (bs, 3H)	**2** (Cp**H**)	-1.97 (bs, 01.3H)	**3** (^{i}Bu$_2$ClAl-**H**-Zr)
	5.44 (bs, 2H)	**2** (Cp**H**)		

Mixture[a]	Cp[b] δ^1H (ppm)[b]	Assignment	M-H δ^1H (ppm)[c]	Assignment
1 + TIBA[e]	6.24 (bs, 4H)	**2** (Cp**H**)	-0.84 (bs, 0.25H)	**3** (^{i}Bu$_2$Al-**H**-Zr)
(0:4:1)	6.04 (bs, 1H)	**3** (Cp**H**)	-1.07 (bd, 8, 1H)	**2** (^{i}Bu$_2$Al-**H**-Zr)
	5.88 (bs, 1H)	**3** (Cp**H**)	-1.48 (bd, 8, 1H)	**2** (^{i}Bu$_2$Al-**H**-Zr)
	5.78 (bs, 4H)	**2** (Cp**H**)	-1.79 (bs, 1H)	**2** (^{i}Bu$_3$Al-**H**-Zr)
	5.73 (bs, 4H)	**2** (Cp**H**)	-1.84 (bs, 0.5H)	**3** (^{i}Bu$_2$ClAl-**H**-Zr)
	5.68 (bs, 4H)	**2** (Cp**H**)		
4 + 24 TIBA[e]	6.21 (bdd, 2, 2H)	**2** (Cp**H**)	-1.09 (bd, 8.2, 1H)	**2** (^{i}Bu$_2$Al-**H**-Zr)
(0:1:0)	5.76 (bdd, 2, 2H)		-1.50 (bd, 8.2, 1H)	**2** (^{i}Bu$_2$Al-**H**-Zr)
	5.70 (bdd, 2, 2H)		-1.81 (bs, 1H)	**2** (^{i}Bu$_3$Al-**H**-Zr)
	5.65 (bdd, 2, 2H)			

a.) ratio of **1**:**2**:**3** as determined by ^{1}H NMR spectroscopy in the given mixture; and b.) splitting pattern, $^2J_{H\text{-}H}$ and ratio shown in parenthesis; c.) splitting pattern, $^1J_{H\text{-}H}$ and ratio shown in parenthesis; d.) toluene-d8; and e.) methylcyclohexane-d14.

Table 5.7. ^{1}H NMR assignments for the Cp-H of the Cp^{b} ligand and M-H from the reactions of **1** or **4** with ^{i}Bu$_3$Al at 10 °C in cyclohexane-d12.

Mixture[a]	Cp^{b} δ^{1}H (ppm)[b]	Assignment	M-H δ^{1}H (ppm)[c]	Assignment
1 + TIBA	6.21 (bs, 2H)	**2** (Cp**H**)	-0.75 (bs, 0.15H)	**3** (^{i}Bu$_2$Al-**H**-Zr)
(0:17:3)	6.06 (bs)	**3** (Cp**H**)	-0.98 (bs, 1H)	**2** (^{i}Bu$_2$Al-**H**-Zr)
	5.86 (bs)	**3** (Cp**H**)	-1.32 (bs, 1H)	**2** (^{i}Bu$_2$Al-**H**-Zr)
	5.78 (bs, 2H)	**2** (Cp**H**)	-1.72 (bs, 1.3H)	**2** (^{i}Bu$_3$Al-**H**-Zr)
	5.75 (bs, 2H)	**2** (Cp**H**)		**3** (^{i}Bu$_2$ClAl-**H**-Zr)
	5.71 (bs, 2H)	**2** (Cp**H**)		
4 + TIBA	6.20 (dd, 2.5, 2H)	**2** (Cp**H**)	-0.97 (bd, 8.4, 1H)	**2** (^{i}Bu$_2$Al-**H**-Zr)
(0:1:0)	5.74 (dd, 2.5, 2H)		-1.32 (bd, 8.0, 1H)	**2** (^{i}Bu$_2$Al-**H**-Zr)
	5.73 (dd, 2.5, 2H)		-1.73 (bs, 1H)	**2** (^{i}Bu$_3$Al-**H**-Zr)
	5.69 (dd, 2.5, 2H)			

a.) ratio of **1**:**2**:**3** as determined by ^{1}H NMR spectroscopy in the given mixture; b.) splitting pattern, $^{2}J_{H\text{-}H}$ and ratio shown in parenthesis; and c.) splitting pattern, $^{1}J_{H\text{-}H}$ and ratio shown in parenthesis.

1 + 12 TIBA: in a N_2 filled glovebox, **1** (8 mg, 20 µmol) was loaded into a teflon – valved NMR tube and dissolved in $C_6D_{11}CD_3$ (0.5 mL) or cyclohexane-d12. TIBA (60 µL, 0.24 mmol) was added and the solution turned pale yellow.

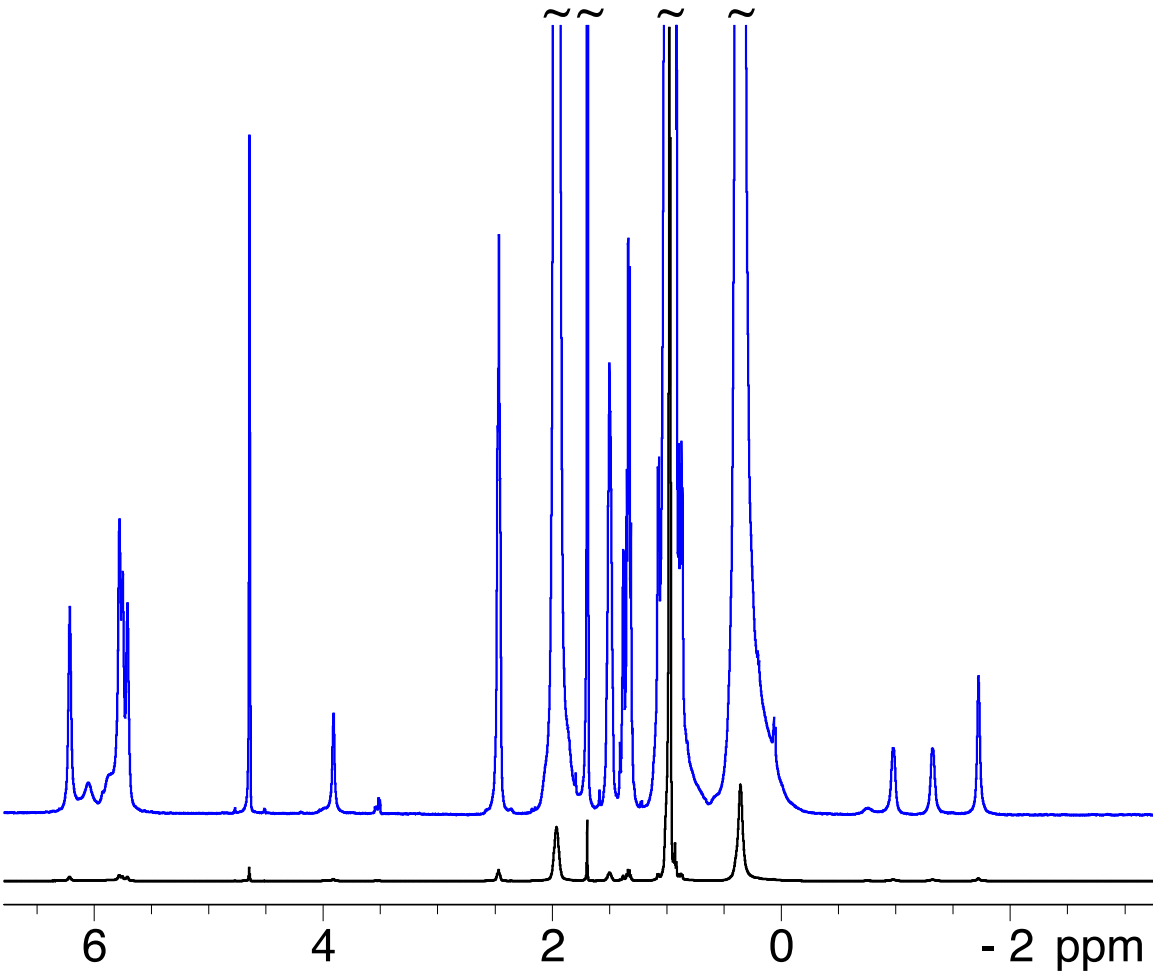

Figure 5.5.19. ^{1}H NMR spectrum of **1** + 12 TIBA in cyclohexane-d12 at 10 °C (black), 10 X zoom (blue).

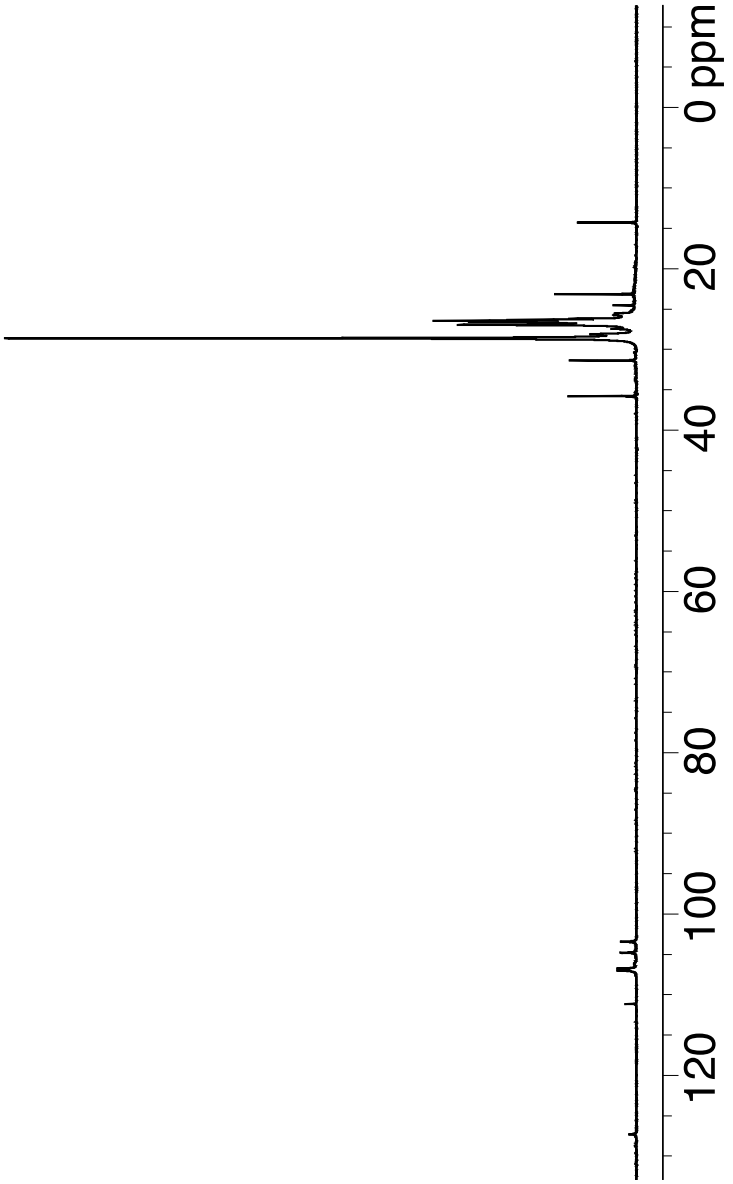

Figure 5.5.20. $^{13}C\{^{1}H\}$ NMR spectrum of **1** + 12 TIBA in cyclohexane-d12 at 10 °C.

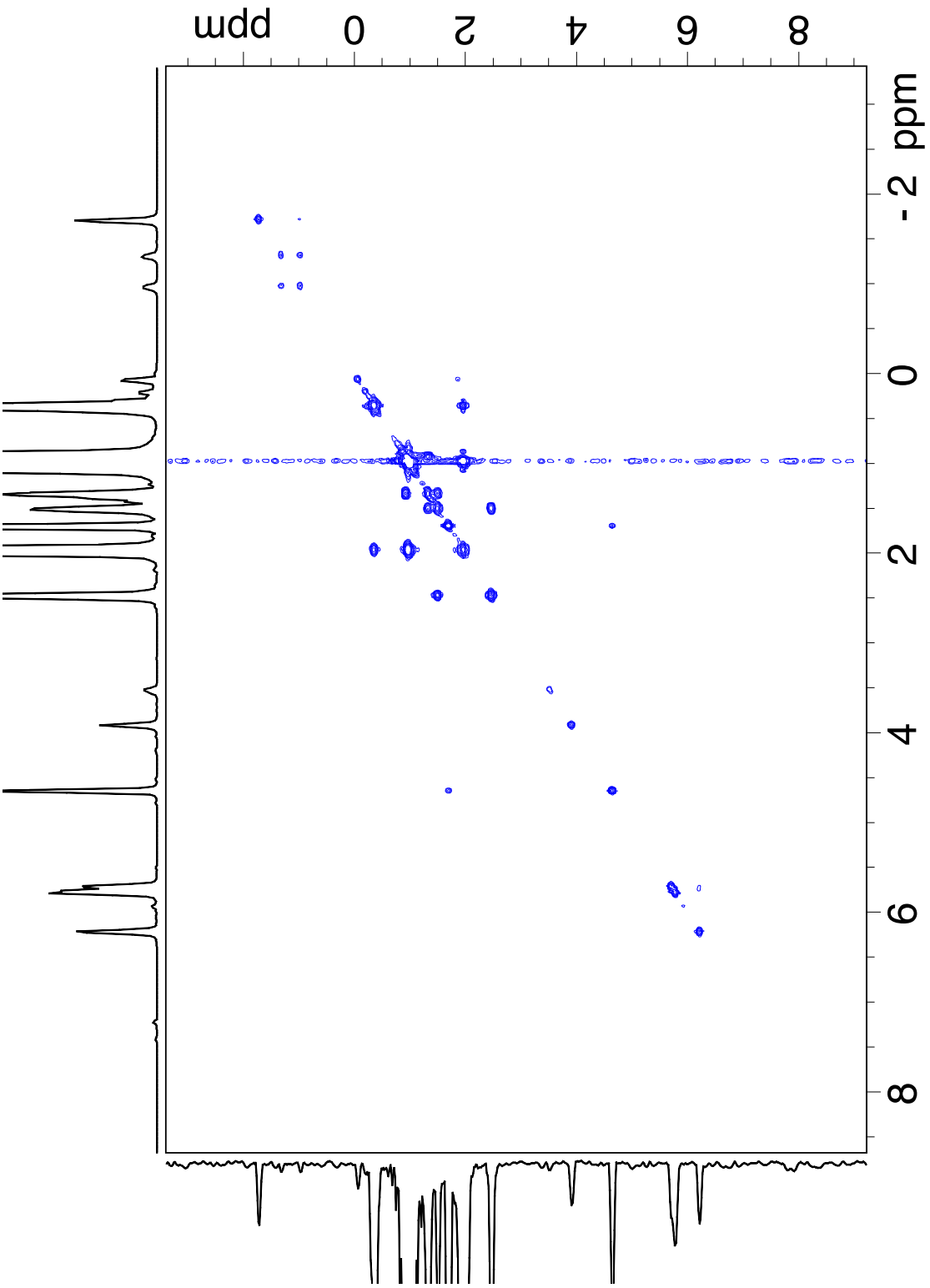

Figure 5.5.21. ^{1}H-^{1}H COSY NMR spectrum of **1** + 12 TIBA in cyclohexane-d12 at 10 °C.

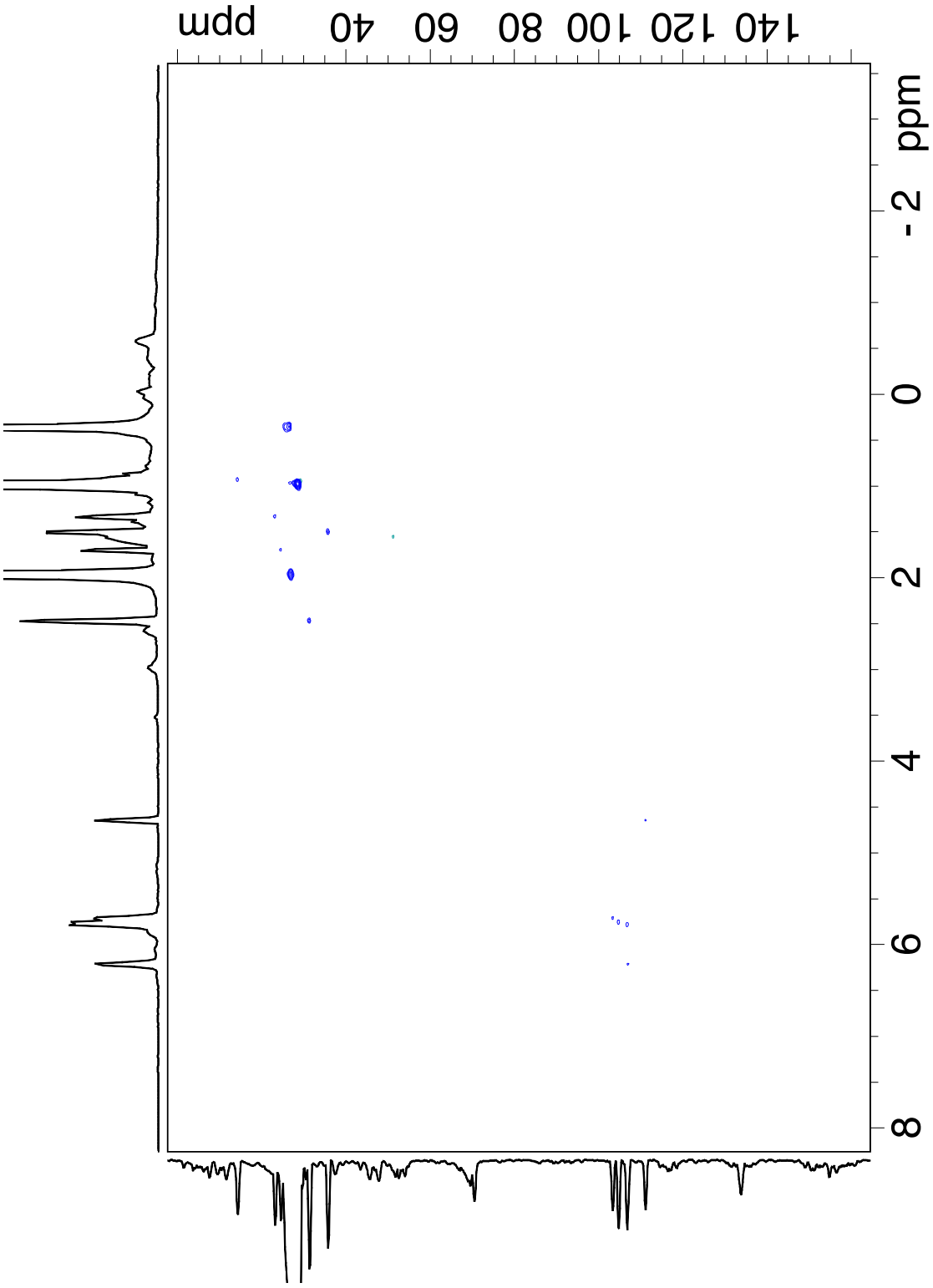

Figure 5.5.22. ^{1}H-^{13}C HSQC NMR spectrum of **1** + 12 TIBA in cyclohexane-d12 at 10 °C.

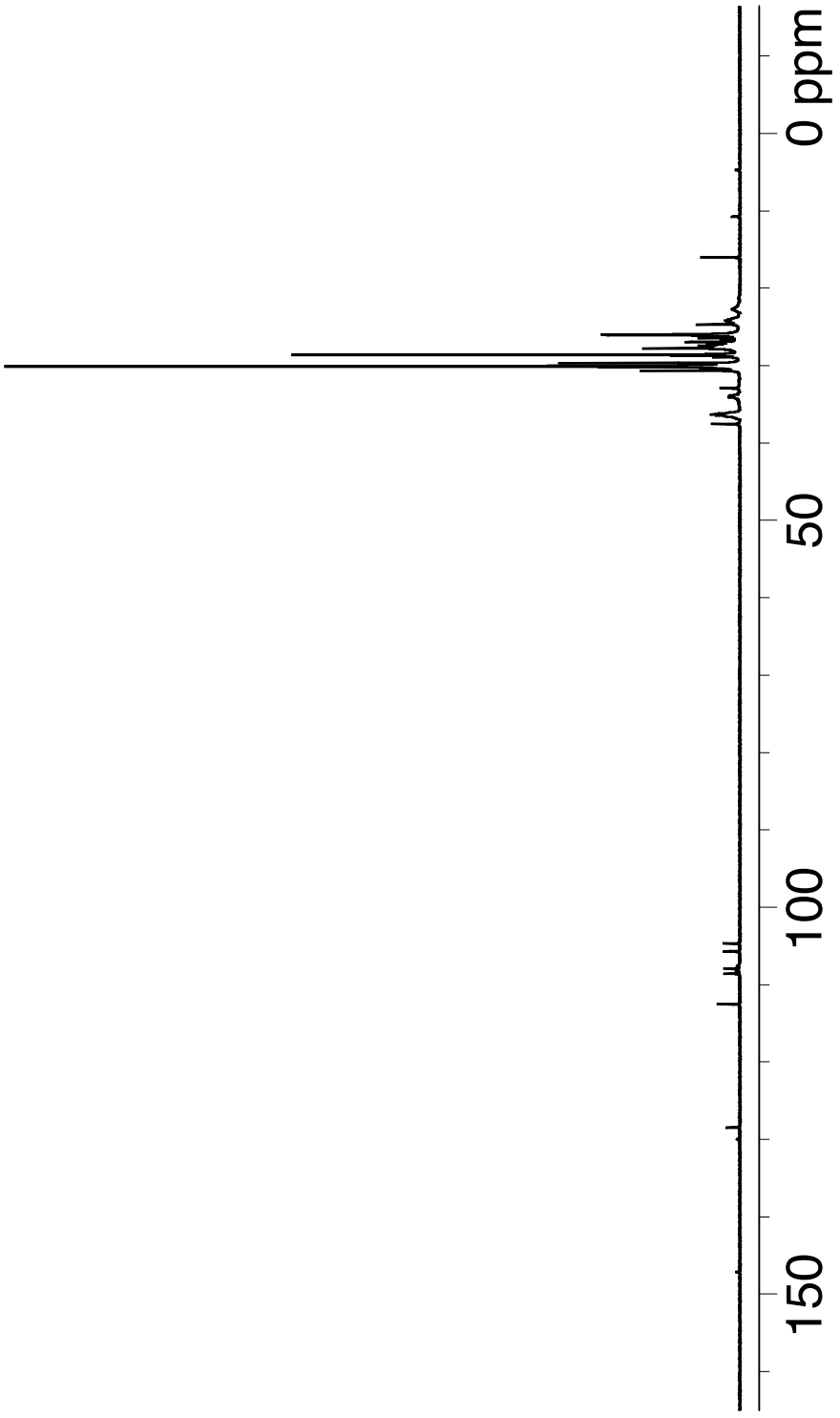

Figure 5.5.23. $^{13}C\{^{1}H\}$ NMR spectrum of **1** + 12 TIBA in methylcyclohexane-d14 at -40 °C.

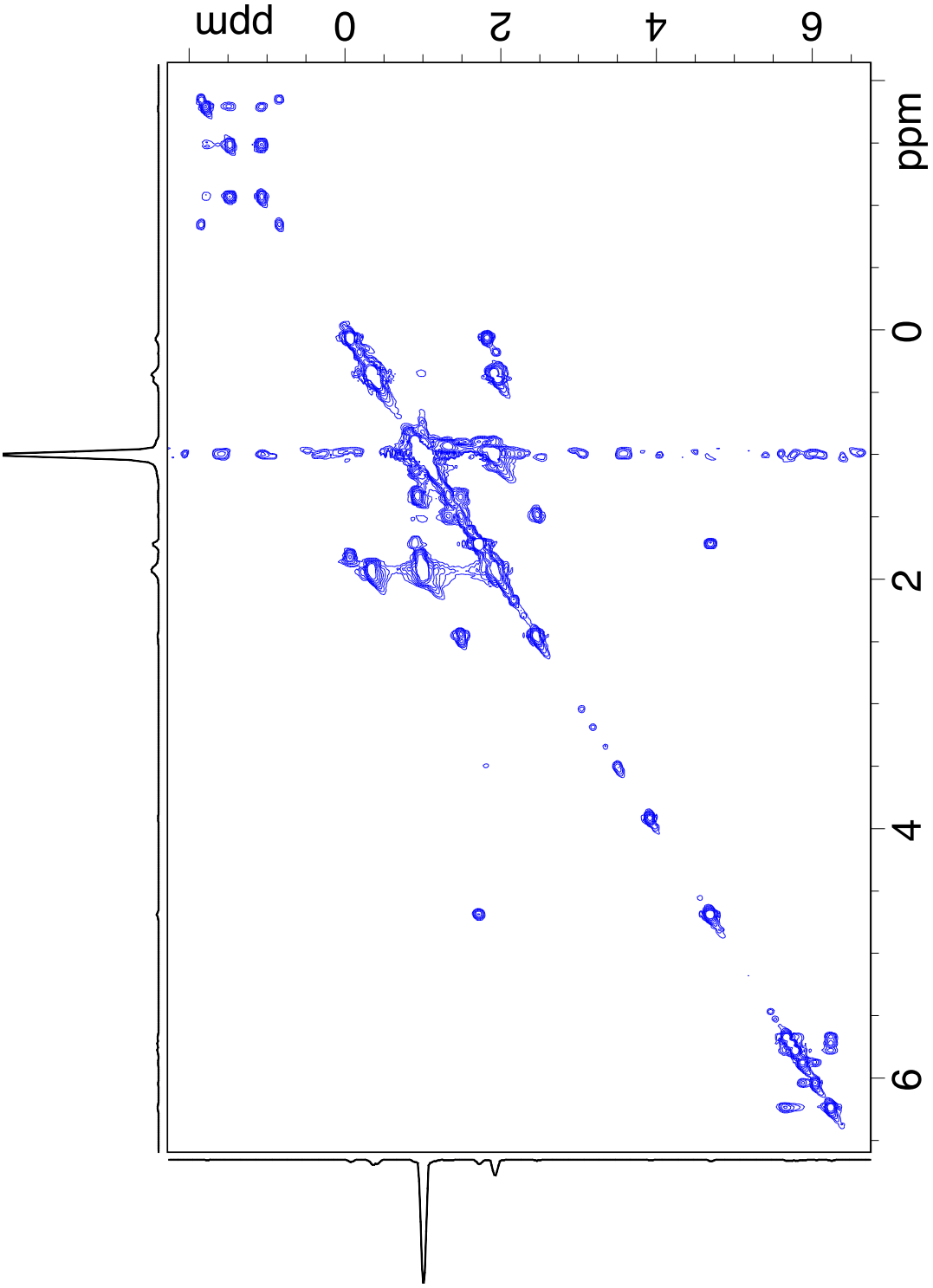

Figure 5.5.24. ^{1}H-^{1}H COSY NMR spectrum of **1** + 12 TIBA in methylcyclohexane-d14 at -40 °C.

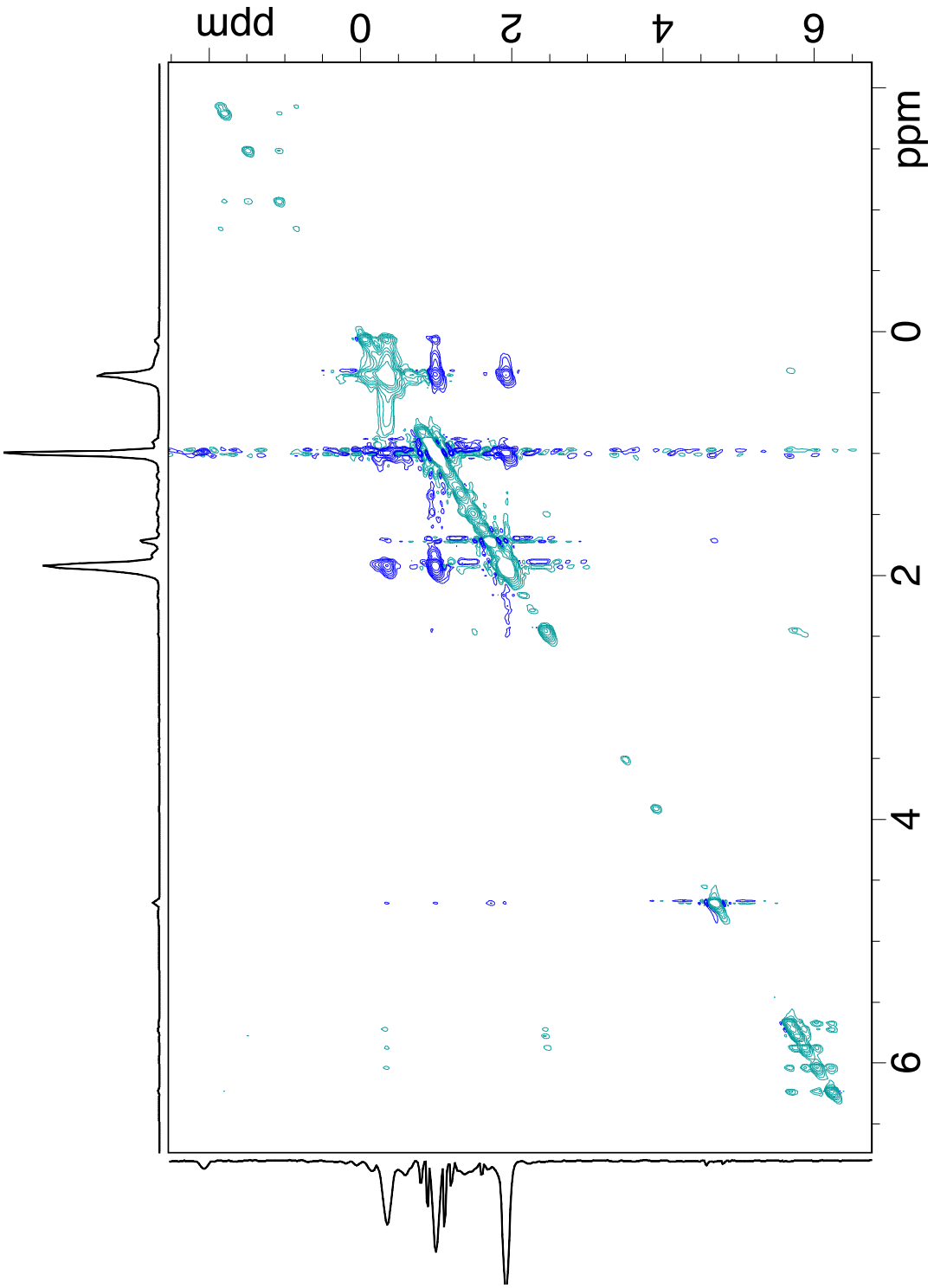

Figure 5.5.25. ^{1}H-^{1}H NOESY NMR spectrum of **1** + 12 TIBA in methylcyclohexane-d14 at -40 °C.

1 + 7 TIBA: in a N_2 filled glovebox, **1** (8 mg, 20 µmol) was loaded into a teflon – valved NMR tube and dissolved in toluene-d8 (0.5 mL). TIBA (35 µL, 0.14 mmol) was added and the solution turned pale yellow. Two equivalents/Zr of isobutene was observed in the ^{1}H NMR.

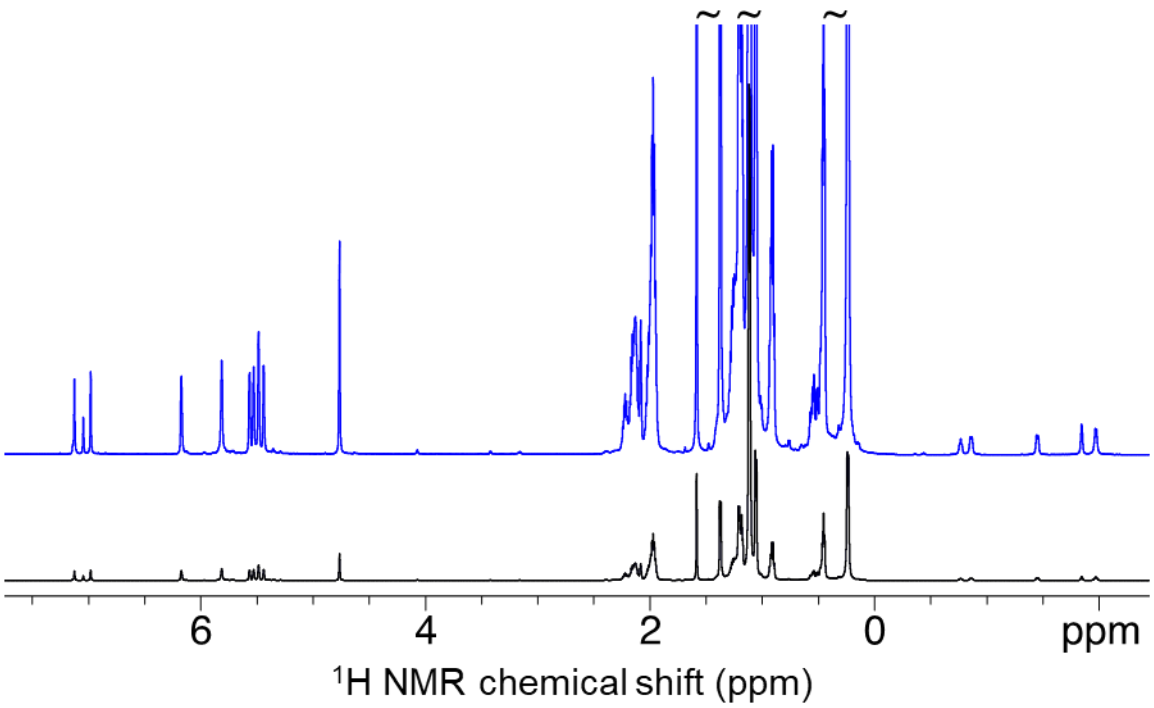

Figure 5.5.26. ^{1}H NMR spectra in toluene-d8 at -40 C of **1** + 7 TIBA.

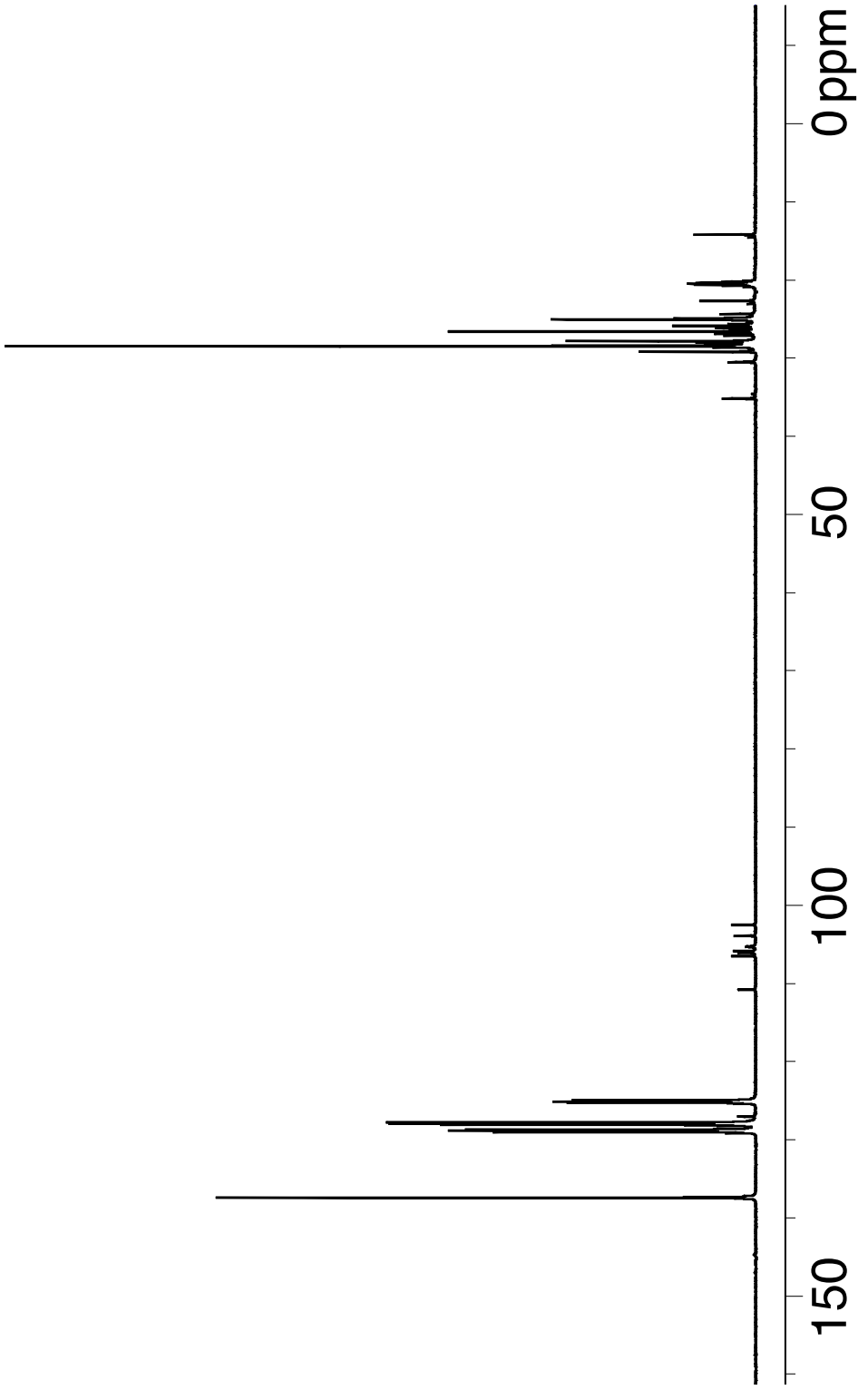

Figure 5.5.27. $^{13}C\{^{1}H\}$ NMR spectrum of **1** + 7 equiv. of TIBA in toluene-d8 at -40 C.

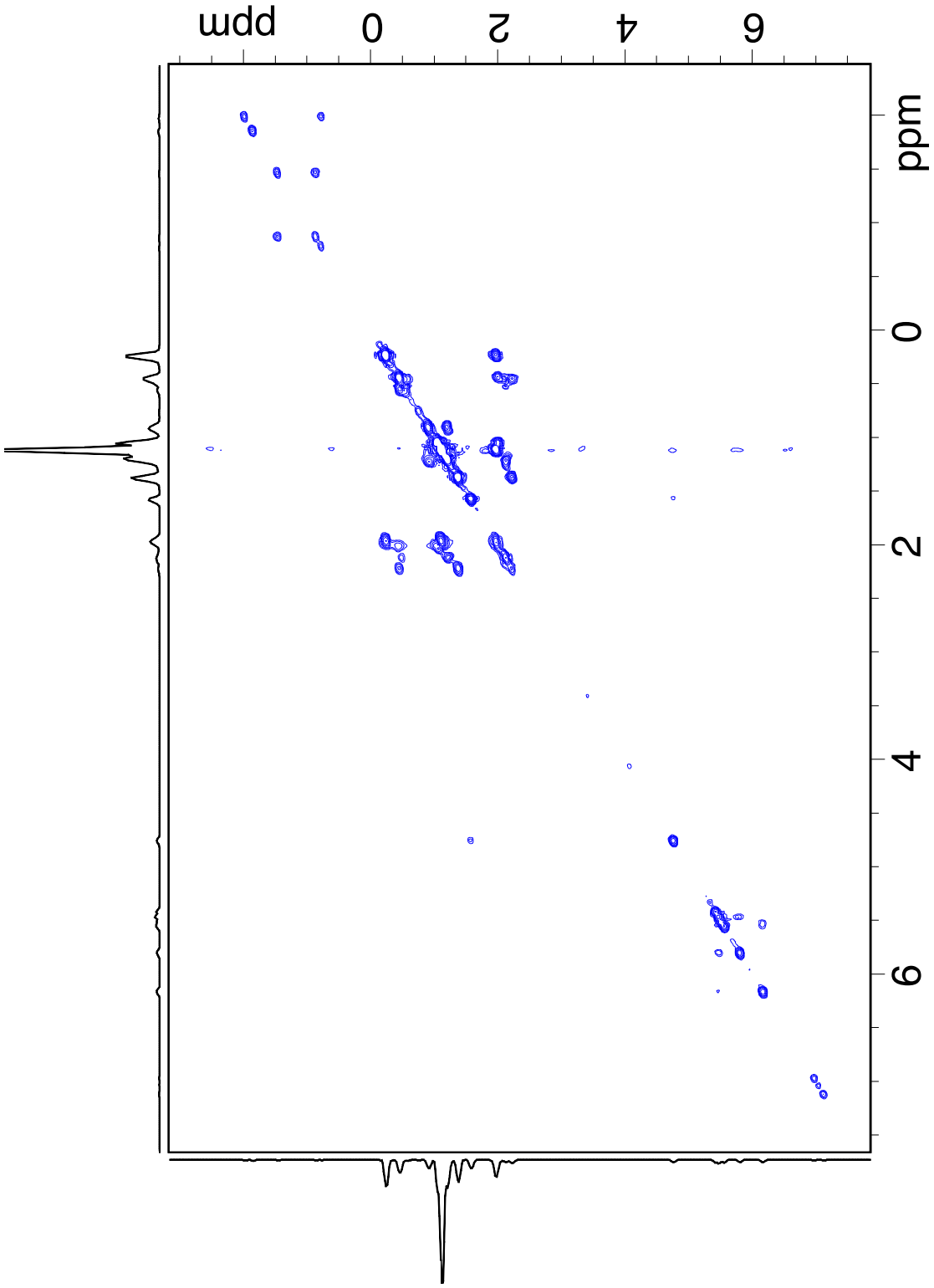

Figure 5.5.28. $^{13}C\{^{1}H\}$ NMR spectrum of **1** + 7 equiv. of TIBA in toluene-d8 at -40 C.

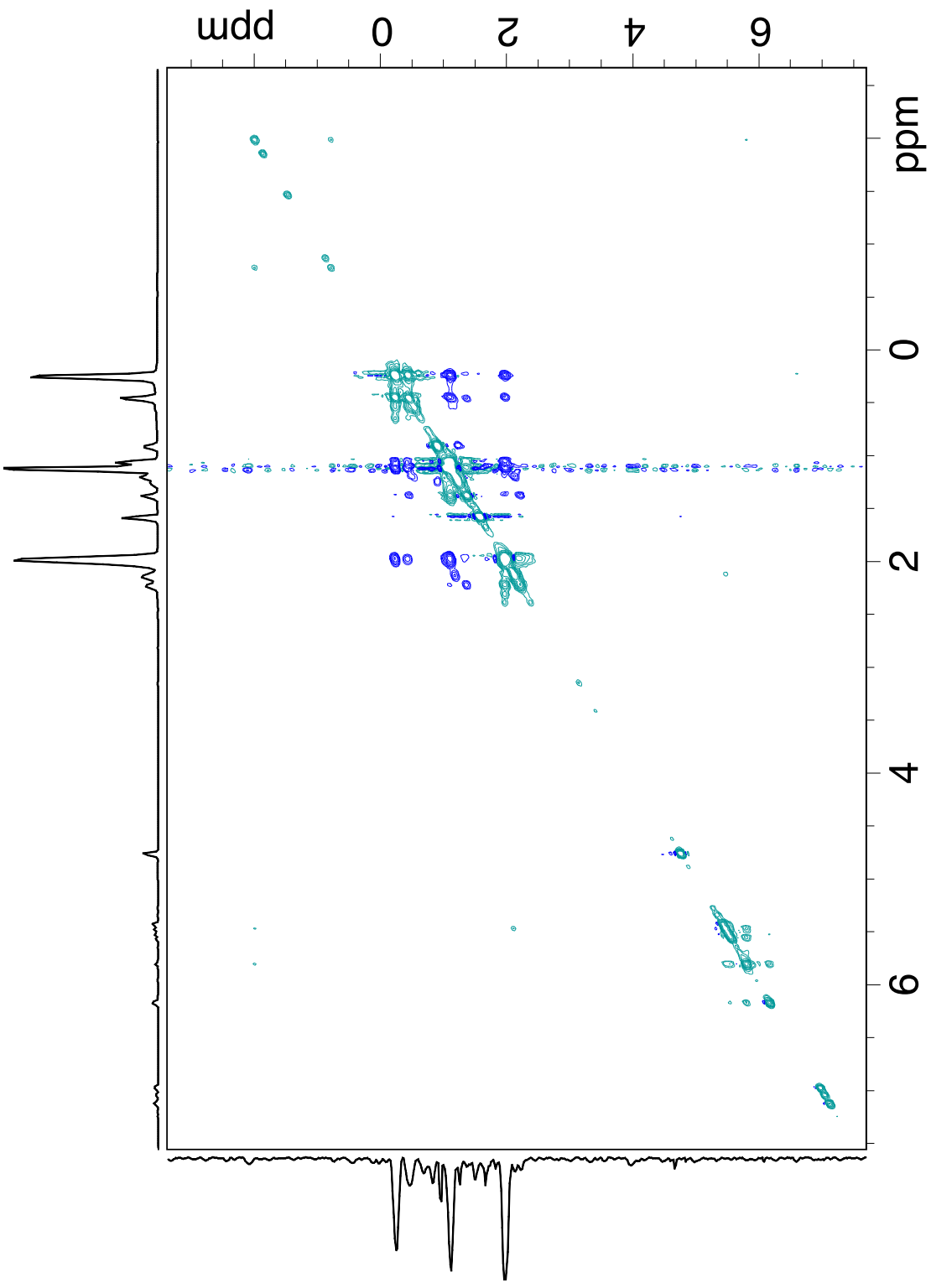

Figure 5.5.29. ^{1}H-^{1}H NOESY NMR **1** + 7 equiv. of TIBA in toluene-d8 at -40 °C.

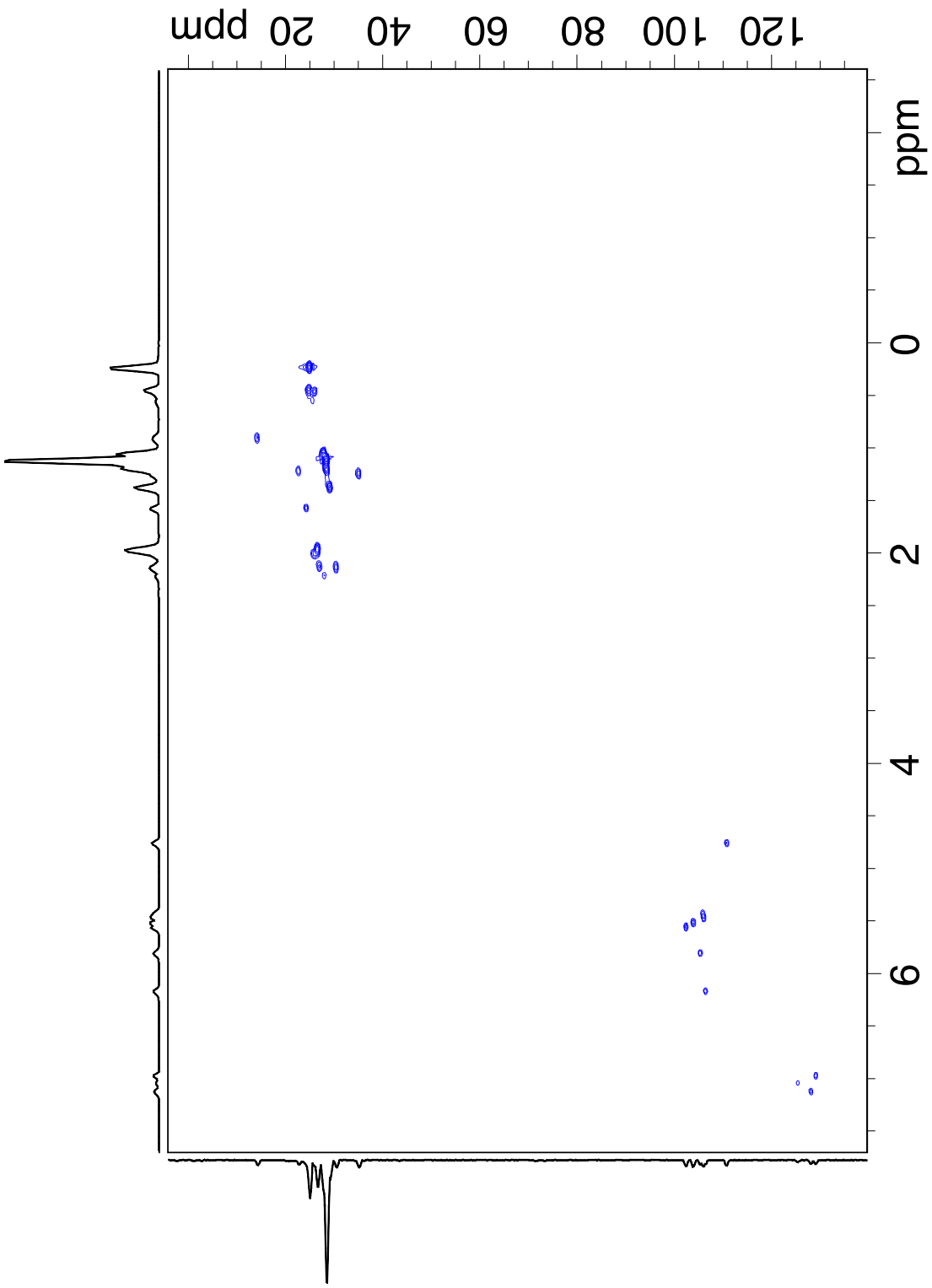

Figure 5.5.30. ^{1}H-^{13}C HSQC NMR spectrum of **1** + 7 TIBA in toluene-d8 at -40 °C.

1 + 2 TIBA: in a N_2 filled glovebox, **1** (8 mg, 20 µmol) was loaded into a Teflon-valved NMR tube and dissolved in toluene-d8 (0.5 mL). TIBA (10 µL, 0.04 mmol) was added and the solution turned pale yellow. Two equivalents/Zr of isobutene was observed in the ^{1}H NMR.

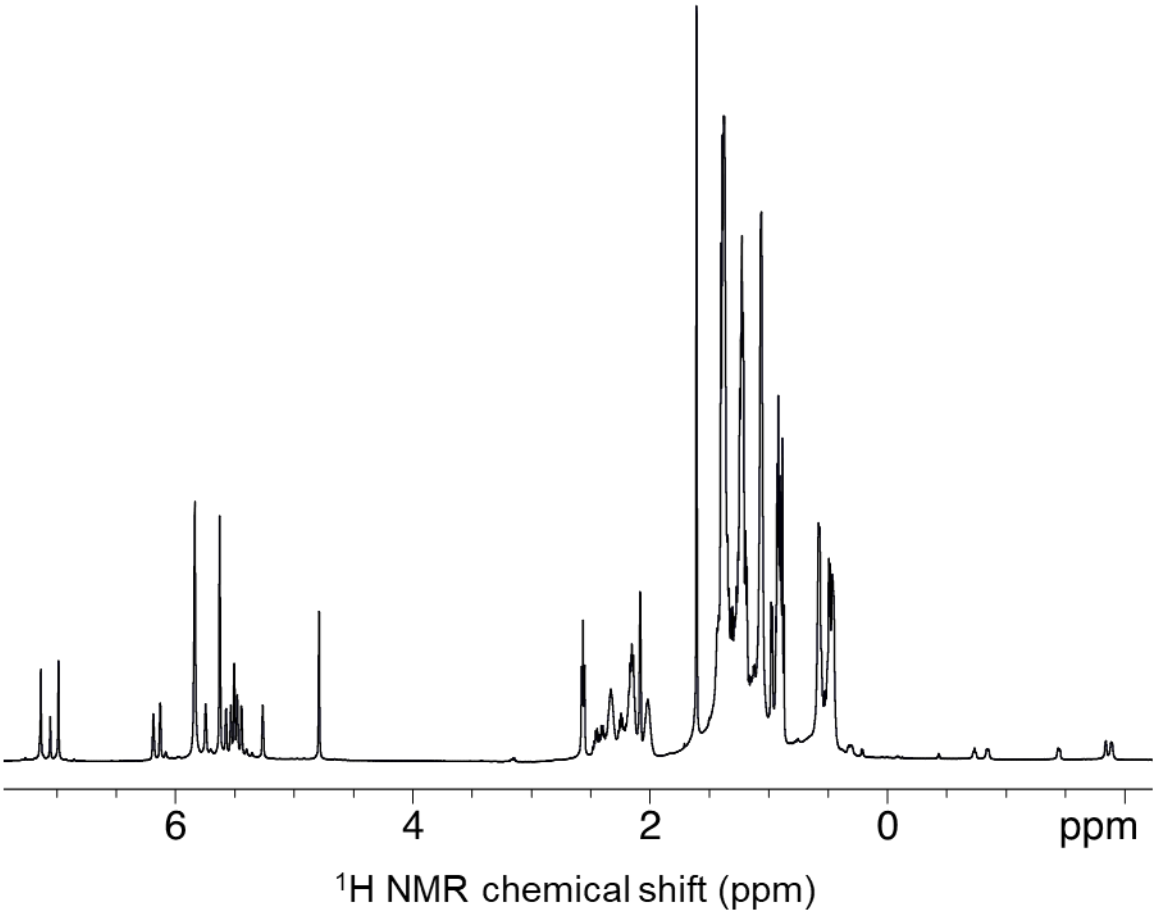

Figure 5.5.31. ^{1}H NMR spectra in toluene-d8 at -40 C of **1** + 2 TIBA.

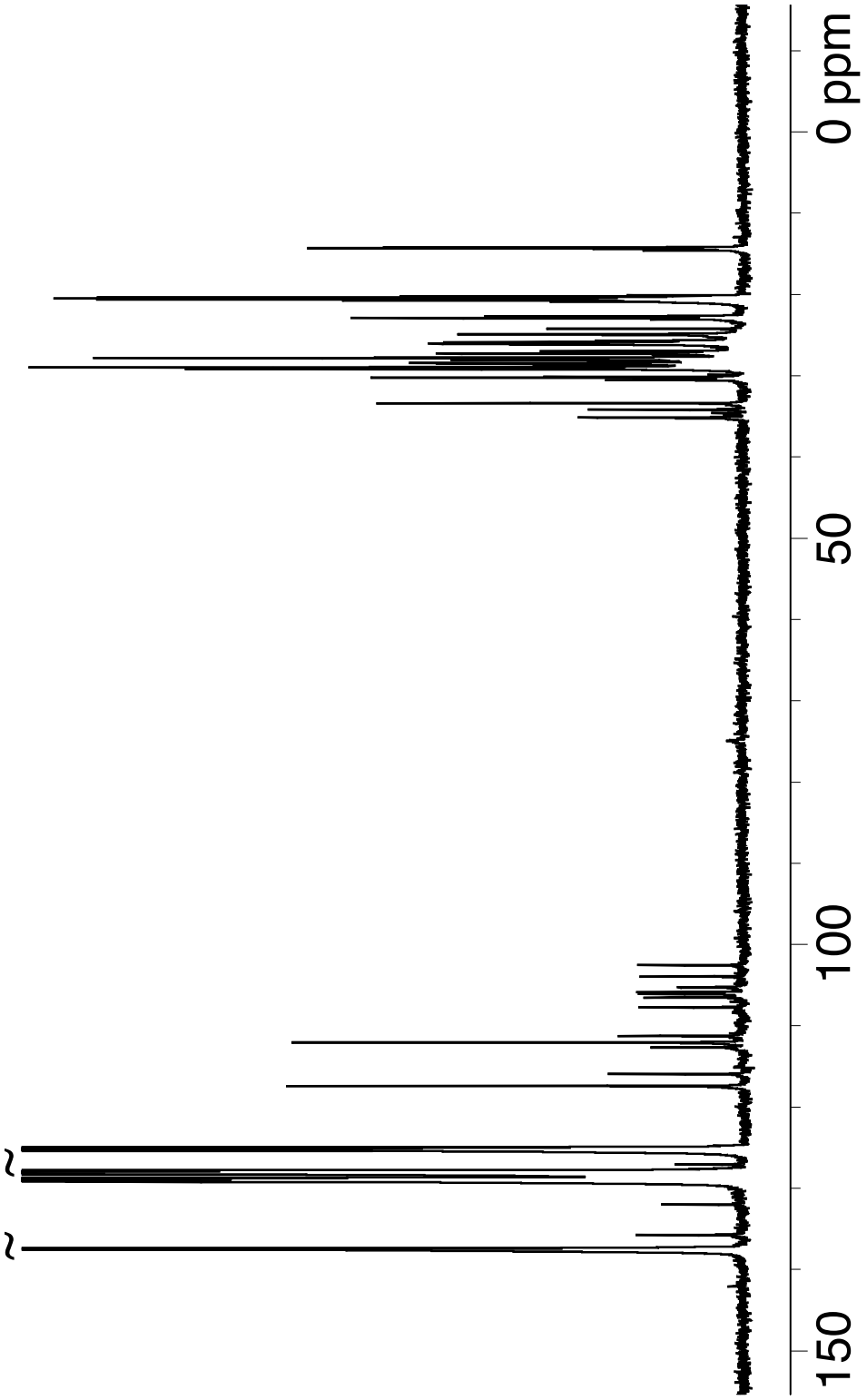

Figure 5.5.32. $^{13}C\{^{1}H\}$ NMR of **1** + 2 TIBA in toluene-d8 at -40 °C.

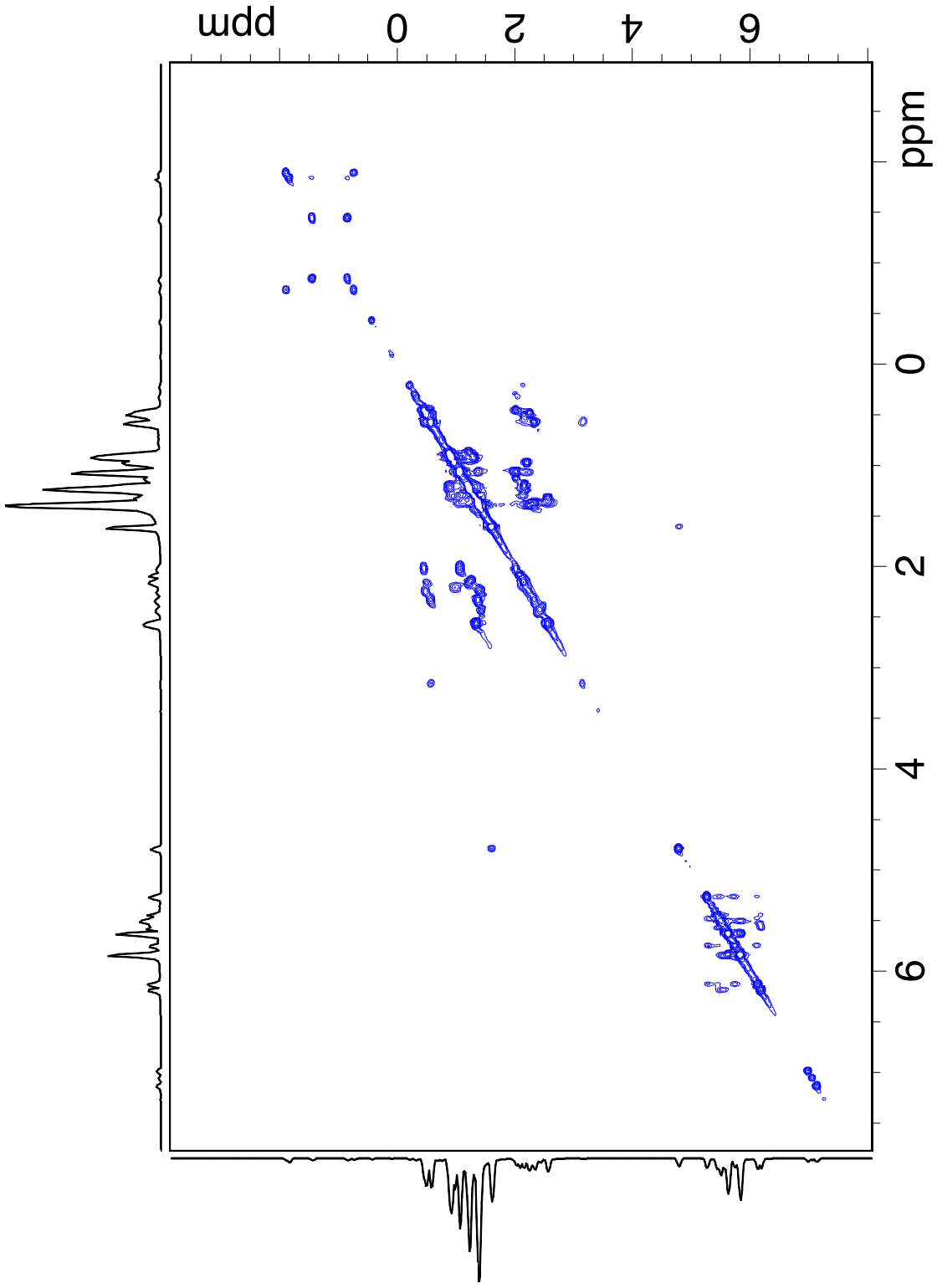

Figure 5.5.33. ^{1}H-^{1}H COSY NMR spectrum of **1** + 2 TIBA in toluene-d8 at -40 °C.

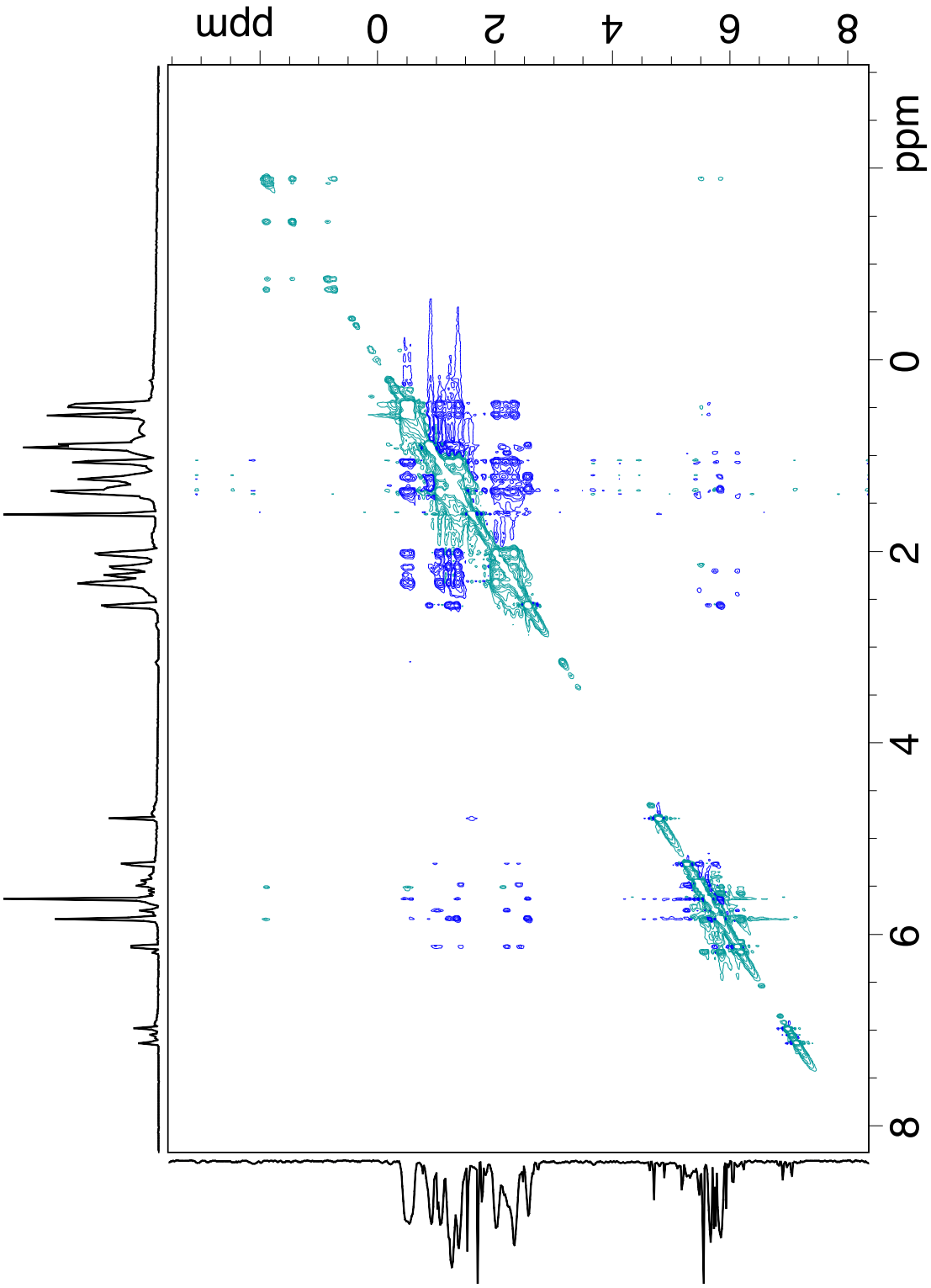

Figure 5.5.34. ^{1}H-^{1}H NOESY NMR spectrum of **1** + 2 TIBA in toluene-d8 at -40 °C.

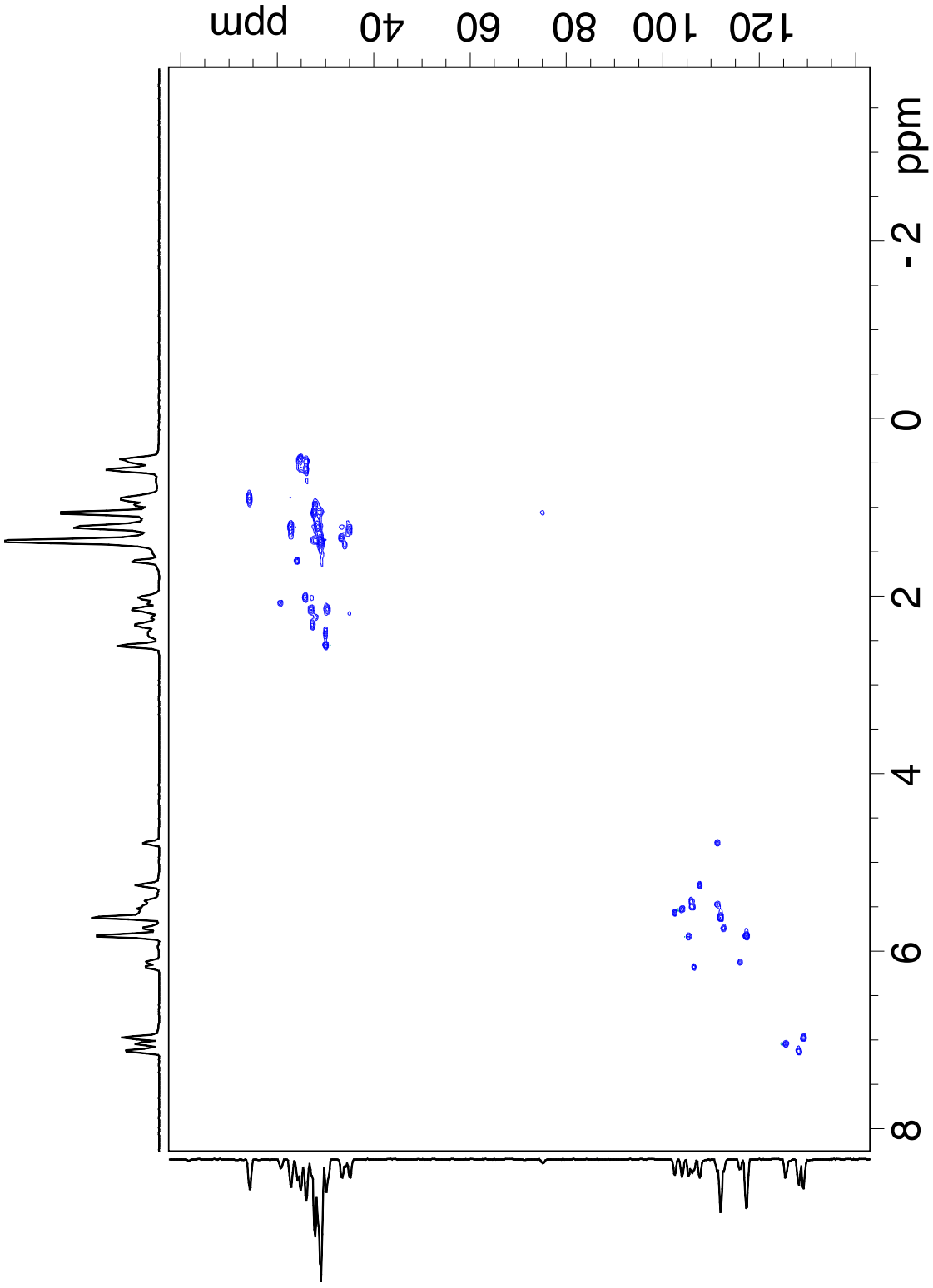

Figure 5.5.35. ^{1}H-^{13}C HSQC NMR spectrum of **1** + 2 TIBA in toluene-d8 at -40 °C.

4 + 24 TIBA: in a glovebox, **4** (8 mg, 12 µmol) was loaded into a teflon – valved NMR tube and dissolved in C_6D_{12} (0.5 mL). TIBA (70 µL, 0.24 mmol) was added and the solution turned pale yellow. Releases two equivalents/Zr of isobutene. The reaction occurs immediately, and the product mixture is stable at room temperature.

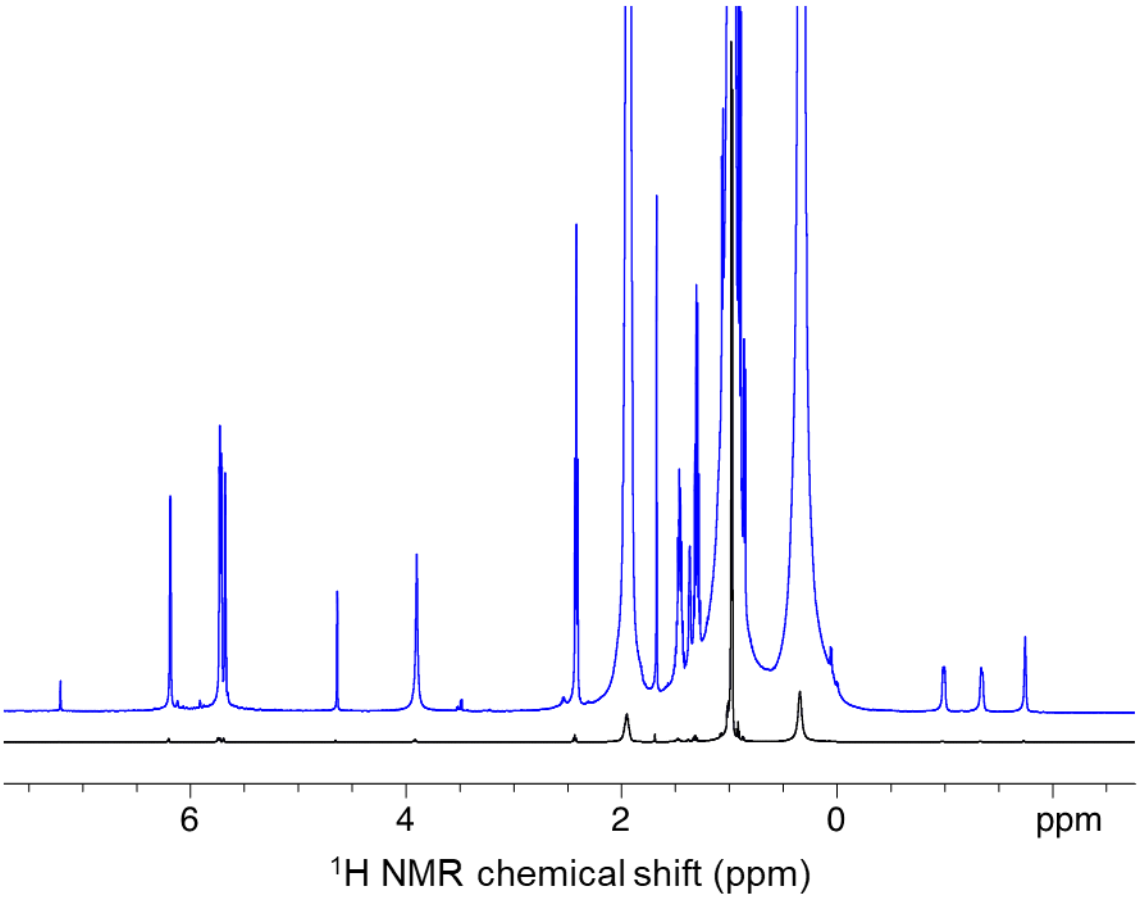

Figure 5.5.36. ^{1}H NMR spectrum of **4** + 24 TIBA in cyclohexane-d12 at 10 °C (black), 10 X zoom (blue).

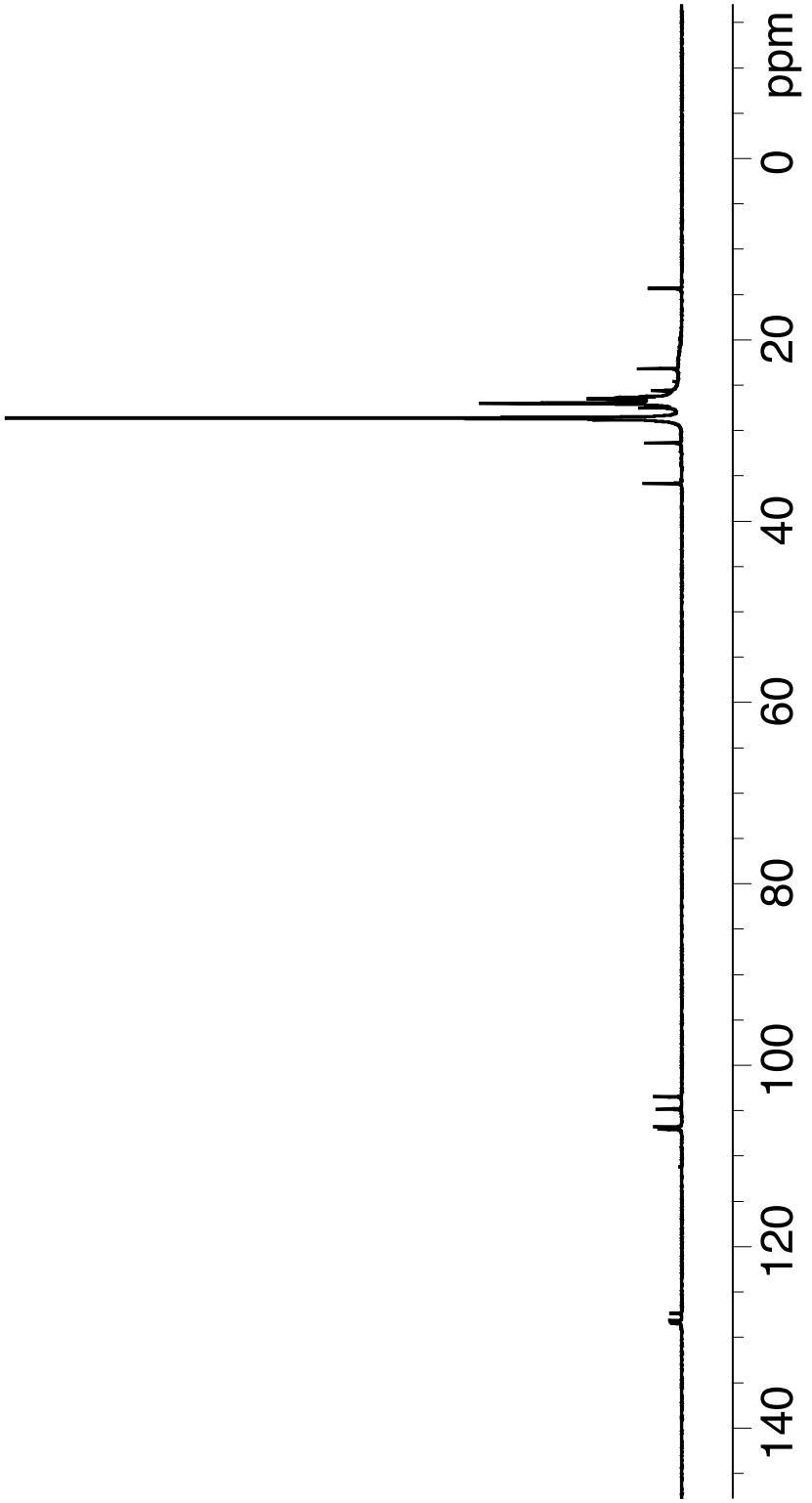

Figure 5.5.37. $^{13}C\{^{1}H\}$ NMR spectrum of **4** + 24 TIBA in cyclohexane-d12 at 10 °C.

Scheme 5.5.3. Formation of **5**

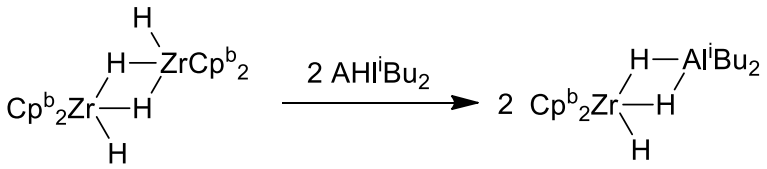

4 **5**

4 + 2 DIBALH (**5**): in a glovebox, **4** (8.0 mg, 20 µmol) was loaded into a teflon – valved NMR tube and dissolved in *toluene-d8*. Diisobutylaluminum hydride (4.3 µL, 20 µmol) was added and the solution turned pale yellow. Other ^{1}H NMR (C_7D_8, -40 °C, 600 MHz): 2.42 (bt, 4H, CpC**H**$_2$CH$_2$CH$_2$CH$_3$), 2.19 (m, 2H, Al(CH$_2$C**H**(CH$_3$)$_2$)$_2$), 1.44 (m, 4H, CpCH$_2$C**H**$_2$CH$_2$CH$_3$), 1.26 (m, 4H, CpCH$_2$CH$_2$C**H**$_2$CH$_3$), 1.24 (d, $^2J_{H\text{-}H}$ = 6.0 Hz, 12H, Al(CH$_2$CH(C**H**$_3$)$_2$)$_2$), 0.91 (t, $^2J_{H\text{-}H}$ = 7.1 Hz, 6H, CpCH$_2$CH$_2$CH$_2$C**H**$_3$), and 0.53 (d, $^2J_{H\text{-}H}$ = 7.1 Hz, 4H, Al(C**H**$_2$CH(CH$_3$)$_2$)$_2$) ppm.

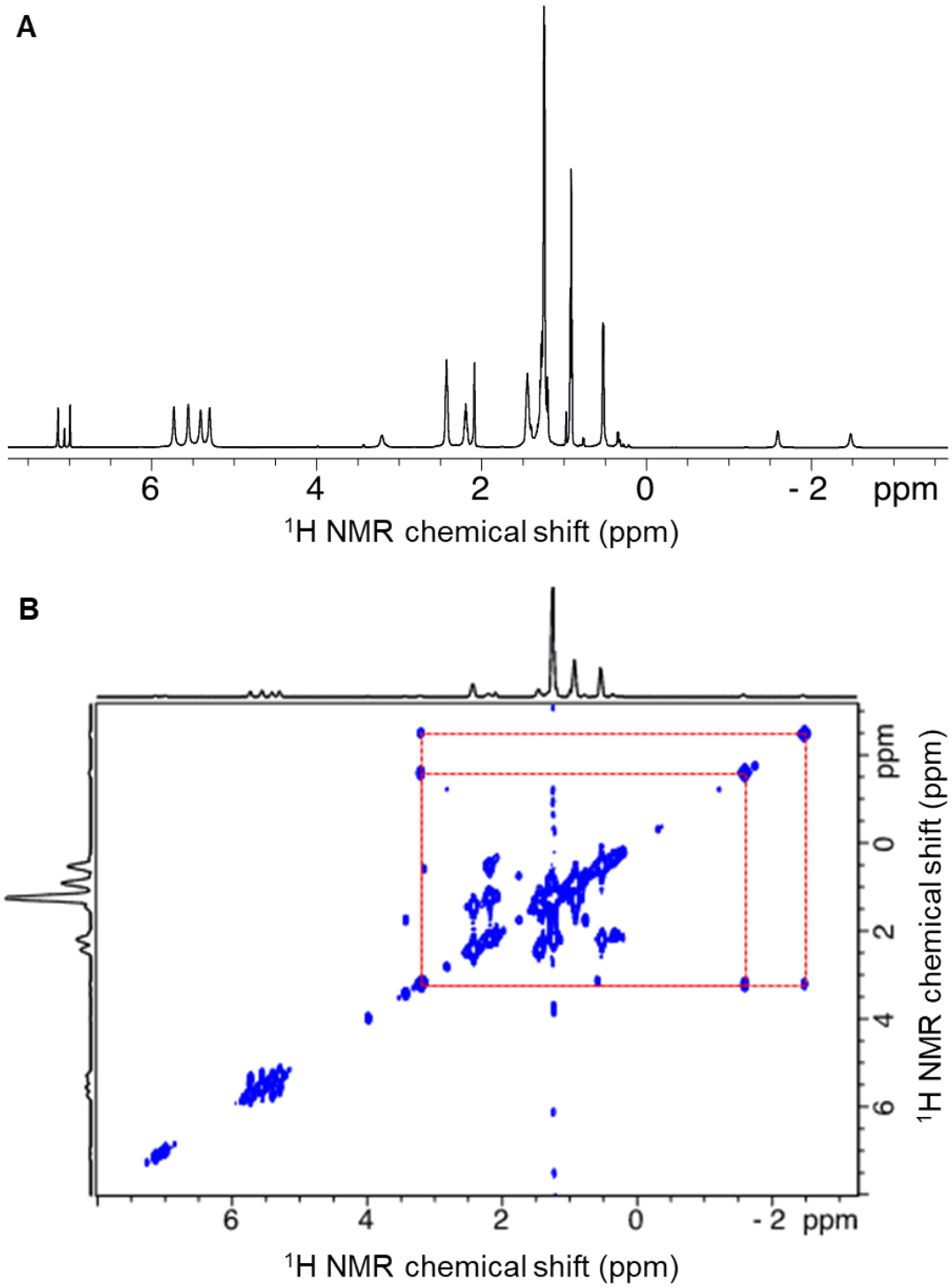

Figure 5.5.38. NMR spectra of **5** in toluene-d8 at -40 °C: A) ^{1}H and B) ^{1}H-^{1}H COSY with the M-H correlations highlighted by the red dashes.

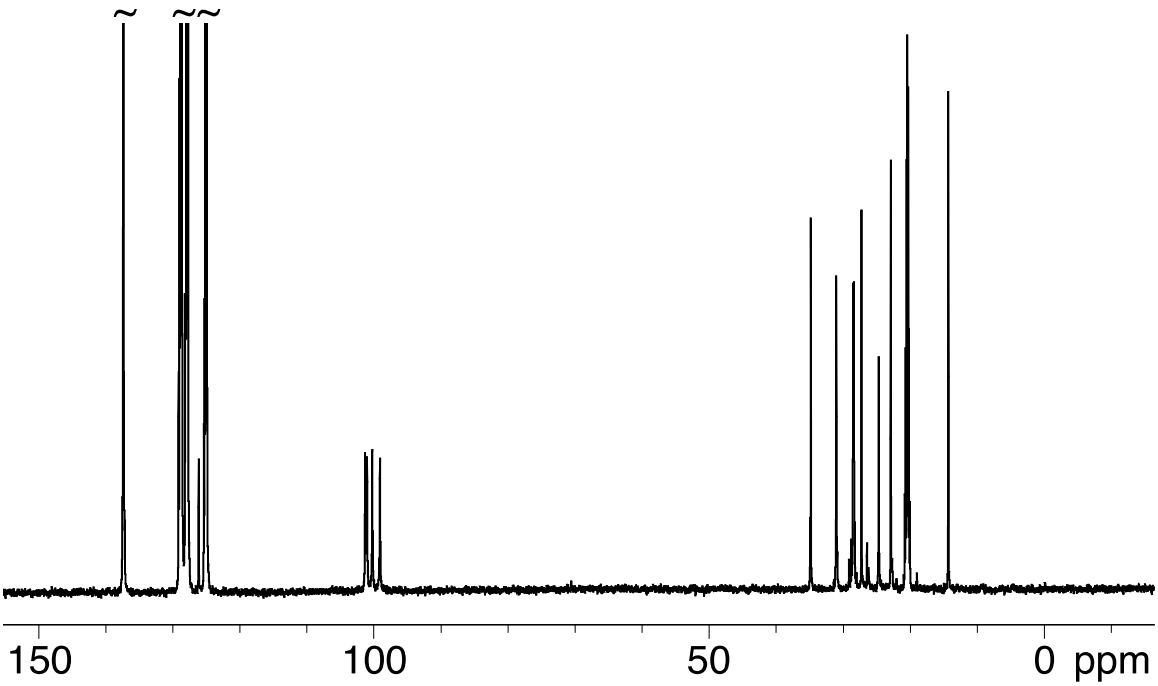

Figure 5.5.39. $^{13}C\{^{1}H\}$ NMR spectrum of **4** + 2 DIBALH in toluene-d8 at -40 °C.

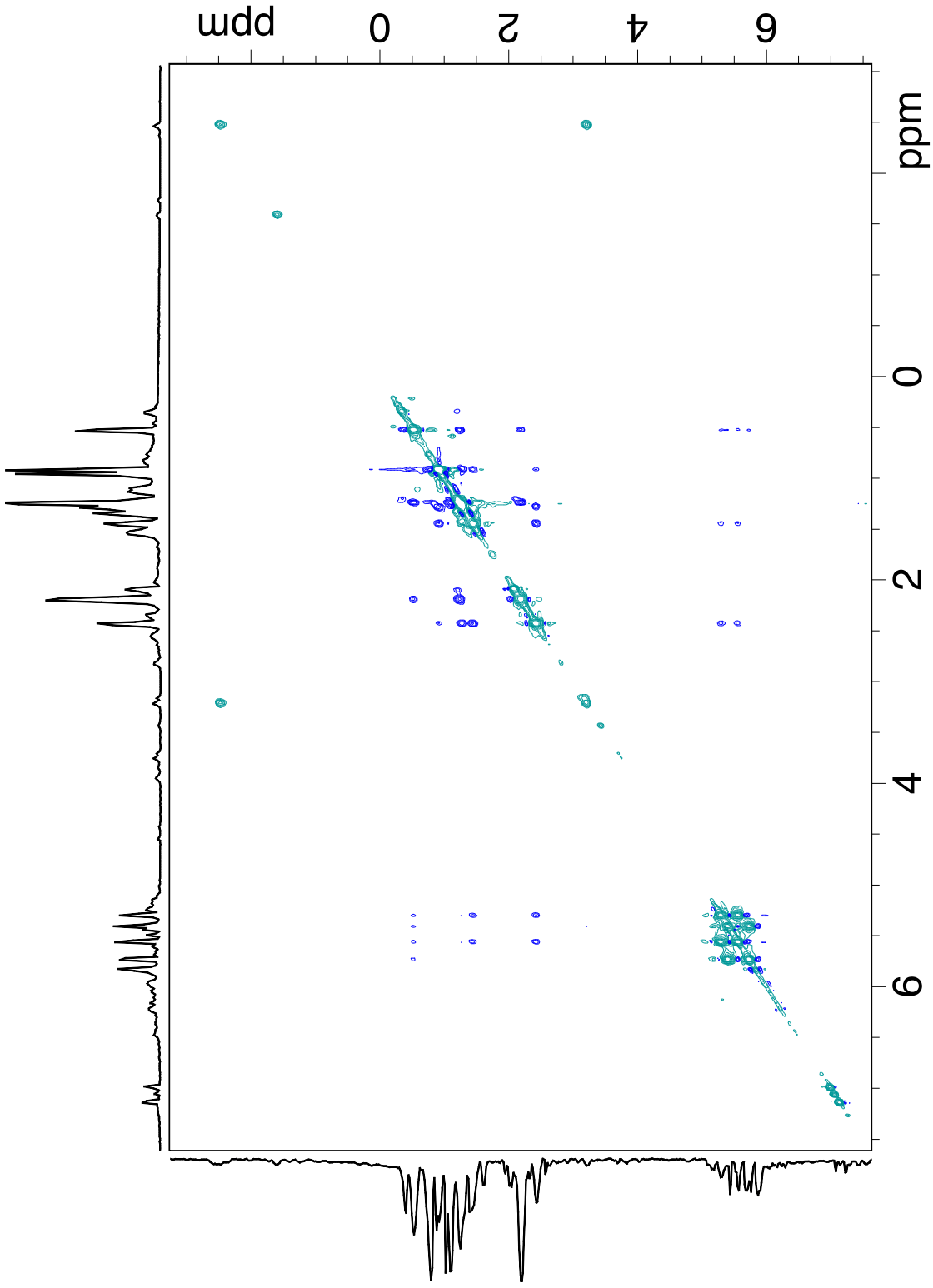

Figure 5.5.40. ^{1}H-^{1}H NOESY NMR spectrum of **4** + 2 DIBALH in toluene-d8 at -40 °C.

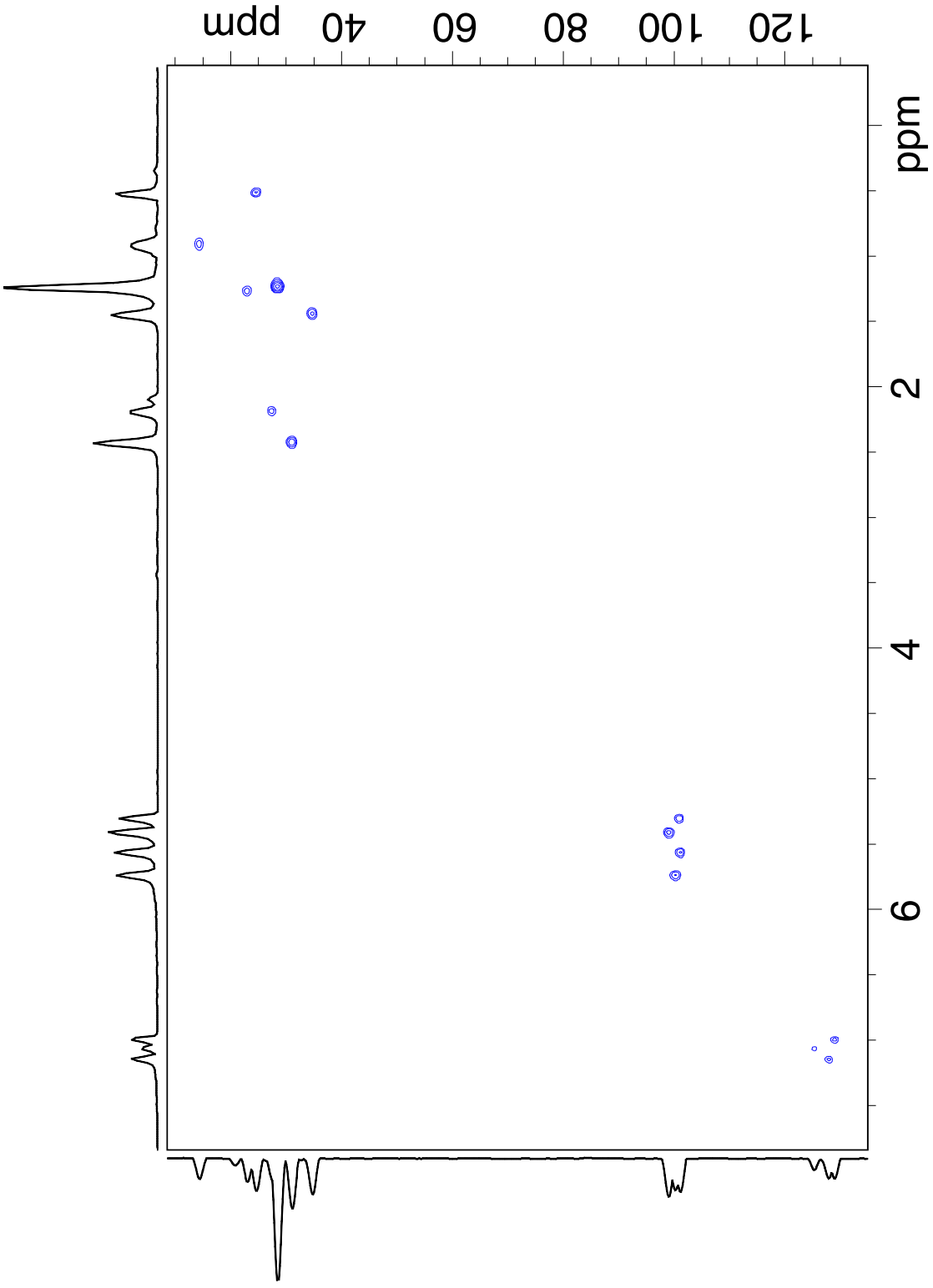

Figure 5.5.41. ^{1}H-^{13}C HSQC NMR spectrum of **4** + 2 DIBALH in toluene-d8 at -40 °C.

4 + 2 DIBALH + 2 TIBA (**2**): in a glovebox, **4** (8.0 mg, 12 μmol) was loaded into a teflon – valved NMR tube and dissolved in $C_6D_{11}CD_3$ (0.5 mL) or cyclohexane-d12. DIBALH (4.3 μL, 24 μmol) then TIBA (6.0 μL, 24 μmol) were added and the solution turned pale yellow. Other ^{1}H NMR (C_7D_{14}, -40 °C, 600 MHz): 2.43 (t, $^2J_{H-H}$ = 7.5 Hz, 4H, CpC**H**$_2$CH$_2$CH$_2$CH$_3$), 1.95 (m, 2H, HAl(CH$_2$C**H**(CH$_3$)$_2$)$_2$), 1.80 (m, 3H, Al(CH$_2$C**H**(CH$_3$)$_2$)$_3$), 1.46 (m, 4H, CpCH$_2$C**H**$_2$CH$_2$CH$_3$), 1.31 (m, 4H, CpCH$_2$CH$_2$C**H**$_2$CH$_3$), 0.99 (m, 12H, HAl(CH$_2$CH(C**H**$_3$)$_2$)$_2$), 0.95 (d, $^2J_{H-H}$ = 6.7 Hz, 18H, Al(CH$_2$CH(C**H**$_3$)$_2$)$_3$), 0.91 (t, $^2J_{H-H}$ = 7.4 Hz, 6H, CpCH$_2$CH$_2$CH$_2$C**H**$_3$), 0.45 (m, 4H, HAl(C**H**$_2$CH(CH$_3$)$_2$)$_2$), and 0..30 (d, $^2J_{H-H}$ = 6.7 Hz, 6H, Al(C**H**$_2$CH(CH$_3$)$_2$)$_3$) ppm. Other ^{1}H NMR (C_6D_{12}, 10 °C, 600 MHz): 2.46 (t, $^2J_{H-H}$ = 7.7 Hz, 4H, CpC**H**$_2$CH$_2$CH$_2$CH$_3$), 1.97 (m, 2H, HAl(CH$_2$C**H**(CH$_3$)$_2$)$_2$), 1.85 (m, 3H, Al(CH$_2$C**H**(CH$_3$)$_2$)$_3$), 1.50 (m, 4H, CpCH$_2$C**H**$_2$CH$_2$CH$_3$), 1.33 (q, $^2J_{H-H}$ = 7.5 Hz, 4H, CpCH$_2$CH$_2$C**H**$_2$CH$_3$), 1.00 (d, $^2J_{H-H}$ = 6.4 Hz, 12H, HAl(CH$_2$CH(C**H**$_3$)$_2$)$_2$), 0.97 (d, $^2J_{H-H}$ = 6.5 Hz, 18H, Al(CH$_2$CH(C**H**$_3$)$_2$)$_3$), 0.92 (t, $^2J_{H-H}$ = 7.3 Hz, 6H, CpCH$_2$CH$_2$CH$_2$C**H**$_3$), 0.34 (d, $^2J_{H-H}$ = 6.5 Hz, 6H, HAl(C**H**$_2$CH(CH$_3$)$_2$)$_2$), and 0.08 (d, $^2J_{H-H}$ = 6.5 Hz, 6H, Al(C**H**$_2$CH(CH$_3$)$_2$)$_3$) ppm.

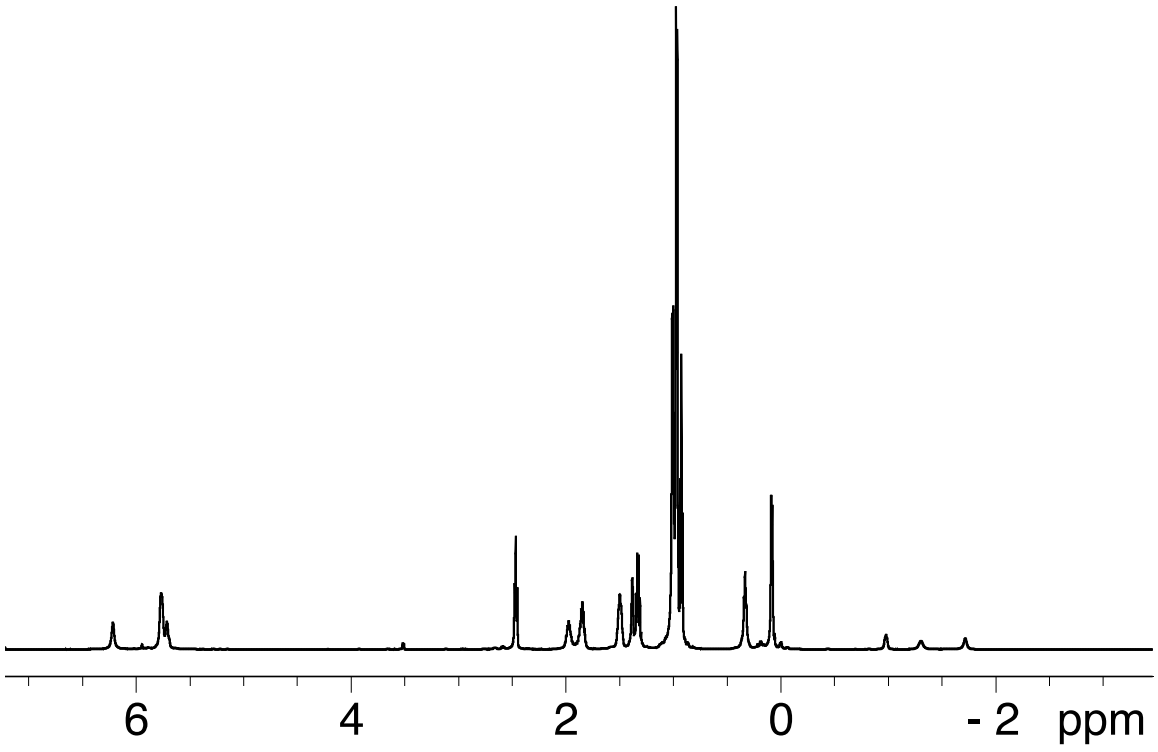

Figure 5.5.42. ^{1}H NMR spectrum of **2** in cyclohexane-d12 at 10 °C.

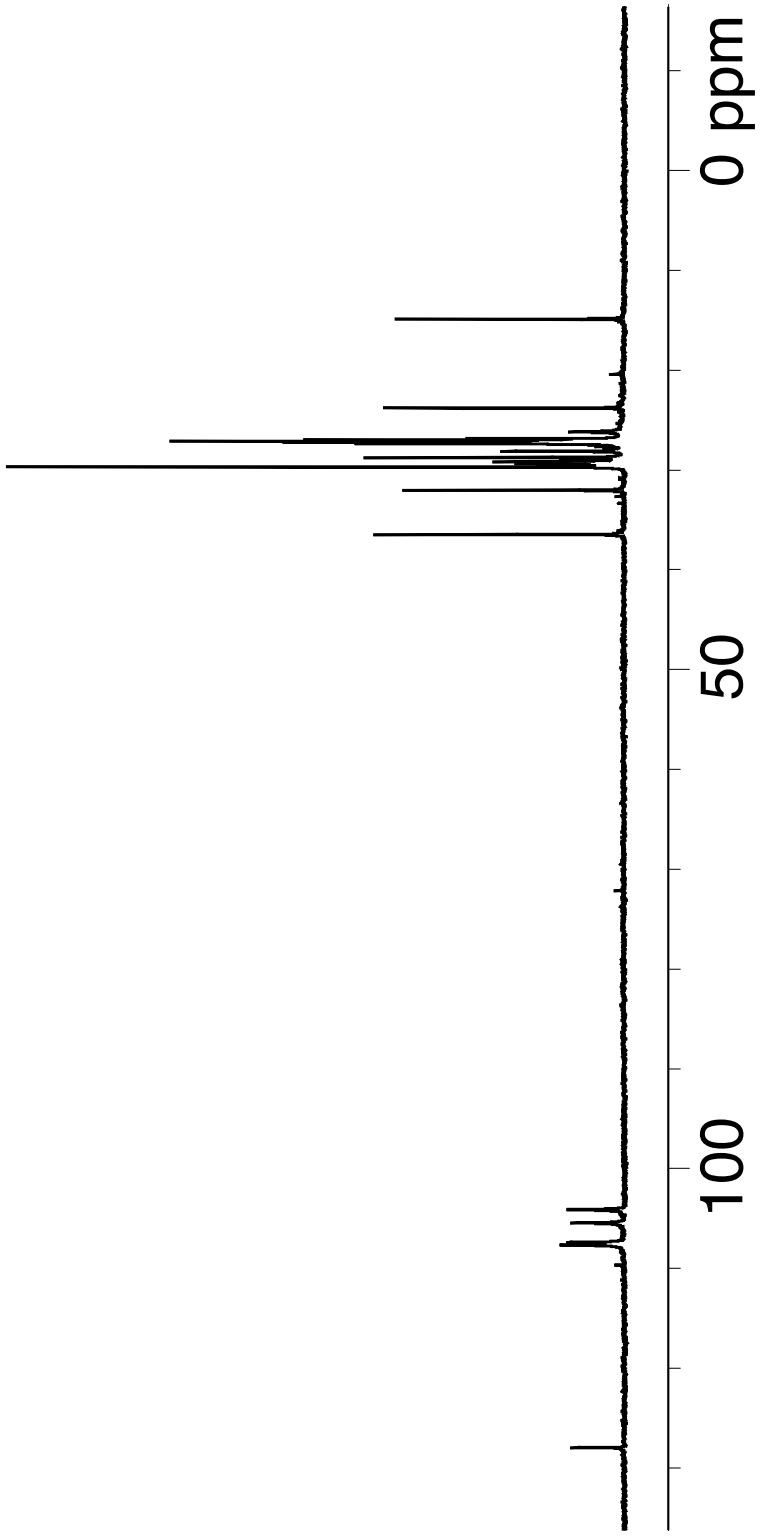

Figure 5.5.43. $^{13}C\{^{1}H\}$ NMR spectrum of **2** in cyclohexane-d12 at 10 °C.

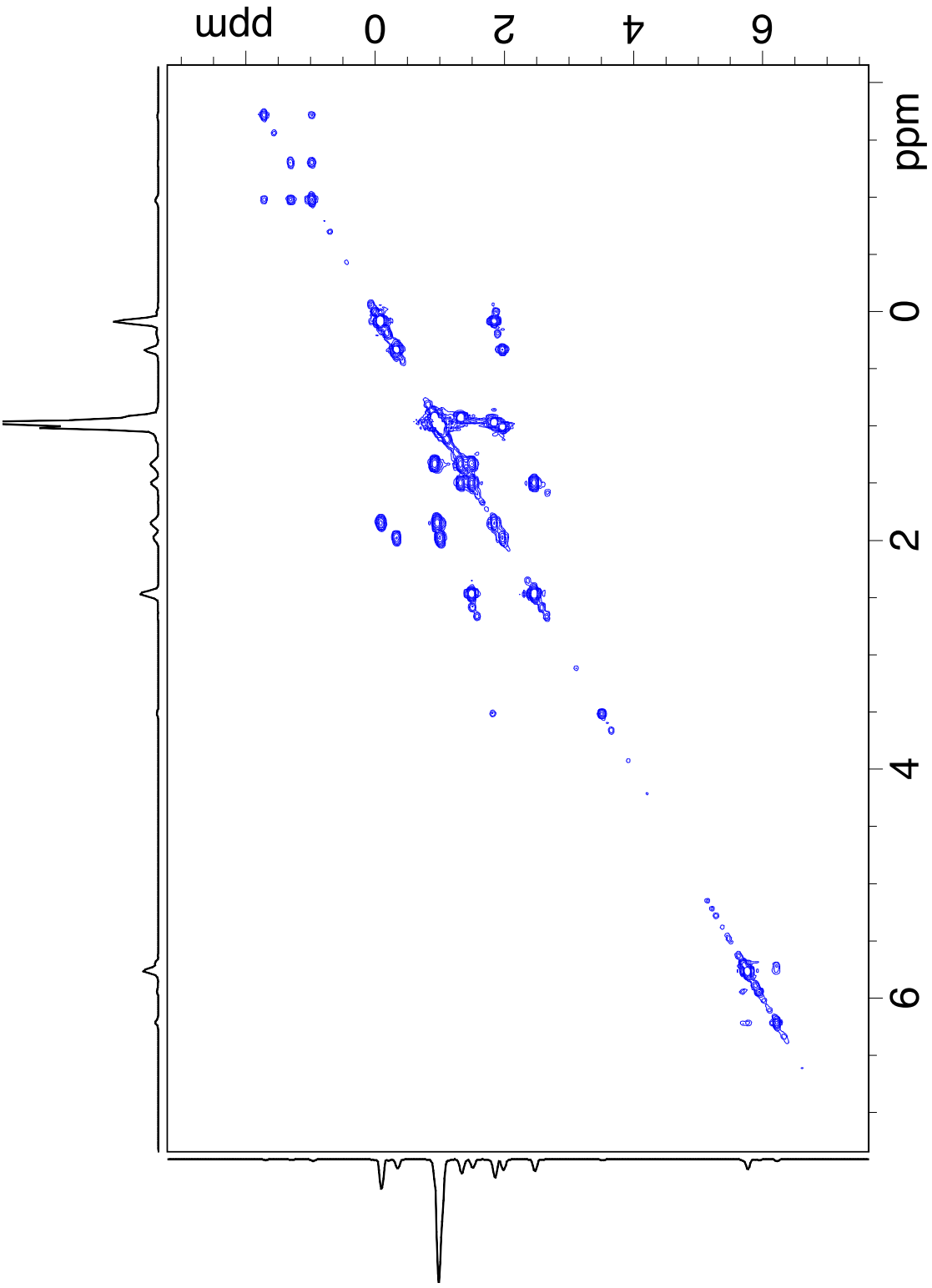

Figure 5.5.44. ^{1}H-^{1}H COSY spectrum of **2** in cyclohexane-d12 at 10 °C.

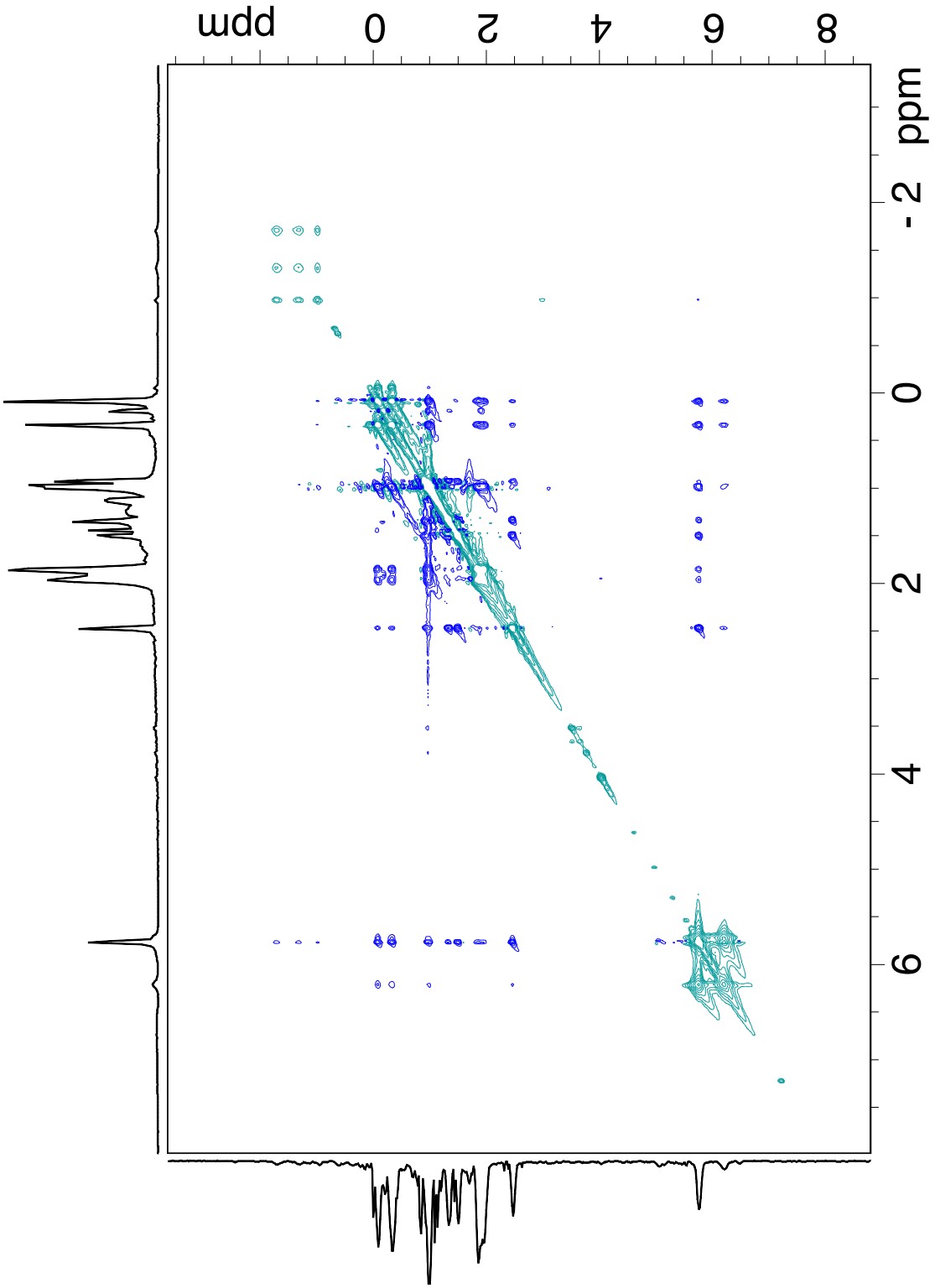

Figure 5.5.45. ^{1}H-^{1}H NOESY spectrum of **2** in cyclohexane-d12 at 10 °C.

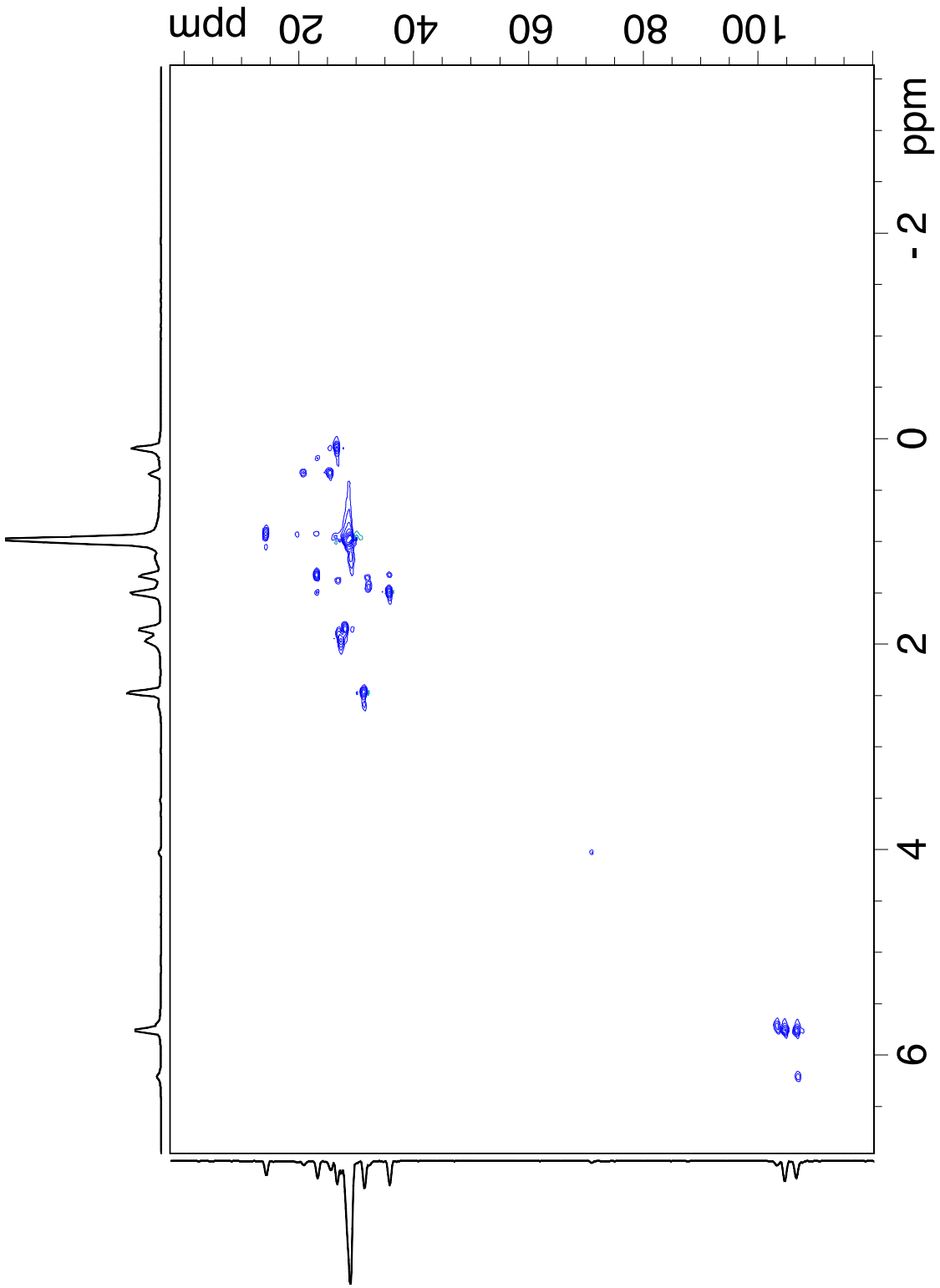

Figure 5.5.46. ^{1}H-^{13}C HSQC NMR spectrum of **2** in cyclohexane-d12 at 10 °C.

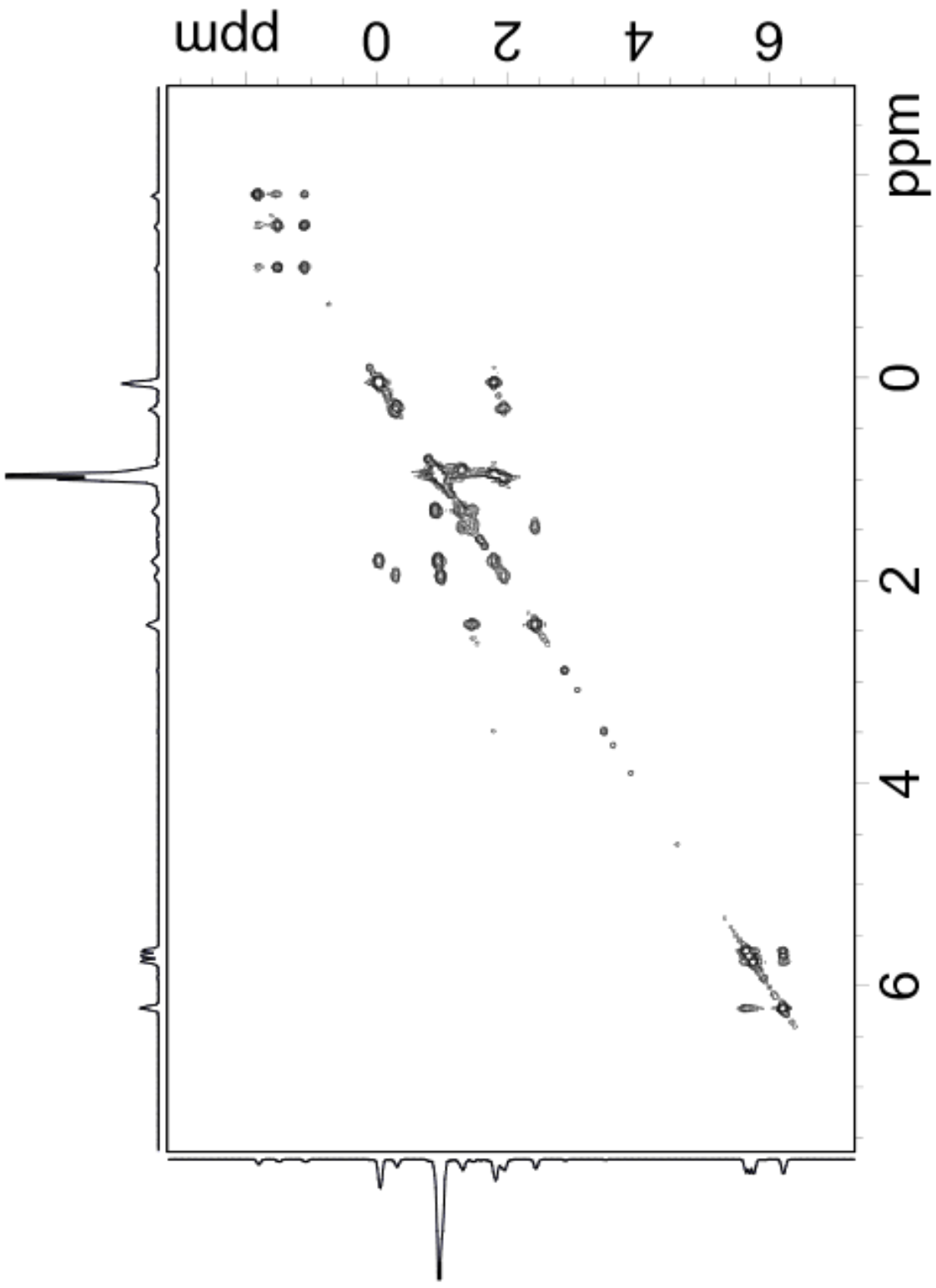

Figure 5.5.47. ^{1}H-^{1}H COSY NMR spectrum of **2** in methylcyclohexane-d14 at -40 °C.

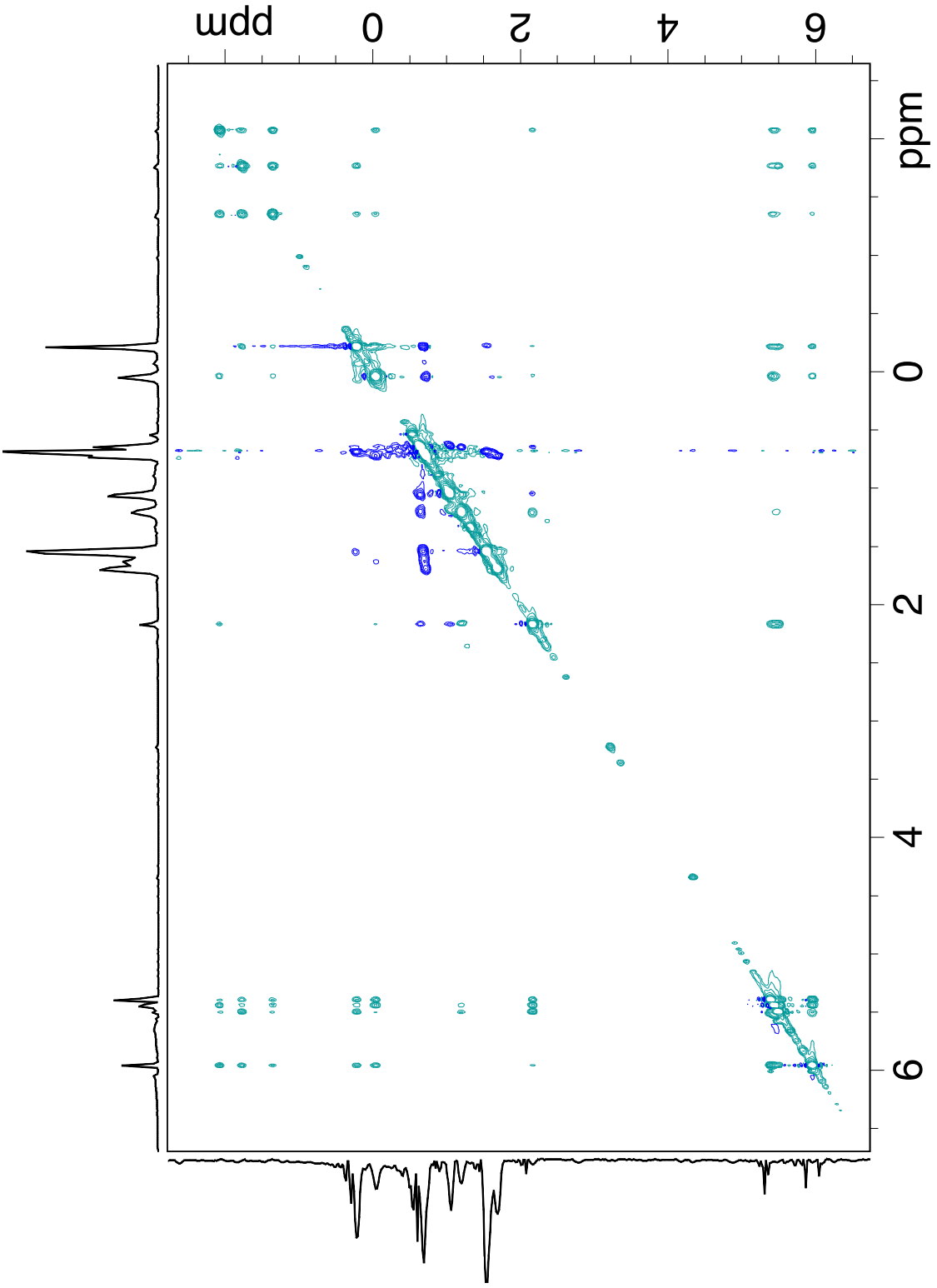

Figure 5.5.48. ^{1}H-^{1}H NOESY NMR spectrum of **2** in methylcyclohexane-d14 at -40 °C.

5.6 References

(1) McDaniel, M. P. A Review of the Phillips Supported Chromium Catalyst and Its Commercial Use for Ethylene Polymerization. In *Advances in Catalysis*; Academic Press, 2010; Vol. 53, pp 123–606. https://doi.org/10.1016/S0360-0564(10)53003-7.

(2) Geyer, R.; Jambeck, J. R.; Law, K. L. Production, Use, and Fate of All Plastics Ever Made. *Sci. Adv.* **2017**, *3* (7), 1–5. https://doi.org/10.1126/sciadv.1700782.

(3) Hoff, R.; Mathers, R. T. *HANDBOOK OF TRANSITION METAL POLYMERIZATION CATALYSTS*; Hoff, R., Mathers, R. T., Eds.; John Wiley and Sons: Hoboken, NJ, USA, 2010. https://doi.org/10.1002/9780470504437.

(4) Bochmann, M. The Chemistry of Catalyst Activation: The Case of Group 4 Polymerization Catalysts. *Organometallics* **2010**, *29* (21), 4711–4740. https://doi.org/10.1021/om1004447.

(5) Kaminsky, W. Highly Active Metallocene Catalysts for Olefin Polymerization. *J. Chem. Soc. - Dalt. Trans.* **1998**, No. 9, 1413–1418. https://doi.org/10.1039/a800056e.

(6) Stalzer, M. M.; Delferro, M.; Marks, T. J. Supported Single-Site Organometallic Catalysts for the Synthesis of High-Performance Polyolefins. *Catal. Letters* **2015**, *145* (1), 3–14. https://doi.org/10.1007/s10562-014-1427-x.

(7) Copéret, C.; Allouche, F.; Chan, K. W.; Conley, M. P.; Delley, M. F.; Fedorov, A.; Moroz, I. B.; Mougel, V.; Pucino, M.; Searles, K.; Yamamoto, K.; Zhizhko, P. A. Bridging the Gap between Industrial and Well-Defined Supported Catalysts. *Angew. Chemie Int. Ed.* **2018**, *57* (22), 6398–6440. https://doi.org/10.1002/anie.201702387.

(8) Breslow, D. S.; Newburg, N. R. Bis-(Cyclopentadienyl)-Titanium Dichloride-Alkylaluminum Complexes as Soluble Catalysts for the Polymerization of Ethylene. *J. Am. Chem. Soc.* **1959**, *81* (1), 81–86. https://doi.org/10.1021/ja01510a018.

(9) Long, W. P.; Breslow, D. S. Der Einfluß von Wasser Auf Die Katalytische Aktivität von Bis(π-Cyclopentadienyl)Titandichlorid-Dimethylaluminiumchlorid Zur Polymerisation von Äthylen. *Justus Liebigs Ann. Chem.* **1975**, *1975* (3), 463–469. https://doi.org/10.1002/jlac.197519750310.

(10) Sinn, H.; Kaminsky, W.; Vollmer, H. -J; Woldt, R. "Living Polymers" on Polymerization with Extremely Productive Ziegler Catalysts. *Angew. Chemie Int. Ed. English* **1980**, *19* (5), 390–392. https://doi.org/10.1002/anie.198003901.

(11) Chen, E. Y. X.; Marks, T. J. Cocatalysts for Metal-Catalyzed Olefin Polymerization: Activators, Activation Processes, and Structure−Activity Relationships. *Chem. Rev.* **2000**, *100* (4), 1391–1434. https://doi.org/10.1021/cr980462j.

(12) Sishta, C.; Hathorn, R. M.; Marks, T. J. Group 4 Metallocene-Alumoxane Olefin Polymerization Catalysts. CPMAS-NMR Spectroscopic Observation of "Cation-like" Zirconocene Alkyls. *J. Am. Chem. Soc.* **1992**, *114* (3), 1112–1114. https://doi.org/10.1021/ja00029a063.

(13) Jordan, R. F.; Dasher, W. E.; Echols, S. F. Reactive Cationical Dicyclopentadienylzirconium(IV) Complexes. *J. Am. Chem. Soc.* **1986**, *108* (7), 1718–1719. https://doi.org/10.1021/ja00267a068.

(14) Jordan, R. F.; Bajgur, C. S.; Willett, R.; Scott, B. Ethylene Polymerization by a Cationic Dicyclopentadienylzirconium(IV) Alkyl Complex. *J. Am. Chem. Soc.* **1986**, *108* (23), 7410–7411. https://doi.org/10.1021/ja00283a047.

(15) Hlatky, G. G.; Turner, H. W.; Eckman, R. R. Ionic, Base-Free Zirconocene Catalysts for Ethylene Polymerization. *J. Am. Chem. Soc.* **1989**, *111* (7), 2728–2729. https://doi.org/10.1021/ja00189a064.

(16) Jia, L.; Yang, X.; Stern, C. L.; Marks, T. J. Cationic Metallocene Polymerization Catalysts Based on Tetrakis(Pentafluorophenyl)Borate and Its Derivatives. Probing the Limits of Anion "Noncoordination" via a Synthetic, Solution Dynamic, Structural, and Catalytic Olefin Polymerization Study. *Organometallics* **1997**, *16* (5), 842–857. https://doi.org/10.1021/om960880j.

(17) Coates, G. W.; Hustad, P. D.; Reinartz, S. Catalysts for the Living Insertion Polymerization of Alkenes: Access to New Polyolefin Architectures Using Ziegler–Natta Chemistry. *Angew. Chemie Int. Ed.* **2002**, *41* (13), 2236–2257. https://doi.org/10.1002/1521-3773(20020703)41:13<2236::AID-ANIE2236>3.0.CO;2-3.

(18) Yang, X.; Stern, C. L.; Marks, T. J. Cationic Zirconocene Olefin Polymerization Catalysts Based on the Organo-Lewis Acid Tris(Pentafluorophenyl)Borane. A Synthetic, Structural, Solution Dynamic, and Polymerization Catalytic Study. *J. Am. Chem. Soc.* **1994**, *116* (22), 10015–10031. https://doi.org/10.1021/ja00101a022.

(19) Jia, L.; Yang, X.; Ishihara, A.; Marks, T. J. Protected (Fluoroaryl)Borates as Effective Counteranions for Cationic Metallocene Polymerization Catalysts. *Organometallics* **1995**, *14*, 3135–3137.

(20) Gordon, C. P.; Shirase, S.; Yamamoto, K.; Andersen, R. A.; Eisenstein, O.; Copéret, C. NMR Chemical Shift Analysis Decodes Olefin Oligo- and Polymerization Activity of D0 Group 4 Metal Complexes. *Proc. Natl. Acad. Sci. U. S. A.* **2018**, *115* (26), E5867–E5876. https://doi.org/10.1073/pnas.1803382115.

(21) Brookhart, M.; Green, M. L. H.; Parkin, G. Agostic Interactions in Transition Metal Compounds. *Proc. Natl. Acad. Sci. U. S. A.* **2007**, *104* (17), 6908–6914. https://doi.org/10.1073/pnas.0610747104.

(22) Amin, S. B.; Marks, T. J. Versatile Pathways for in Situ Polyolefin Functionalization with Heteroatoms: Catalytic Chain Transfer. *Angew. Chemie - Int. Ed.* **2008**, *47* (11), 2006–2025. https://doi.org/10.1002/anie.200703310.

(23) Beck, S.; Brintzinger, H. H. Alkyl Exchange between Aluminum Trialkyls and Zirconocene Dichloride Complexes - A Measure of Electron Densities at the Zr Center. *Inorganica Chim. Acta* **1998**, *270* (1–2), 376–381. https://doi.org/10.1016/s0020-1693(97)05871-4.

(24) Bochmann, M.; Lancaster, S. J. Monomer–Dimer Equilibria in Homo- and Heterodinuclear Cationic Alkylzirconium Complexes and Their Role in Polymerization Catalysis. *Angew. Chemie Int. Ed. English* **1994**, *33* (15–16), 1634–1637. https://doi.org/10.1002/anie.199416341.

(25) Baldwin, S. M.; Bercaw, J. E.; Brintzinger, H. H. Alkylaluminum-Complexed Zirconocene Hydrides: Identification of Hydride-Bridged Species by NMR Spectroscopy. *J. Am. Chem. Soc.* **2008**, *130* (51), 17423–17433. https://doi.org/10.1021/ja8054723.

(26) Baldwin, S. M.; Bercaw, J. E.; Henling, L. M.; Day, M. W.; Brintzinger, H. H. Cationic Alkylaluminum-Complexed Zirconocene Hydrides: NMR-Spectroscopic Identification, Crystallographic Structure Determination, and Interconversion with Other Zirconocene Cations. *J. Am. Chem. Soc.* **2011**, *133* (6), 1805–1813. https://doi.org/10.1021/ja1050428.

(27) Marks, T. J. Surface-Bound Metal Hydrocarbyls. Organometallic Connections Between Heterogeneous and Homogeneous Catalysis. *Acc. Chem. Res.* **1992**, *25* (2), 57–65. https://doi.org/10.1021/ar00014a001.

(28) McDaniel, M. P.; Jensen, M. D.; Jayaratne, K.; Collins, K. S.; Benham, E. A.; McDaniel, N. D.; Das, P. K.; Martin, J. L.; Yang, Q.; Thorn, M. G.; Masino, A. P. Metallocene Activation by Solid Acids. In *Tailor-Made Polymers: Via Immobilization of Alpha-Olefin Polymerization Catalysts*; John Wiley and Sons, 2008; pp 171–210. https://doi.org/10.1002/9783527621668.ch7.

(29) He, M. Y.; Marks, T. J.; Xiong, G.; Toscano, P. J.; Burwell, R. L. Supported Organoactinides. Surface Chemistry and Catalytic Properties of Alumina-Bound (Cyclopentadienyl)-and (Pentamethylcyclopentadienyl)Thorium and -Uranium Hydrocarbyls and Hydrides. *J. Am. Chem. Soc.* **1985**, *107* (3), 641–652. https://doi.org/10.1021/ja00289a016.

(30) He, M. Y.; Burwell, R. L.; Marks, T. J. Surface and Catalytic Chemistry of Organoactinldes. Evidence for Surface-Stabilized Alkylidenes. *Organometallics* **1983**, *2* (4), 566–569. https://doi.org/10.1021/om00076a023.

(31) Bowman, R. G.; Nakamura, R.; Fagan, P. J.; Burwell, R. L.; Marks, T. J. Catalytic Activity of Supported F-Element Organometallic Complexes. *J. Chem. Soc. Chem. Commun.* **1981**, No. 6, 257–258. https://doi.org/10.1039/c39810000257.

(32) Dahmen, K.-H.; Hedden, D.; Burwell, R. L.; Marks, T. J. Organometallic Molecule-Support Interactions. Highly Active Organozirconium Hydrogenation Catalysts and the Formation of Cationic Species on Alumina Surfaces. *Langmuir* **1988**, *4*, 1212–1214.

(33) Jezequel, M.; Dufaud, V.; Ruiz-Garcia, M. J.; Carrillo-Hermosilla, F.; Neugebauer, U.; Niccolai, G. P.; Lefebvre, F.; Bayard, F.; Corker, J.; Fiddy, S.; Evans, J.; Broyer, J. P.; Malinge, J.; Basset, J. M. Supported Metallocene Catalysts by Surface Organometallic Chemistry. Synthesis, Characterization, and Reactivity in Ethylene Polymerization of Oxide-Supported Mono- and Biscyclopentadienyl Zirconium Alkyl Complexes: Establishment of Structure/Reactivity R. *J. Am. Chem. Soc.* **2001**, *123* (15), 3520–3540. https://doi.org/10.1021/ja000682q.

(34) Egger, K. W. Kinetics of the Intramolecular Four-Center Elimination of Isobutylene from Triisobutylaluminum in the Gas Phase. *J. Am. Chem. Soc.* **1969**, *91* (11), 2867–2871. https://doi.org/10.1021/ja01039a007.

(35) Kermagoret, A.; Kerber, R. N.; Conley, M. P.; Callens, E.; Florian, P.; Massiot, D.; Copéret, C.; Delbecq, F.; Rozanska, X.; Sautet, P. Triisobutylaluminum: Bulkier and yet More Reactive towards Silica Surfaces than Triethyl or Trimethylaluminum. *Dalt. Trans.* **2013**, *42* (35), 12681. https://doi.org/10.1039/c3dt51005k.

(36) Pelletier, J.; Espinas, J.; Vu, N.; Norsic, S.; Baudouin, A.; Delevoye, L.; Trébosc, J.; Le Roux, E.; Santini, C.; Basset, J. M.; Gauvin, R. M.; Taoufik, M. A Well-Defined Silica-Supported Aluminium Alkyl through an Unprecedented, Consecutive Two-Step Protonolysis-Alkyl Transfer Mechanism. *Chem. Commun.* **2011**, *47* (10), 2979–2981. https://doi.org/10.1039/c0cc04986g.

(37) Sauter, D. W.; Popoff, N.; Bashir, M. A.; Szeto, K. C.; Gauvin, R. M.; Delevoye, L.; Taoufik, M.; Boisson, C. The Design of a Bipodal Bis(Pentafluorophenoxy)Aluminate Supported on Silica as an Activator for Ethylene Polymerization Using Surface Organometallic Chemistry. *Chem. Commun.* **2016**, *52* (26), 4776–4779. https://doi.org/10.1039/c6cc00060f.

(38) González-Hernández, R.; Jianfang, C.; Charles, R.; Pérez-Camacho, O.; Kniajanski, S.; Collins, S. Catalytic System for Homogeneous Ethylene Polymerization Based on Aluminohydride-Zirconocene Complexes. *Organometallics* **2006**, *25* (22), 5366–5373. https://doi.org/10.1021/om0604730.

(39) Stockland, R. A.; Jordan, R. F. Reaction of Vinyl Chloride with a Prototypical Metallocene Catalyst: Stoichiometric Insertion and β-Cl Elimination Reactions with Rac-(EBI)ZrMe+ and Catalytic Dechlorination/Oligomerization to Oligopropylene by Rac-(EBI)ZrMe2/MAO. *J. Am. Chem. Soc.* **2000**, *122* (26), 6315–6316. https://doi.org/10.1021/ja000939k.

(40) Stockland, R. A.; Foley, S. R.; Jordan, R. F. Reaction of Vinyl Chloride with Group 4 Metal Olefin Polymerization Catalysts. *J. Am. Chem. Soc.* **2003**, *125* (3), 796–809. https://doi.org/10.1021/ja028530d.

(41) Watson, L. A.; Yandulov, D. V.; Caulton, K. G. C-D0 (D0 = π-Donor, F) Cleavage in H2C=CH(D0) by (Cp2ZrHCl)n: Mechanism, Agostic Fluorines, and a Carbene of Zr(IV). *J. Am. Chem. Soc.* **2001**, *123* (4), 603–611. https://doi.org/10.1021/ja0024340.

(42) Comas Vives, A.; Schwarzwälder, M.; Copéret, C.; Sautet, P. Carbon−Carbon Bond Formation by Activation of CH3F on Alumina. *J. Phys. Chem. C* **2015**, *119* (13), 7156–7163. https://doi.org/10.1021/jp512598p.

(43) Butler, L. G.; Keiter, E. A. Interpretation of Electric Field Gradients at Deuterium as Measured by Solid-State NMR Spectroscopy. *J. Coord. Chem.* **1994**, *32* (1–3), 121–134. https://doi.org/10.1080/00958979408024242.

(44) Pyykkö, P.; Pedersen, B. Measurement of the Deuteron Quadrupole Coupling Constant in LiAlD4. *Chem. Phys. Lett.* **1968**, *2* (5), 297–298. https://doi.org/10.1016/0009-2614(68)80079-X.

(45) Jarrett, W. L.; Farlee, R. D.; Butler, L. G. Observation of Bridging and Terminal Metal Hydrides by Solid-State Deuterium NMR Spectroscopy: Application to Bis(Cyclopentadienyl)Zirconium Dideuteride. *Inorg. Chem.* **1987**, *26* (1), 1381–1383.

(46) Liang, F.; Schmalle, H. W.; Fox, T.; Berke, H. Hydridic Character and Reactivity of Di[1,2-Bis(Dimethylphosphino)Ethane]Hydridonitrosylmolybdenum(0). *Organometallics* **2003**, *22* (17), 3382–3393. https://doi.org/10.1021/om021032t.

(47) Macholl, S.; Matthes, J.; Limbach, H. H.; Sabo-Etienne, S.; Chaudret, B.; Buntkowsky, G. High-Resolution 2H MAS NMR Applied to Deuterium Analogs of Hydrido H2-Dihydrogen Complexes. *Solid State Nucl. Magn. Reson.* **2009**, *36* (3), 137–143. https://doi.org/10.1016/j.ssnmr.2009.08.001.

(48) Gutmann, T.; Walaszek, B.; Yeping, X.; Wächtler, M.; Del Rosal, I.; Grünberg, A.; Poteau, R.; Axet, R.; Lavigne, G.; Chaudret, B.; Limbach, H. H.; Buntkowsky, G. Hydrido-Ruthenium Cluster Complexes as Models for Reactive Surface Hydrogen Species of Ruthenium Nanoparticles. Solid-State 2H NMR and Quantum Chemical Calculations. *J. Am. Chem. Soc.* **2010**, *132* (33), 11759–11767. https://doi.org/10.1021/ja104229a.

(49) Prack, E.; Okeefe, C. A.; Moore, J. K.; Lai, A.; Lough, A. J.; Macdonald, P. M.; Conradi, M. S.; Schurko, R. W.; Fekl, U. A Molecular Rotor Possessing an H-M-H "Spoke" on a P-M-P "Axle": A Platinum(II) Trans-Dihydride Spins Rapidly Even at 75 K. *J. Am. Chem. Soc.* **2015**, *137* (42), 13464–13467. https://doi.org/10.1021/jacs.5b08213.

(50) Manriquez, J. M.; McAlister, D. R.; Sanner, R. D.; Bercaw, J. E. Reduction of Carbon Monoxide Promoted by Alkyl and Hydride Derivatives of Permethylzirconocene. *J. Am. Chem. Soc.* **1978**, *100* (9), 2716–2724. https://doi.org/10.1021/ja00477a025.

(51) Yang, X.; Stern, C. L.; Marks, T. J. Cationic Metallocene Polymerization Catalysts. Synthesis and Properities of the First Base-Free Zirconocene Hydride. *Angew. Chemie Int. Ed. English* **1992**, *31* (10), 1375–1377. https://doi.org/10.1002/anie.199213751.

(52) Copéret, C.; Comas-Vives, A.; Conley, M. P.; Estes, D. P.; Fedorov, A.; Mougel, V.; Nagae, H.; Núnez-Zarur, F.; Zhizhko, P. A. Surface Organometallic and Coordination Chemistry toward Single-Site Heterogeneous Catalysts: Strategies, Methods, Structures, and Activities. *Chem. Rev.* **2016**, *116* (2), 323–421. https://doi.org/10.1021/acs.chemrev.5b00373.

(53) Brown, H. C.; McFarlin, R. F. The Reaction of Lithium Aluminum Hydride with Alcohols. Lithium Tri-t-Butoxyaluminohydride as a New Selective Reducing Agent. *J. Am. Chem. Soc.* **1958**, *80* (20), 5372–5376. https://doi.org/10.1021/ja01553a013.

(54) Pool, J. A.; Bradley, C. A.; Chirik, P. J. A Convenient Method for the Synthesis of Zirconocene Hydrido Chloride, Isobutyl Hydride, and Dihydride Complexes Using Tert-Butyl Lithium. *Organometallics* **2002**, *21* (6), 1271–1277. https://doi.org/10.1021/om011090z.